PHYSICAL MODEL ANALYSIS OF ICEBERG SCOUR IN DRY AND SUBMERGED SAND

MICHAEL J. PAULIN, B.Eng.

PHYSICAL MODEL ANALYSIS OF ICEBERG SCOUR IN DRY AND SUBMERGED SAND

by

© Michael J. Paulin, B.Eng.

A thesis submitted to the School of Graduate
Studies in partial fulfilment of the
requirements for the degree of
Master of Engineering

Faculty of Engineering and Applied Science
Memorial University of Newfoundland
April 1992

St. John's Newfoundland Canada

ISBN 0-315-73337-3

Abstract

Ice scour is still a phenomena of great concern in the development of offshore oil and gas fields located in a cold ocean environment. Ice scour could also create problems for power cables or pipelines which pass through inland waters such as the Great Lakes. Cables, pipelines, and wellheads are in danger offshore. Direct impact between ice and a subsea installation will most likely cause damage. A seabed installation, such as buried pipeline, might be subjected to additional loading or intolerable displacements through close proximity of an ice keel. The question still remains as to how deep is safe.

In an attempt to further understand the ice scour process, a series of four physical model tests was carried out at Memorial University's scour tank facility. The first two tests were conducted in a clean, dry silica sand while the remaining two were conducted in the same sand in a submerged state. The objectives of this experimental program were to measure forces and pressures on the model, to measure the response of the soil in the testbed, and, most importantly, to measure displacements in the testbed below the scour.

The measured results compare well with computed values. The results have also been compared with previous works and models. The analysed experimental results show that there is seabed response and displacement up to 3 1/2 scour cut depths below the unscoured testbed surface. Finally, it was observed that the scouring process was similar for tests in both the dry and submerged state; measured forces and loads less for the submerged tests.

Acknowledgements

This thesis was completed at Memorial University of Newfoundland through funding made available by the Natural Sciences and Engineering Research Council of Canada. Funding in the form of a university bursary from my supervisors, a Career Development Award from the Government of Newfoundland and Labrador, a F.A. Aldrich Alumni Award from the M.U.N. Alumni Association, and a C-CORE Fellowship from C-CORE are all gratefully acknowledged.

I am greatly thankful to my supervisors, Dr. Jack Clark, Director of C-CORE, and Dr. Farrokh Poorooshasb, Assistant Professor of Civil Engineering and Research Engineer at C-CORE, under whose guidance and supervision the project was carried out. Thanks to Dr. Poorooshasb for the theoretical lessons and great patience shown in the beginning of my program. Thanks to both for the invaluable comments and suggestions during the review of this thesis

I would also like to thank Mr. Chris Woodworth-Lynas for his help during my program of study and also fellow graduate student, Mr. Paul Lach for his helpful conversations. Sincere thanks go out to the faculty technical personnel and the staff of technical services, without whose help, understanding, and cooperation, the experimental program might have taken much longer. Finally, thanks to all my fellow graduate students who took time out of their busy schedules to lend those extra pair of hands that every graduate student needs sometime during the course of his study.

Contents

List of Figures

List of Tables

List of Symbols

A_B	cross-sectional area of berms
A_{LB}	cross-sectional area of left berm
A_{RB}	cross-sectional area of right berm
A_T	cross-sectional area of trough
B	breadth of foundation
B'	effective breadth of the foundation
c	apparent cohesion intercept
c'	effective cohesion intercept
c'	modified cohesion intercept for local shear bearing capacity calculations
c_u	undrained shear strength
cm	centimeter
C_c	curvature coefficient
C_u	uniformity coefficient
d_c, d_q, d_γ	bearing capacity depth factors
D	grain diameter
D	depth of foundation beneath ground
D_f	depth of foundation beneath ground
D_1	average depth of the scour below the unscoured surface
D_2	berm height above unscoured surface
D_3	average depth of scour below peak of berm
D_{10}	effective grain size
e	eccentricity of load along the breadth of foundation
e	void ratio

e_L	longitudinal eccentricity of the foundation load
e_{max}	void ratio in loosest state
e_{min}	void ratio in densest state
$F_{H(AVG)}$	average of F_{H1} and F_{H2}
F_{H1}	maximum horizontal force calculated through the dead wedge
F_{H2}	maximum horizontal force calculated acting directly on the model face
F_V	total vertical force acting on the model
F_{V1}	vertical force acting on the horizontal face of the model
F_{V2}	vertical force acting through the dead wedge of soil
g	gravity
H	height of retaining wall
i_c, i_q, i_γ	bearing capacity load inclination factors
I_D	density index
km	kilometer
kPa	kiloPascal
K_p	coefficient of passive earth pressure
L	length of foundation
L'	effective length of the foundation
L_L	length of soil-model interface
L_W	length of dead wedge
L_1	length of the horizontal face of the model
L_2	length of the dead wedge of soil
m	meter
m_B, m_L	load inclination exponents
mm	millimeter

N	Newton
N_c, N_q, N_γ	bearing capacity factors
N'_c, N'_q, N'_γ	modified bearing capacity factors
p	pressure acting normal to model face
p_H	horizontal component of pressure acting on the model face
p_V	vertical component of pressure acting on the model face
p_1	average pressure on the horizontal face of the model
p_2	vertical component of average pressure on the inclined face of the model
P	horizontal component of inclined foundation load
P_h	maximum horizontal force measured on the model
P_p	passive earth pressure resistance
q	bearing capacity
q	applied axial pressure
q_d	bearing capacity
q_p	point resistance pressure
Q	applied axial load
Q	vertical component of inclined foundation load
Q_p	point resistance force
s	second
s	plate-grouser length
s_c, s_q, s_γ	bearing capacity shape factors
S_r	degree of saturation
t	time
v	velocity
v	volts

w	water content
w_{exp}	water content of air-dried sand
W	width of model
W_1	width of scour trough
W_2	peak to peak width of berms
W_3	apparent scour influence width
α	outer berm angle
α	inclination of the slope of backfill with horizontal
β	inner berm angle
β	angle of failure surface with horizontal
β	characteristic angle of a plate-grouser
δ	angle of wall friction
δ	inclination of load
δ	soil-model friction angle
γ	unit weight
γ'	submerged unit weight
γ_d	dry unit weight
γ_{d-min}	minimum dry unit weight
γ_{d-max}	maximum dry unit weight
γ_{exp}	experimental unit weight
γ_s	unit weight of solid particles
γ_{sat}	saturated unit weight
γ_w	unit weight of water
ϕ	apparent angle of internal friction
ϕ'	effective angle of internal friction

ϕ'	modified internal angle of friction
ϕ_{exp}	internal angle of friction at γ_{exp}
ρ	density
ρ'	submerged density
ρ_d	dry density
ρ_{d-min}	minimum dry density
ρ_{d-max}	maximum dry density
ρ_{exp}	experimental density
ρ_s	density of solid particles
ρ_{sat}	saturated unit weight
ρ_w	density of water
σ	total normal stress
σ'	effective normal stress
τ	shear stress
θ	instantaneous direction of plate-grouser movement with the horizontal at failure
θ	inclination of the back face of retaining wall with the vertical
ξ	angle at which the resultant force on a plate-grouser is inclined to the vertical
$\zeta_c, \zeta_q, \zeta_\gamma$	foundation shape correction factors
$\zeta_{ci}, \zeta_{qi}, \zeta_{\gamma i}$	foundation load inclination factors

Chapter 1

Introduction

1.1 General

The search for oil, gas, and other natural resources has led to searches in the oceans to supplement land based reserves. Economical exploitation of these natural resources through the use of floating structures or seabed installations will depend on overcoming seabed geotechnical and oceanographical problems.

The engineer involved in design for an offshore environment should be aware that certain natural phenomena exist that may be hazardous to a project. Potential hazards which are present in an ocean environment must be evaluated. This evaluation will determine whether or not a feature is truly a hazard or merely a constraint. Sea ice, icebergs, freezing spray, currents, waves, tides, seabed morphology, and sediment characteristics are all examples of factors which must be considered when involved with offshore activity.

1.2 Sea Ice and Icebergs

Two types of ice are commonly found in a cold ocean environment such as that found on Canada's offshore. The first is glacial ice in the form of icebergs and the

second is sea ice which is the result of the freezing of seawater in cold climates.

Most of the icebergs encountered in the Western North Atlantic originate from glaciers in Greenland, but some also find their way down from the eastern Canadian Arctic archipelago. The Greenland ice cap can produce as many as 40,000 icebergs per year but normally 10,000 to 30,000 are produced annually (Nadreau, 1986).

The drift pattern of an iceberg depends on a number of phenomena, some of which are ocean currents, bottom topography, wind, wind generated currents, and the Coriolis effect. Of these, ocean currents are the main factor (NORDCO, 1975). The usual drift pattern of a Greenland iceberg bound for the Grand Banks is shown in Figure 1.1. Icebergs follow the West Greenland Current to the north end of Baffin Bay where they then turn southward with the Baffin Island Current. During this journey south, the icebergs may be diverted by secondary currents and spend some time in sounds and straits. They finally continue their journey by following the Labrador Current which leads them onto the Grand Banks (Murray, 1969). Along the Labrador Coast, 500 to 2500 icebergs are spotted annually and this area is sometimes known as *iceberg alley* (Gustajtis, 1979).

Of all the icebergs produced by the Greenland ice cap, only an average of 400 drift into the Grand Banks region each year (Dinsmore, 1972). Icebergs begin to deteriorate and melt when they feel the effects of the North Atlantic Current and the Gulf Stream and the period of time for which they can exist depends primarily upon sea temperature and sea state.

Sightings off the northeast coast of Newfoundland have estimated some bergs to be of the order of tens of millions of tons but these huge floating masses of ice often run aground and break into smaller pieces before reaching the Grand Banks region. Other sources have reported sightings in the order of 8 million tons near the Grand

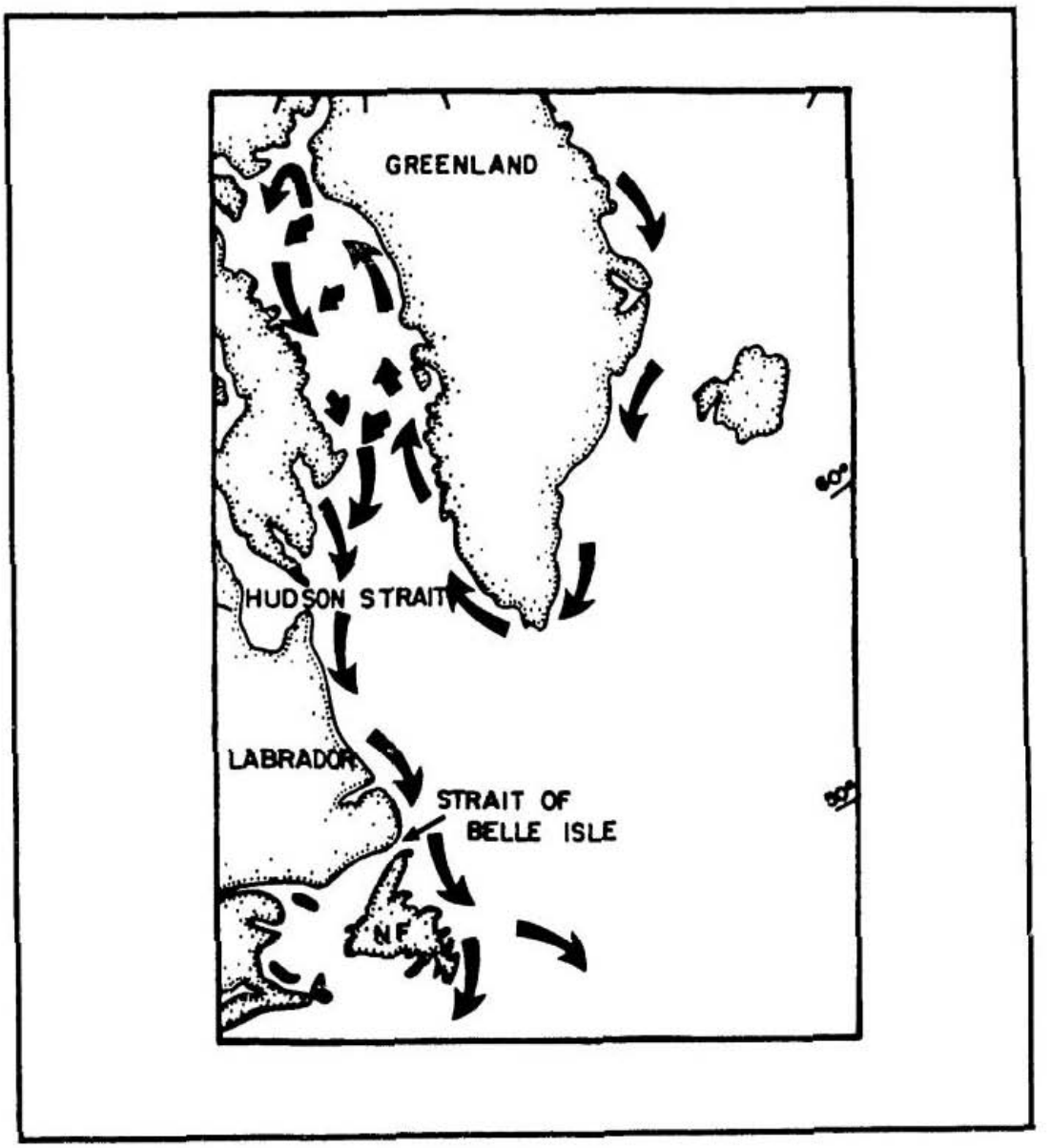

Figure 1.1: Drift Pattern for Canadian East Coast Icebergs (After Murray, 1969).

Banks, but these are rare (Venkatesh and El-Tahan, 1988). The size distribution of 232 icebergs tracked by radar from drilling sites on the Grand Banks during the period of 1984 to 1987 are presented in Table 1.1.

Table 1.1: Iceberg Sightings from Grand Banks Drill Sites, 1984 to 1987 (After Venkatesh and El-Tahan, 1988).

Mass Range (tonnes)	No. of Sightings
25 - 275	9
275 - 2750	32
2750 - 27,500	51
27,500 - 275,000	64
275,000 - 2,750,000	59
2,750,000 - 27,500,000	17

Sea ice is the ice of concern in the Beaufort Sea. Annual freezeup along the coast of the Beaufort Sea is widely varied but could occur as early as September 1st and breakup could occur as late as the end of August (Kovacs and Mellor, 1974). Sea ice in the Beaufort Sea has been subdivided into three zones by Wadhams (1975). The Fast Ice Zone extends to the 18 to 20 m bathymetric contour. It experiences ridging and hummocking during early winter storms but is eventually frozen in place. The Shear Zone extends from the edge of the Fast Ice Zone to the edge of the continental shelf. This zone is continuously changing through much ridging and hummocking. Seaward, beyond this zone, is the Polar Pack Ice Zone. During the winter, the Polar Pack Ice Zone is for the most part covered with multi-year ice. These zones are shown in Figure 1.2. Sea ice which is driven onto itself in the Shear Zone will tend to pile up creating a pressure ridge which has a keel extending below the water surface. Pressure ridges are driven primarily by ocean currents and secondarily by wind, wind generated currents, and loading from other ice. These pressure ridges are classified

into either first year or multi-year pressure ridges. These ridges (and thus their keels) can grow to a very large size and therefore, if they enter shallow areas, they might ground. A large pressure ridge has been described in the literature (Wright et al, 1978) in which the ridge was 150 m in length, had a sail height of 11 m and had a keel depth over 31 m.

1.3 Ice Scour

Driving forces may direct icebergs and pressure ridge keels into areas in which their keel draft is greater than the depth of the water. If this is the case, the keel comes in contact with the seabed and, depending on the strength of the seabed and the driving forces, may continue moving, forcing the keel into the sea bottom.

Ice scours are created when an iceberg or pressure ridge keel moves while in contact with the seabed. These scours are of great concern in the development of oil and gas deposits in ice infested waters such as on the Grand Banks or in the Arctic. Scouring could easily rupture a pipeline on the seabed or destroy a subsea installation. Buried pipelines could be affected as well if they are displaced through subscour soil movements or subjected to additional loading during scouring. The work presented in this thesis is intended to give further insight into this scouring process.

Physical modelling is one means by which further information can be gained into the ice scour process and is the topic of this thesis. Through model analysis, insight may be gained into forces acting on a scouring keel, the stresses in the soil beneath the scouring model, and displacements below the scour. This is all pertinent information in the design and analysis of seabed installations for an ice scoured environment.

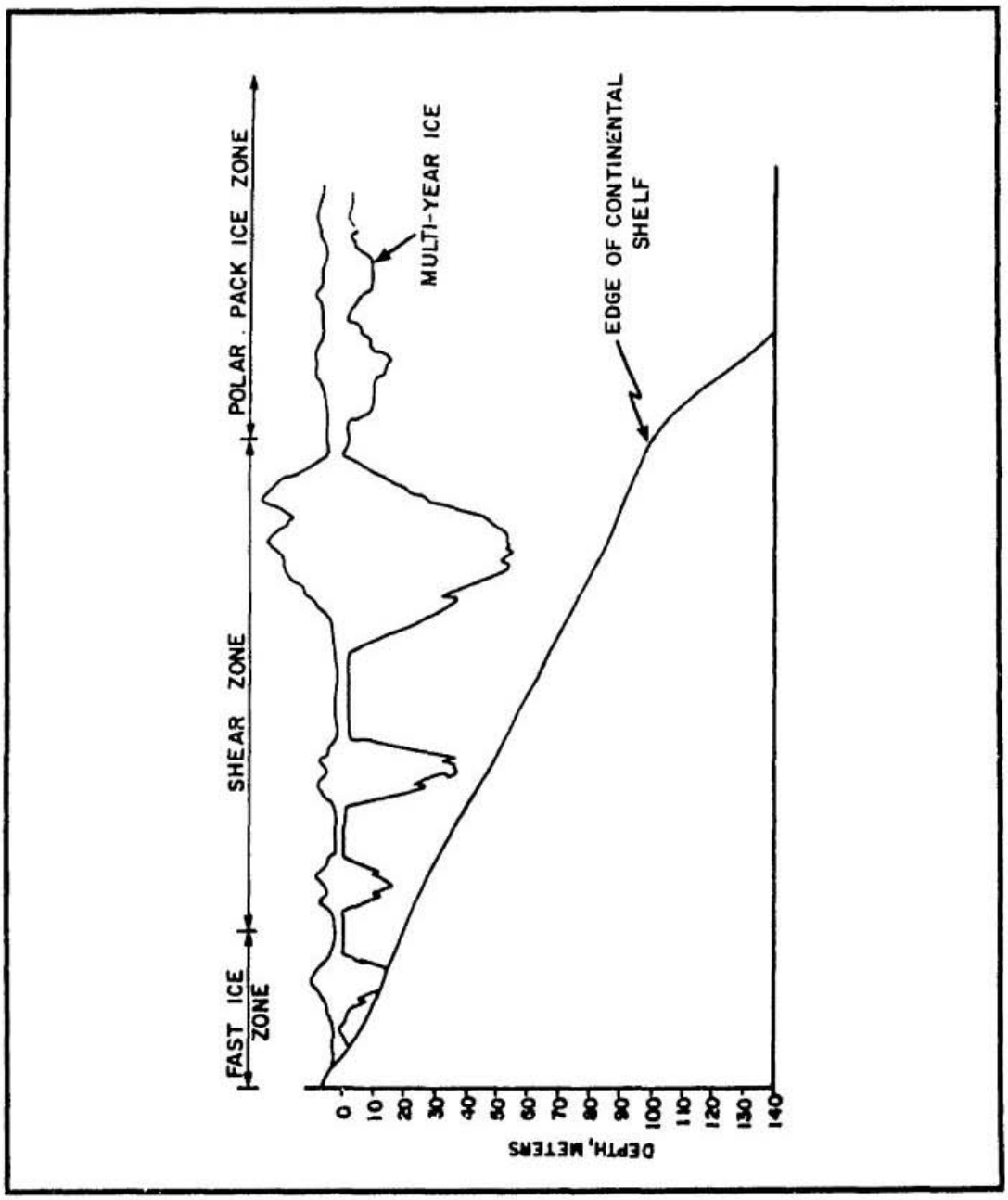

Figure 1.2: Beaufort Sea Winter Ice Zones (After Wadhams, 1975).

1.4 Thesis Outline

The organization of this thesis is divided into eight chapters in an attempt to logically proceed through the reasoning behind the work, the work itself, the results, and the conclusions arising from the results.

Chapter 2 reviews the literature relevant to this study concentrating on North American regions. Different areas are covered in which scouring occurs or has occurred, how the scours were formed, and their descriptions. The later part of the chapter looks at suggested methods of protection against scour and concludes with a look at the research and studies which have been carried out to date on the subject.

Chapter 3 states the experimental objectives and outlines the scope of the experimental program.

Chapter 4 describes the experimental facilities and equipment which were used including the scour tank facilities, the model, instrumentation, and the data acquisition system.

Chapter 5 outlines the experimental procedures followed during the various stages of the experimental program.

Chapter 6 presents the results obtained from the experimental program.

Chapter 7 analyses these results using basic geotechnical and soil mechanic principles and compares the results to those obtained from other test programs.

The thesis closes with a summary, conclusions, recommendations for future research, and a description of current research, all of which is contained in Chapter 8.

Chapter 2

Literature Review

2.1 General

Charles Darwin (1855) was one of the first scientists to hypothesize about the driving mechanisms behind icebergs and their ability to scour or create grooves in the seabed. Since then, these features, incised into the seabed by grounded ice, have been called various names in the literature. Iceberg marks, ice gouges, ice scours, ice grooves, iceberg furrow marks, and iceberg plough marks are some of the names associated with such features. In this thesis, the name scour is preferred, whether it has been created by an iceberg or a pressure ridge keel. Figure 2.1 shows areas in the world where scouring is known to exist and where it is thought to exist.

Some differences exist between these features although they are generally characterized as a U, V, or U-shaped trough surrounded by berms on either side (depending on the seabed material the berms may not be present). The shape depends on the nature of the seabed, the shape of the keel, and the depth of the sea bottom along with the draft and speed of the iceberg. Another factor which must be taken into account is the strength of the ice. If the ice is weak as compared to the strength of the seabed, then, as the keel comes in contact with the seabed, a piece of the ice keel

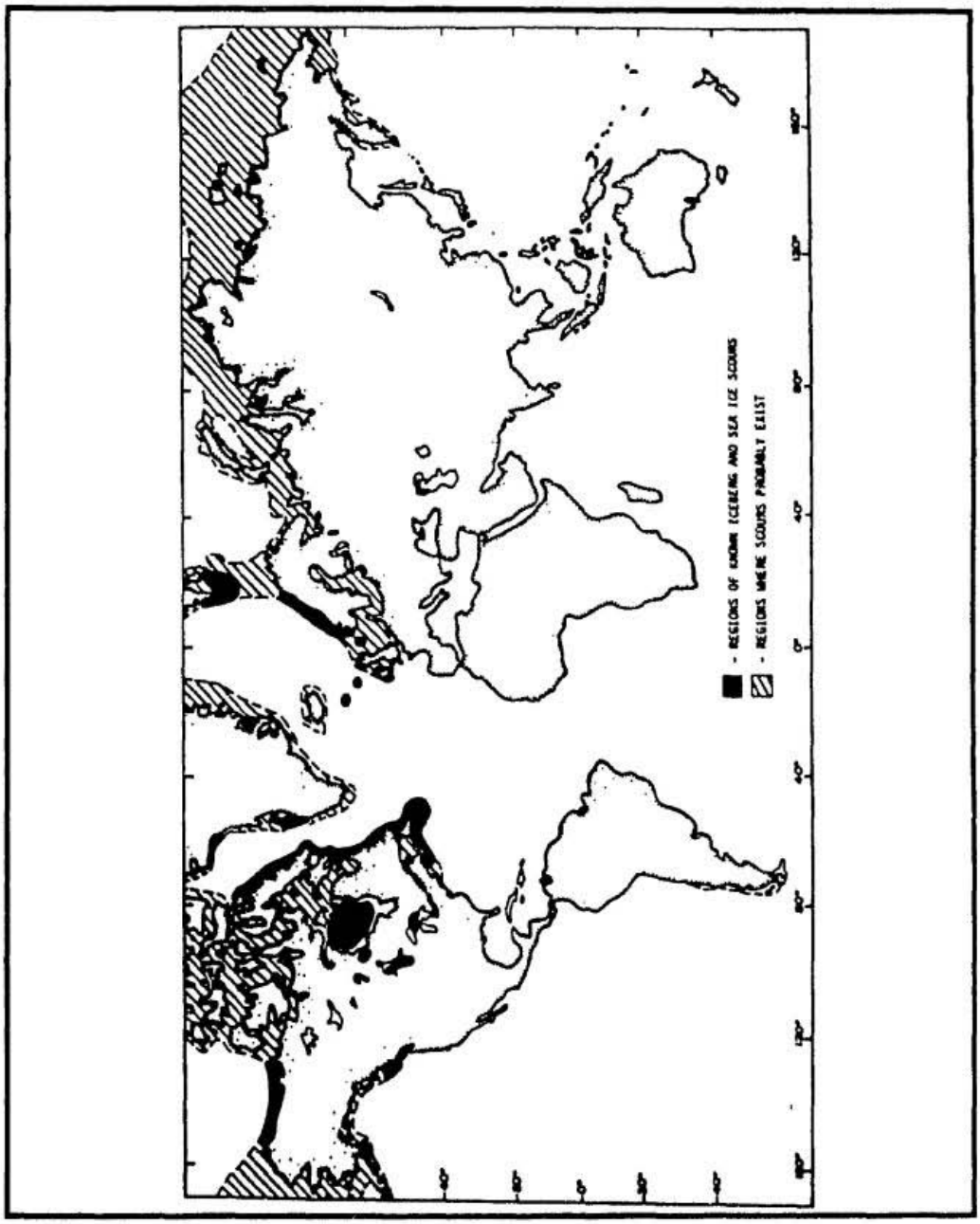

Figure 2.1: Areas of Probable and Known Ice Scours (Diagram Courtesy of C. Woodworth-Lynas, C-CORE).

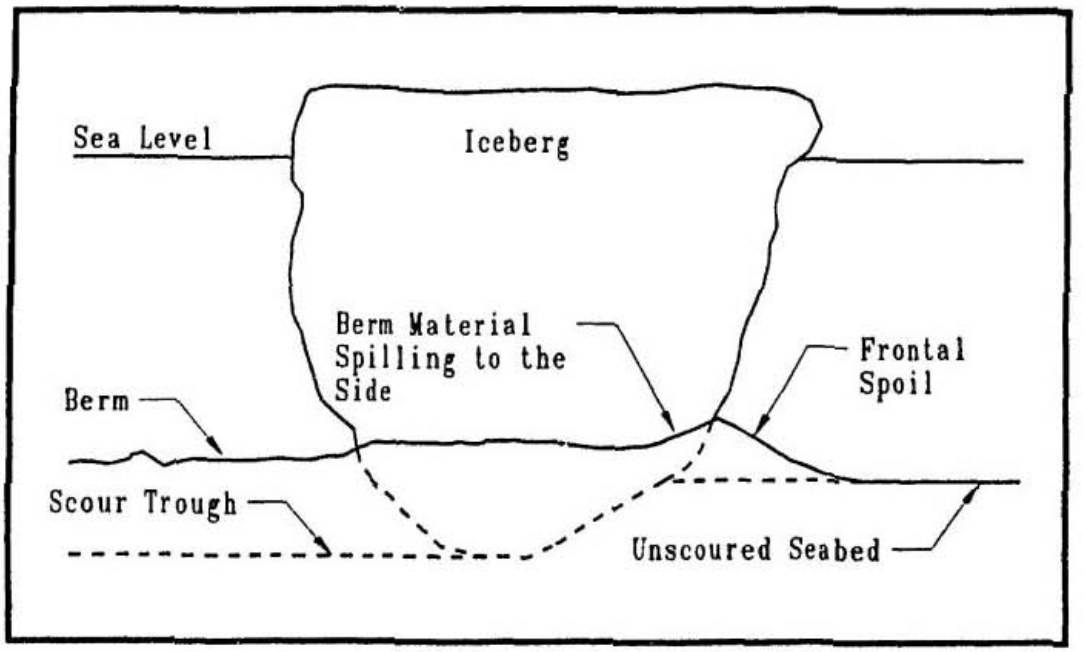

Figure 2.2: Profile View of an Iceberg Scouring Event.

might shear off and the iceberg or pressure ridge will continue to drift. Figure 2.2 depicts an iceberg scouring event. As the iceberg scours, it throws material up in front of it through a bulldozing or gouging action and may also plough some material under. The material which is built up in front of the keel may spill to the sides creating part of the berm.

Analysis of ice scours is important in order to determine risks and requirements associated with seabed structures and installations. Data collection can be made through sidescan sonograms, seismic work, manned submersible observations, or ROV observations. From these observations, data can be analysed on the types of scours and their characteristics. A sidescan sonogram of a scoured seabed is shown in Figure 2.3.

One method of scour analysis includes repetitive mapping surveys of the seabed

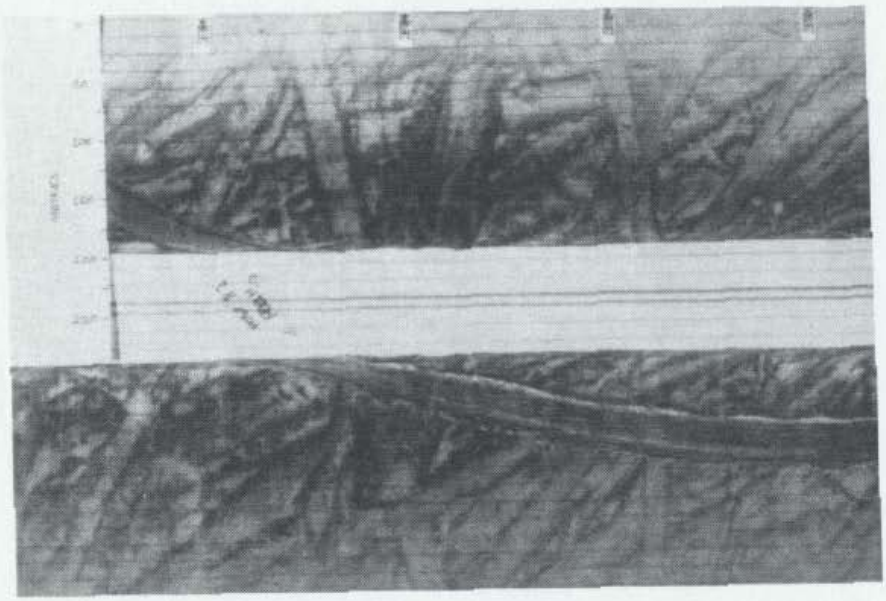

Figure 2.3: Sidescan Sonogram Showing a Scoured Seabed (Photo Courtesy of C. Woodworth-Lynas, C-CORE).

as conducted by Woodworth-Lynas and Barrie (1985). By comparing the sidescan records obtained from year to year, new scours created during the past year can be distinguished and a new scouring rate for that year calculated. Woodworth-Lynas (1983) has used cross-cutting relationships to determine the relative ages of scours. Other methods of dating scours include the dating of biogenic sediment material in the scours or using infilling rates and the amount of infill in the scour to date the scour. Ages of scours have also been estimated by direct observation and comparison with surrounding features (Barrie and Woodworth-Lynas, 1982). For example, trawling has only taken place on a large scale for the past 30 to 40 years, so if scours cross trawl marks, then the scouring must have occurred during this time.

Scours which occurred a long time ago and were created by processes which are no longer in place today are termed relict. It may not always be an easy task to determine if scours are modern or relict. If no sediment transport or migration of bedforms is taking place in an area and the scour is partially filled in, then it may be relict. Migration of bedforms tend to cover scours, therefore an area may appear free of scouring when really it is not.

2.2 Canadian East Coast Waters

The presence of iceberg scouring is most readily observed in the northern portion (above 46°N) of the Grand Banks (See Figure 2.4) in water deeper than 100 m (d'Apollonia and Lewis, 1981).

A study of iceberg scours on the Grand Banks was conducted by Fader and King (1981). To the northeast (Zone A), they identified partially buried iceberg scours in water depths greater than 110 m, but overlaying these older scours were fresh-looking scours, identified as such due to their physical appearance. They conclude

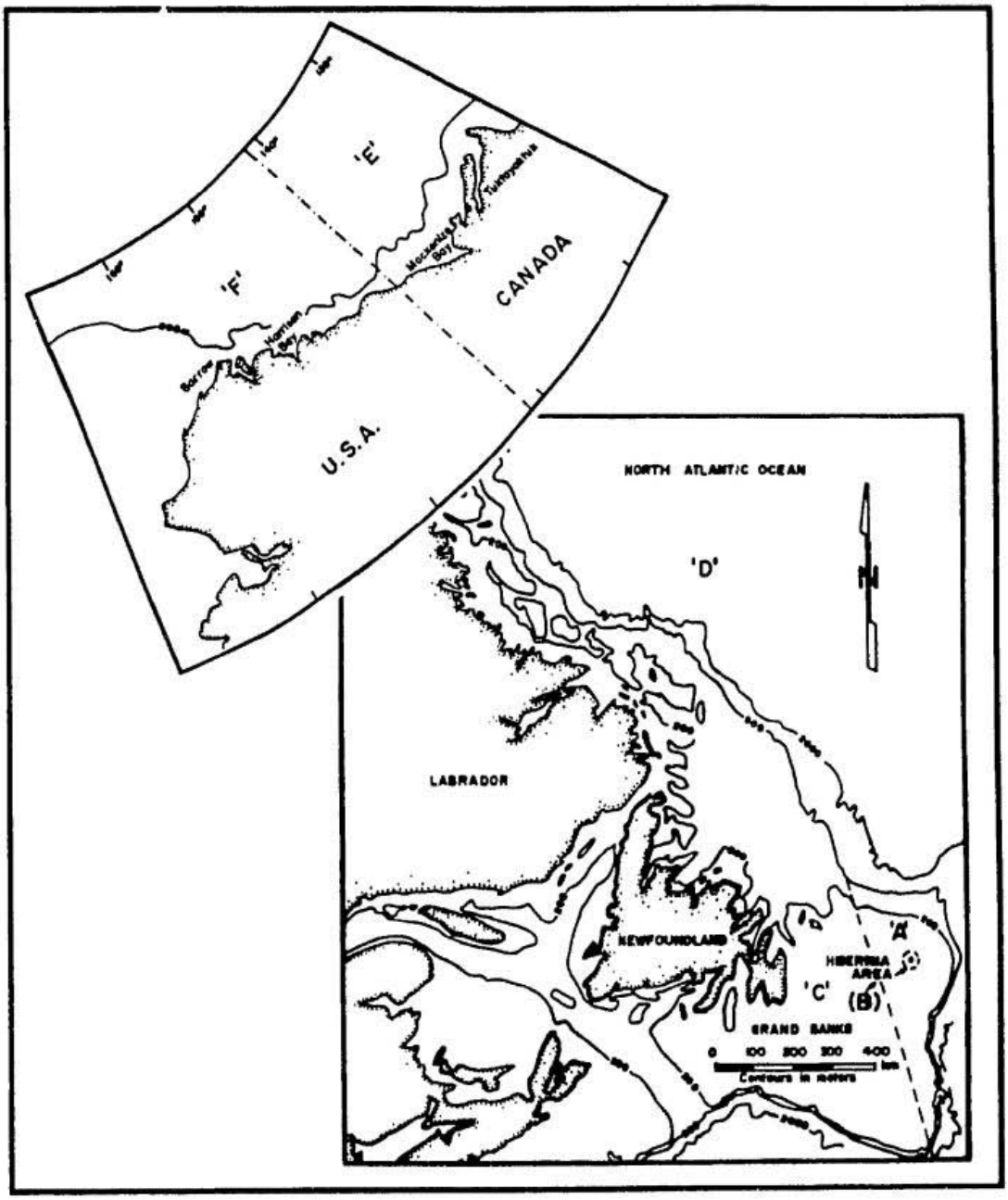

Figure 2.4: Researched Ice Scoured Areas of North America.

that scours in less than 110 m of water (and thus the Hibernia study area (Zone B)) have been created during the last 10,000 to 12,000 years, after the last low sea level stand when the sea level stood 110 to 120 m lower than it does today (Fader and King, 1981). In this zone, relict scours are only found in water depths greater than 100 to 110 m and these relict scours may be superimposed by younger scours which are found above as well as below a water depth of 100 m (King and Gillespie, 1982). In water depths less than 100 m, scour densities are very low. The scours are usually less than 1 m deep and change direction often. In deeper water, scour density and linearity increases (d'Apollonia and Lewis, 1981). The maximum scour depth and the maximum scour width for the northeastern area is 2.5 m and 124 m respectively with a total percent seabed disturbance value of approximately 17 %. Scour orientations on the northeastern Grand Banks are aligned in water deeper than 120 m but are more variable in shallow water. This reflects the increase in the control of iceberg drift patterns in deeper water by ocean currents. In shallow water, the primary driving forces are more variable, and include winds, diurnal tidal currents and storms. Therefore the scours are more irregular and lack a distinct orientation (King and Gillespie, 1982).

To the west (Zone C), partially buried iceberg scours cover extensive areas in water depths greater than 125 m. Maximum scour depths and maximum scour widths up to 9 m and 188 m respectively can be found in this area (northwest Grand Banks) and approximately 95 % of the seabed is disturbed (d'Apollonia and Lewis, 1981).

The Hibernia discovery area (Zone B), located in 80 m of water on the northeast margin of the Grand Banks, is clearly vulnerable to the threat of iceberg scouring. Two populations of iceberg scours have been recognized in this area: a partially buried scoured surface, and a set of fresh looking scours. The partially buried scours

only occur in water depths greater than 110 m. These are believed to be relict, and to have been formed during the last low sea level stand. In water depths of 60 to 160 m, fresh-looking iceberg scours are present, in some cases superimposed on the relict population. Most of these recent-looking scours are less than 1 m deep and may range from just a few meters to over 75 m wide (Lewis and Barrie, 1981). Total seabed disturbance ranges from 0 % in some areas to 15 % in other areas (Lewis and Barrie, 1981).

A recent study by Lewis and Blasco (1990), on east coast iceberg scouring, reports a mean scour depth of 1.3 m, an extreme scour depth of 5 m for scours and 10 m for pits, a mean scour width of 25 m, and an extreme scour width of 100 m. All these scours were found in water depths less than 200 m and are believed to be modern.

Pits up to 100 m in diameter (Lewis and Barrie, 1981) in the Hibernia area of the Grand Banks have been observed. Barrie et al (1986) investigated a pit which was 10 m deep and had plan dimensions of 125 by 80 m. The pit, observed with a manned submersible, was several times deeper than any of the scours located in the area. A mechanism by which these pits were created has been put forth by Clark and Landva (1986) and is described in a later section. Discontinuous berms up to 2.5 m in height around the pit were noted. The pit is estimated to be less than 100 years old and of all the pits found on the Grand Banks, only 3.5 % exceed 5 m in depth (Clark and Landva, 1986).

Relict scours on the Laurentian Channel and western Grand Banks (Zone C) have been surveyed by King (1976) in water depths between 170 and 200 m. This survey revealed iceberg scours with an average depth of approximately 2 m with the largest scours being 3 to 5 m deep. The widths were found to be highly variable but averaged 30 to 50 m with the two widest scours being 80 and 110 m across.

Iceberg scour marks are reported as widespread on the Labrador Continental Shelf (Zone D). Scours are typically greater than 1 km in length and with a maximum width of 210 m but average widths are in the range of 30 m. The depth of the scour below the berm peaks is typically less than 6 m. Scours were found in depths of more than 350 m in some locations along the coast (Harris, 1974).

Barrie (1980) studied sidescan sonograms from the northern Labrador Sea (Zone D). Modern as well as relict scours are present in water depths greater than 180 m of water. Lengths of observed scours exceeded 3 km and their paths ranged from linear to curvilinear. Average widths were approximately 30 m and the mean scour depth was 5 m, but the maximum scour width and depth reported was 200 and 17 m respectively.

Woodworth-Lynas and Barrie (1985) report on a repetitive mapping program carried out over the Labrador and Grand Banks shelf regions between 1976 and 1982. This program was useful in that it gave rates of scour and of scour degradation. Typical values obtained from this program are annual scouring rates of 3.3 % on Makkovik Bank and 4.3 % on Saglek Bank, both located on the Labrador Shelf.

2.3 Beaufort Sea

Pelletier and Shearer (1972) conducted a marine geological investigation in the Canadian Beaufort Sea (Zone E) during the summers of 1970 and 1971. During this survey, they discovered groups of parallel scours, generally in water depths of 10 to 30 m but as deep as 75 m, which they thought were caused by multiple keels of pressure ridges. These scours ranged from a few meters to tens of meters in width. They had a top-of-berm to base-of-trough relief up to 10 m and lengths up to 8 km.

Lewis (1977) studied the morphology of ice scours in the Canadian Beaufort Sea

(Zone E). He reported that the sea floor was practically covered with scours in the 15 to 40 m water depth area, but scours were present up to depths of 80 m. Scour depths ranged from 0.5 to 6 m (nominally 0.5 to 1.0 m) and widths varied from several meters to hundreds of meters. Rare occurrences are described where scour depths of 7.6 m were recorded. Relict scours in this area have been infilled and generally occur beyond the 50 m isobath.

A study of frequency and scour depth (Zone E) was conducted by Hnatiuk and Wright (1983) which determined that most of the scours had an average depth which ranged between 0.91 and 1.52 m (3 and 5 feet). The deepest scour mentioned was 9.14 m (30 feet) deep but it is also mentioned that this might be relict. Of all the scours analysed, 97 % were between 0.6 and 2.1 m (2 to 7 feet) in depth and most of the scours occurred in the 15 to 45 m (50 to 150 foot) water depth range.

More recent updates to mean dimensions of scours (Zone E) by Lewis and Blasco (1990) through analysis of sidescan sonar and echo sounder profiles suggest a mean depth of 0.5 m and a mean width of 26 m. Maximum values of these parameters are 7.1 m and 1375 m respectively. In water depths between 10 and 40 m the sea floor is covered with scours and recent-looking scours appear to occur up to water depths of 72 m.

A study conducted over 4 years by the U.S. Geological Survey (Reimnitz and Barnes, 1974) in the U.S. Beaufort Sea (Zone F) measured scours typically 0.5 to 1.0 m in depth but scours up to 5.5 m in depth have been observed. Gouges were generally oriented parallel to the bathymetric contours and the highest scour densities were observed in water depths between 10 and 30 m. Below 50 m the observed scours are believed to be relict. They also noted that the shape of a scour often changes as the ice rotates. Kovacs and Mellor (1974) reported that there are no ice keels over

Table 2.1: Scour Measurements, Various Sources.

Zone	Reported By	Water Depth (m)	Scour Width (m)			Scour Depth (m)		
			Min.	Mean	Max.	Min.	Mean	Max.
A	Fader and King, 1981	> 110	—	—	—	—	—	—
A	Fader and King, 1981	< 110	—	—	75	—	—	1
A	King and Gillespie, 1982	< 100	—	—	—	—	—	< 1
A	d'Apollonia and Lewis, 1981	All	—	—	124	—	—	2.5
B	Lewis and Barrie, 1981	60-160	3	—	75	0.5	< 1	1.2
A,B,C,D	Lewis and Blasco, 1990	< 200	—	25	100	—	1.3	5
A,B,C,D	Lewis and Blasco, 1990	< 750	—	58	330	—	1.6	11.5
C	d'Apollonia and Lewis, 1981	> 125	—	—	188	—	—	9
C	King, 1976	170-200	—	30-50	110	—	2	5
D	Harris, 1974	< 350	—	—	210	—	—	6
D	Barrie, 1980	< 200	—	30	200	—	5	17
D	Woodworth-Lynas and Barrie, 1985	< 220	—	—	—	—	—	—
E	Pelletier and Shearer, 1972	10-75	< 10	—	> 50	—	—	10†
E	Lewis, 1977	15-80	< 10	—	> 100	0.5	—	7.6
E	Hnatiuk and Wright, 1977	15-45	—	—	—	0.91	—	9.1
E	Lewis and Blasco, 1990	10-72	—	26	1375	—	0.5	7.1
F	Barnes et al, 1978	2-25	< 20	—	70	0.5	—	1.8
F	Rearic, 1982	5-25	—	—	—	—	0.18	1

† - Measured Overall Relief

60 m in depth in the U.S. Beaufort Sea today, therefore any scours found below this depth must be an extremely rare modern day event or else they must be relict.

Barnes et al (1978) conducted a study in the Beaufort Sea of Alaska (Zone F) between 1975 and 1977 as part of a repetitive mapping survey. They also found that the scour trend in their survey area was linear and parallel to the bathymetric contours. Gouge depths were observed that ranged from 0.5 to 1.8 m. Maximum observed widths were in the order of 70 m, with the majority of widths being less than 20 m. Observations of new scour events (those since the last survey) indicated they were evenly distributed and had a maximum depth of 1.2 m. New scour events varied from 10.5 to 63 scours per year per line of collected data. They estimate that (based on data that they obtained) 50 % of the seabottom would be scoured in 40 years and about 90 % would be scoured in 150 years (scour rate of 1.6 % per year).

A resurvey (4 to 5 years later) of an area in Harrison Bay, Alaska (Zone F) revealed only two new scours with a depth greater than 1 m (Rearic, 1982). From data collected, it was estimated that between 77 and 98 % of the seabed is reworked every 100 years (1.5 to 3.8 % per year). Average scour depths of new scours measured only 18 cm and an average of only 8 to 9 new scours were added to the seabed each year per kilometer of testing. The findings from Sections 2.2 and 2.3 are summarized in Table 2.1.

Table 2.1, Continued.

Zone	Reported By	Water Depth (m)	% Seabed Disturbance (Total)	% Seabed Scoured (Per Year)	Comments
A	Fader and King, 1981	> 110	—	—	Relict & Modern
A	Fader and King, 1981	< 110	—	—	Modern
A	King and Gillespie, 1982	< 100	—	—	Modern
A	d'Apollonia and Lewis, 1981	All	17	—	—
B	Lewis and Barrie, 1981	60-160	0-15	—	Relict & Modern
A,B,C,D	Lewis and Blasco, 1990	< 200	—	—	—
A,B,C,D	Lewis and Blasco, 1990	< 750	—	—	—
C	d'Apollonia and Lewis, 1981	> 125	95	—	—
C	King, 1976	170-200	—	—	—
D	Harris, 1974	< 350	—	—	—
D	Barrie, 1980	< 200	—	—	Modern & Relict Below 180 m
D	Woodworth-Lynas and Barrie, 1985	< 220	—	3.3-4.3	—
E	Pelletier and Shearer, 1972	10-75	—	—	Usually in 10-30 m of Water
E	Lewis, 1977	15-80	—	—	Usually in 15-40 m of Water
E	Hnatiuk and Wright, 1977	15-45	—	—	—
E	Lewis and Blasco, 1990	10-72	—	—	—
F	Barnes et al, 1978	2-25	—	1.6	—
F	Rearic, 1982	5-25	—	1.5-3.8	Scours Created Between 1977-82

2.4 Lakes

One lake in which scouring has been observed to have occurred in North America is Lake Erie (Grass, 1982; Comfort et al, 1982). These scours are important because they are found in areas for which Ontario Hydro had planned high-voltage submarine cable routes. On the Canadian side of the lake (Nanticoke), scours reach a maximum depth of 1.7 m and these scours are located in 9 to 22 m of water. On the American side (Coho), the scours only reach a depth of 0.6 m in 15 to 23 m of water (Comfort et al, 1982). The scours extend in length up to 6 km and in width up to 100 m (Grass, 1982).

Weber (1958) reported scours in Great Slave Lake, N.W.T., which ranged from small scours, a few meters in length, to large scours up to 33 m wide and over 4.5 km in length. The majority of these scours were linear but some were curvilinear. It was concluded that these scours were formed by wind driven ice keels during spring breakups.

One of the few incidents reported in the literature concerning damage to a submarine installation has been presented by Noble and Comfort (1980). In this case, the installation was a 0.6 m diameter water intake pipeline located in Great Slave Lake from shore to 8 km off the shore, sitting on the bottom and not buried. After spring breakup in 1979, problems were encountered which indicated that the pipeline had failed. The damage consisted of an approximately 250 m section of pipe which was fractured at three separate locations. Not only was the pipeline broken, but the broken sections had been displaced laterally 90 m. Several scours were present in the area which the damage had occurred, ranging in depth from 0.6 to 1.8 m.

2.5 Other Ice Scour Studies

2.5.1 Relict Land Scours

The direct observation of offshore scours is difficult and can only be done in a submersible or by diving. Sampling in areas of scours or excavating a scour in order to observe possible deformations is even more difficult, if even possible. One way to observe scours is to look at relict land-based scours created during a period of higher sea level. Several large fields of relict land-based scours have been identified in Canada and have been researched (Woodworth-Lynas et al, 1985; Woodworth-Lynas and Guigné, 1990).

In northern Manitoba, relict ice scours are present in a glacial lake, Lake Agassiz. These ice scour marks are clearly visible in aerial photographs as is shown in Figure 2.5, but are also visible from the ground. The maximum depth of these scours is 2 m, and they are preserved in both clayey and sandy materials. Widths of the scours usually range from 6 to 40 m and lengths, although generally less than 600 m, do extend up to 1.8 km (Dredge, 1982).

Woodworth-Lynas and Guigné (1990) conducted an examination of two of these relict scours incised into clay and covered with silt. The scours were trenched to a depth of 4 m using a backhoe. Several geotechnical measurements were made in and adjacent to the scour. Each scour was approximately 50 m wide and 6 and 8.5 km in length respectively. Subscour deformations were observed in the form of faults and highly visible slip planes. Poorooshasb et al (1989) have suggested that these faults might be caused by the same mechanism responsible for a two-dimensional shallow foundation failure proving that subscour deformations exist.

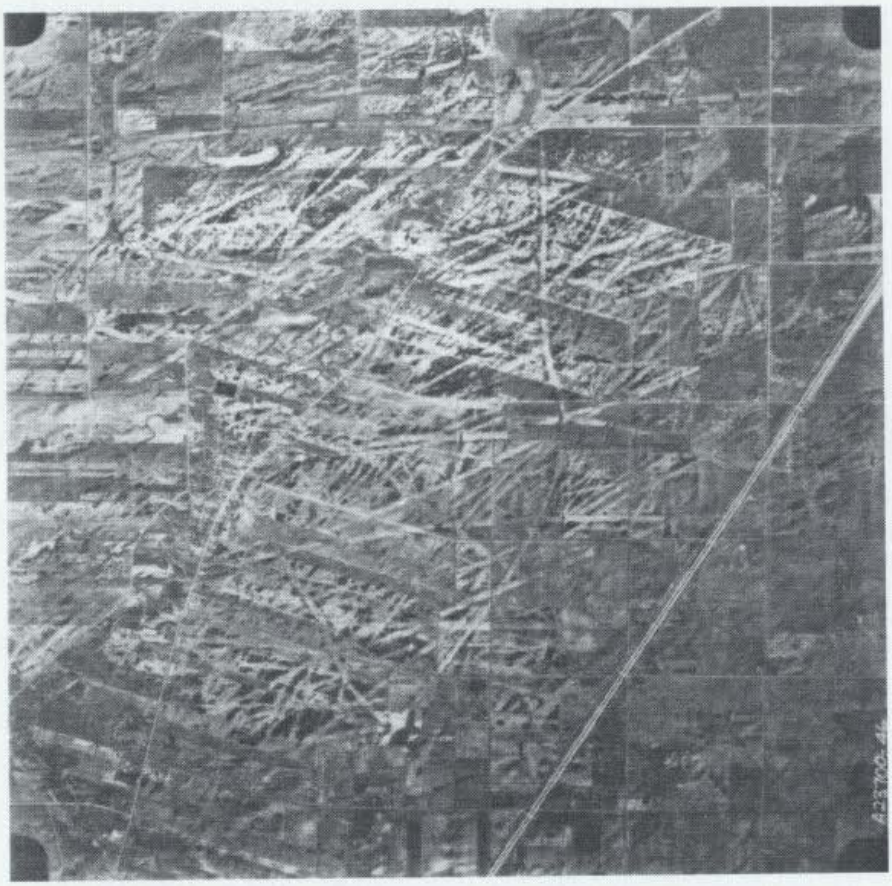

Figure 2.5: Aerial Photograph of Glacial Lake Agassiz.

2.5.2 Small Scale Observations

Field programs have been carried out on the tidal flats of the St. Lawrence estuary to observe small scale ice scouring (Poorooshasb and Clark, 1990). During spring breakup of the river ice, scouring of the river bottom by small ice chunks up to 25 tonnes occurs with every tidal cycle. These pieces of ice leave highly visible scour marks which can be physically observed and measured at low tide. Site investigations through the scours revealed very little in the way of visible subscour deformations. However, tests conducted with a shear vane through the scour indicated that subscour disturbance of the layered riverbed had occurred.

2.5.3 Ice Scour Statistics and Probabilities

Research on ice scour statistics and probabilities, which are imperative to the burial and protection of offshore pipelines and seabed installations, has been carried out by Wheeler and Wang (1985), Gaskill and Lewis (1988), and Weeks et al (1983). These authors present statistical and probabilistic characteristics of ice scouring in the determination of scour depth, scour length, scour orientations, and the probability of ice/pipeline interaction based on phenomenological data and analysis. In most cases, it is assumed that in order for the pipeline or installation to be damaged there has to be a direct impact, which may not be the case. There could also be damage incurred through close proximity of an ice keel and this aspect of the problem is generally ignored. Therefore, the probability of damage is probably being underestimated, but the research is valuable in that it adds to the overall analysis of the ice scour problem.

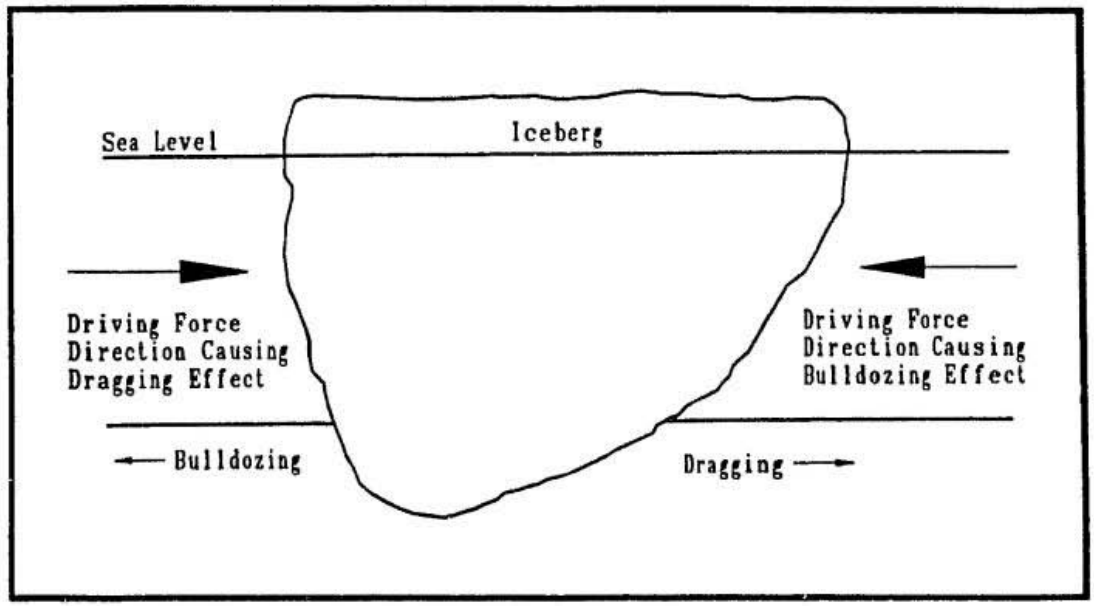

Figure 2.6: Ice Scour Mechanisms as Determined by the Direction of Driving Forces Relative to Keel Shape (After Clark and Landva, 1986).

2.5.4 Ice Scour Mechanisms

An iceberg which has become grounded can create a seabed feature in one of three ways as described by Clark and Landva (1986). These ice/seabed failure mechanisms will create a scour or a pit and are summarized below.

Figure 2.6 depicts an iceberg which has grounded. If the driving forces are directed to the left then the scour will be created by what has been described as a bulldozing keel mechanism. If an iceberg is scouring in this direction then the keel will tend to rotate about a vertical axis so that the scour is created by a trailing keel mechanism, shown in the figure if the driving force is to the right. This is the position of least scour resistance and local failure of the iceberg keel might take place in order to assume this least resistance position (Clark and Landva, 1986).

Computer simulation of iceberg instability was conducted by Bass and Peters

(1984). The work concluded that an icebergs shape when changed, either through ablation under wave action, or by splitting, will yield a new center of buoyancy and gravity. As the iceberg moves to a new stable position, its draught could increase by as much as 50 %.

On the Labrador Shelf, Bass and Woodworth-Lynas (1988) describe linear systems of craters or pits, termed crater chains, in which it appears that keel-seabed contact is lost between craters and that the keel of the iceberg touches down and then lifts off. The distance reported between craters varies from 25 to 70 m and the diameter of the pits themselves range from 25 to 40 m. The length of the crater chains are usually less than 0.5 km and contain anywhere from three to eight craters. This process was modelled mathematically and it was demonstrated that a rolling iceberg could create these crater chains (Bass and Woodworth-Lynas, 1988)

Woodworth-Lynas et al (1986) conducted studies on iceberg scours that cross isobaths and determined that icebergs could scour upslope as well as downslope. Changes in bathymetry up to 45 m were interpreted along the path of a scouring iceberg. They postulated that the bergs can scour for long distances because as the depth of the water changes, the iceberg will change its orientation (through rotation) due to resistance of the seabed. The iceberg will then be in a trailing keel mode and this might have serious implications to glory holes or trenches which have not been backfilled as the iceberg will increase its draft (due to its righting moment) as it passes over an open area.

Another feature observed on the Grand Banks which are not scours but whose mechanism of creation could cause similar problems are iceberg generated pits. Pits up to 100 m in diameter and 6.5 m deep have been observed in the Hibernia area of the Grand Banks (Lewis and Barrie, 1981). Clark and Landva (1988) concluded that

pits the size of which are seen on the Grand Banks could be created in somewhat soft soil but because the soil on the Grand Banks is described as stiff to very stiff, pits created by the earlier described mechanism proposed by Bass and Peters (1984) would yield depths less than 5 m. Clark and Landva (1988) proposed that after initial impact, the pit could be enlarged (to the size found on the Grand Banks) through continual failure of the pit walls as the iceberg continued to be moved against the walls by horizontal loading from environmental forces. As the strength of the ice may be close to that of the seabed, the ice could fail, and the iceberg, assuming a new stable position, could lift off the seabed and continue to drift, leaving an isolated pit behind.

2.6 Protection Against Ice Scour

Seabed installations located in areas scoured by icebergs must be protected and various means of protection have been proposed. Some methods of protection consider the iceberg to be a hazard which must be deflected from the seabed structure and include towing, blasting, bombing, and deflecting with a water cannon, but these methods have met with limited success. An alternative approach is that of protecting pipelines (or other seabed installations) on the sea bottom by means of trenching, gravel covers, concrete covers, or tunnels. Wellheads or caissons are easier to protect than a pipeline as they are isolated installations and might be protected through a glory hole.

Trenching has probably been viewed as the means of protection with the most likely rate of success. If trenching can be conducted, then the pipeline can be trenched to a safe depth, however the cost to conduct this trenching must also be taken into account. Safe trenching depths must be calculated by a method which not only assumes

pipe failure through direct impact but also analyses the effects of proximity loading by the ice. Trenching methods include ploughing (Brown and Palmer, 1985), jetting (Andrier, 1981), dredging (deVries, 1981), and mechanical trenching techniques (Gibson, 1981). Trenching dimensions play a major part in the total cost of a buried subsea pipeline. Therefore, it is important to develop optimal protection strategies to balance risk and cost (Nessim and Jordan, 1985). In some cases, the design and installation of a pipeline might be feasible but due to high risk, safe operation of a pipeline might not be possible as has been suggested to be the case in the case of the Hibernia field (Timmermans, 1981). In most cases, trenches will have to be backfilled for extra protection so that load is transmitted to the soil and not directly to the pipeline. The type of backfill used is also very important. If it is softer than the surrounding material, then a narrow iceberg keel could drop into the trench. On the other hand, if the material is much harder than the surrounding material, then scouring icebergs could encounter such resistance that they are stopped from scouring and remain pinned against the trench backfill by currents, transmitting loads through the trench material to the pipeline and also wearing away at the trench backfill. The soil around the pipeline might also be frozen for added protection (Palmer et al, 1979) or the soil might be mixed with cement in the vicinity of the pipeline to offer additional resistance to ice forces (Morgenstern and Sterne, 1980) but again this might also act to collect icebergs.

Concrete or gravel covers for a pipeline would be very expensive and would also cause the same type of problem; that the cover might act as a barrier to further scouring and collect icebergs. Polar Gas has looked at the feasibility of using large tunnels (4.3 to 4.9 m in diameter) to protect pipelines from iceberg scour in the Canadian Arctic (O'Donnell, 1976). These tunnels would minimize environmental

disturbance, allow for easy maintenance, and allow readily available, current technology and equipment to be used, however, they would probably be very expensive.

As an example of trenching technology, a specially designed underwater trenching plough was used to bury a flowline bundle in the Canadian Arctic near Melville Island in 1978 (Palmer et al, 1979). The 1.2 km long pipeline was constructed on shore and pulled into place into the 1.5 m deep trench with an ice-based winch. After burying the pipeline, the trench was backfilled with gravel and the soil around the flowline frozen using a mechanical refrigeration system installed in the bundle. The refrigeration system circulated a methanol-water mixture through the space between an inner and outer casing and was capable of growing permafrost to a minimum diameter of 3 m after approximately 1.5 months of operation.

2.7 Ice Scour Research

2.7.1 Theoretical and Analytical Research

Memorial University Model

A work-energy balance analytical model was developed by Chari (1975) to analyze the effects of an iceberg scouring the seabed. A simple prismatic shape was considered which would scour into a uniformly sloping seabed of weak sediment, without ride-up or change in draft. The only driving force behind the iceberg was its own kinetic energy, energy input from currents and wind ignored. The kinetic energy of the moving idealized iceberg was balanced with the work done in displacing the soil along the scour, which was computed based on soil mechanics theory. From this model, theoretical iceberg scour lengths and depths were computed for various physical parameters.

Chari and Muthukrishnaiah (1978) extended the model to account for the effect of current drag experienced when the iceberg begins to decelerate after making initial contact with the seabed. Theoretical scour lengths computed using this model, which takes into account current effects, could be up to 160 % longer than those values computed using the initial model.

Chari and Green (1981) further extended the work-energy model to analyze the effects of side friction during the scouring of frictional soils. They found that by ignoring the effect of side friction, an overestimation of scour depths of about 10 % would result.

Refinements to the model by Prasad (1985) incorporated the effects of nonlinear velocity of the iceberg during the creation of the scour. This modification of the model yielded scour depths up to 16 % higher than those computed using linear velocity variation.

This model may not be directly applicable to full scale events because uplift and/or vertical forces on the model are not considered. Research has revealed that icebergs do ride-up as scour depths remain constant during travel upslope as well as downslope (Woodworth-Lynas et al, 1986). Also, the simple model shape may not be very applicable to a full scale event.

FENCO Model

FENCO (1975) also developed a work-energy model in which a block-shaped body was driven into an evenly sloping seabed, again allowing no ride-up. Friction between the model and the seabed was not considered and only horizontal motion of the body was permitted (1 degree of freedom).

A second model developed by FENCO (1975) was a time step dynamic model

which takes a force-balance approach to the scour process. Again, the model assumes an evenly sloping seabed, but in this case allows for rotation, vertical movement, and horizontal movement of the body (3 degrees of freedom). This model solves the differential equations of motion of the block-shaped body being pushed into the seabed. From these two FENCO models, scour depths and lengths could be calculated for a given set of input parameters.

An evaluation of the deterministic model of Chari (1975) and the two deterministic models of FENCO (1975) was carried out by Comfort and Graham (1986). They concluded that the work-energy models overpredicted scour depths by as much as a factor of two, the Chari (1975) model yielding greater scour depths than the FENCO (1975) model by about 20 %. Again, the model shape considered by FENCO may not be directly applicable to a full scale event.

Been and Palmer's Work

The fact that a pipeline might still be damaged, even when it is buried below the maximum scour depth, has been discussed by Palmer (1990). It is an important objective to determine how far below the scour deformation extends and the forces associated with this deformation.

Palmer (1990) examined the mechanics of scouring and potential forces due to subscour disturbance directly from a pipeline design point of view. A *dead wedge* of soil is considered in front of the ice which moves with the ice as it scours and modifies the leading face of the keel as shown in Figure 2.7. Three zones of deformation in the scour and subscour region have been identified. These zones have been described as follows by Palmer (1990):

- Zone 1 - "An uppermost Zone 1, within which the soil is first carried up into the mound in front of the ice, and then sideways into the berm"

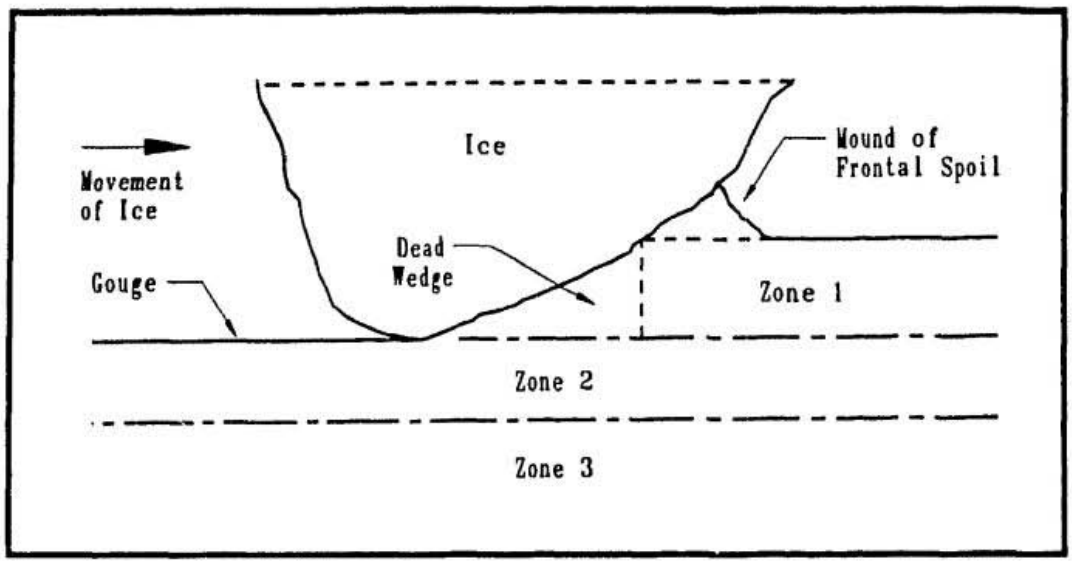

Figure 2.7: Zones of Ice Scour Deformation (After Palmer, 1990).

- Zone 2 - "An intermediate Zone 2, in which the soil is deformed plastically under the mound, but ultimately continues under the ice; and"
- Zone 3 - "A lowest Zone 3, in which the soil passes under the ice, but is subject to stress transmitted from Zone 2."

As can be seen from Figure 2.7, the boundary between Zones 1 and 2 is easily distinguished but the boundary between Zones 2 and 3 is not so readily observed.

Pipeline response in each of these zones has also been hypothesized by Palmer (1990). A pipeline in Zone 1 would be lifted with the churning mound of soil in front of the ice keel. As the scour progressed, the pipeline would be pulled through the soil between the pipeline and the ice until they were in direct contact and, depending on the scouring forces, the pipeline would likely fail. In Zone 2, the soil beneath the ice is pushed down to some extent, but it is also dragged forward or entrained with the ice mass. More than likely, a pipeline in this zone would be dragged with the soil as well and axial forces, bending moments, and compressive forces would develop. The

potential loadings would have to be analysed for each particular case. The pipeline in Zone 3 would experience very little, if any, soil movement but would experience additional loading from forces transmitted through the soil. Pipeline analysis in each of these three zones has been presented by Palmer (1990) in which forces transmitted through the soil and bending and buckling strains of the pipeline were considered. However, even with this analysis, the question remains as to the extent of Zone 2 with respect to different ice keel shapes, different soil properties, and different soil types.

Been et al (1990a) looked at the failure mechanisms typically associated with ice scour and developed an energy-force model. Been et al (1990a) stated that most Beaufort Sea ice keels have a very low angle to the horizontal, typically less than 30° and that the keel widths are large as compared to the depths and that this must be considered in the analysis of scour. A dead wedge of soil is again considered to form in front of the keel moving with the ice. Mathematical models of ice scour have usually been thought of as a combination of passive earth pressure failure acting in the horizontal direction and a bearing capacity failure acting in the vertical direction as shown in Figure 2.8. However, the inclined plate (representing the ice keel) is not moving into the soil in a direction normal to the plate as in cases (a) and (b), but is rather being displaced in a horizontal direction as shown in case (c). Been et al (1990a) thought that serious errors could occur using this approximation plus the fact that the ice is continually moving and that soil mechanics theories are usually only concerned with small displacements. For this reason, they developed a solution to the problem using plasticity theory. Results of the model agreed reasonably well with an observed Beaufort Sea scour in that scour depths matched reasonably well (and thus the uplift of the model) over a considerable portion of the scour length and

over a change in water depth of approximately 6.5 m. However, further refinements and validations to the model have to be made.

2.7.2 Experimental Research

Chari's Tests

Chari (1975) realized that verification of his derived analytical model could not be conducted in a laboratory (at 1 g) due to problems with geotechnical modelling, namely the problems in scaling the sediment size, density and strength. However, it was felt that the soil resistance on the model should be verified through a series of model tests. These model tests were also designed to observe the mechanics of scouring during the model/soil interaction. The purpose of the experimental program was to measure the pressures and forces on the model during a scouring event and to observe soil displacements around the model.

A towing tank was built which allowed the preparation of a testbed as a soil-water slurry settled while the tank was in a tilted position. By bringing the tank to an upright position, a sloping testbed was achieved. The main model was constructed out of plexiglass, was rectangular prismatic in shape, and was 23 cm wide, 45 cm long and 40 cm deep. Models of other shapes were used to some extent and all models were instrumented with pressure transducers on the face and bottom.

The model was driven into the sloping testbed while measurements of towing forces and pressures were recorded. These measured values agreed well with those values calculated using the theoretical part of the analytical model if the force lost due to sediment compression in front of the model is taken into account. The primary resistance to the model motion was passive soil resistance in front of the model and soil movement in front of and below the model occurred during the creation of the

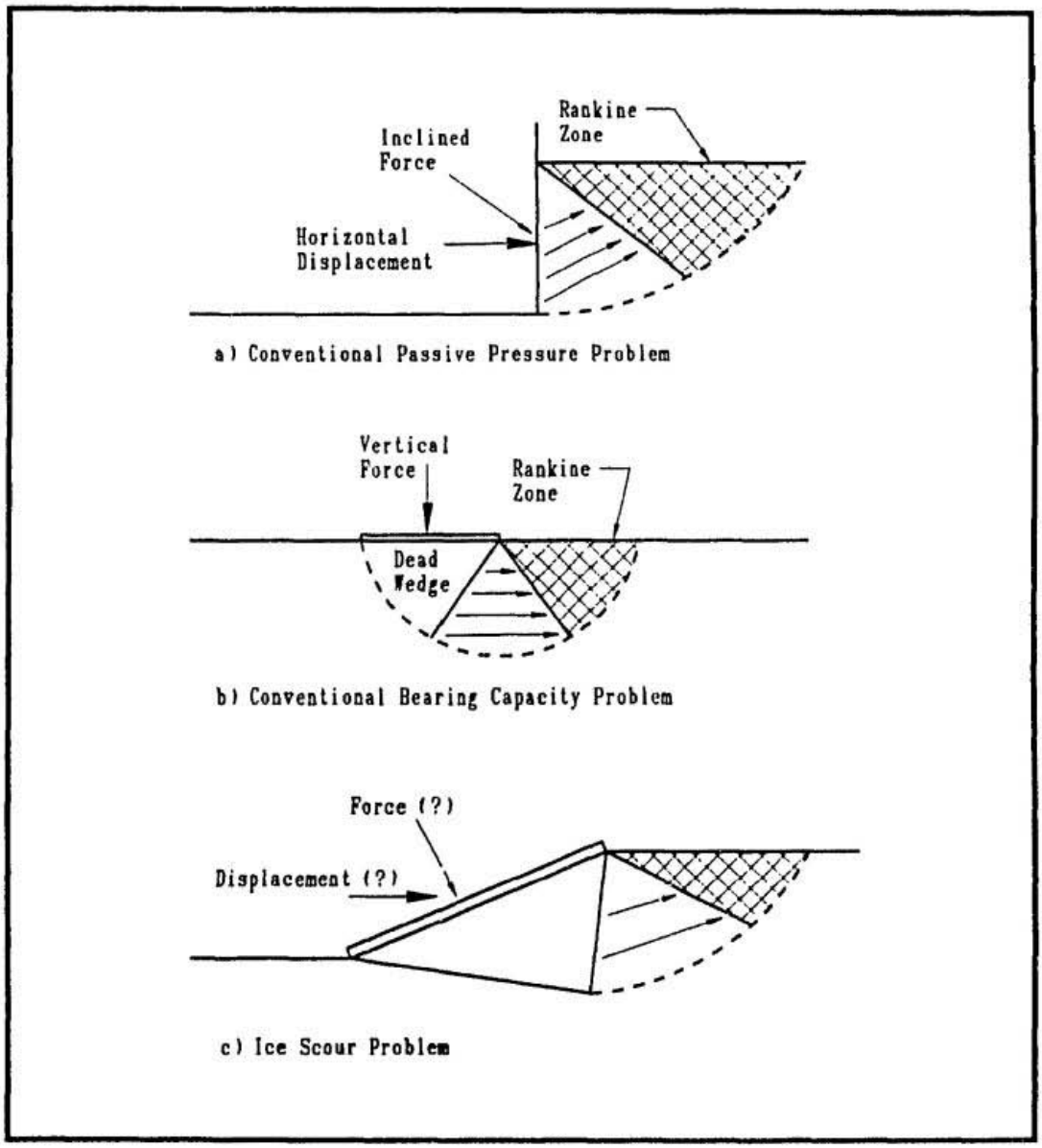

Figure 2.8: Relationship Between Passive Pressure, Bearing Capacity and the Ice Scour Problem (After Been et al, 1990a).

scour (pressure increases were recorded up to 1.5 m away by pressure transducers buried in the testbed). Chari (1975) also concluded that pressure on the sides of the model added very little resistance to the movement of the model and results also showed that varying the speed of scouring between 0.11 and 0.35 m/s, did not influence the sediment resistance to scouring.

In these tests, some description of a failure pattern in front of the model is given as the tank had a plexiglass wall. Failure surfaces were observed to originate at the toe of the iceberg model and run at an angle of 25 to 30° to the horizontal towards the testbed surface. Failure surfaces were also observed up to 0.5 m in front of the model. A smaller set of experiments was conducted in which layered bands of colored sand and clay were scoured to observe the soil movement. The results showed that movements in the testbed occurred far ahead of the model. The results presented also describe failure surfaces which begin or extend below the maximum scour depth but no indication as to the magnitude of displacements is given.

Green's Tests

Green (1984) conducted physical model tests in a sloping testbed of cohesionless sand. The purpose of these experiments was to observe the process in dry sand, to investigate the effect of using different size models and keel shapes, and to measure pressures and forces on the model as well as on an instrumented model pipeline buried in the testbed.

The tests were conducted in a concrete tank at Memorial University which is 6 m wide, 14 m long, and approximately 1 m deep. Spanning the tank is an electrically powered gantry to which the models were attached. Six different iceberg models, of varying size and shape, were used in the tests. Pressure cells were mounted flush

to the model face and load cells were positioned to measure horizontal force. The testbed was prepared by raking through the soil and smoothing the surface to create a surface with a slope of 1:35. A plexiglass model pipeline, instrumented with pressure transducers was also rigidly mounted in the testbed at predetermined distances and locations below the scouring model.

The primary resistance on the model was developed through passive earth pressure and failure planes were observed to develop in front of the model. Soil resistance measured during the model tests was directly related to the width of the model but a change in shape from a vertical front face to a sloping front face increased soil resistance by as much as 35 %. The speed of the model did not affect the forces measured during testing. The pipeline pressure cells responded to pressures when buried to a depth of 116 mm below the scour which was the deepest point measured. The model pipeline was designed to be very rigid compared to the soil, therefore the tests do not take into account possible displacements of the pipeline with the surrounding soil.

Prasad's Tests

Recommendations by Green (1984) suggested that further experimental analysis be conducted to analyse the effect of the model keel shape. Prasad (1985) extended this work to study the influence of iceberg keel shape on seabed resistance while scouring into a sloping sand testbed. The experimental program also measured soil resistance acting on the model and pressures on the face of the model. The six model shapes used in this series of experiments is shown in Figure 2.9.

While the model was towed through the testbed, it was observed that failure planes surfaced in front of the model and this process was also reflected in the model's

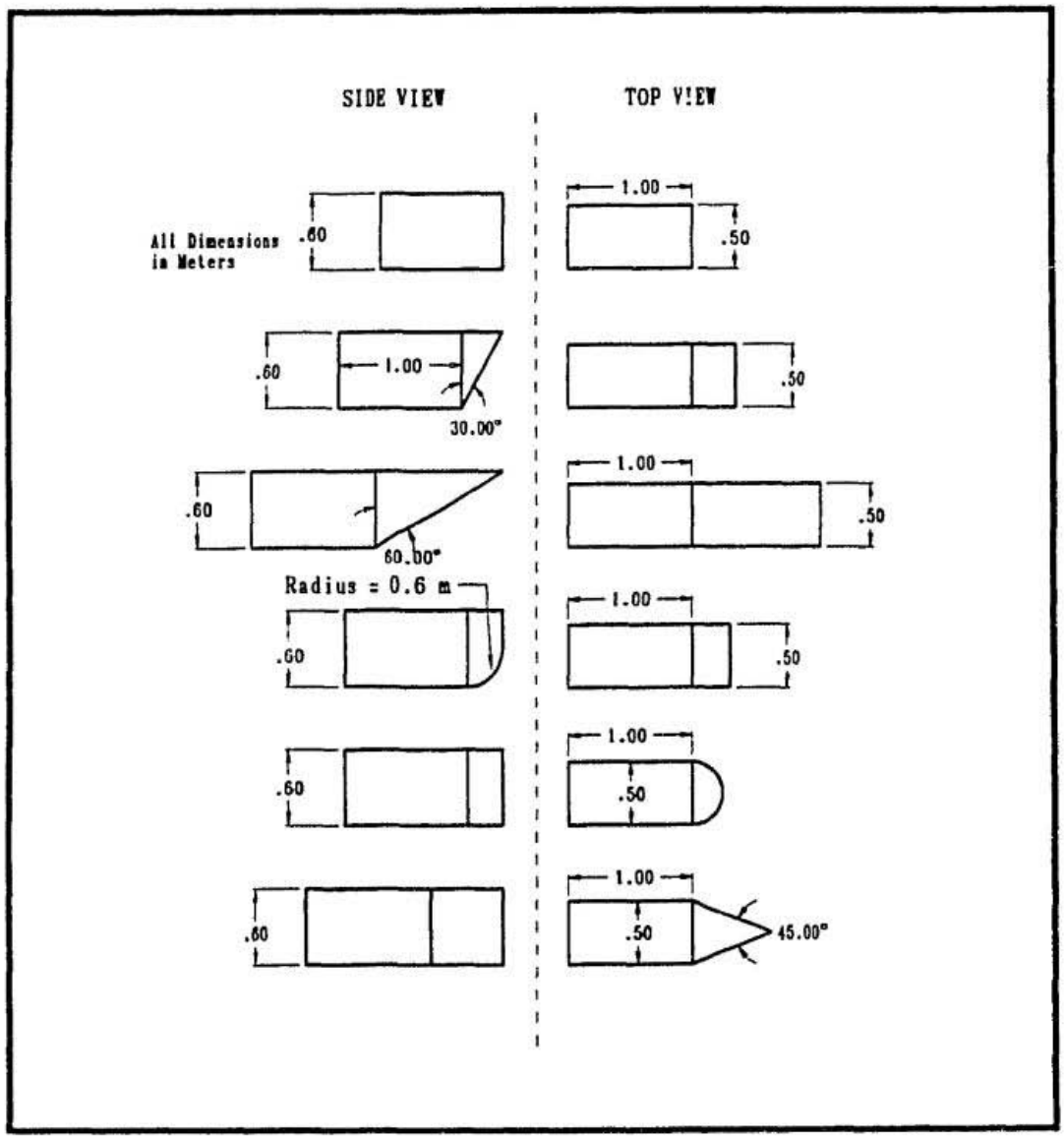

Figure 2.9: Model Shapes used by Prasad (After Prasad, 1985).

horizontal load plot (saw-toothed). The scour profile did not vary much from model to model but the measured pressures on the face of the model and towing resistances did.

Prasad (1985) concluded that soil resistance on the model increased with increasing model face inclination, however, no measurements of pressures or displacements below the scouring model were made.

Abdelnour's Tests

Model tests of ice scour were conducted in 1979 as part of an APOA (Arctic Petroleum Operator's Association) project (Abdelnour et al, 1981). The program consisted of 110 test runs or scours in which the soil types, model keel shape, model scale, scour cut depth, and towing velocities were varied. The purpose of the tests was to gather information on the model resistance during scouring, the pressures generated in the testbed, the pressures on the face of the model, and the morphology of the scour and how the results varied with the parameters outlined above.

Model shapes consisted of an inverted pyramid (63° with the horizontal) and rectangular prismatic shapes. The two rectangular models were 26 cm wide and 52 cm wide. Prepared testbeds of soil consisted of submerged sand, silt, and clay, and scour cut depths ranged from approximately 1 to 30 cm (Abdelnour and Graham, 1984).

Pressure cells and piezometers were placed in the testbed to measure the soil response during the tests. Pressure transducers were located in the face of the model and force blocks were incorporated in the mounting frame for the model to measure horizontal and vertical forces. After the tests, the scour trench depths and scour profiles were measured.

The results were analysed for geometrically similar models in the same soil types and the findings presented in dimensional and non-dimensional semi-empirical relationships. Results of the testing program yielded several results, one of which was that the scale factor used for the model did not alter the non-dimensionalized results to any great extent. The results of these tests do not give any indication of subscour deformations, failures, or pressures.

Dunwoody's Tests

Another physical model experimental program was undertaken as part of an APOA project to study the process of ice/berm interaction (Dunwoody et al, 1984). The main purpose of this test program was to study the forces on and the uplift of the leading edge of the ice floe as it penetrated the berm. Variables during the 34 tests included vertical resistance of the model to ride-up, attack angle of the model face, geometry of the berm (slope), the buoyant specific weight of the soil, the internal angle of friction of the soil, and the angle of friction between the soil and the ice.

The 0.5 m wide model was constructed out of aluminum and the leading edge or face of the model could be varied from 30 to 105° to the horizontal. The slope of the berm was 5:1 and was built out of clean dry sand. Springs of varying stiffness were used to vary the vertical resistance of the model to uplift. Artificially roughened models as well as smooth models were used to observe the effect of the angle of friction between the soil and the model. The model was forced into the berm approximately 90 cm by means of an electrically powered hydraulic ram.

Vertical movement of the model and horizontal forces were measured during each test as a function of the penetration depth. Observations made during the tests indicated that the model would always experience both uplift and penetration to

some extent as it encountered the slope of the berm, the amount of ride-up depending on the vertical resistance of the model (i.e. spring stiffness). A mound of spoil was built up in front of the model as the test progressed and failure planes were observed to uplift in front of the model. The model face angle was found to have no effect on the non-dimensionalized horizontal force and vertical deflection except when the face of the model was inclined to 105° to the horizontal. But when this angle is greater than 90°, the model becomes more of a *cutting tool.* Again with this test series, no mention is made of any subscour disturbance.

Golder Associates Ltd. Tests

Golder Associates carried out 46 small scale indentor tests to provide information on deformations around a scouring model and to provide input for the verification of analytical models (Been et al, 1990b). The indentors were driven into sand and clay testbeds into which small ball bearings had been placed in order to measure displacements. Forces on the indentors were also measured during testing.

As with earlier model tests in sand, failure planes were also observed in these tests and this was again reflected in the load records for the model. The tests were highly repeatable and *dead wedges* of material in front of the sloping indentors were observed. Calculated pressures and loads agreed well with measured values.

These tests showed subscour displacements below the indentor in small scale tests in sand. In medium and dense sand, subscour disturbance extended to only about 2 cm below the indentor while in the loose sand, disturbances were observed to a depth of 7 cm. These observations were attributed to the fact that below the indentor in the dense soil, dilation and strain softening takes place while in the loose soil, contraction and shear strains are associated with the scouring. Clays were observed to behave

similarly to loose sands but subscour disturbances were found to be minimal.

Been (1990) presented two mechanisms for the failure of soil during scouring and these are depicted in Figure 2.10. The first mechanism involved the formation of rupture surfaces due to bearing capacity or passive earth pressure failure. The second mechanism occurred when an iceberg keel drags or entrains soil beneath the keel and this is referred to as the shear dragging mechanism. The movements below the scour in the Golder tests (Been et al, 1990b) are attributed to the shear dragging mechanism because rupture surfaces were not observed below the leading edge of the indentor (Been, 1990).

It was concluded that it is important to determine the thickness of the layer of the shear dragging zone and that the burial of a pipeline should be far enough out of this zone to ensure the safety of the pipeline. This zone will be deeper for very loose sands and in softer clays. In order for a rupture plane to extend below the toe of the indentor, there would have to be significant vertical movement of the indentor or a change in soil strength. No detailed information on the ball bearing movements or subscour deformations is available because these test results have not been made public.

C-CORE's Tests

Experimental programs have been conducted at Memorial University's scour tank facility in silt (Poorooshasb et al , 1989) and in sand (Poorooshasb and Clark, 1990; Poorooshasb, 1990) in order to investigate the ice scour process. In both experimental programs, the scour was created by a rigid model and the observation and analysis of subscour disturbance and failure was a primary objective.

Two tests were carried out in gravity consolidated silt in the scour tank facility in

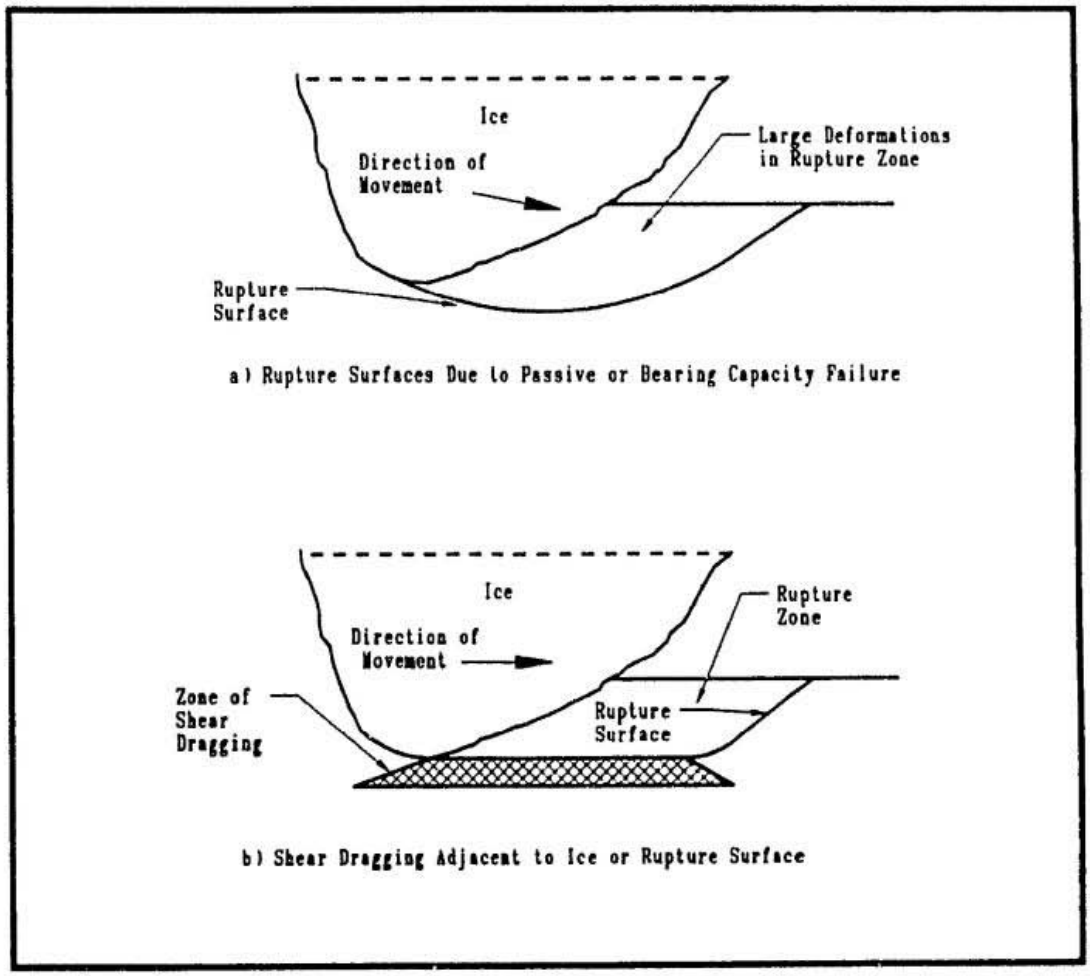

Figure 2.10: Potential Soil Failure Mechanisms During Scouring (After Been, 1990).

which the average strength of the silt was measured to be approximately 4 kPa. Pore pressure transducers were buried in the silt at various depths and horizontal distances off the scour centerline. The aluminum model was mounted to the gantry spanning the tank through a mounting system which gave the model limited ability to pitch and heave through springs while controlling horizontal movement. Instrumentation was positioned to measure heave of the model, and horizontal and vertical forces acting on the model.

The purpose of these experiments was to measure and observe subsurface deformations below the scoured testbed, shown by the displacement of horizontal layers of fine sand. Also, the pore pressure response during scouring was recorded as it was an indication of the depth to which scouring affected the testbed. The surface morphology of the scour was also measured and recorded. (Poorooshasb et al, 1989). Two scour cut depths were used in the tests; the first at an average scour depth of 40 mm and the second at an average scour depth of 70 mm.

The model did not penetrate the clay surface in Test 1, but rather created a groove which caused a deformation of sublayers to a depth of 0.2 m. This was observed by excavating the scour after completing the tests. Pore pressure response was measured up to a considerable distance away from the scour. The model penetrated the test bed during Test 2 and created a scour through a process likened to that of a bulldozer. Again subscour deformations were noted (Poorooshasb and Clark, 1990).

Four model tests were conducted in sand to investigate the extent and magnitude of the displacement field below the scour, to determine if the attack angle, model width, and sand density affect the scour process, and to measure the forces required to create the scours.

The testbed used in the sand tests is depicted in Figure 2.11 and was constructed

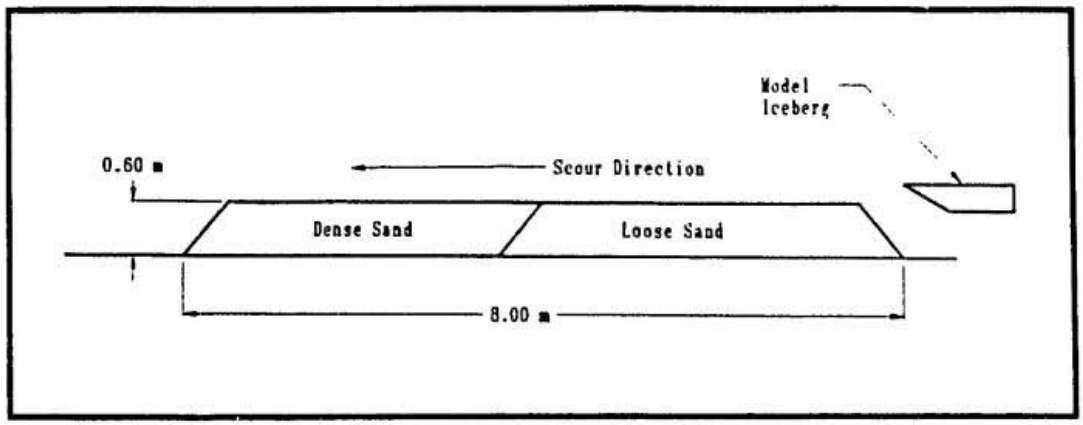

Figure 2.11: Experimental Testbed Used by Poorooshasb (After Poorooshasb, 1990).

by raining sand through a hopper. Load cells and displacement markers were placed in the testbed between sand rainings. The displacement markers consisted of 1/2 inch steel ball bearings, and lengths of solder laid across the scour path at various depths. From these displacement markers, soil movements could be obtained.

Four different configurations of the iceberg model were possible by varying the attack angle and width. The aluminum model was rigidly attached to the gantry in such a manner that the scour cut depth was 75 mm. Pressure and load cells were located at various positions on the model iceberg face and frame to measure face pressures and horizontal and vertical forces acting on the model.

Data obtained during the tests revealed that the soil density significantly affects the amount of subscour deformation. In the loose sand, deformations of the solder strands were observed to a depth 65 mm below the scour while in the dense sand, deformations were restricted to immediately below the scour (5 mm). Attack angle was also observed to affect subscour deformation. Very little subscour disturbance in both the loose and dense sand was detected in the test which utilized a 30° attack angle as compared to the other tests in which a 15° attack angle was used.

2.8.2 Bearing Capacity Failure

Generally, in the literature, three possible failures are described in discussions on bearing capacity failure; punching shear failure, local shear failure, and general shear failure. These failure mechanisms are depicted in Figure 2.12. Punching shear failure occurs when there is compaction of the soil beneath the foundation, accompanied by vertical shear around the edges of the foundation (Craig, 1987). During local shear failure, the soil undergoes compaction in Zones I, II, and III (Bowles, 1977) and there is only bulging and slight displacement at the soil surface. Most of the present bearing capacity theories depend on or are based upon the case of general shear failure. In this case, the soil undergoes failure as Zones II and III are displaced by the wedge of soil in Zone I (Bowles, 1977) and there is a noticeable bulging and uplifting of soil adjacent to the footing. All theories assume long, narrow footings but if the foundation is rectangular in shape then a shape correction factor can be incorporated into calculations. Also, theories often consider whether or not a foundation is deep or shallow. In order for the foundation to be considered shallow, then

$$B \geq D_f \tag{2.1}$$

where B is the breadth of the foundation and D_f is the depth of the foundation above the original surface of the soil. Bearing capacity theories which could be considered in the analysis of ice scour are (a) Terzaghi's (Modified Prandtl's) Theory, and (b) Meyerhof's Theory. These theories are depicted in Figure 2.13 where Q is the applied axial load and failure could occur if this applied load is greater than the bearing capacity of the soil. Another theory, Prandtl's Theory, can only be solved for special cases, those of which are not directly applicable in this analysis (Vésic, 1973). In Terzaghi's Theory (Figure 2.13a), Zone I is an elastic zone, Zone II is a radial shear

Comments

The physical models presented in this subsection were all used in an attempt to study the ice scour process. The shape of some of the models may not be as applicable to the process as others. According to Been et al (1990a), the angle of model keel should be shallow with respect to the horizontal; typically less than 30°. According to the results of some of the testing programs, it appears that the horizontal resistance of the testbed to scouring increases with increasing inclination from the vertical of the front face of the model. Measurement of stresses in the testbed below the scouring model revealed that stress increased with inclination from the vertical of the model face. Maximum subscour disturbances were observed in loose sands and softer clays especially when models with shallow attack angles (with respect to the horizontal) were used. Therefore, the use of a simple prismatic model probably would not yield a *worse-case* scenario. Some models did not allow uplift or did not measure vertical forces acting on the model. Results from testing have shown that at some inclination angle of the front face, the dominant force on the model changes from horizontal to vertical. This is important where bearing capacity failure of the soil might occur.

2.8 Soil Failure Models

2.8.1 General

Existing soil mechanics theory can be used in an attempt to analyse soil failure associated with the ice scour process. The geotechnical models and theories which might be used in this analysis are briefly described below. Generally, the process below and in front of an iceberg are likened to that of a bearing capacity failure and a passive earth pressure failure respectively.

zone, and Zone III is a Rankine passive zone (Das, 1985). In Meyerhof's Theory (Figure 2.13b), Zone I is an elastic zone, Zone II is a radial shear zone, and Zone III is a wedge of soil, not under failure, whose weight can be replaced by stresses along the equivalent free surface (Meyerhof, 1951). Terzaghi's theory ignores the shearing strength of the overburden above Zone III and considers its weight simply as a surcharge as shown in the figure. This method will yield conservative results as the assumed failure mechanism is not like those which were observed during failure (Meyerhof, 1951).

Terzaghi's equation for bearing capacity, based on general shear failure, is given as (Terzaghi and Peck, 1967)

$$q_d = cN_c + \gamma D_f N_q + \frac{1}{2}\gamma B N_\gamma \tag{2.2}$$

in which c is the cohesion of the soil and N_c, N_q, and N_γ are bearing capacity factors. N_c is the bearing capacity factor for cohesion, N_q is the bearing capacity factor for the surcharge, and N_γ is the bearing capacity factor accounting for the self weight of the soil. The bearing capacity factors to be used in the Terzaghi equation are given by Vésic (1973) as

$$N_c = (N_q - 1)\cot\phi, \tag{2.3}$$

$$N_q = e^{\pi \tan\phi} \tan^2(\frac{1}{4}\pi + \frac{1}{2}\phi), \tag{2.4}$$

and

$$N_\gamma = 2(N_q + 1)\tan\phi \tag{2.5}$$

in which ϕ is the internal angle of friction of the soil.

In the case of a rectangular, circular, or square footing, shape correction factors must be applied to each term in the Terzaghi equation. Corrections must also be

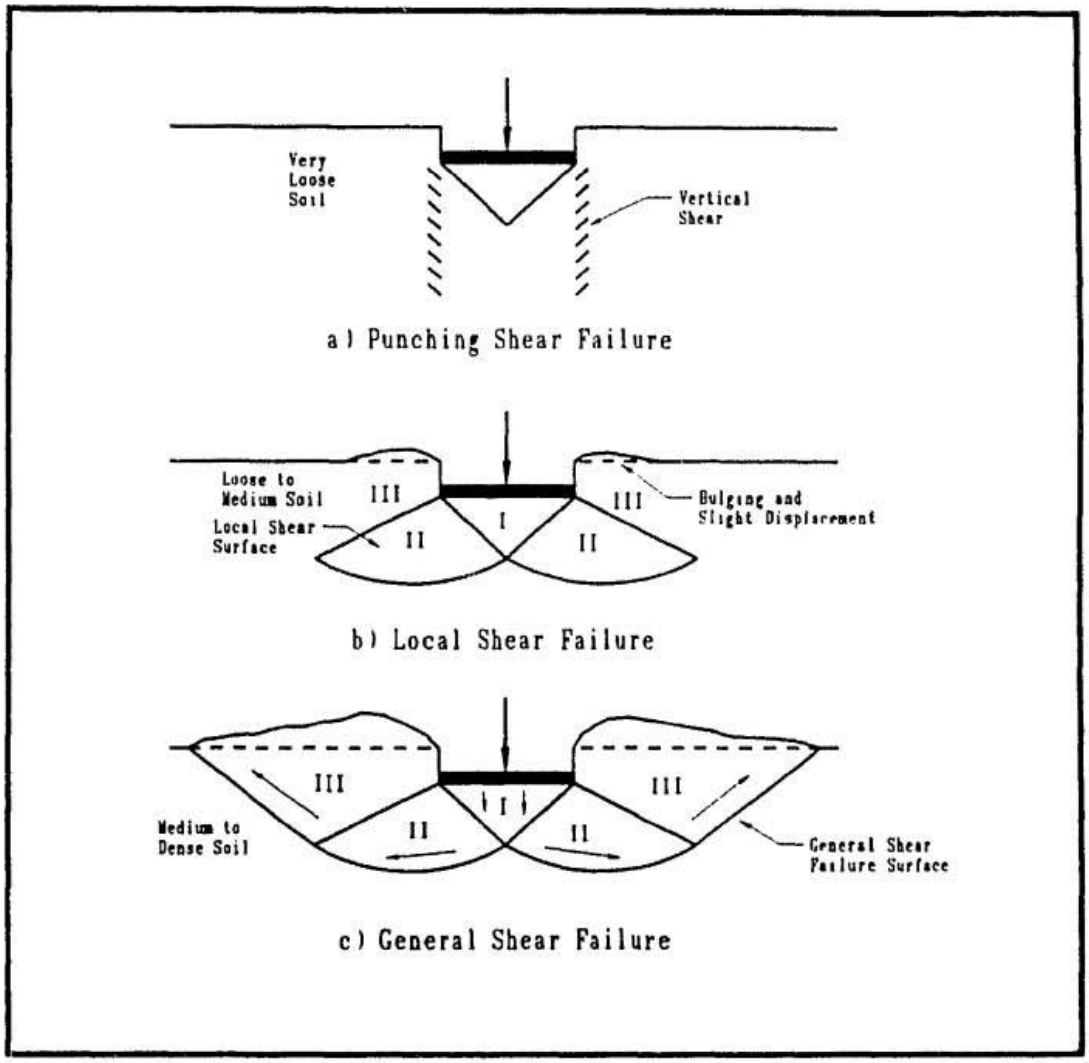

Figure 2.12: Modes of Bearing Capacity in Soil (After Craig, 1987).

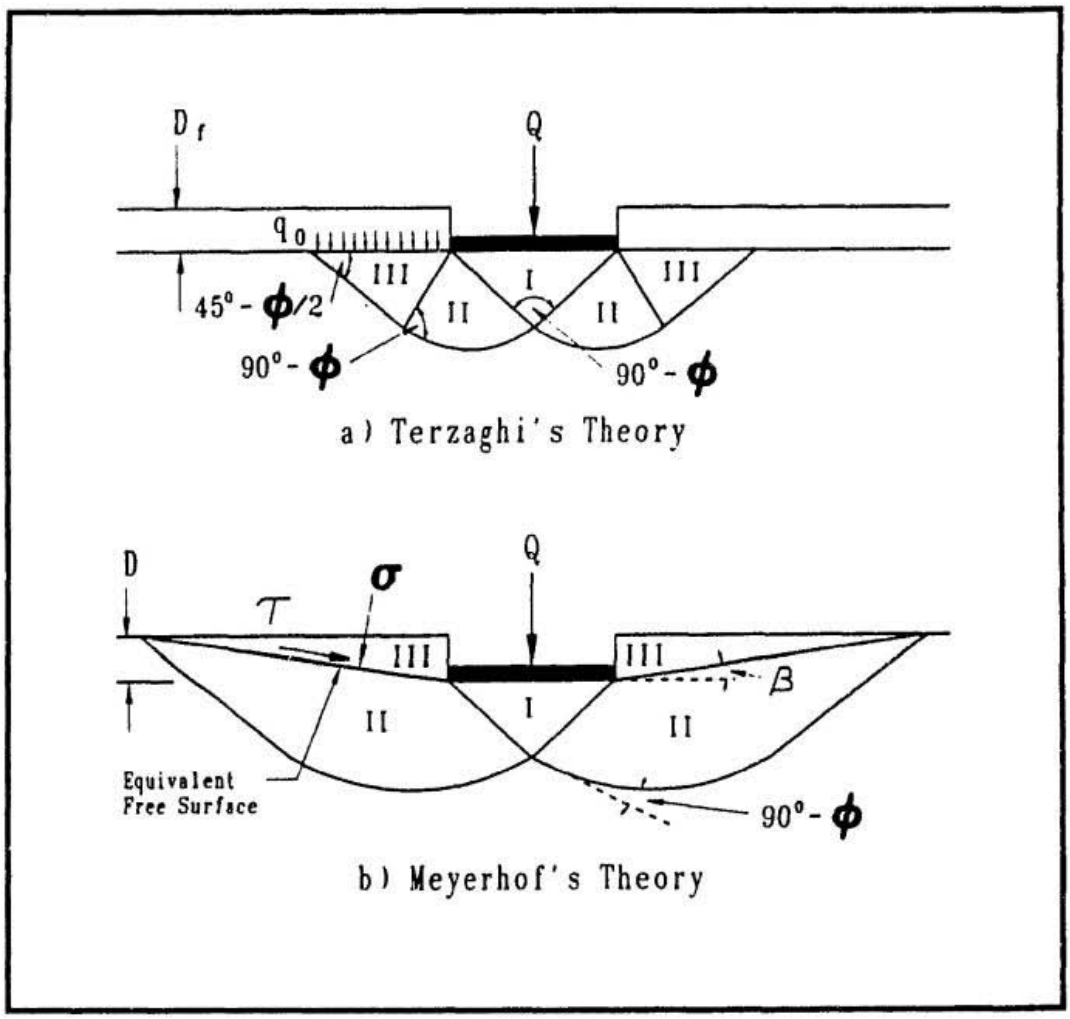

Figure 2.13: Terzaghi's and Meyerhof's Bearing Capacity Failure Theories (After Meyerhof, 1951).

made for the case of eccentric and inclined loading and Eq. 2.2 becomes (Vésic, 1973)

$$q_d = cN_c\zeta_c\zeta_{ci} + \gamma D_f N_q \zeta_q \zeta_{qi} + \frac{1}{2}\gamma B N_\gamma \zeta_\gamma \zeta_{\gamma i} \tag{2.6}$$

in which ζ_c, ζ_q, and ζ_γ are the respective shape factors and are given by the following equations for a rectangular foundation (Vésic, 1973)

$$\zeta_c = 1 + (B/L)(N_q/N_c) \tag{2.7}$$

$$\zeta_q = 1 + (B/L)\tan\phi \tag{2.8}$$

$$\zeta_\gamma = 1 - 0.4(B/L) \tag{2.9}$$

where L is the length of the foundation and the other terms have already been defined. ζ_{ci}, ζ_{qi}, $\zeta_{\gamma i}$ are the respective inclination factors and are expressed by (Vésic, 1975)

$$\zeta_{qi} = [1 - \frac{P}{Q + cB'L'\cot\phi}]^m \tag{2.10}$$

$$\zeta_{ci} = \zeta_{qi} - \frac{1 - \zeta_{qi}}{N_c \tan\phi} \tag{2.11}$$

$$\zeta\gamma i = [1 - \frac{P}{Q + cB'L'\cot\phi}]^{m+1} \tag{2.12}$$

where P and Q are the horizontal and vertical components of the inclined load. L′ and B′ are the effective length and effective breadth of the foundation to take into account the eccentricity (e) of the load and are calculated (Vésic, 1975) from

$$B' = B - 2e \tag{2.13}$$

and

$$L' = L - 2e_L. \tag{2.14}$$

The exponent m is calculated from (Vésic, 1975)

$$m_B = \frac{2 + (B/L)}{1 + (B/L)} \tag{2.15}$$

when the inclination of the load is in the direction of the breadth of the foundation, and

$$m_L = \frac{2 + (L/B)}{1 + (L/B)} \tag{2.16}$$

when the inclination of the load is in the direction of the length of the foundation.

The Terzaghi Theory presented above was based on the assumption of general shear failure. For the case of local shear failure, Terzaghi's bearing capacity equation becomes (Das, 1985)

$$q_d = c' N'_c \zeta_c \zeta_{ci} + \gamma D_f N'_q \zeta_q \zeta_{qi} + \frac{1}{2} \gamma B N'_\gamma \zeta_\gamma \zeta_{\gamma i} \tag{2.17}$$

where

$$c' = \frac{2}{3} c \tag{2.18}$$

and the modified bearing capacity factors N'_c, N'_q, and N'_γ are calculated using Eq. 2.3, Eq. 2.4, and Eq. 2.5 but ϕ is substituted by ϕ' which is calculated from

$$\phi' = \tan^{-1}(\frac{2}{3} \tan \phi) \tag{2.19}$$

yielding

$$N'_c = (N'_q - 1) \cot \phi', \tag{2.20}$$

$$N'_q = e^{\pi \tan \phi'} \tan^2(\frac{1}{4}\pi + \frac{1}{2}\phi'), \tag{2.21}$$

and

$$N'_\gamma = 2(N'_q + 1) \tan \phi'. \tag{2.22}$$

Meyerhof (1963) considered the bearing capacity of shallow foundations, based on general shear failure, and also suggested that various factors be included to account for the depth of the foundation, to account for the eccentricity of the load, and to account for the inclination of the load. The resulting formula is

$$q = d_c i_c s_c c N_c + d_q i_q s_q \gamma D N_q + \frac{1}{2} d_\gamma i_\gamma s_\gamma \gamma B' N_\gamma \tag{2.23}$$

where d_c, d_q, and d_γ are the respective depth factors, s_c, s_q, and s_γ are the respective shape factors, i_c, i_q, and i_γ are the respective inclination factors, B′ is the effective foundation width to account for the eccentricity of the load, D is the same as D_f, and all other factors have been previously defined. The bearing capacity factors N_c and N_q are the same as those presented in Eq. 2.3 and Eq. 2.4 but N_γ is expressed by Meyerhof (1963) as

$$N_\gamma = (N_q - 1)\tan(1.4\phi). \tag{2.24}$$

The shape factors are given by (Meyerhof, 1963)

$$s_c = 1 + 0.2N_\phi(B/L) \tag{2.25}$$

$$s_q = s_\gamma = 1, (\phi = 0) \tag{2.26}$$

and

$$s_q = s_\gamma = 1 + 0.1N_\phi(B/L), (\phi > 10°) \tag{2.27}$$

where

$$N_\phi = \tan^2(\frac{1}{4}\pi + \frac{1}{2}\phi) \tag{2.28}$$

and the corresponding depth factors are suggested by Meyerhof (1963) as

$$d_c = 1 + 0.2\sqrt{N_\phi}(D/B) \tag{2.29}$$

$$d_q = d_\gamma = 1, (\phi = 0) \tag{2.30}$$

and

$$d_q = d_\gamma = 1 + 0.1\sqrt{N_\phi}(D/B), (\phi > 10°). \tag{2.31}$$

The inclination factors are presented by Das (1985) as

$$i_c = [1 - \frac{\alpha°}{90°}]^2 \tag{2.32}$$

$$i_q = [1 - \frac{\alpha^\circ}{90^\circ}]^2 \tag{2.33}$$

$$i_\gamma = [1 - \frac{\alpha^\circ}{\phi^\circ}]^2 \tag{2.34}$$

where α is the angle of inclination of the load on the foundation and ϕ is the internal angle of friction of the soil.

A foundation whose base is below the watertable should be analysed for bearing capacity using the submerged unit weight of the soil, γ', as opposed to using the unit weight, γ (Vésic, 1975). In this case, Eq. 2.6, Eq. 2.17, and Eq. 2.23 become

$$q_d = cN_c\zeta_c\zeta_{ci} + \gamma' D_f N_q \zeta_q \zeta_{qi} + \frac{1}{2}\gamma' B N_\gamma \zeta_\gamma \zeta_{\gamma i} \tag{2.35}$$

$$q_d = c' N'_c \zeta_c \zeta_{ci} + \gamma' D_f N'_q \zeta_q \zeta_{qi} + \frac{1}{2}\gamma' B N'_\gamma \zeta_\gamma \zeta_{\gamma i} \tag{2.36}$$

and

$$q = d_c i_c s_c c N_c + d_q i_q s_q \gamma' D N_q + \frac{1}{2} d_\gamma i_\gamma s_\gamma \gamma' B' N_\gamma. \tag{2.37}$$

2.8.3 Passive Earth Pressure Failure

The soil movement in front of a horizontally moving ice keel can be analysed using existing passive earth pressure theories developed for retaining walls. If, at some moment in time, the keel is considered a retaining wall at rest, then the forces required to initiate successive earth pressure failure in the soil in front of the wall can be calculated. Small strains in front of the retaining wall yield an elastic action in the soil. Larger strains result in constrained plastic flow. If the wall continues to move, unrestricted plastic flow will occur just prior to collapse load. This collapse load will be the passive earth pressure failure (Chen and Scawthorn, 1970).

The two classical solutions for passive earth pressure problems are the Rankine's solution and the Coulomb's solution. The Rankine failure surface for passive earth

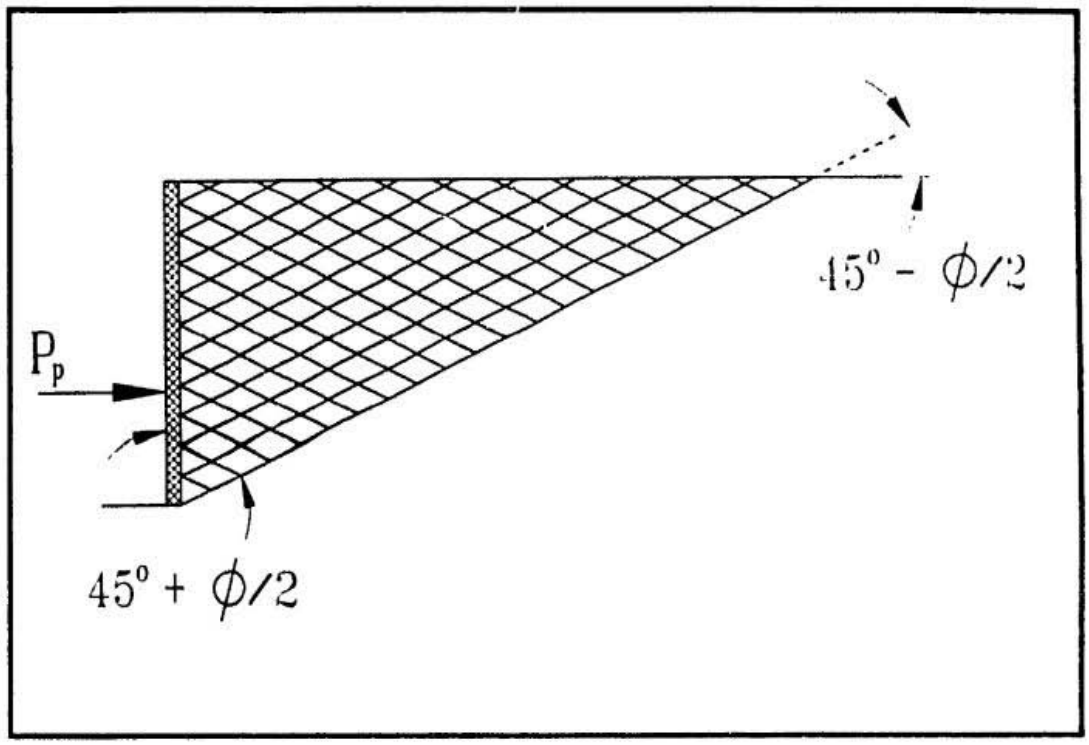

Figure 2.14: Rankine Earth Pressure Passive Failure Surface (After Craig, 1987).

pressure is presented in Figure 2.14. The passive force, P_p, per unit width of wall is given by (Das, 1985)

$$P_p = \frac{1}{2} K_p \gamma H^2 \tag{2.38}$$

where H is the height of the retaining wall and

$$K_p = \tan^2(45 + \frac{1}{2}\phi) \tag{2.39}$$

for cohesionless soil.

However, this is for a retaining wall without friction when in fact retaining walls have friction and the failure surface is a curve near the bottom of the retaining wall (Craig, 1987) as shown in Figure 2.15. Coulomb's theory takes wall friction into

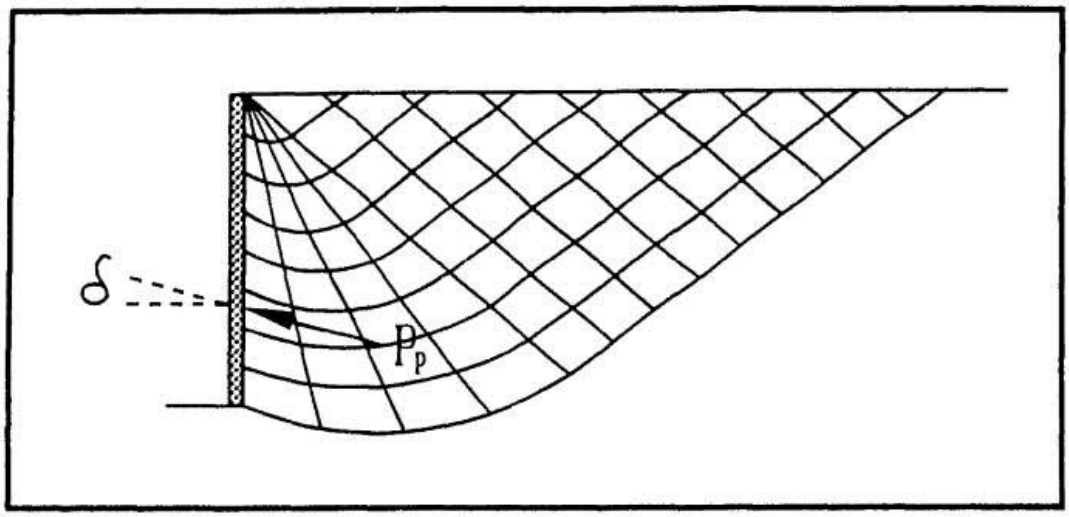

Figure 2.15: Passive Earth Pressure Failure in Front of Retaining Wall With Friction (After Craig, 1987).

account but assumes a plane failure surface as shown in Figure 2.16. The equation for P_p is the same as presented in Eq. 2.31 but now K_p is given by

$$K_p = \frac{\cos^2(\phi + \theta)}{\cos^2\theta \cos(\delta - \theta)[1 - \frac{\sin(\theta-\delta)\sin(\phi+\alpha)}{\cos(\delta-\theta)\cos(\alpha-\theta)}]^2}. \tag{2.40}$$

The terms ϕ, θ, δ, and α in the equation are defined in Figure 2.16. Coulomb's solution therefore overestimates the total passive resistance of the soil mass due to the assumption that the failure surface from the toe of a retaining wall to the surface of the soil is planar. This solution is considered an upper bound solution to the true collapse load (Craig, 1987). When δ is large (greater than $\phi/3$), errors using Coulomb's solution are large, as great as 30 % (Terzaghi and Peck, 1967).

In reality, the failure surface of a passive earth pressure failure will not have a planar surface but will be curved as shown in Figure 2.17. The curved lower portion of the failure surface is assumed to be the arc of a logarithmic spiral (Terzaghi and Peck, 1967). This arc eventually meets the straight Rankine failure surface as shown

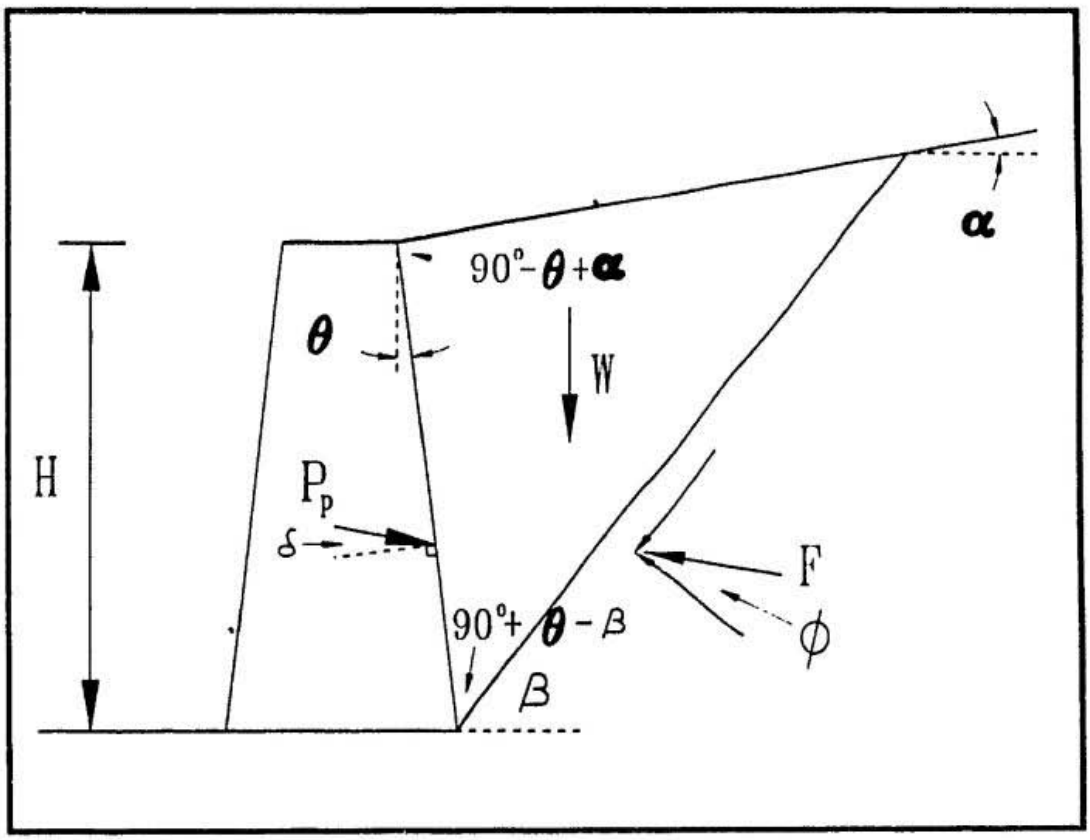

Figure 2.16: Coulomb's Assumed Passive Earth Pressure Failure (After Das, 1985).

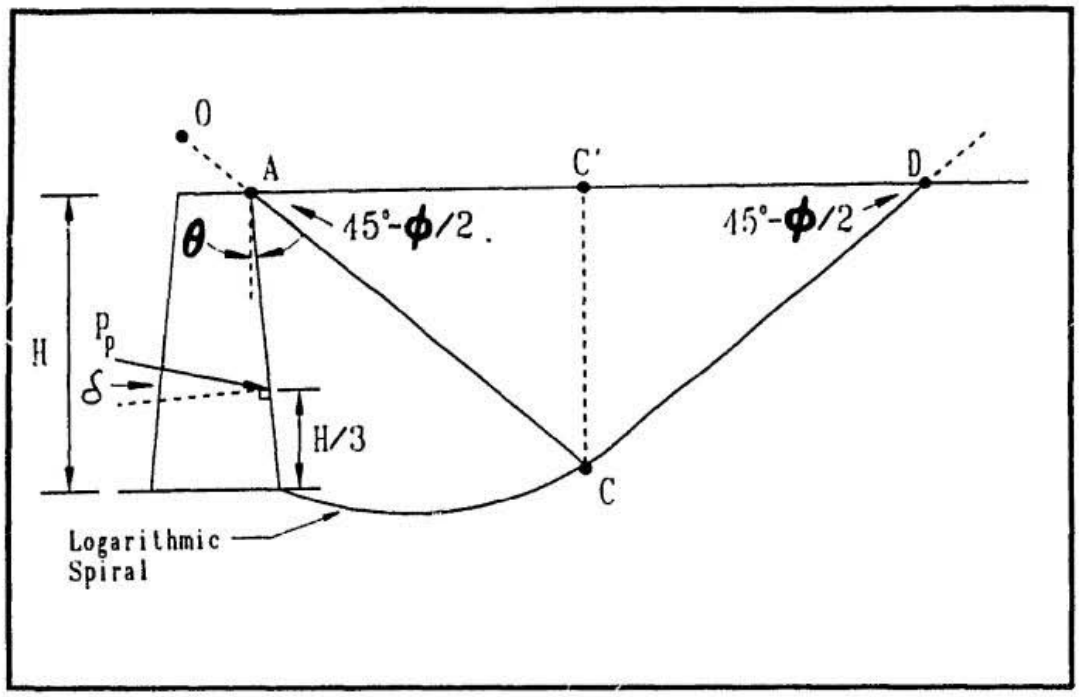

Figure 2.17: Terzaghi and Peck's Assumed Failure Surface for Passive Earth Pressure Failure (After Das, 1985).

in the figure. The method of analysis consists of evaluating several failure surfaces for the passive resistance and assuming that passive failure occurs along the surface of least resistance. This method is referred to here as the Terzaghi and Peck Log Spiral Analysis but it has also been referred to as the Trial Wedge Procedure (Das, 1985).

Shields and Tolunay (1973) improved Terzaghi and Peck's Log Spiral Analysis by calculating the passive earth pressure using the method of slices. This method is similar to the logarithmic spiral method, but the determination of the failure surface yielding the least passive resistance is not required. Details of the derivation of the values of K_p are not given here but can be found in the above reference. Values of

K_p for a retaining wall with a vertical back ($\theta = 0$), a horizontal ground surface, and a cohesionless backfill material are given in Table 2.2. The passive earth pressure is then determined from (Shields and Tolunay, 1973)

$$P_p = \frac{1}{2}\gamma H^2 K_p \tag{2.41}$$

where all terms have been previously defined.

Table 2.2: Shields and Tolunay's Values for K_p (After Shields and Tolunay, 1973).

φ in	δ in Degrees									
Degrees	0	5	10	15	20	25	30	35	40	45
20	2.04	2.26	2.43	2.55	2.70	—	—	—	—	—
25	2.46	2.77	3.03	3.23	3.39	3.63	—	—	—	—
30	3.00	3.43	3.80	4.13	4.40	4.64	5.03	—	—	—
35	3.69	4.29	4.84	5.34	5.80	6.21	6.59	7.25	—	—
40	4.60	5.44	6.26	7.05	7.80	8.51	9.18	9.83	11.03	—
45	5.83	7.06	8.30	9.55	10.80	12.04	13.26	14.46	15.69	18.01

Harrison (1972) conducted research into the forces required to translate a single-plate grouser, without rotation, into different types of soil. Such a grouser is shown in Figure 2.18. The soil between the plates of the grouser is considered to be a dead zone, moving with the grouser. Therefore, the angle of friction between the grouser and the soil is the internal angle of friction of the soil. The failure/rupture pattern postulated by Harrison (1972) is shown in Figure 2.19. It is assumed that the failure surface [B-C] is parallel to the direction of the movement of the plate grouser. The wedge [A-B-C] moves in the same direction as [A-B] and the failure plane is along [A-C] making the required angles with [B-C]. The rupture surface is a logarithmic spiral [A-C-D] connected to a Rankine passive zone. The interface at [A-C] and [A-B]

is treated as a retaining wall with $\delta=\phi$ (perfectly rough surface). Exact details of the method of calculating the required pressures to fail the soil are not presented here but are fully explained in Harrison (1972).

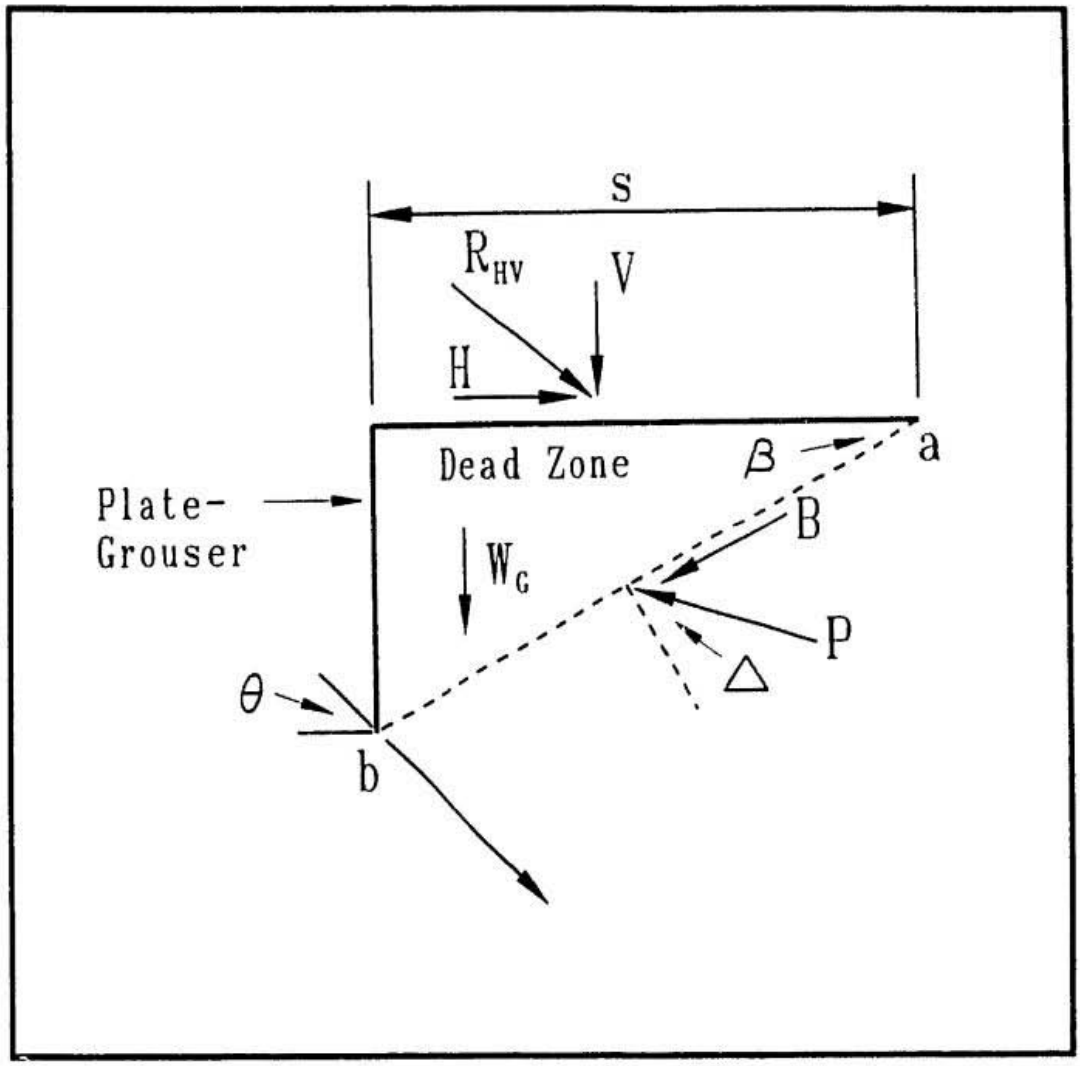

Figure 2.18: Forces on a Plate-Grouser at Critical Equilibrium (After Harrison, 1972).

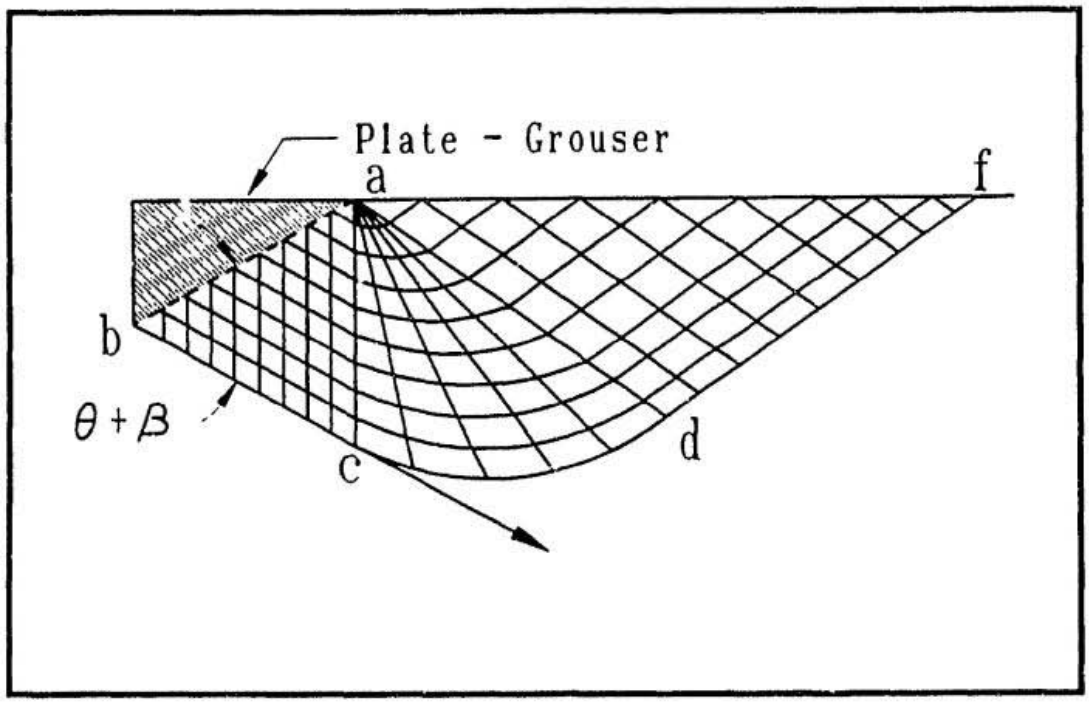

Figure 2.19: Soil Failure Produced by a Plate-Grouser (After Harrison, 1972).

Chapter 3

Experimental Scope and Objectives

3.1 Scope of the Experiments

The safe implementation of subsea facilities such as pipelines or cables in a cold ocean environment, requires knowledge on how deep they should be buried or trenched so they are protected from ice scour. It is not sufficient to bury them just below the maximum scour cut depth predicted by a statistical approach. Potential soil movements and pressures below the scours must be taken into account and evaluated.

An actual ice scour taking place is a difficult event to observe and would not reveal much information about the process taking place under the ice keel. The phenomenological studies indicate the magnitude of the problem and can be used to determine probabilities of a certain area being scoured. These studies also give us ideas about protecting subsea installations. Since actual scours are difficult to observe, similar events have been studied. The study of relict scours has revealed displacements and potential failure mechanisms below the scours. Observations of small scale scouring on tidal flats has done the same. Analytical models and theories have been developed in the study of ice scouring in order to predict depths and lengths

of scours and to define the soil failure mechanisms and subscour forces associated with scour. However, these models and theories must be validated or calibrated by some means.

Several sets of physical model tests have been conducted in order to study ice scouring as were presented in Chapter 2. These test programs were conducted in an attempt to observe and monitor a scouring event under controlled conditions. In most cases, during the testing programs, forces on the models were recorded, but no measurements were made of subscour displacements and pressures. These subscour displacements may be the determining factor in pipeline design; axial forces and bending moments generated in the pipeline through movement with the soil might be the limiting design factor in the calculation of pipeline burial depths. Therefore, it is extremely important that the zone of influence below a scour be identified. The tests done as a part of this thesis work are a continuation of the sand tests conducted by C-CORE at Memorial University (Poorooshasb, 1990), in which the measurement of subscour displacements was a primary objective.

There are problems in modelling soil/iceberg interaction in the laboratory because all of the laws of similitude cannot be followed. Some of these problems arrive from trying to scale sediment grain size, density, and shear strength and consequently these properties could not be scaled properly. Therefore, the results of this experimental program cannot be scaled up to a prototype event; however, by observing the scour process at this smaller scale, the observations and measurements give further insight into the full scale process and reveal trends and parameters which are useful.

The four tests were conducted using the same iceberg model geometry in order to examine the repeatability of the process. The last two tests were conducted in a submerged testbed so that the results from dry and submerged tests could be com-

pared. The sand testbed was prepared at a low relative density because Poorooshasb and Clark (1990) as well as Been et al (1990b) reported the greatest subscour displacements in loose sand. Poorooshasb and Clark (1990), Green (1984), and Prasad (1985) all reported changes in measured forces, pressures, and displacements resulting from a change in model keel geometry. From these results, it was decided to use a model keel with a small attack angle because this should yield the greatest subscour displacements.

3.2 Experimental Objectives

The experimental objectives outlined at the beginning of this experimental program were as follows:

- to measure displacements in the soil below the scoured surface;
- to measure the stress response in the soil below the scouring model;
- to measure the pore pressure response in the soil beneath the scouring model;
- to measure the horizontal forces acting on the model;
- to measure the vertical forces acting on the model;
- to measure the pressures acting on the face of the model;
- to measure the post scour profiles;
- to measure soil density changes across the scour profile, and
- to compare the results from the dry tests to those of the submerged tests.

The results of the experimental program are presented in Chapter 6.

Chapter 4

Experimental Facilities and Equipment

4.1 Scour Tank

4.1.1 The Tank

The tank used for these tests was the ice scour research tank at Memorial University, which was the same tank used by Green (1984), Prasad (1985), and Poorooshasb (1990). The watertight tank is approximately 14 m long, 6 m wide, and 1.1 m deep and is subdivided into two smaller tanks by a center wall as shown in Figure 4.1. The tank used for this experimental program was the tank nearest to the facility entrance, termed the sand scour tank (as opposed to the silt scour tank on the other side). Also shown in Figure 4.1 is the coordinate convention used during the experiments. The scour tests proceeded in a negative Y-direction. The figure also shows pipes on the floor of the tank which were connected to an exterior faucet. These pipes were full of small holes and wrapped in geotextile so the sand could not plug the holes. Flooding and drainage of the tank took place through these pipes. During drainage, the exterior water supply was disconnected and the tank allowed to drain through gravity forces into a sump located outside the tank.

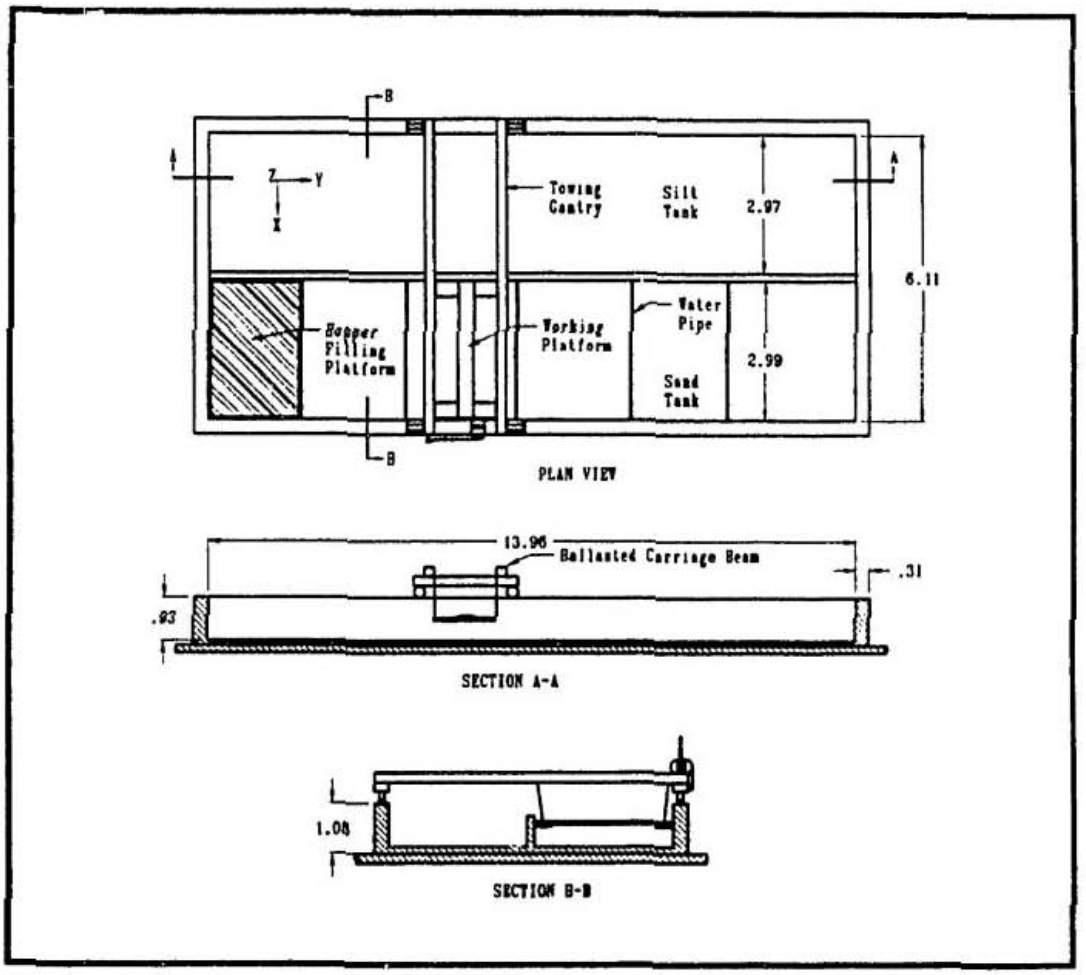

Figure 4.1: Ice Scour Research Tank, Memorial University (After Green, 1984).

4.1.2 The Gantry

Spanning the scour tank was a moving gantry (also shown in Figure 4.1) that ran on tracks bolted to the tops of the two extreme tank walls. The gantry is ballasted in order to provide a resistance to overturning when forces on the gantry become large. The rectangular beams comprising the gantry also provide a base to which the iceberg models, sand raining hopper system, working platform, and a 3-dimensional pointer system could be mounted. These pieces of equipment will be described later.

The gantry is driven by a 7.5 H.P., variable speed, electric motor capable of constant towing speeds ranging from 0.06 to 0.30 m/s. Movement of the gantry is controlled by a spring loaded switch connected to the motor by means of an electrical cable so the switch can be moved around the working platform. Limit switches at the ends of the travel extremes ensure that the gantry does not go off the ends of the tank. The gantry's position was continuously recorded by means of the data acquisition system.

4.1.3 The Sand Raining Hopper System

Connected to the front of the gantry was an aluminum, sand raining hopper used to prepare the experimental testbed. The hopper was filled by hand from the hopper filling platform located at the end of the tank. This hopper was operated from the gantry working platform and was opened and closed by means of a lever system. The hopper could be raised, lowered, and levelled by means of winches and wire cables attached to the gantry. Two long square-section bars kept the sway of the hopper to a minimum and also prevented contact with the sides of the tank. The sand raining hopper system is shown in Figure 4.2.

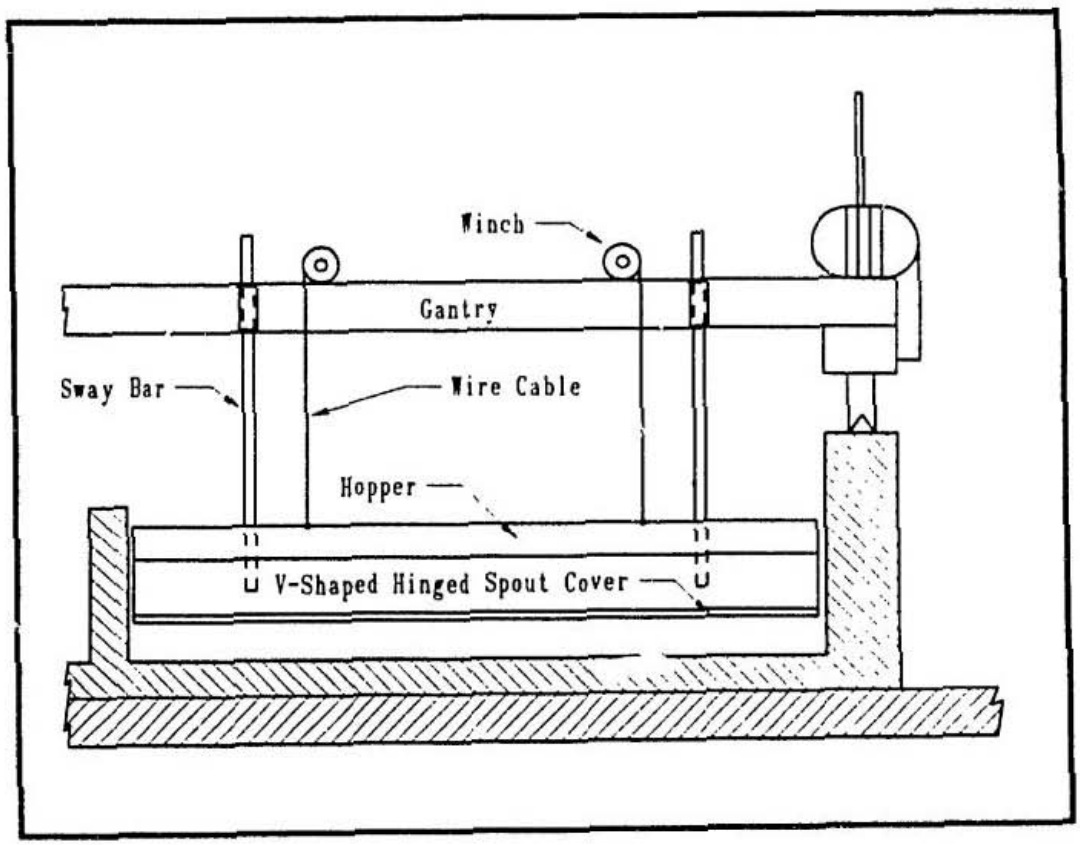

Figure 4.2: Sand Raining Hopper System, Frontal View.

4.1.4 Working Platforms

A working platform was needed between the rectangular beams of the gantry to operate the hopper system, to place and retrieve testbed instruments, and to take measurements with the 3-dimensional pointer system. The platform consisted of a 3x16-inch plank, 2.9 m in length, which rested upon two short end planks as was shown in Figure 4.1. The end planks were connected to the main gantry beams by means of a rope and pulley system thereby allowing the working platform to be raised or lowered to a convenient or comfortable working height. A hopper filling platform was also constructed in the forward end of the tank so that the hopper could be loaded or its height adjusted (see Figure 4.1).

4.2 Experimental Testbed

4.2.1 Experimental Testbed Soil

The experimental testbed was made up of 6 to 7 m^3 of clean, dry silica sand (type 0) which was commercially available from Nova Scotia Sand and Gravel. This replaced the sand used by Green (1984) and Prasad (1985) due to the amount of fine particles present in the earlier sand. The testbeds were prepared by raining the sand from about 2 to 10 cm above the sand surface. As a result of this procedure, the dust level would have been too high using the older sand. Sand is easier to handle than other soils and is also a material which is commonly found in offshore environments. Therefore, it was decided to use this testbed material for the experimental program. Properties of this sand were determined and are presented in Table 4.1. The grain size analysis is presented in Figure 4.3.

The angle of friction between the model (aluminum) and the sand at its desired

Table 4.1: Soil Properties.

Sand Type	:	Type 0 Silica Sand
Experimental Density, ρ_{exp}	:	1361.9 kg/m^3 $\pm$ 2.4%
Maximum Grain Size	:	1-2 mm
Effective Grain Size, D_{10}	:	0.325 mm
Coefficient of Uniformity, C_u	:	1.662
Coefficient of Curvature, C_c	:	1.154
Experimental Unit Weight, γ_{exp}	:	13.36 kN/m^3 $\pm$ 2.4%
Minimum Dry Unit Weight, γ_{d-min}	:	13.46 kN/m^3
Maximum Dry Unit Weight, γ_{d-max}	:	15.79 kN/m^3
Minimum Dry Density, ρ_{d-min}	:	1373 kg/m^3
Maximum Dry Density, ρ_{d-max}	:	1610 kg/m^3
Density Index of Testbed, I_D	:	-5.41 %$\pm$ 2.4%
Internal Angle of Friction at γ_{exp}, ϕ_{exp}	:	35°
Soil-Model Friction Angle, δ	:	23°
Maximum Void Ratio, e_{max}	:	0.923
Minimum Void Ratio, e_{min}	:	0.640
Water Content of Air-Dried Sand, w_{exp}	:	0%

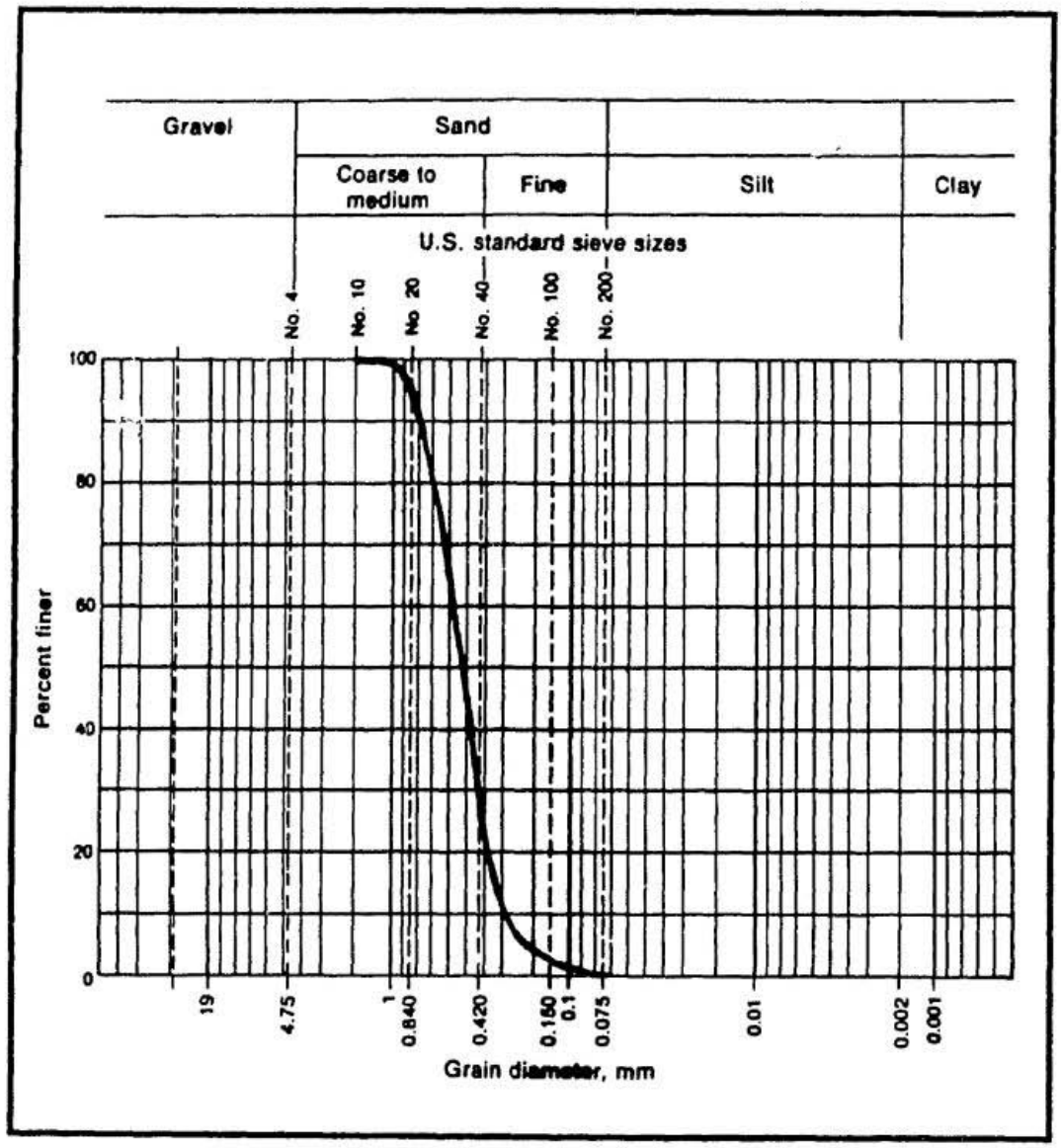

Figure 4.3: Grain Size Analysis of the Sand Used in the Experimental Program.

density (0 % relative density) was determined by shearing samples of the sand against a block cut from the same type of aluminum as that used in the construction of the model. This angle of friction is also presented in Table 4.1.

4.2.2 Testbed Instrumentation

Several pieces of instrumentation were placed in the prepared testbed in order to measure pore pressures, stresses, and displacements. The precise location of each piece of instrumentation could be recorded using the 3-dimensional pointer and data acquisition systems. All electronic instrumentation was calibrated prior to the start of the testing program and the calibrations and characteristics of this equipment are given in Appendix A.

Pore pressures in the soil during the submerged tests were measured using six Druck pore pressure transducers (PPT's). Four of the cells had a range of 0 to 35 kPa while the other two had a range of 0 to 105 kPa. These transducers were powered by 5 v and both supply and output signal were monitored during testing.

Total stresses in the soil were measured using two waterproof load cells (TSC's). These cells were manufactured at Memorial University and consist of a low-profile machined cylinder, the inside of which was strain gauged. The TSC output was amplified through a 10-channel amplifier before it proceeded to the data acquisition system. The amplifier also supplied the 10 v input to the TSC's.

One type of displacement marker used was 1/2 inch diameter, stainless steel ball bearings, engraved with identification numbers. These ball bearings were buried in the testbed and their movements in the soil measured to yield displacements. Also placed in the testbed were solder strands, 1 mm in diameter. This solder was very pliable and it was assumed that it would deform rather easily in the testbed,

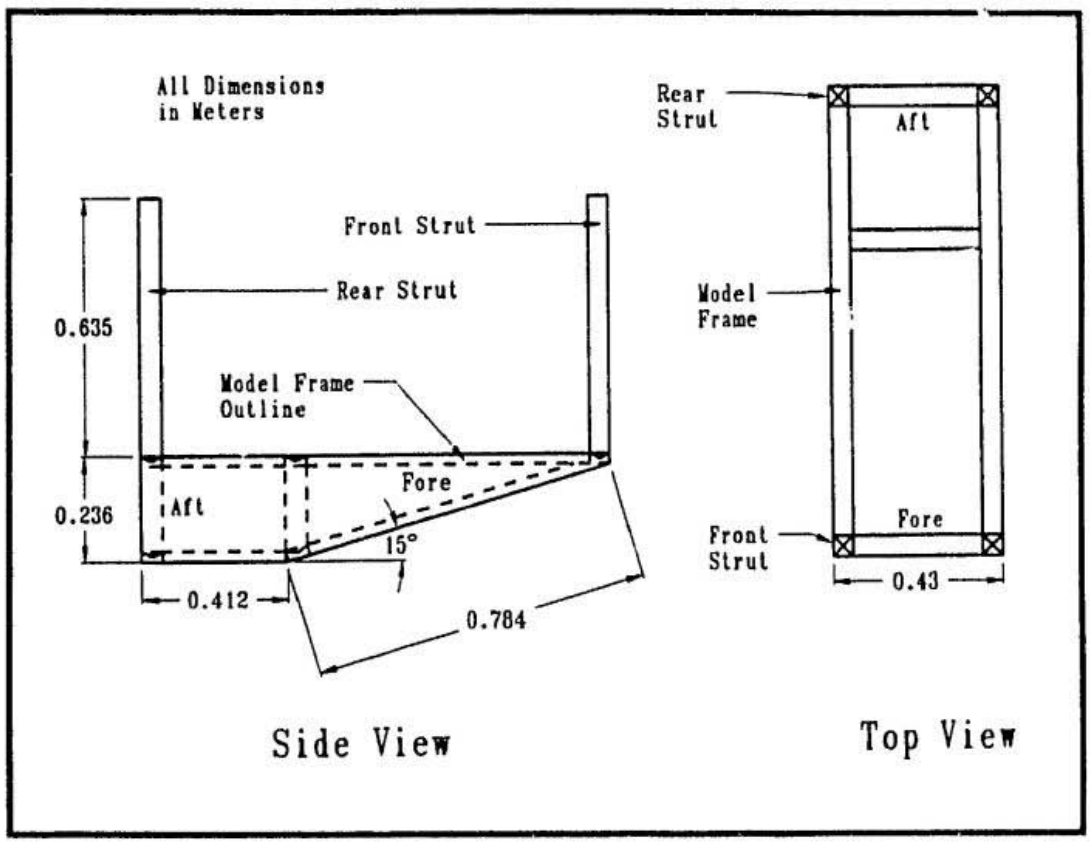

Figure 4.4: The Iceberg Model.

indicating movements. The last items placed in the testbed (submerged tests) were spaghetti strands. Spaghetti becomes soft when exposed to moisture and it was assumed that the strands would also deform in the testbed yielding information on soil displacements.

4.3 Model Iceberg

4.3.1 The Model Iceberg

The model iceberg consisted of a steel frame constructed out of square hollow tubing to which 1/2 inch aluminum plates were bolted. The frame and completed model are shown in Figure 4.4. The model was 0.43 m wide, 1.2 m long, and had an attack angle of 15°. Bolts which were used to assemble the model were countersunk into the aluminum plate and all remaining holes and small cracks were filled with a metal bodyfiller and sanded smooth. The cracks and seams on the inside of the model were caulked with waterproof caulking to prevent leakage into the model during the submerged tests.

The model was connected to the gantry by means of the aluminum mounting frame shown in Figure 4.5. The swing plate connected to the bottom of the aluminum frame allowed slight forward and reverse motion of the model in the Y-direction. The top mounting brackets were set so that when the iceberg model was mounted, it would be the correct distance above the floor of the tank. The aluminum mounting frame was in turn rigidly bolted to the gantry beams by means of two L-shaped sections as shown in Figure 4.5. These L-shaped sections were only in place during the tests and were removed when the iceberg was removed.

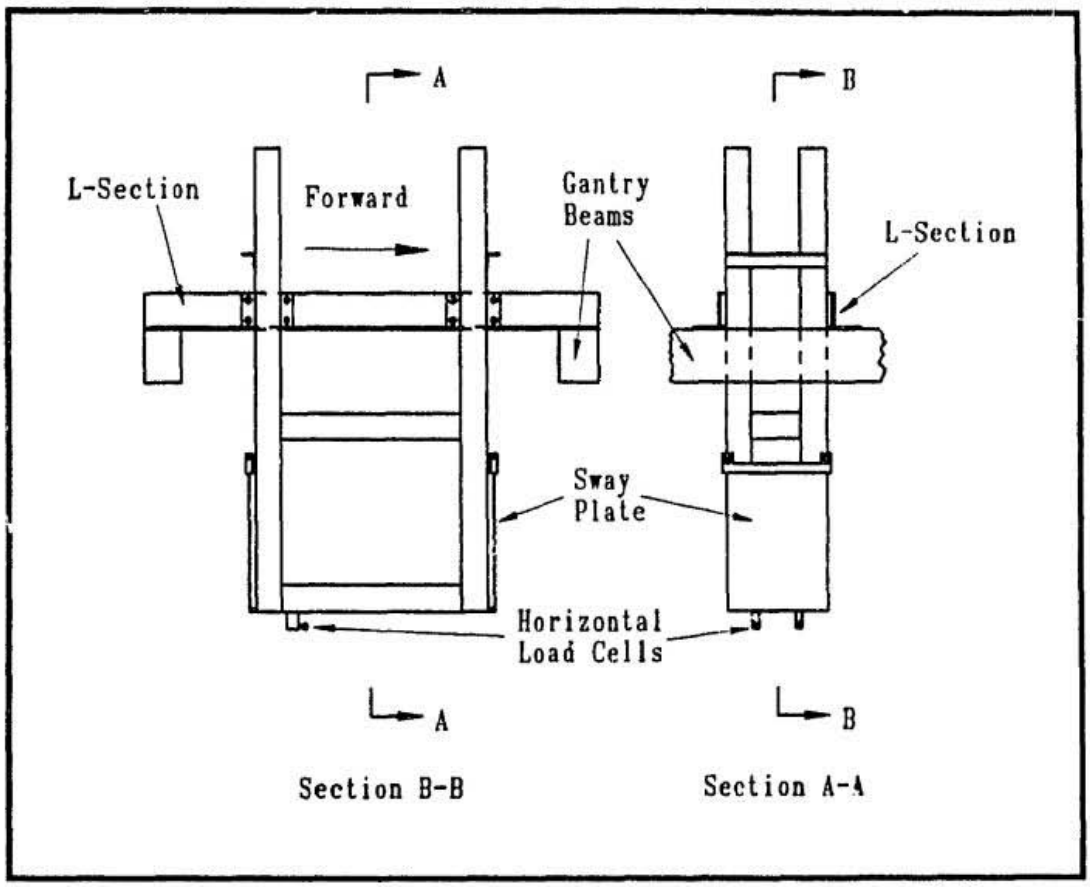

Figure 4.5: Model Iceberg Mounting Frame.

4.3.2 Instrumentation on the Model

Three main pieces of instrumentation were attached to the model iceberg to measure various parameters. These instruments were all calibrated prior to the start of the testing program. Calibrations and a full description of the instrumentation is given in Appendix A.

The iceberg model was connected to the aluminum mounting frame by four beam load cells (BLC's) as shown in Figure 4.6. These load cells were used to measure vertical forces acting on each of the frame struts of the model. The BLC's were free to rotate about the axis of the connecting pins through the sway plate and therefore the model was able to move slightly back and forth as was mentioned earlier. These beam load cells operated off of 5 v supplied by the data acquisition system to which the output from the cells was also connected.

Two load cells were used to measure the horizontal forces acting on the model. These horizontal load cells (HLC's) were positioned as shown in Figure 4.7. Increases and decreases in the horizontal force acting on the model could thus be measured because of the movement of the sway plate. These load cells tended to drift and had to be zeroed and grounded before the start of each test. Amplifiers were required for these cells and were positioned directly on the aluminum mounting frame. Output from the load cell amplifiers ran directly into the data acquisition system.

Pressures on the model iceberg face were measured by means of five (four for the last two tests) face pressure cells (FPC's). These cells were positioned on the face of the model as shown in Figure 4.8. The FPC's were threaded and screwed into threaded holes cut in the aluminum plates. The transducers were mounted flush on the model face and small clearances between the aluminum plates and the pressure cells filled with metal bodyfiller and sanded smooth. The part of the pressure cell

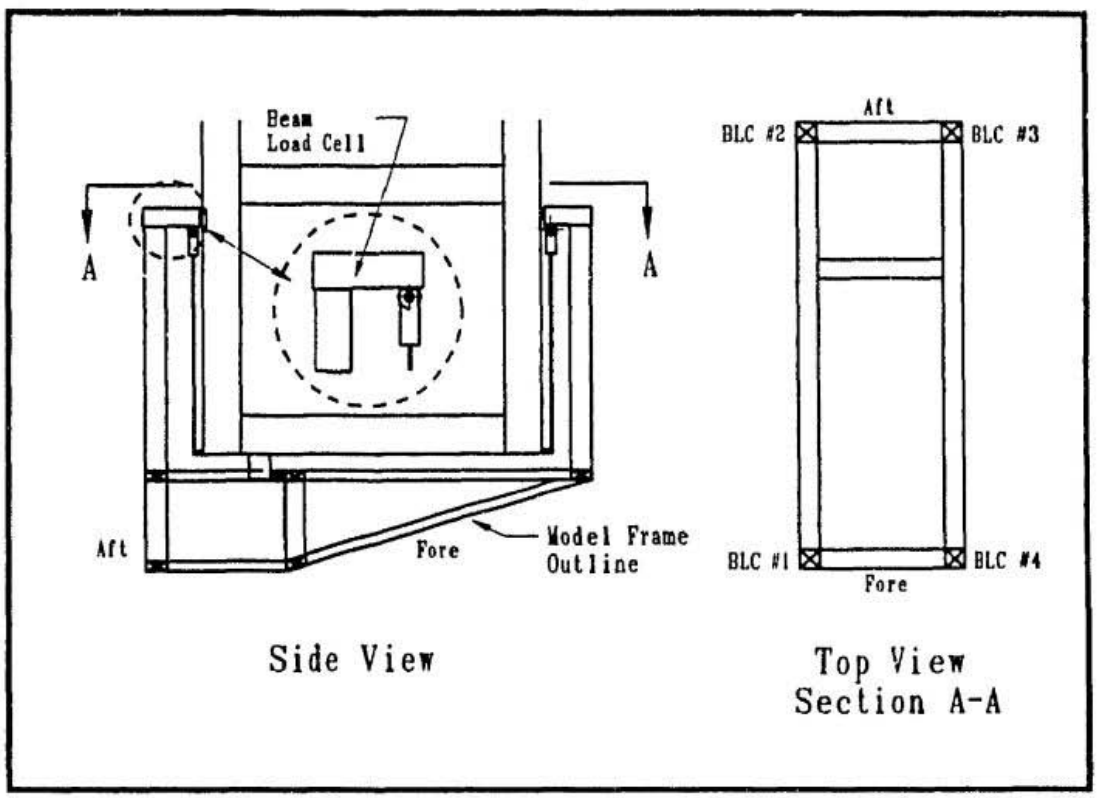

Figure 4.6: Beam Load Cell Connection.

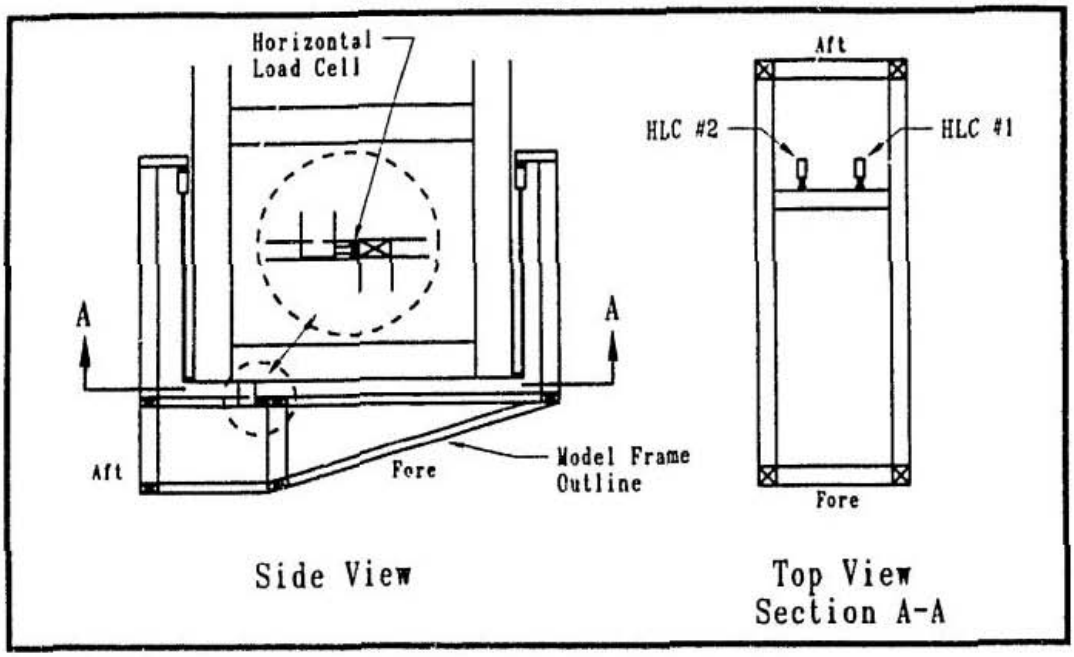

Figure 4.7: Horizontal Load Cell Connection.

inside the model was completely waterproofed to prevent water from shorting out the instrumentation. The power supplies/amplifiers for these pressure cells were placed in the iceberg itself and the output was directed to the data acquisition system.

4.4 3-Dimensional Pointer System

A 3-dimensional pointer system was used in order to measure the position of instrumentation and other test features in the tank. The ranges of the system were from -0.8 to 0.8 m in the X-direction, 3.5 to 10.3 m in the Y-direction, and 0.0 to 0.55 m in the Z-direction.

The actual pointer was a 1.5 m long (1/2 inch diameter) brass rod which had been machined to a point at one end and had a hole drilled in the other end so that a linear position transducer could be attached. A stepper motor mechanism raised and

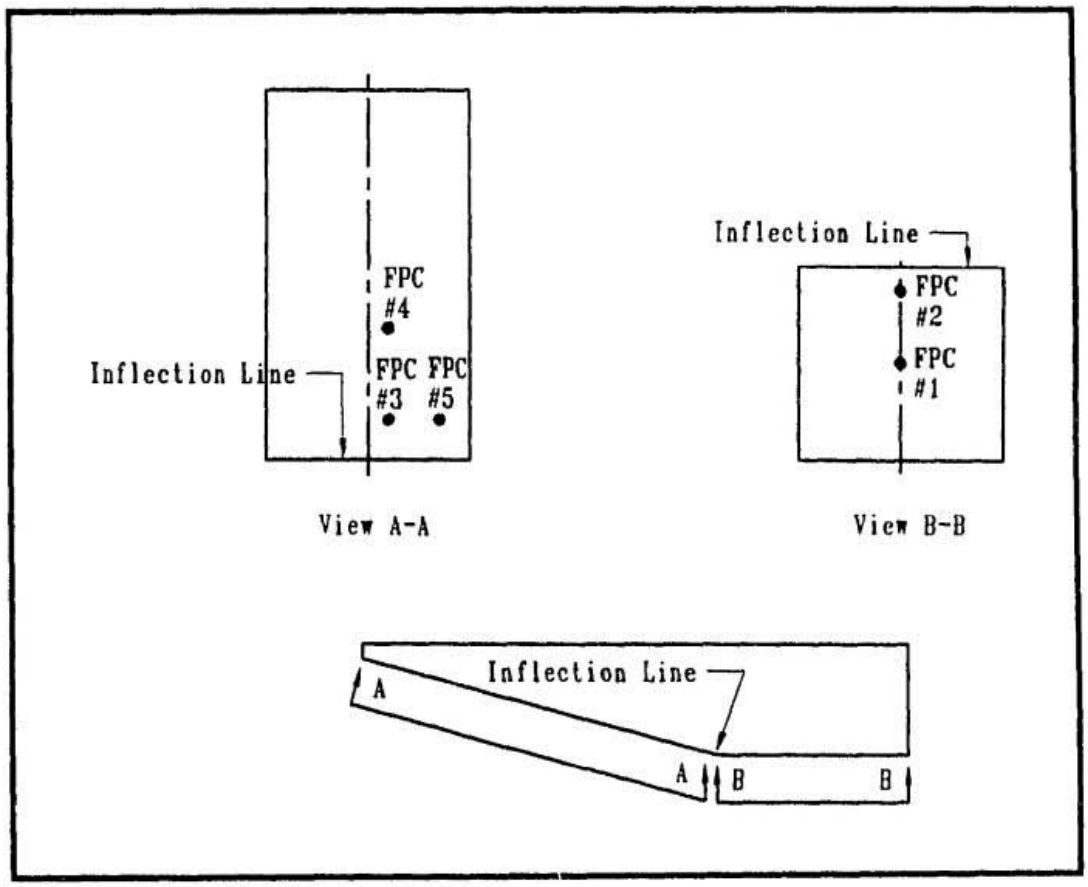

Figure 4.8: Face Pressure Cell Locations.

lowered the pointer rod. A linear position transducer was mounted directly over and connected to the top of the rod. This entire system was mounted on a small truck which moved in the Y-direction and is shown in Figure 4.9.

The small truck described above ran on rails attached to the pointer system gantry which is shown in Figure 4.10. The small truck propelled itself along the pointer system gantry by means of the stepper motor mounted on the truck. The pointer system gantry ran on rails bolted to the tank gantry and was propelled by a stepper motor as well. This setup is also seen in the figure. The step size of the stepper motors was set to a small enough setting to allow accurate positioning of the pointer.

The stepper motors were controlled by a stepper motor controller connected to 3 m of cable so that it could be moved easily around on the gantry working platform. The speed of the stepper motors could be adjusted as desired through the stepper motor controller.

The pointer system was connected to linear position transducers in the X, Y, and Z-directions. Details of the transducers are given in Appendix A. These position transducers were supplied with 5 v which was monitored at all times because full scale output was equal to input. The output from the transducers was connected to the data acquisition system which is described in the next section. The pointer system was calibrated with respect to the tank coordinate system. A QuickBasic program could then convert output voltages from the transducers into an X, Y, and Z-coordinate and display these values on a computer screen. Therefore, at any time, the position of the pointer in the tank could be determined by executing the QuickBasic program.

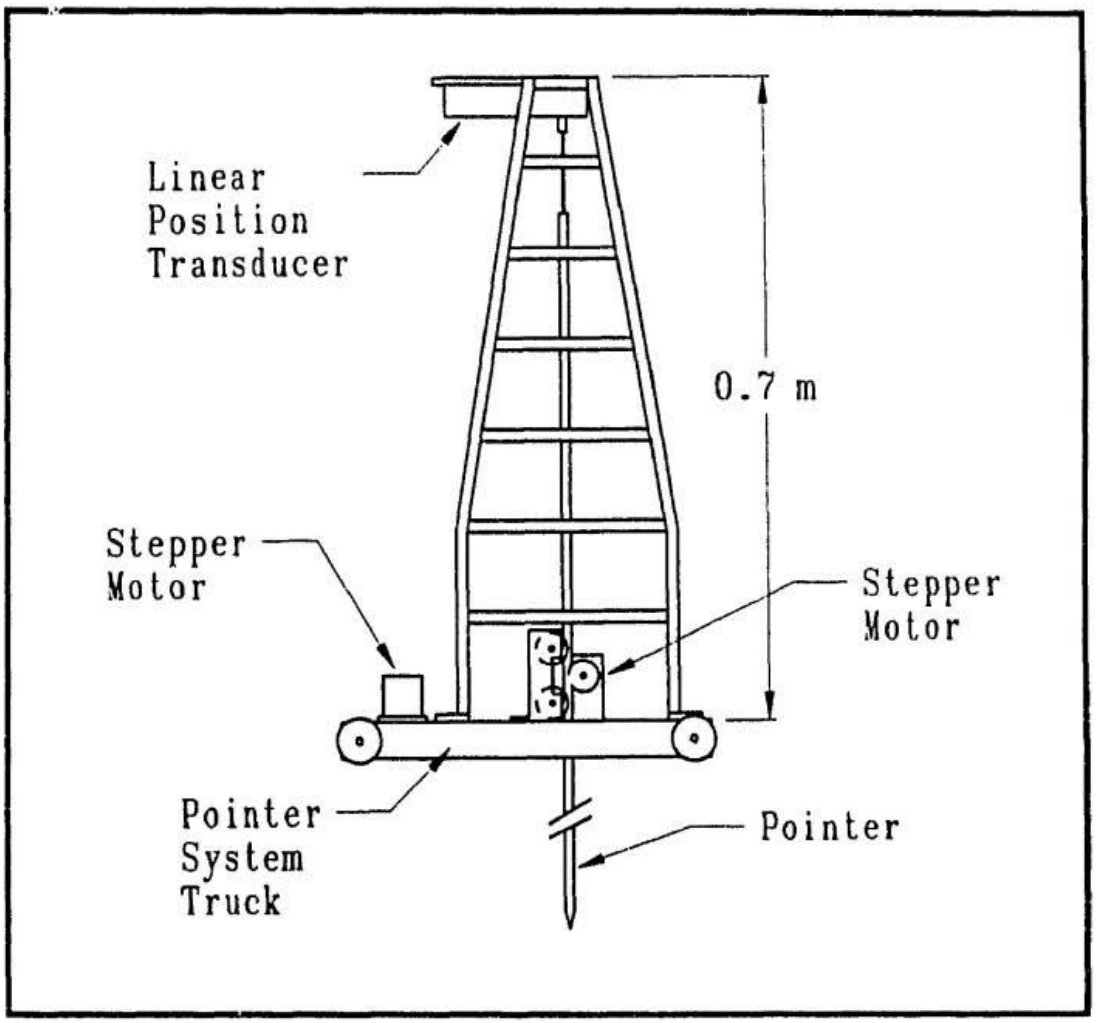

Figure 4.9: Pointer System Truck.

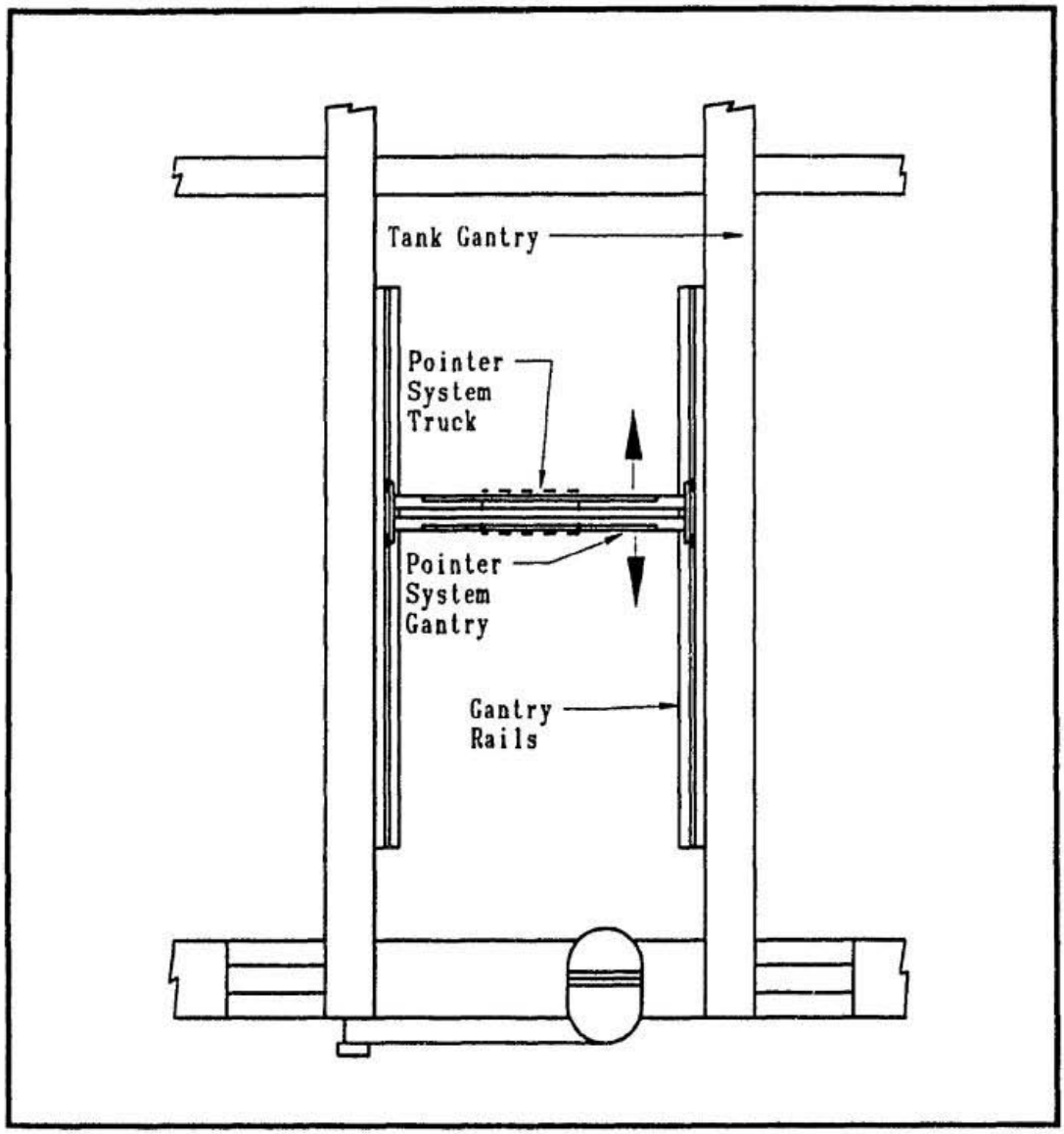

Figure 4.10: Pointer System Gantry, Plan View.

4.5 Data Acquisition System

The data acquisition system consisted of a COMPAQ III portable computer, a Metrabyte DAS-8 analog to digital converter, and two Metrabyte EXP-16 multiplexers. A Hewlett Packard power supply was used to provide 5 v to those instruments requiring input voltage. The data acquisition system equipment is described in Appendix A.

The data acquisition system was located outside of the room containing the scour tank, but a computer monitor was also located on the gantry. By bringing the keyboard to the gantry working platform by means of an extension cord, the data acquisition system could be operated from inside the tank and the output monitored on the gantry mounted screen. As much of the equipment as possible was kept outside of the tank to prevent dust and dirt from contaminating the equipment. The data acquisition system and electrical instrumentation used in the experiments is outlined in Figure 4.11.

The data acquisition system had three primary functions during the experimental program. A computer program was used that allowed the system to act as a voltmeter, displaying the output voltages of instrumentation on the computer screen. This program was useful during calibrations. The second function of the system was to display and/or record the position of the pointer. When this program was used, the pointer system position could be displayed or it could be displayed and simultaneously recorded to a file, the measurement corresponding to a measurement number. This program was extensively used to measure and record the locations of displacement markers and testbed instrumentation. The final acquisition program was used to record the response of the electrical instrumentation and equipment during a test.

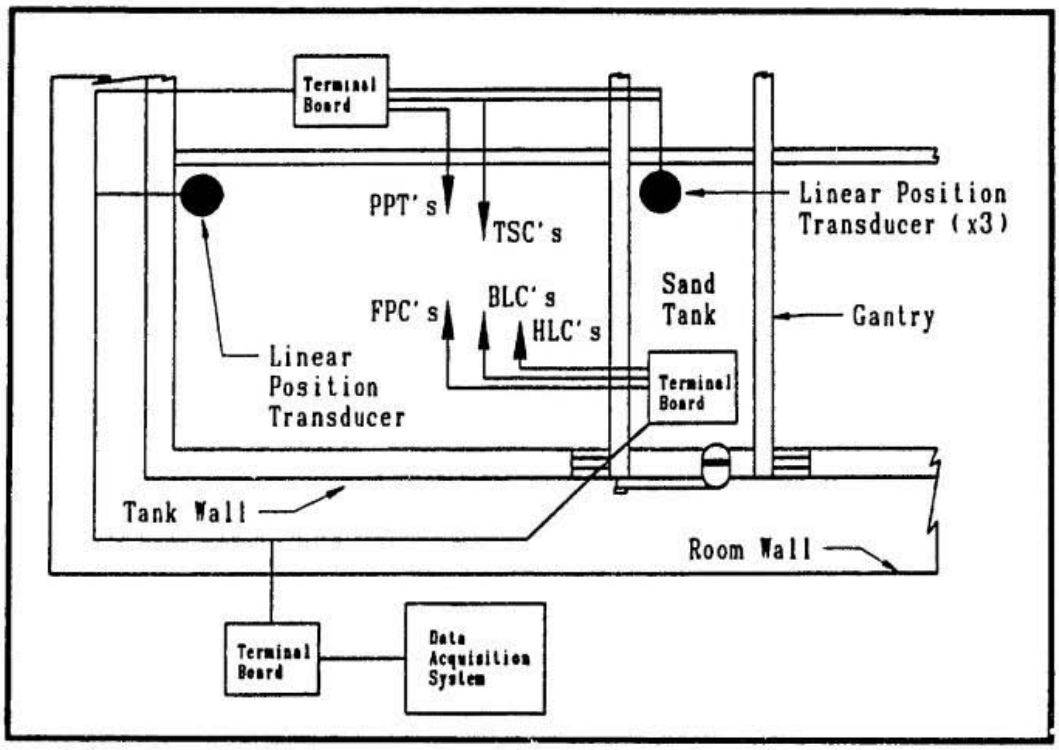

Figure 4.11: Electrical Instrumentation Layout.

In this mode, the system would acquire all the necessary channels of data and write this data to a file.

4.6 Miscellaneous Equipment

Several pieces of miscellaneous equipment were used during the course of this experimental program and are described briefly below.

A vacuum system was used to prepare a flat testbed surface by *shaving* the surface of the sand. This system is shown in Figure 4.12. The vertical rigid vacuum pipe was clamped to the pointer system gantry by means of a mounting bracket and clamps. These clamps allowed the desired shaving height to be set. The rigid pipe was in turn connected to a commercially available vacuum system, located outside the tank, by means of a flexible hose. This system could shave a maximum of 2 cm of sand per pass of the vacuum. Because the rigid pipe was connected to the pointer system gantry which was in turn connected to the main gantry, the vacuum could be moved in two directions allowing almost the entire testbed surface to be shaved.

A Soiltest nuclear densitometer was used to measure the density of the testbed inside and outside of the scour during the first two tests. In the last two tests, a hand-held penetrometer was used in an attempt to measure changes in the penetration resistance of the sand. Density cups which could hold approximately 1×10^{-4} m^3 of sand were used to take density samples of the sand being rained from the hopper system. A 6-inch grain auger was used to move sand around the tank or to fill sand bags when necessary. A hand-held metal detector was used to locate instrumentation in the testbed.

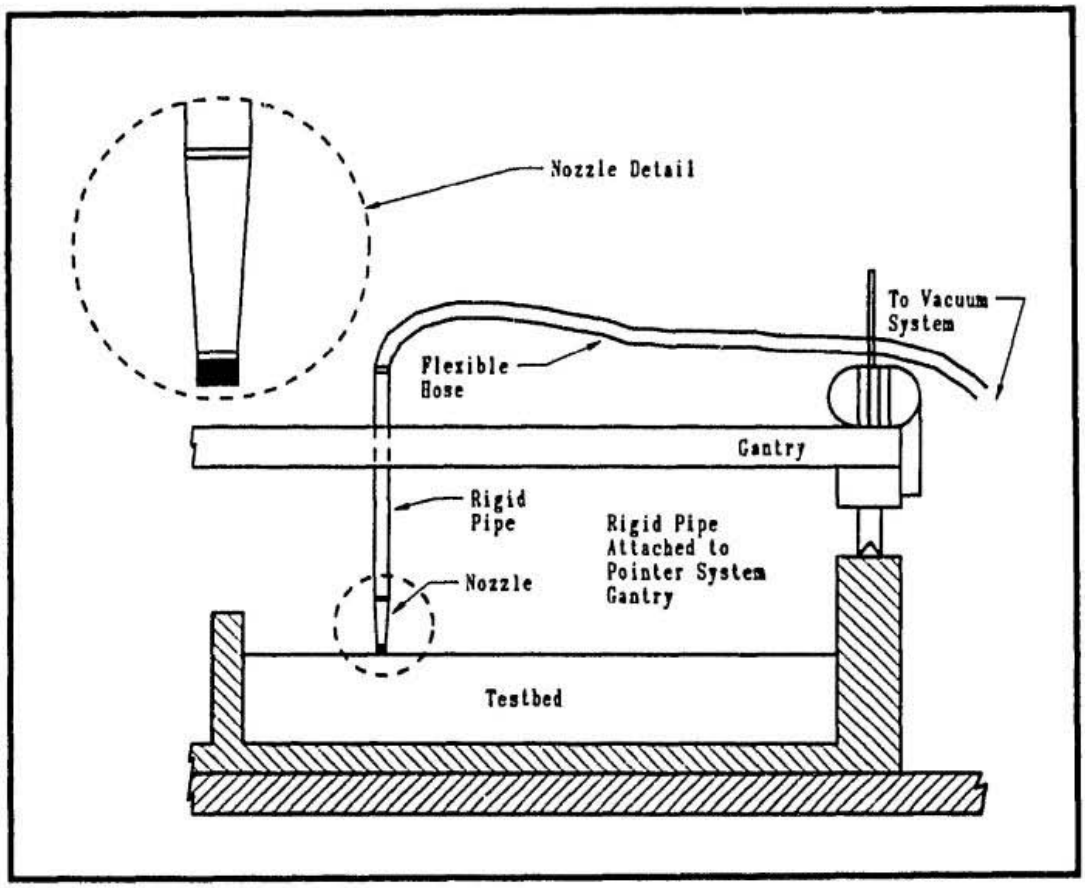

Figure 4.12: Vacuum Shaving System.

Chapter 5

Experimental Procedure

5.1 Preparation of the Sand Testbed

5.1.1 Dry Tests

The hopper system was used to build-up the testbed, layer by layer, by the sand raining method, to the dimensions shown in Figure 5.1. The completed height of the testbed was 0.40 m and the length was 4 to 5 m. The density of the sand could be controlled by varying the drop height of the sand and the transverse speed of the hopper. After some experimentation, it was concluded that in order to obtain the minimum relative density, the sand should be dropped from a minimum height ($\approx$ 4 cm) and the speed adjusted so that a full hopper of sand was laid over approximately 5 m of the tank. At this height and speed, the sand was practically slumped into position. Density measurements for verification were taken throughout each test by placing an empty density cup on the testbed and allowing it to be filled with rained sand. The cup was then picked up, the overflowing sand carefully removed, and the void in the testbed filled with sand slumped from a beaker. The density of the sand in the cup could then be calculated as the volume of the cup was known. Density measurements and the positions of these measurements are given in Appendix B. Average densities

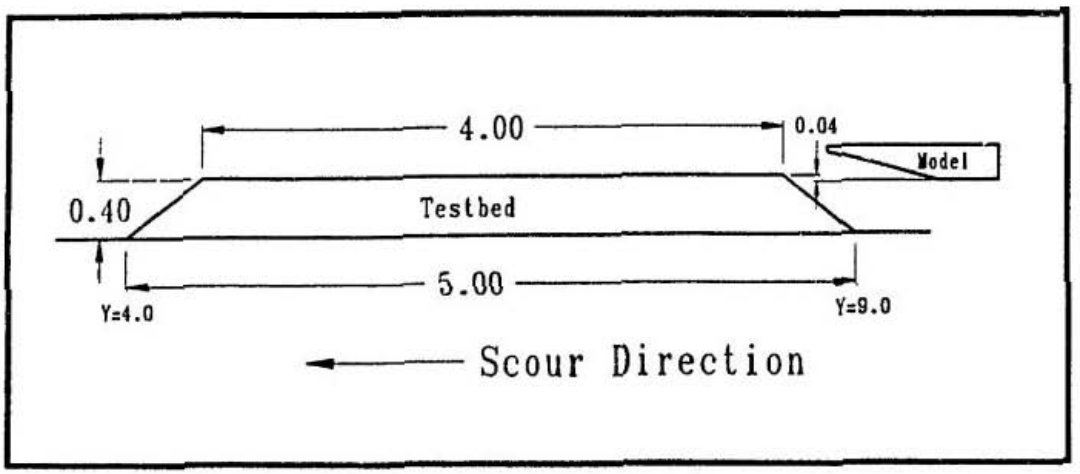

Figure 5.1: Completed Testbed Dimensions.

for all four tests are given in Table 5.1.

Table 5.1: Testbed Densities

Test #	Min. ρ_d (kg/m^3)	Max. ρ_d (kg/m^3)	Avg. ρ_d (kg/m^3)
1	1353.0	1390.6	1370.4
2	1354.7	1380.1	1367.1
3	1348.7	1382.1	1365.5
4	1329.5	1394.3	1363.9

The basic procedure for the preparation of the testbed is briefly outlined here. The tank was empty to begin with and the four density cups were placed on the floor. The hopper was adjusted so that it was approximately 4 cm above the floor and level. The hopper was then filled with sand. One person would move to the gantry working platform to open and close the hopper while another person would operate the gantry. The gantry would start at the Y=1.5 m coordinate and at Y=4.4 m, the hopper was

opened until all of the sand ran out, at about Y=9.5 m. The hopper is shown in Figure 5.2. One run with the hopper produced a 1.5 to 2.0 cm layer of sand. The gantry was then driven back to its starting position, the hopper closed, and its height raised approximately 2 cm. The process was then repeated. It would usually take two runs with the hopper to fill the density cups so that they could be picked up.

Certain instrumentation had to be placed in the testbed as it was built up layer by layer. In order to ensure a flat surface on which to place this instrumentation, the surface of the testbed was shaved flat at desired heights and locations using the vacuum system. Figure 5.3 shows the shaving edge of the vacuum system in the process of shaving the testbed. This process took considerable time, sometimes an entire day. Once the surface was prepared, the instrumentation could be put into position, and this position recorded.

The first instrumentation to go into the testbed were the 1/2 inch engraved, metal ball bearings. The ball bearings were placed on two X-Z planes; one located at Y=5.5 m and the other located at Y=7.5 m. The locations of the balls placed on one of these planes are shown in Figure 5.4. The balls were put in position by first bringing the pointer to that position and then placing the ball under the pointer, as close to centered as possible. A corrected measurement of the balls position could then be made by moving the pointer so that it just touched the apex of the ball bearing as shown in Figure 5.5. These measurements could be out ± 1 mm due to inaccuracies in lining up the pointer to the apex of the ball. Although the positions were recorded to a file using the data acquisition program, all data was backed up manually in the event of a system crash. The I.D. number of each ball was also recorded along with its position. These balls would move with the soil and their post-scour positions could be found and recorded yielding displacements and giving

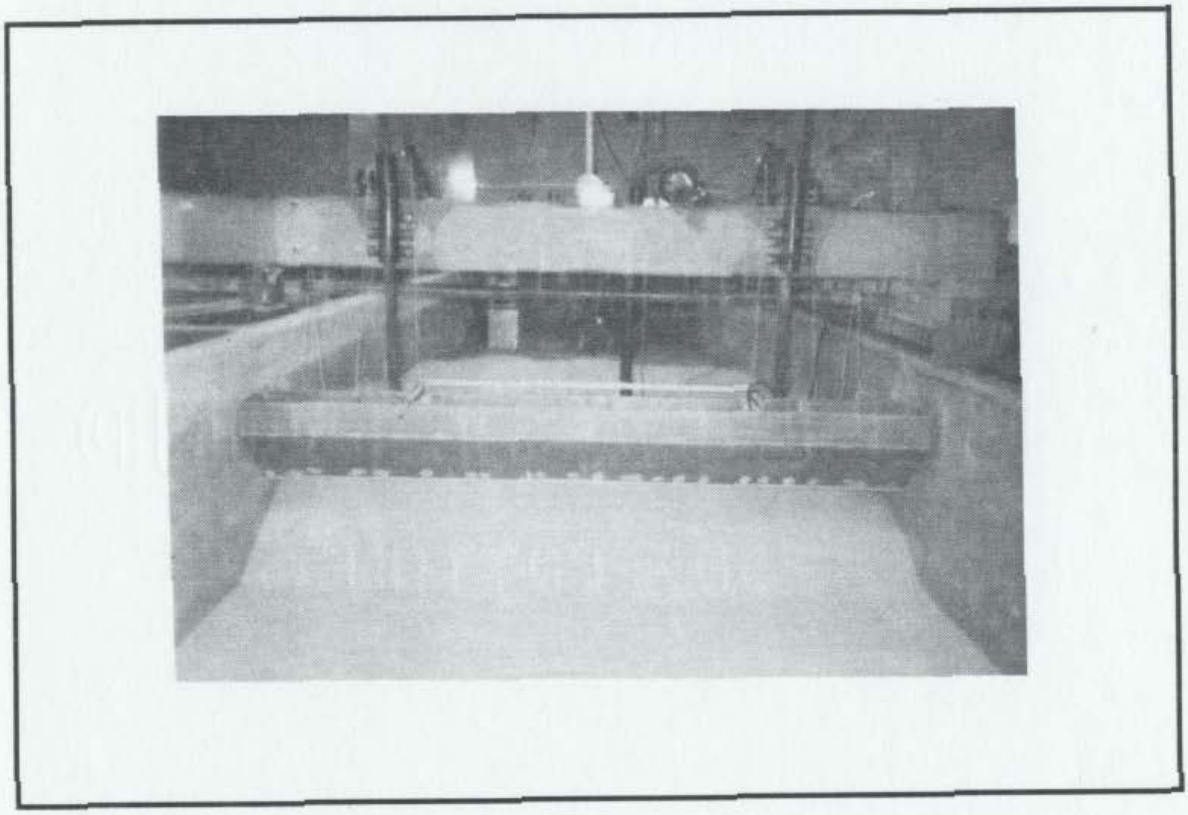

Figure 5.2: Hopper System Preparing to Rain Sand.

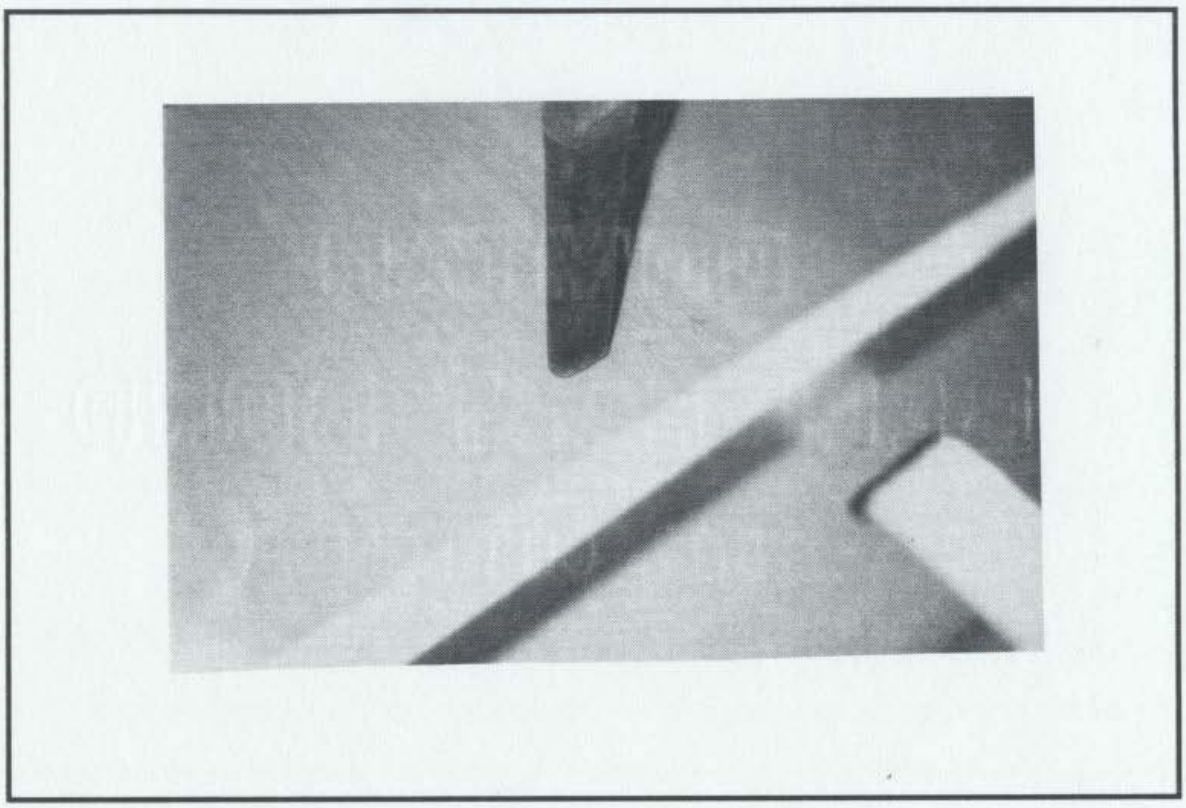

Figure 5.3: Testbed Being Shaved.

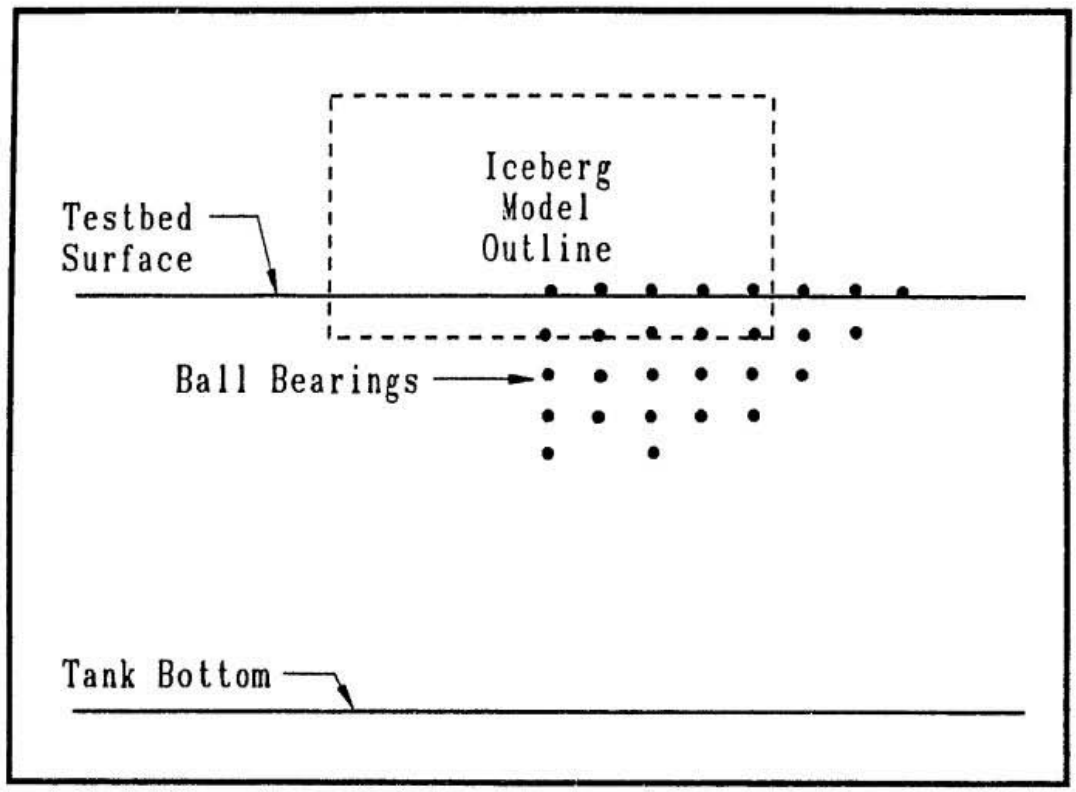

Figure 5.4: Ball Bearing Locations, X-Z Plane.

information about the movement of the sand around and beneath the scouring model.

The next item to go into the testbed were horizontally laid solder strands, positioned as shown in Figure 5.6. These strands were laid perpendicular to the impending scour track as shown in Figure 5.7. The pointer system was then moved along the length of the solder and a measurement of its position taken every 5 to 10 cm. These solder strands would move as the sand moved and would give information about movement of the soil beneath the scouring model.

The final instrumentation to go into the dry testbed were the total stress cells. These were positioned as shown in Figure 5.8. They were put into place in the same manner as the ball bearings and the electrical cable run directly out to the sides of

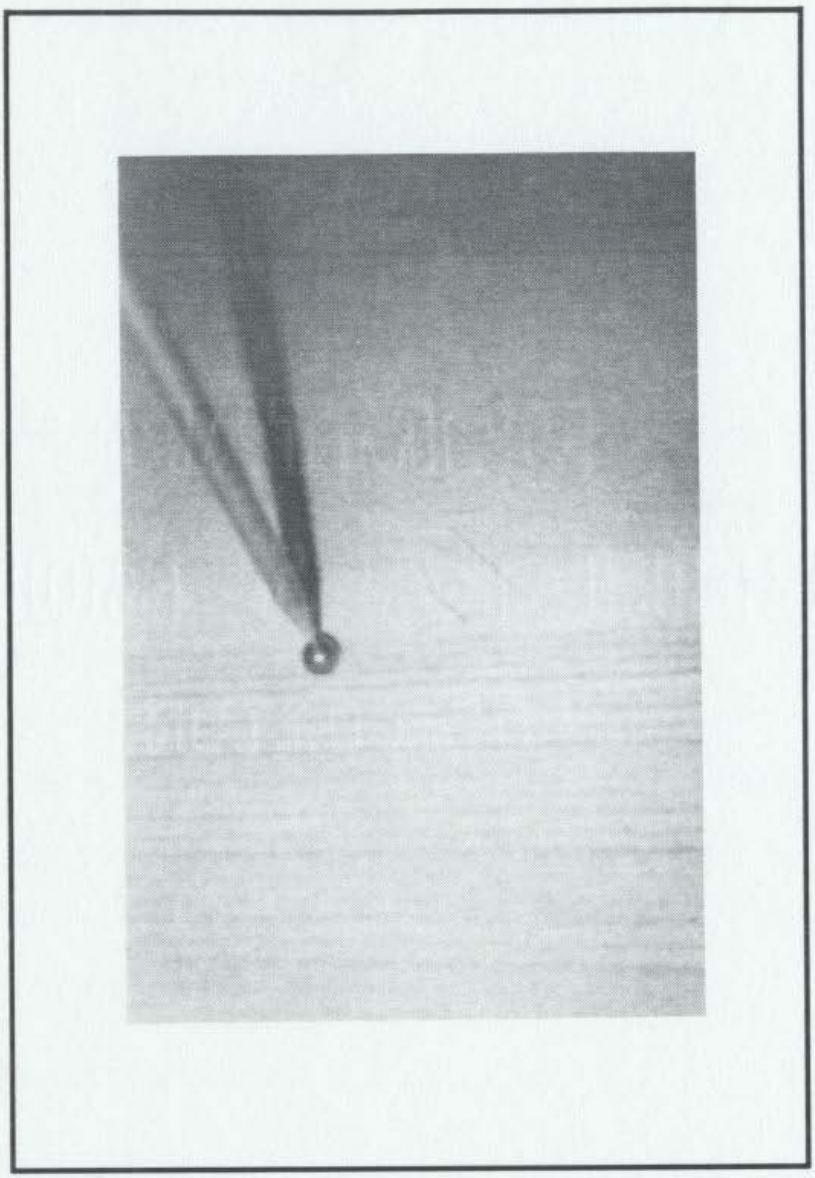

Figure 5.5: Ball Bearing Measurement.

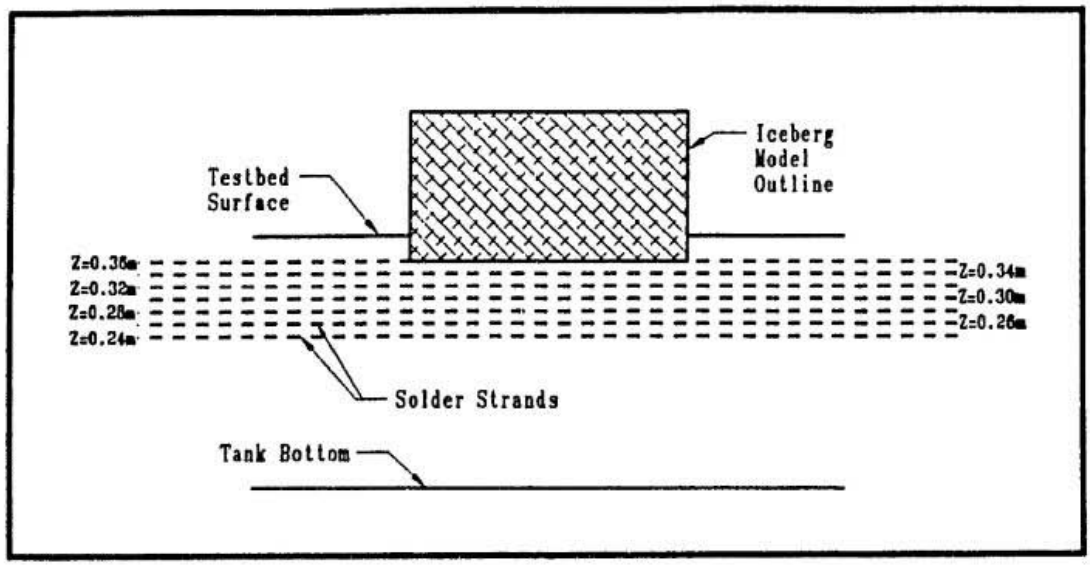

Figure 5.6: Solder Strand Locations, X-Z Plane.

the tank where it was taped to the side of the tank before proceeding out to the amplifier. The positions of the total stress cells were recorded.

Subsequent to the placement of instrumentation, a new layer of sand was laid. An exception to this was at the surface (Z=0.40 m) of the testbed where a layer of ball bearings was placed on the surface as shown in Figure 5.9. A plan view of the instrumentation in the completed testbed is shown in Figure 5.10. Testbed preparation time was typically 5 to 7 days.

5.1.2 Submerged Tests

The logistics involved in the preparation of the submerged testbeds were more complex. In these tests, six pore pressure transducers had to be positioned as shown in Figure 5.11. Other than the addition of the pore pressure transducers, the testbed instrumentation and displacement markers remained the same as for the dry tests. The pore pressure transducers had to be put into position under water because of

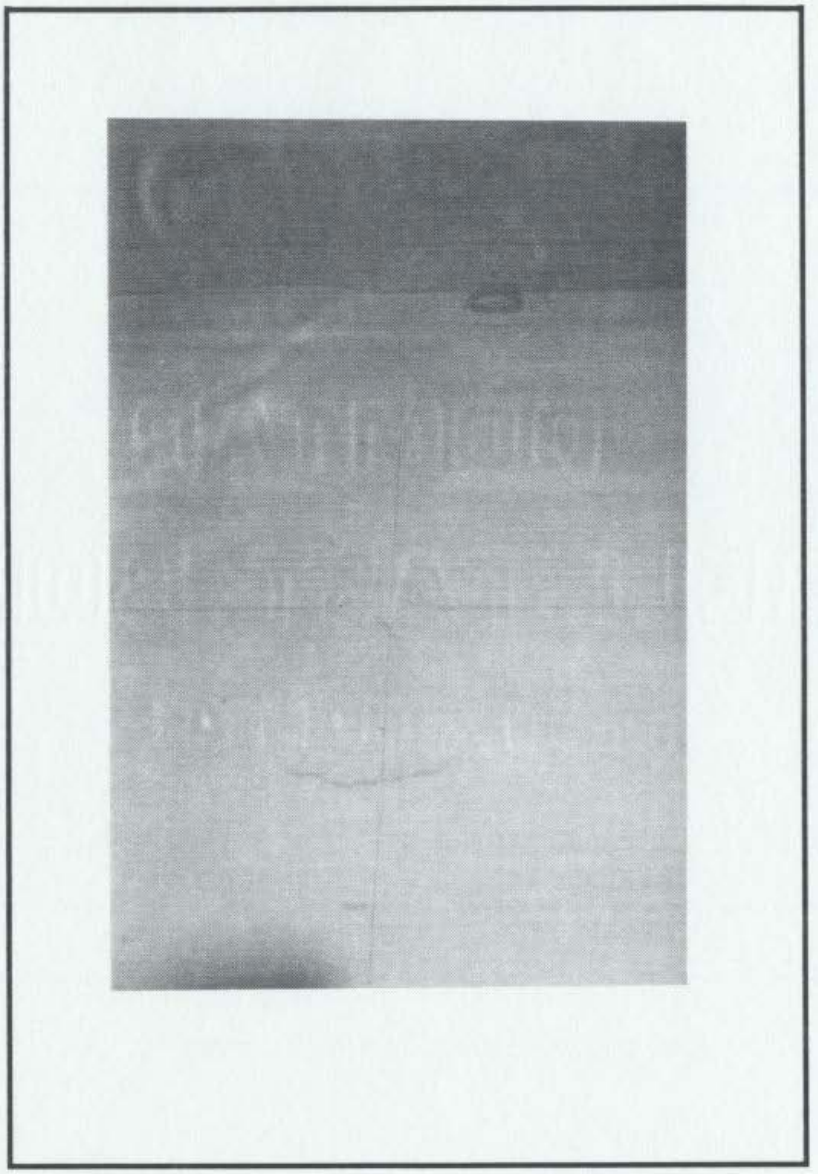

Figure 5.7: Solder Strand in Position.

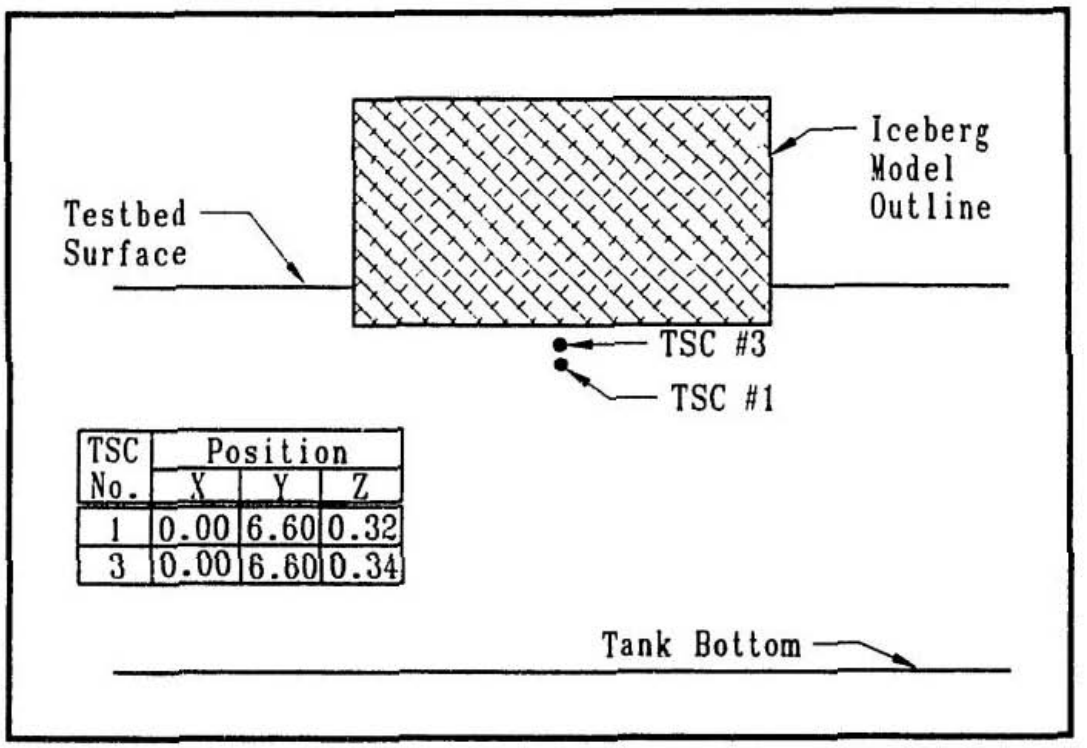

TSC No.	Position		
	X	Y	Z
1	0.00	6.60	0.32
3	0.00	6.60	0.34

Figure 5.8: Total Stress Cell Locations.

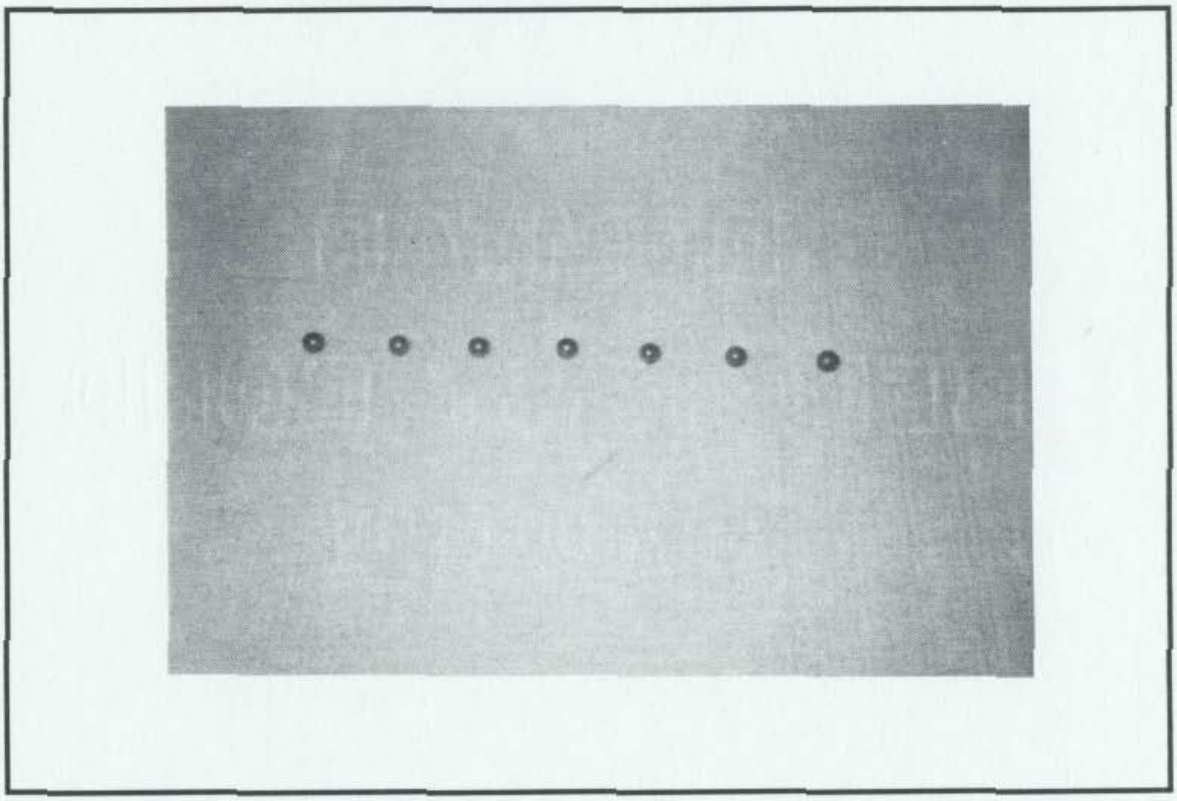

Figure 5.9: Surface Ball Bearings.

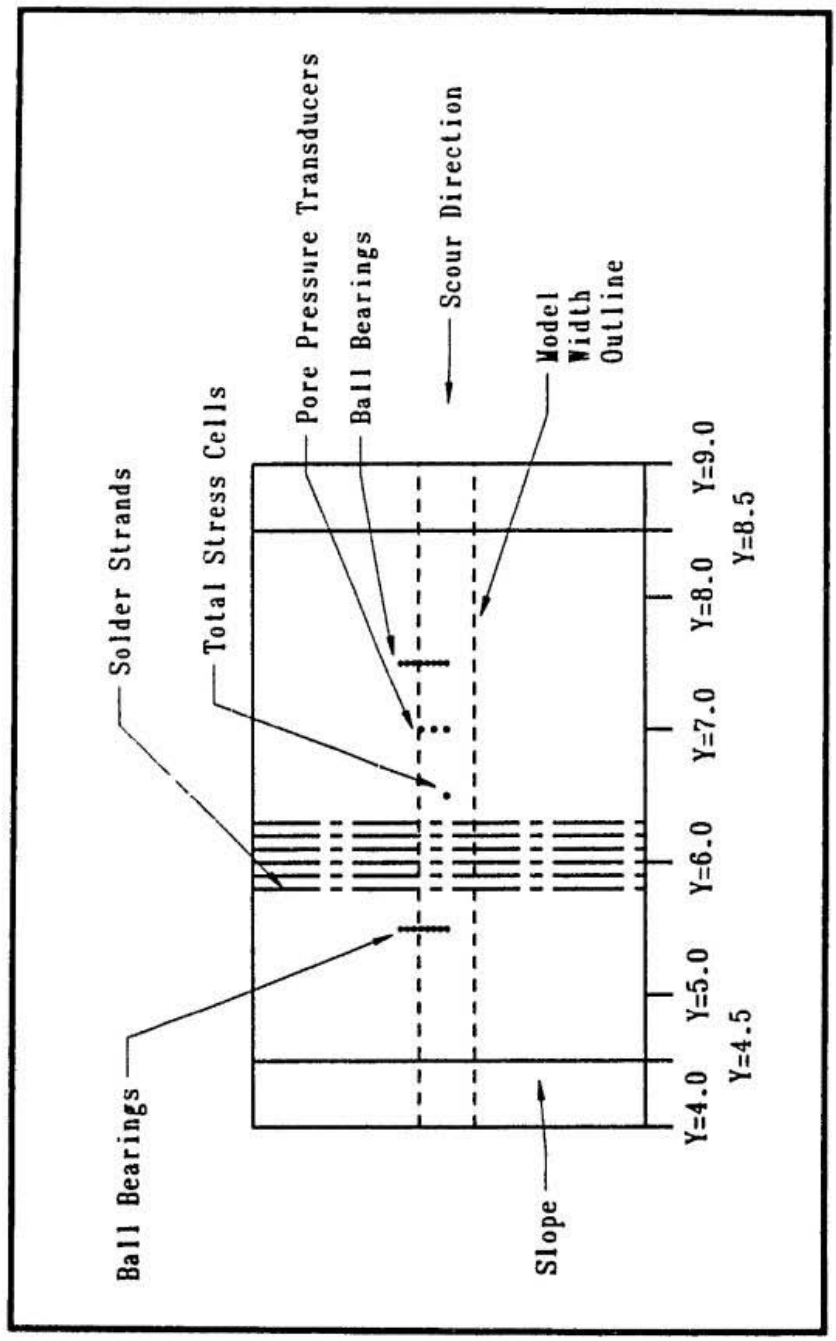

Figure 5.10: Testbed Instrumentation.

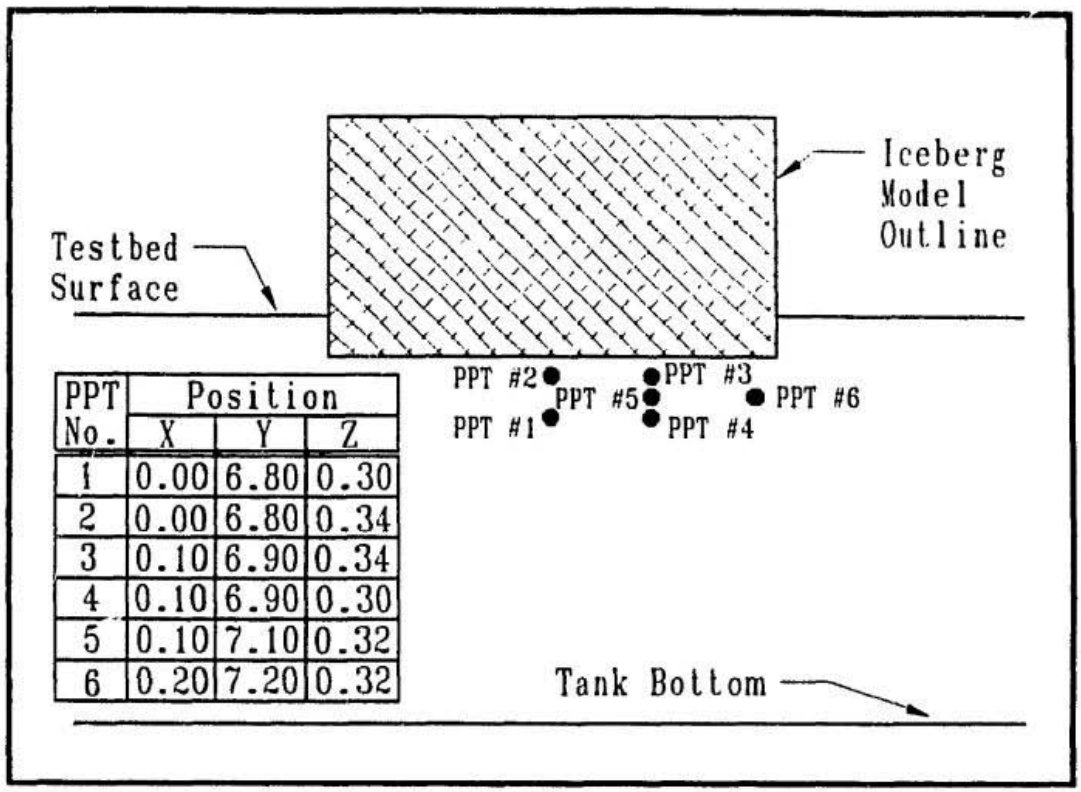

PPT No.	Position		
	X	Y	Z
1	0.00	6.80	0.30
2	0.00	6.80	0.34
3	0.10	6.90	0.34
4	0.10	6.90	0.30
5	0.10	7.10	0.32
6	0.20	7.20	0.32

Figure 5.11: Pore Pressure Transducer Locations.

the saturated porous stones of the transducers. Therefore, it was not possible to put all of the instrumentation into place and flood the tank. Density measurements were also taken during the preparation of the submerged testbeds and these values are shown in Table 5.1.

During preparation for the first submerged test, the testbed was prepared in a dry state up to the height where the first PPT was to be placed (Z=0.30 m). Planks were placed at the ends of the testbed to prevent washing away of the testbed due to water disturbance. The testbed was then flooded through the pipes on the bottom of the tank until approximately 2 cm of water covered the PPT location. The water used in these tests was tap water. The PPT's were saturated by boiling them in

water and were stored in water filled balloons. The PPT's were then put in position under water and these positions recorded using the pointer system. The PPT cables were run to the side of the tank and taped firmly to the side. The PPT's were then covered with subsequent rainings of sand. The water level would then be raised, more sand would be rained, and so on. When shaving was required, the water level was dropped just below the shaving height so the vacuum system was not sucking water. Vacuuming the partially saturated testbed proved to be difficult, requiring much time and effort. S_r (the degree of saturation) was calculated from density cup samples to be only 85 % for this test.

Experiments in the lab suggested that a S_r of 97 % might be attained if the sand was rained through approximately 10 cm of water. Therefore, this was the procedure which was followed during the preparation of the testbed for the final test. As the testbed was built up, layer by layer, the water level was also raised. The water level was lowered to just below the testbed surface during vacuuming. An attempt was made to place a layer of colored sand into the testbed during the final test but the sand could not be dyed to be colorfast and colored sand could not be found locally. Strands of pasta (spaghetti) were inserted vertically into the testbed at various locations both inside and outside the models path. Because the spaghetti would become soft in the water, it would deform easily and, when excavated, yield information on displacements.

A photo of a completed testbed just prior to flooding is shown in Figure 5.12. The tank was then flooded until the water level was approximately 10 cm above the prepared testbed surface. The testbed layout for the submerged tests is also shown in Figure 5.10.

Figure 5.12: Completed Testbed Prior to Flooding.

5.2 Iceberg Model Preparation

The gantry working platform was removed once the preparation of the testbed was completed. The pointer system did not have to be removed but was rather only moved to one side. The aluminum mounting frame was then put in position as was described in Chapter 4.

The beam load cells were then attached to the sway plate, the model lifted into position, and the beam load cells bolted to the model iceberg struts. The model on the mounting frame is shown in Figure 5.13. When in position, the horizontal face of the iceberg model was located at Z=0.36 m. This would give a scour cut depth of 4 cm for the tests. The face pressure cells were also in position by this stage. The only remaining instrumentation to install were the load cells to measure the horizontal force on the iceberg.

Connections were then made to terminal strips on a wooden platform attached to the aluminum mounting frame on which were also located the HLC amplifiers. The power supply/amplifier for each FPC was placed inside the waterproofed iceberg model. All instrumentation was then hooked in to the data acquisition system. The pointer tip was lined up with the inflection line on the model face as this was the reference point for the model's travel.

5.3 Data Acquisition System

The instrumentation was connected to the data acquisition system as shown in Figure 5.14. Prior to running a test, the instrumentation and data acquisition system were turned on and allowed to warm up for at least one hour. Output values from instrumentation were checked by running the data acquisition program and

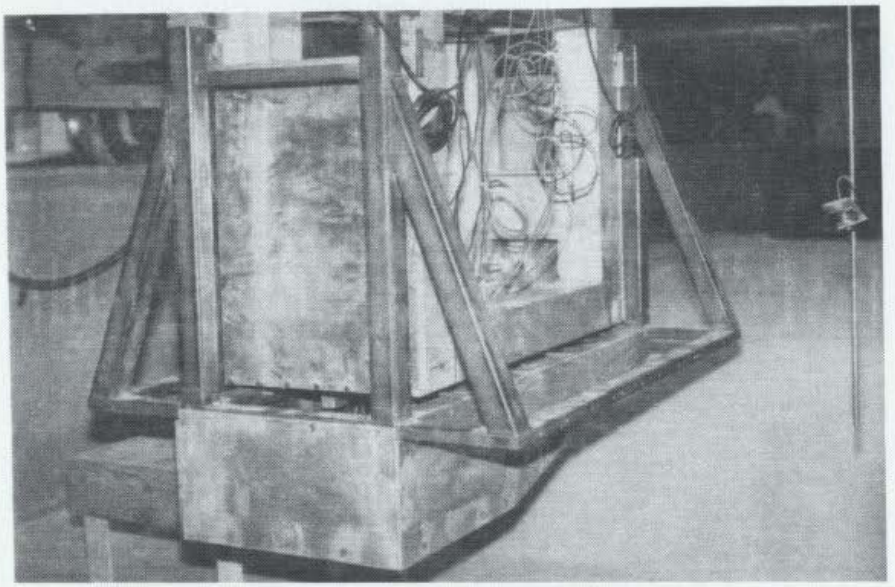

Figure 5.13: Iceberg Model in Position.

comparing acquired values to those obtained with a voltmeter. Some channels of the data acquisition system were expressly used for monitoring the input voltages to instrumentation. Instrumentation that could be checked by loading or movement was checked to ensure that it was working properly. The experiment did not commence until it was confirmed that everything was working properly.

5.4 Ice Scour Testing

Immediately prior to the commencement of a test, the HLC's were zeroed and the water level during the submerged tests measured and recorded. The water level was measured at Z=49.1 cm during Test 3 and at Z=49.6 cm during Test 4.

Once the photographers and video camera were ready to go, the data acquisition program was started and approximately 5 s later, the test began, the gantry being controlled by an operator sitting on the large beams. Data acquisition ceased approximately 10 s after the test completion. Each test required only 100 to 120 s for completion. The travel of the model for a typical test (Test 1) is shown in Figure 5.15 and from this it can be seen that the model speed was relatively constant throughout the test. The tests were all recorded on video camera and photographed from two different angles although it was hard to make out what was going on in front and around the model during the submerged tests.

Everything was shut down and the acquired data checked after the completion of a test. The instrumentation was then disconnected from the data acquisition system and the pointer system re-established. Model instrumentation was disconnected, removed where applicable, and the model with mounting frame removed from the gantry. The gantry working platform was then put back into place. If the test was a submerged one, drainage was allowed to take place overnight, otherwise post-scour

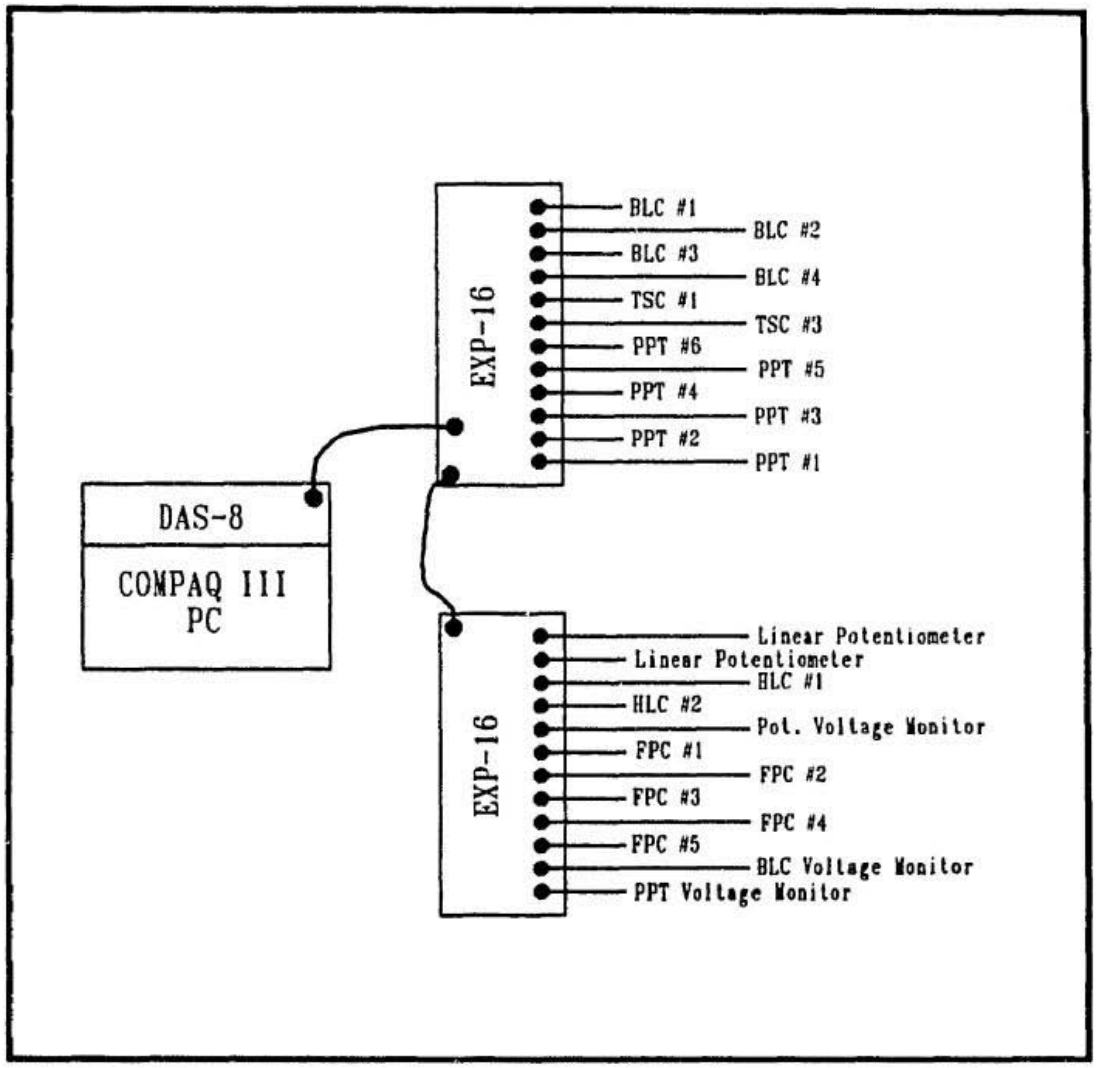

Figure 5.14: Data Acquisition System.

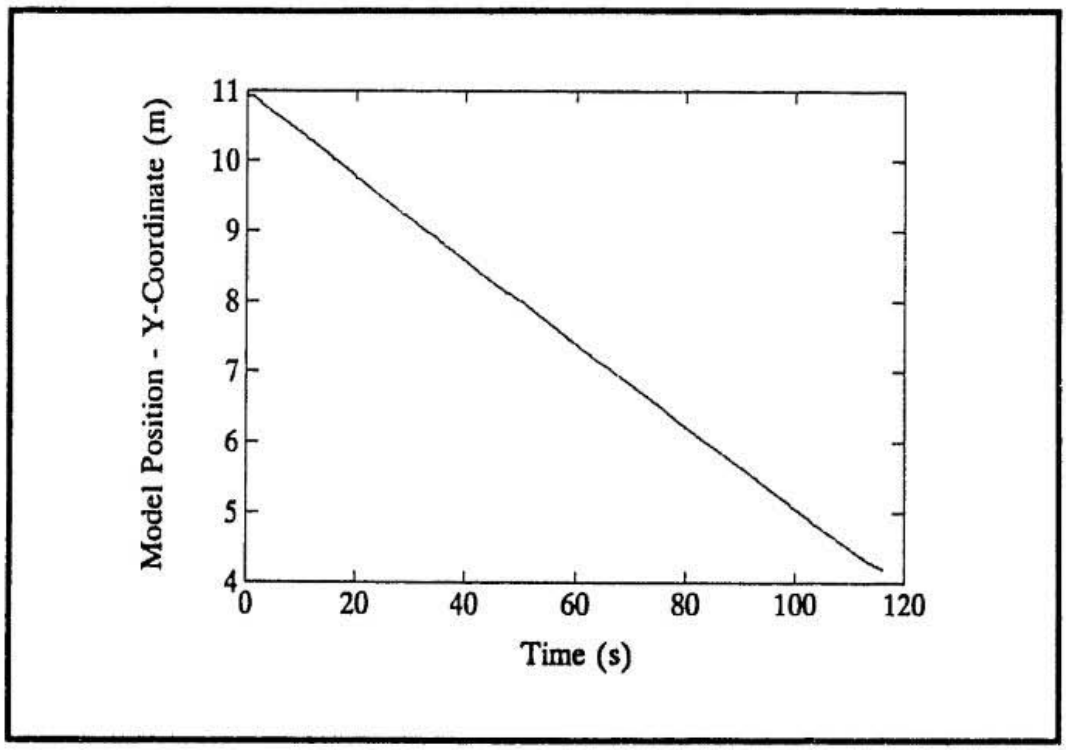

Figure 5.15: Model Position vs. Time, Test 1.

measurements commenced immediately.

5.5 Post-Scour Measurements

The first measurements which were taken before the testbed was disturbed were post-scour profiles of the resulting scour. These were obtained every 0.5 m along the scour, using the pointer system, and were achieved by setting the pointer on the desired Y-coordinate and moving the pointer in the X-Z plane, taking measurements when the pointer just touched the testbed.

The post-scour locations of the ball bearings were found using the metal detector. Once the approximate location was found, the area was carefully excavated using the vacuum system until the apex of the ball was uncovered, care being taken not to disturb the position of the ball. The pointer could then be positioned over the apex and the post-scour position recorded. The ball was then picked up using a magnet and the I.D. number recorded.

The solder strands were located by starting at one end of the strand and excavating along the strand's length. The post-scour location of the strand was measured in the same manner as the pre-scour locations with the pointer system. Generally, more data points were needed to define the curvature of the solder strands after scouring. During excavation, the post-scour locations of the PPT's and TSC's were also determined and recorded.

An attempt was made in Tests 1 and 2, to measure the density changes across the scour profile using the nuclear densitometer. The densitometer was placed outside the scour, inside the scour, and on the scour berms. These tests were done before the commencement of excavating, care being taken not to disturb the testbed. The hand-held penetrometer was used after Tests 3 and 4 to measure penetration resistance

across the scour profile. These penetrations were conducted in intact sections of the excavated testbed and the position of each penetration recorded with the pointer system.

Chapter 6

Experimental Results

6.1 General

There was a build-up of a mound of spoil in front of the model as the test proceeded. This is shown in the photograph of Figure 6.1 where the model is approaching the end of the testbed. This build-up took place during both the dry and submerged tests but it could not be noticed in the photographs of the submerged tests due to the reflection of the lighting off of the water. This spoil continued to build until it appeared to reach a maximum height of $\approx$15 cm above the testbed surface at approximately Y=6.5 m. This spoil would then spill to the sides of the scour creating part of the berm shown in Figure 6.2. It was also noticed that there was some infilling of sand behind the model as the scour progressed.

In front of the spoil, successive blocks of soil were seen to surface between rupture planes during scouring. These failures were noticed up to 50 cm in front of the model and are shown in Figure 6.3. These failures appeared to be not unlike those expected during a passive earth pressure failure. A similar process was observed to the sides of the model but these failure surfaces were, for the most part, covered by the frontal spoil material spilling to the sides. A ruptured surface to the side of the scour which

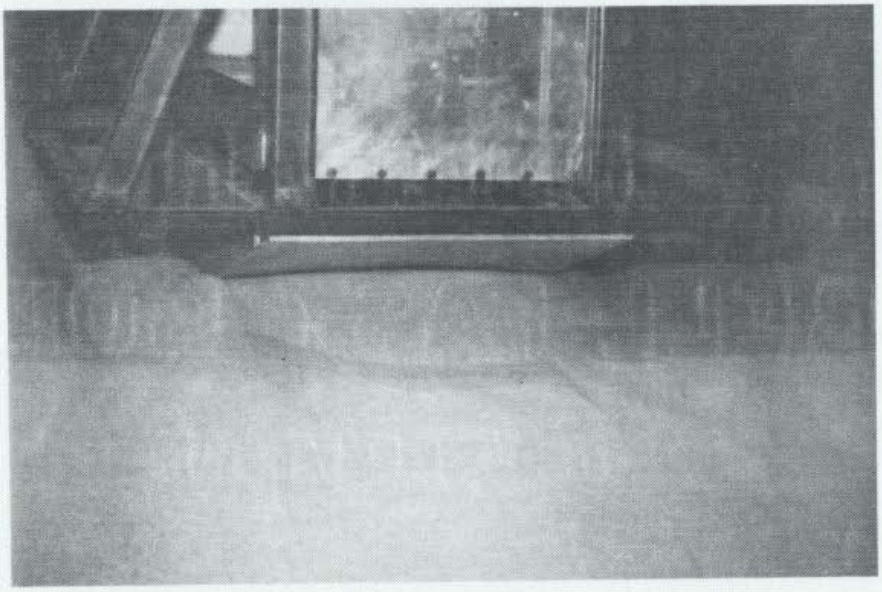

Figure 6.1: Build-up of Frontal Spoil.

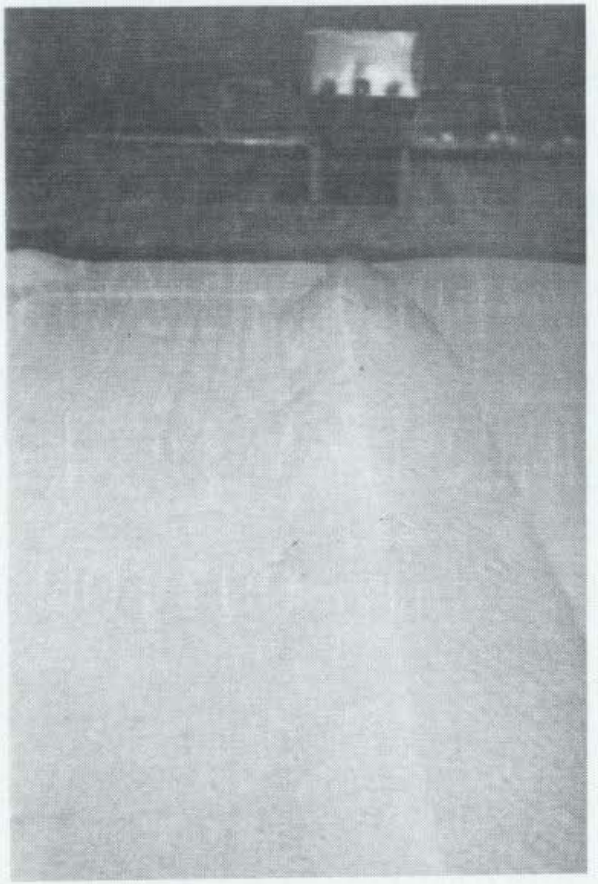

Figure 6.2: Scour Berm.

was not covered by the berm material is shown in Figure 6.4.

The metal ball bearings were also observed to move with the soil before actual contact with the model (see Figure 6.5). As the model approached, they were churned with the frontal spoil, except for the outermost bearings which appeared to move on the intact failure surface which they sat.

The post-scour testbed is shown in Figure 6.6. In this photo, the model has moved away from the camera towards the front of the tank. The berms and trough created by the scour can be clearly seen, the berm height increasing to a steady-state along the scour path.

6.2 Post-Scour Profiles

Post-scour profiles were measured with the pointer system as described in Chapter 5. These profiles were then plotted as shown in Figure 6.7, which shows a measured scour profile from both a dry and a submerged test. Superimposed on these profiles are the model dimensions. It appears that there has been a greater amount of infill behind the model during the submerged tests as both of the profiles were measured at the same position along the scour track. The scour profiles from all four tests are presented in Appendices C through F. Measurements were made of these scour profiles as shown in Figure 6.8 and these measurements are presented in Appendix B.

6.3 Vertical Forces on the Iceberg Model

Vertical forces on the iceberg model were measured using the four beam load cells. These were numbered BLC #1 through #4 as was shown in Figure 4.6. A typical result from one of these beam load cells is shown in Figure 6.9. It can be seen from the plot that there is an increase in load to a relative steady-state which is maintained

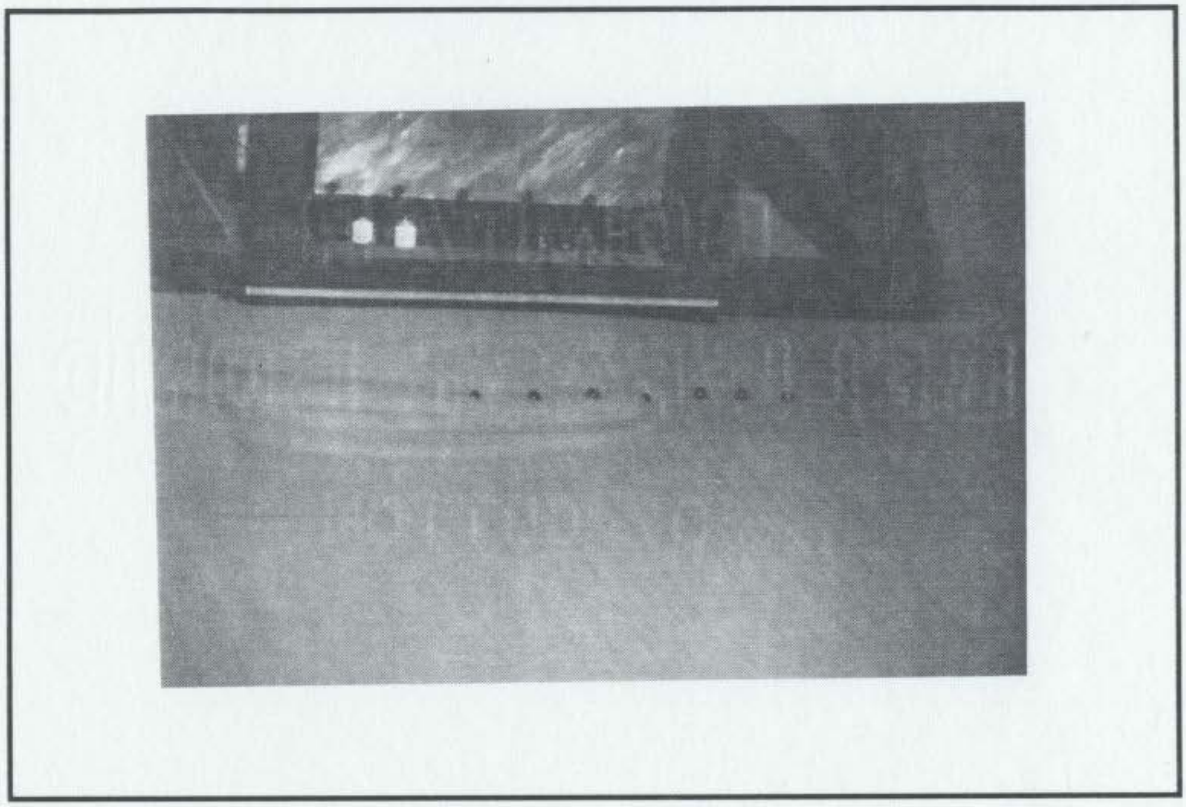

Figure 6.3: Front Failure Surface During Scour.

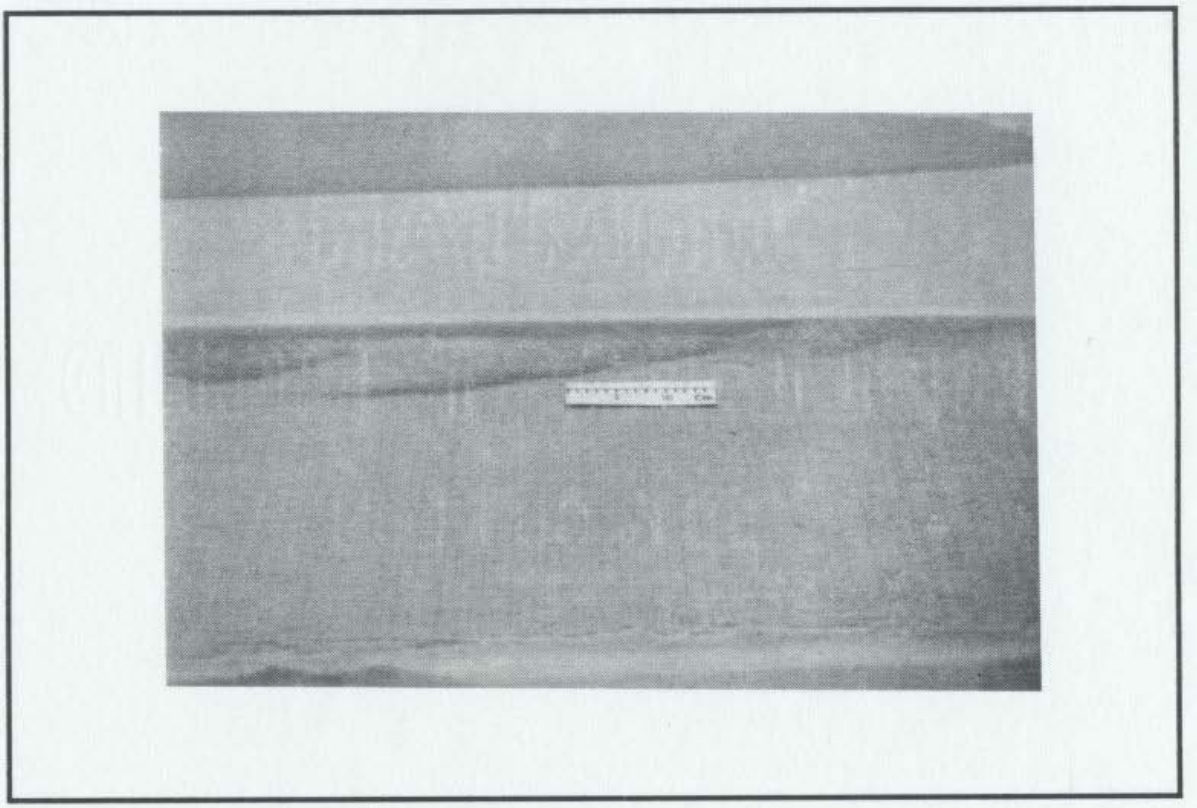

Figure 6.4: Side Failure Surface.

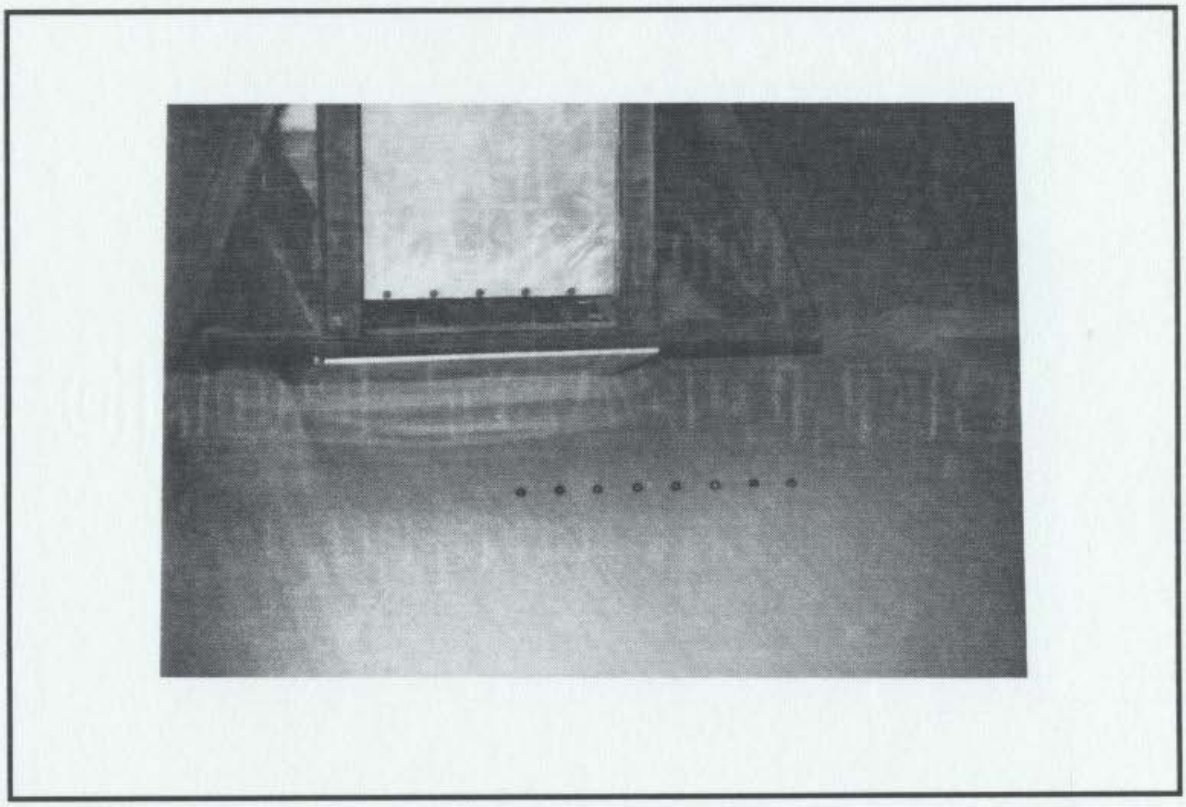

Figure 6.5: Model Approaching Ball Bearings.

Figure 6.6: Post-Scour Testbed.

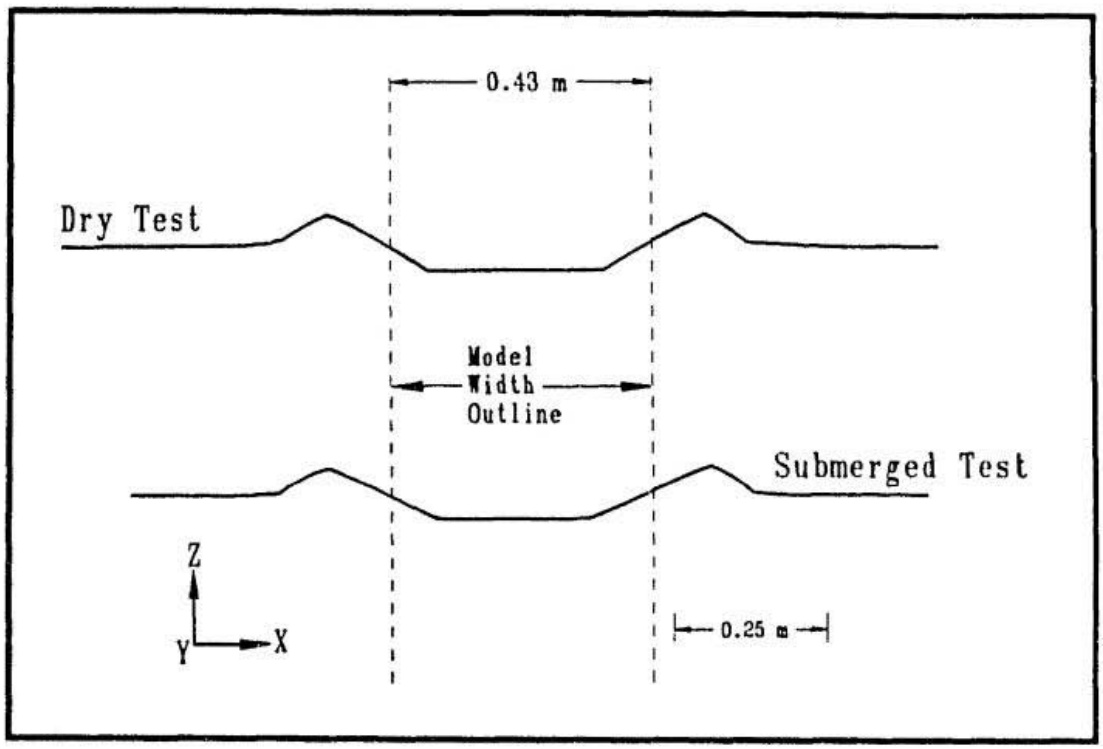

Figure 6.7: Measured Scour Profiles, Dry and Submerged Tests, Y=6.5 m.

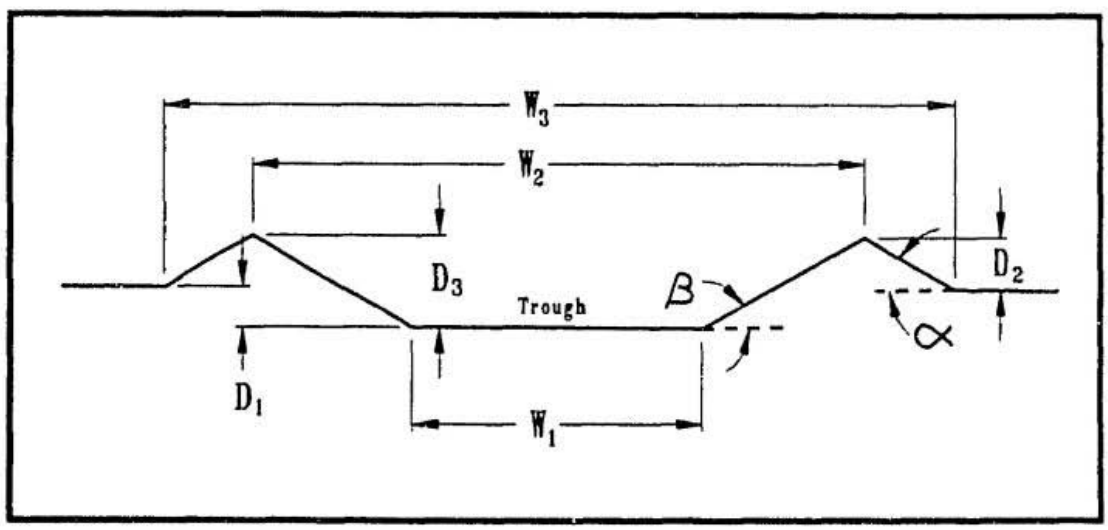

Figure 6.8: Scour Profile Measurements.

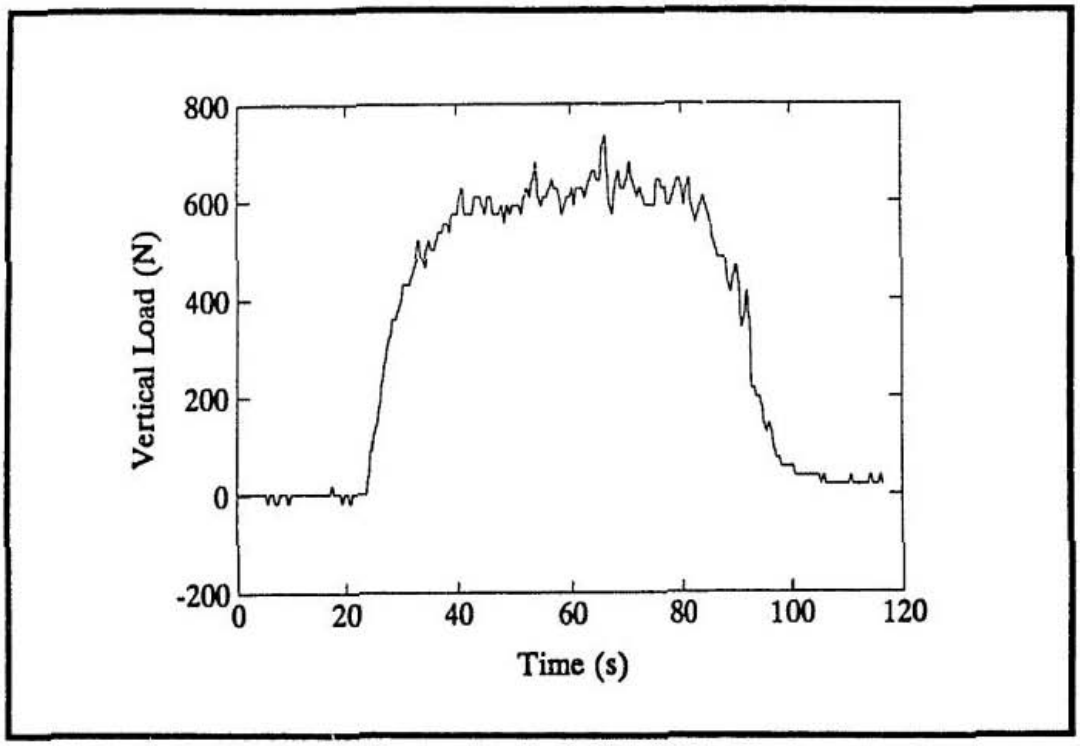

Figure 6.9: Beam Load Cell #2 Response vs. Time, Test 2.

until the model reaches the end of the testbed. At this time, there is a drop off of load to the original value because the model is no longer in contact with the testbed. This plot has been zeroed to show the net increase in load on the model, assuming zero load when the model is hanging freely and not contacting the testbed.

Plots from all tests showing the variation of vertical load with model position are presented in Appendices C through F. The peak values for these tests are summarized in Table 6.1 where the front strut vertical load (FSVL) is the sum of BLC #1 and BLC #4, the rear strut vertical load (RSVL) is the sum of BLC #2 and BLC #3, and the total vertical load (TVL) is the sum of all four beam load cells. These plots are also presented in the appendices. The beam load cell results in Appendix C, for

Test 1, have been adjusted because these values were measured with a gain of 1 on the data acquisition system but the calibration constants were derived using a gain of 100.

Table 6.1: Beam Load Cell Results.

Test	Maximum Load (kN)						
#	BLC #1	BLC #2	BLC #3	BLC #4	FSVL	RSVL	TVL
1	0.3277	0.7143	0.3566	0.3563	0.6840	1.0709	1.7549
2	0.2213	0.7341	0.3883	0.2853	0.5066	1.1224	1.6290
3	0.1425	0.4107	0.2556	0.1603	0.3028	0.6663	0.9691
4	0.1603	0.3452	0.1605	0.1603	0.3206	0.5057	0.8263

6.4 Horizontal Forces on the Iceberg Model

Horizontal forces on the model were measured using the two horizontal load cells, HLC #1 and HLC #2, described in Chapter 4, and positioned as was shown in Figure 4.7. The response from HLC #2, Test 1, is presented in Figure 6.10 as a typical response from one of these load cells. As with the BLC's, there is a build-up to a relative steady-state value followed by a drop off at the end of the test.

Appendix C through F contains plots from the HLC's for all four of the tests. Peak values and total horizontal load (THL) are summarized in Table 6.2. These plots have also been zeroed for convenience. A problem was observed with the response of HLC #1, Test 3, as can be seen in Appendix E. It is thought that the load cell slipped out of position during the test and also began to drift. In order to arrive at an estimate for the total horizontal load on the model, the response was assumed to be the same as for HLC #2. Comparing the total load from this test with the actual total horizontal load in Test 4 suggests that this was a reasonable assumption.

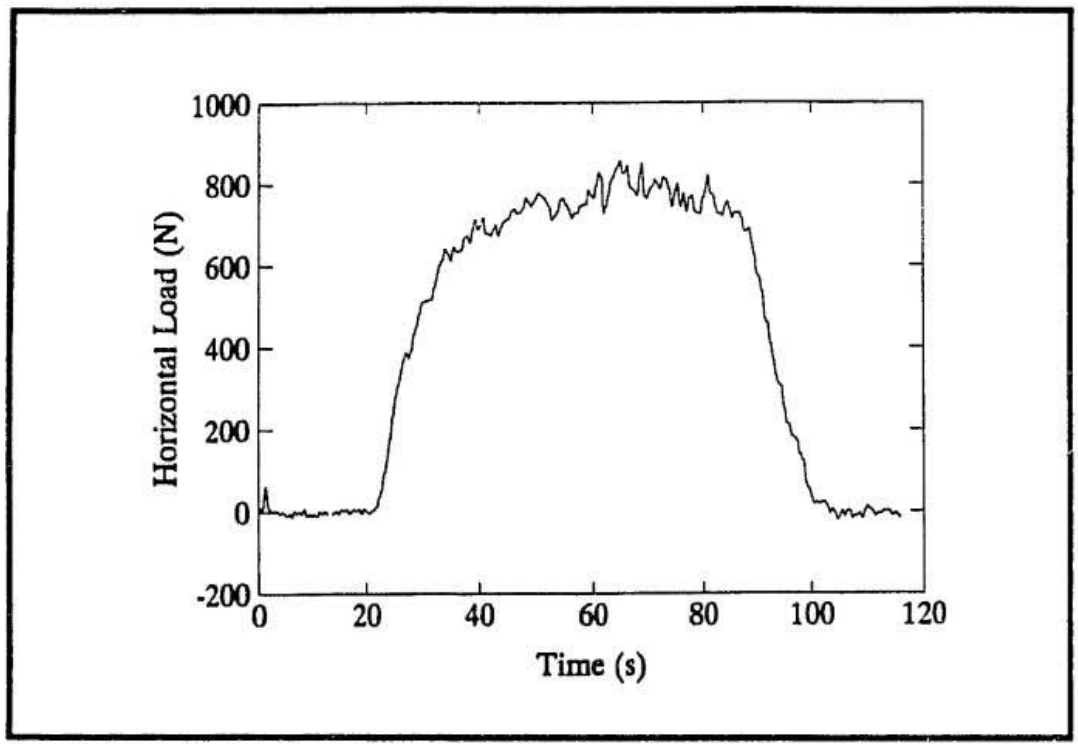

Figure 6.10: Horizontal Load Cell #2 Response vs. Time, Test 1.

Table 6.2: Horizontal Load Cell Results.

Test #	Maximum Load (kN)		
	HLC #1	HLC #2	THL
1	0.5032	0.8548	1.3580
2	1.0228	0.1007	1.1235
3	0.3840	0.3840	0.7680
4	0.4223	0.3770	0.7993

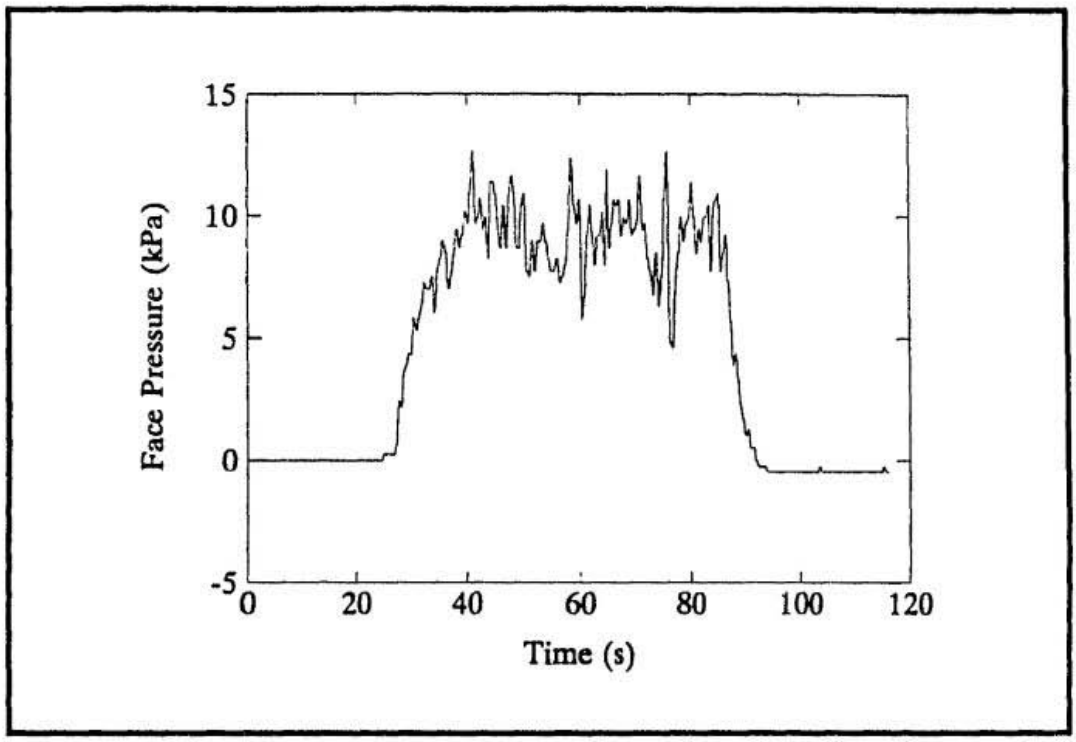

Figure 6.11: Face Pressure Cell #4 Response vs. Time, Test 2.

6.5 Face Pressure Cell Results

The typical response from a face pressure cell is given in Figure 6.11. This plot shows a build-up in pressure to a steady-state value followed by a drop off at the end of the test.

The response from the FPC's for all of the tests are given in Appendices C through F. These plots have been zeroed to reflect face pressures exerted by the testbed on the model and not from hydrostatic pressure during the submerged tests. Peak values of response from all tests are given in Table 6.3. It should be noted that some discrepancy might exist between actual values and measured values because the FPC's were calibrated using pressurized gas which might yield different values

from direct soil loading. Also, the effects of shear on the face of the FPC's were not considered.

Table 6.3: Face Pressure Cell Results.

Test #	Maximum Pressure (kPa)				
	FPC #1	FPC #2	FPC #3	FPC #4	FPC #5
1	2.374	2.407	26.701	13.894	22.285
2	2.971	1.823	19.443	12.584	22.311
3	1.074	—	15.855	8.450	17.620
4	0.987	—	11.023	7.502	9.840

6.6 Pore Pressure Transducer Response

Figure 6.12 shows a plot of the typical response from one of the pore pressure transducers used during the submerged tests. The same pattern could be picked out from the responses of all the pore pressure transducers. As the model approached the PPT, there was a slight increase in pore pressure, followed by an even larger decrease. This was typically followed by a large increase before a return to steady-state. These values were termed *initial peak* (IP), *initial trough* (IT), *secondary peak* (SP), and *steady-state* (SS) respectively. Table 6.4 summarizes these values from Test 3 and Test 4.

The pore pressure response recorded during these two tests are presented in Appendices E and F. These plots have been zeroed to reflect pore pressure response above hydrostatic.

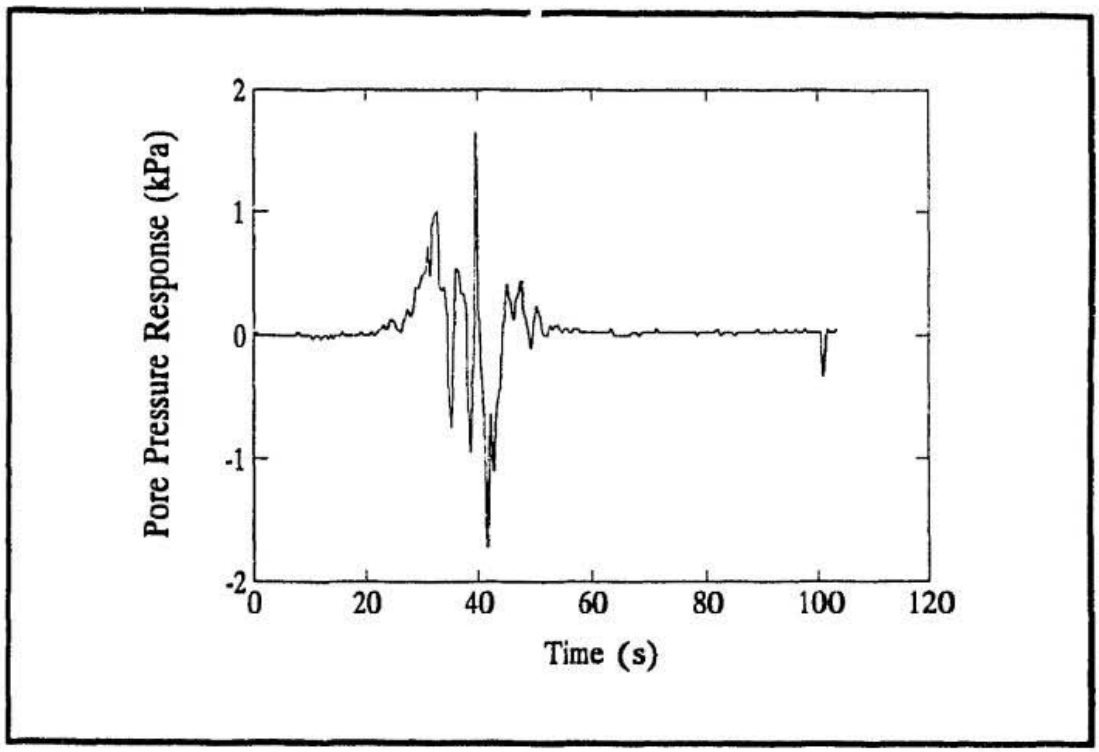

Figure 6.12: Pore Pressure Transducer #6 Response vs. Time, Test 3.

Table 6.4: Pore Pressure Transducer Results.

Test #	Pore Pressure Transducer Number	Initial Peak (kPa)	Initial Trough (kPa)	Secondary Peak (kPa)	Steady-State (kPa)
3	1	0.112	-0.143	0.261	0.040
	2	0.062	-0.395	0.168	-0.120
	3	0.085	-0.347	0.229	-0.080
	4	0.136	-0.090	0.276	0.045
	5	0.396	0.000	0.542	-0.050
	6	1.000	-0.957	1.642	0.050
4	1	0.150	-0.053	0.376	0.035
	2	0.145	-0.276	0.286	-0.180
	3	0.095	-0.143	0.384	0.050
	4	0.143	-0.082	0.391	0.030
	5	0.141	-0.007	0.338	0.042
	6	0.077	-0.078	0.281	0.025

6.7 Total Stress Cell Response

There was no total stress cell data obtained during Test 1 due to equipment problems. The response from one of the cells used in Test 2 is shown in Figure 6.13. The typical response from these cells is a peak in load followed by a dip and then a return to steady-state. These values have been termed such and are presented in Table 6.5.

Appendix D through F contains the TSC data obtained during the testing program. These plots have been zeroed to reflect the increase in total stress.

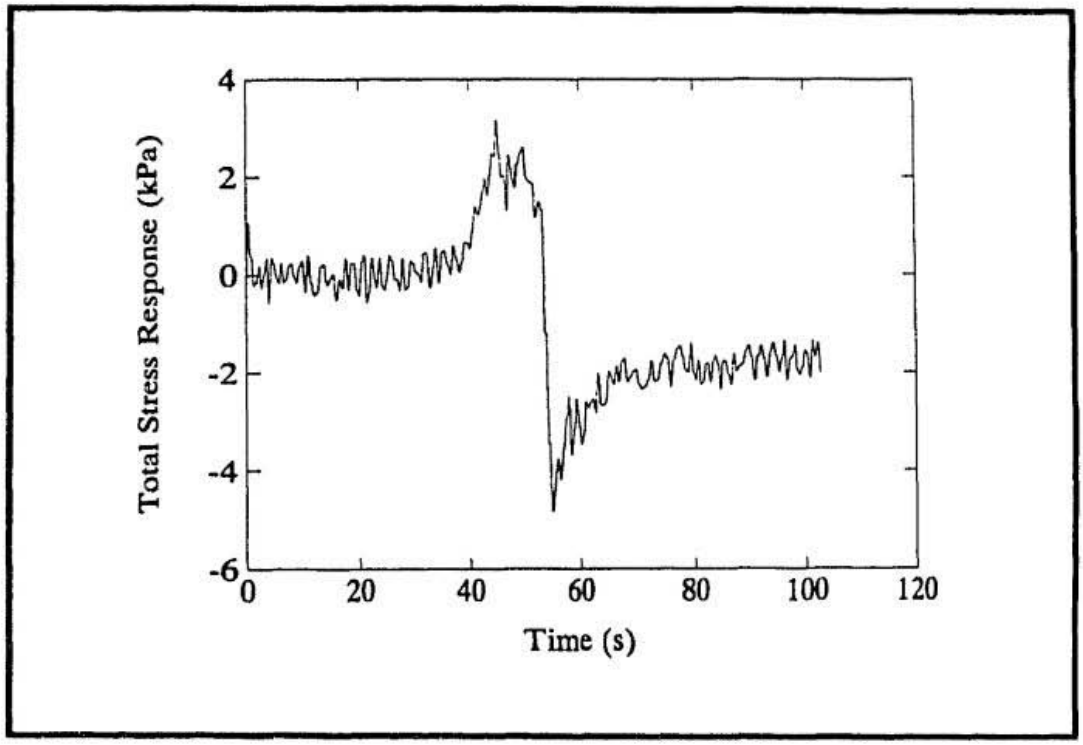

Figure 6.13: Total Stress Cell #1 Response vs. Time, Test 3.

Table 6.5: Total Stress Cell Results.

Test #	Maximum Pressure (kPa)					
	TSC #1			TSC #3		
	Peak	Dip	Steady-State	Peak	Dip	Steady-State
1	—	—	—	—	—	—
2	20.137	0.784	1.471	15.078	-11.388	-3.195
3	3.156	-4.816	-1.676	5.865	-9.843	2.100
4	4.515	-1.882	-0.682	3.325	-28.102	-3.846

6.8 Ball Bearing Displacements

Figure 6.14 shows the post-scour positions of some surface and near-surface ball bearings after excavation. The ball bearing displacements were calculated and these are presented in the form of vectors in Appendices C through F. A typical plot showing the movements of some of the displaced ball bearings is presented in Figure 6.15. In the appendices, displacement vectors are shown for both the X-Y and the X-Z planes. The tail of the vector represents the position where the apex of the ball bearing started and the head is where the ball bearing ended up. The dashed line outlines the model's path.

6.9 Solder Strand Displacements

A photograph of one of the uncovered solder strands is shown in Figure 6.16. Figure 6.17 shows the measured undeformed (pre-scour) and deformed (post-scour) position of this solder strand displacement marker as measured by the pointer system. The broken line represents the pre-scour position and the solid line represents the post-scour position. All of the solder strand displacements are presented in Appendices C through F. Measurements were made of the horizontal and vertical movement of the solder strands along the scour centerline as shown in the figure and these are presented in Table 6.6. During excavation of the testbeds from the submerged tests, the spaghetti strands could not be uncovered but were rather removed with the sand into the vacuum system.

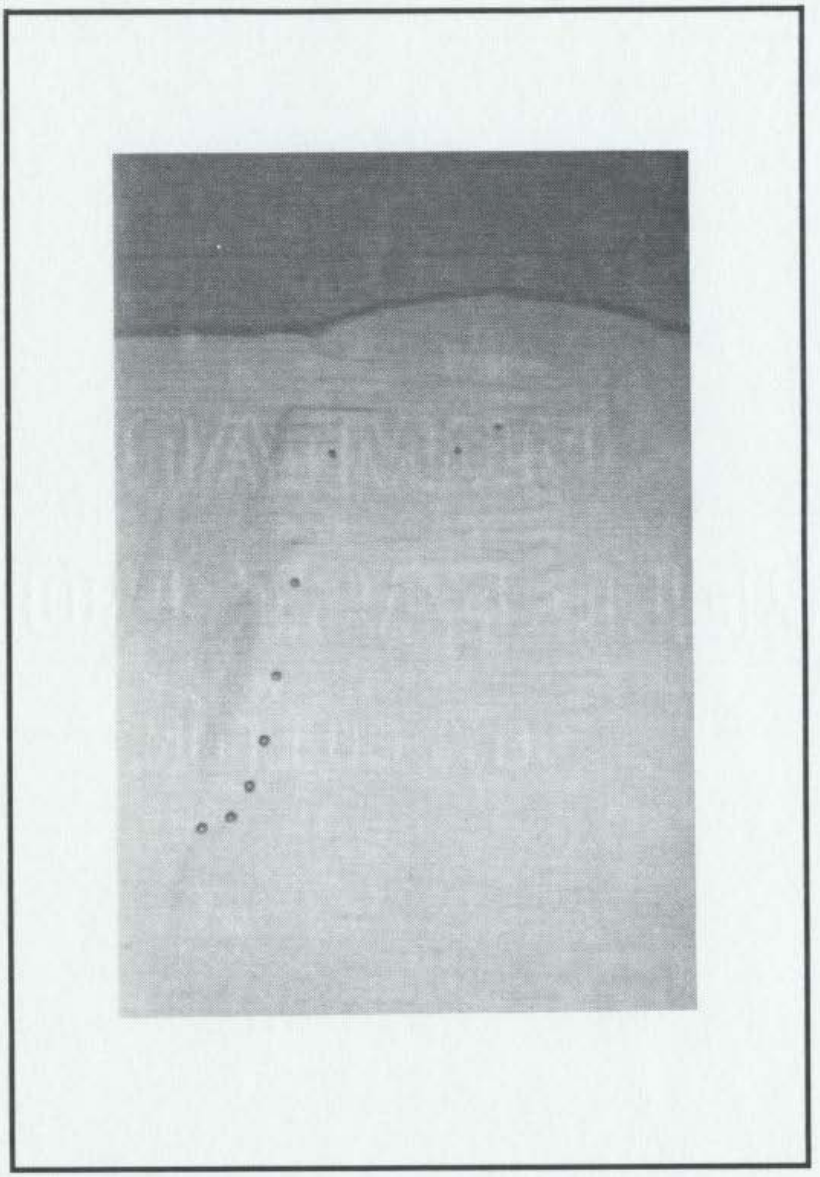

Figure 6.14: Displaced Ball Bearings.

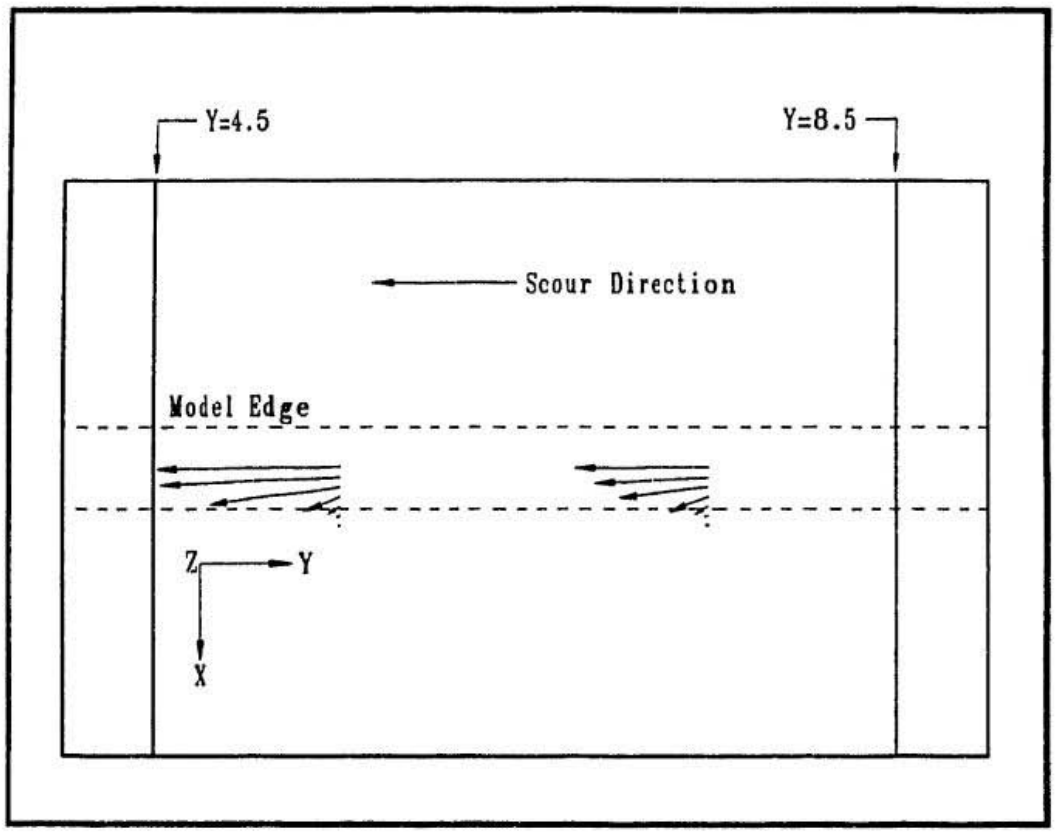

Figure 6.15: Ball Bearing Displacements, Test 1, Z=0.36 m Plane.

Table 6.6: Solder Strand Displacements.

Solder Strand (Z)	Test 1		Test 2		Test 3		Test 4	
	ΔY (m)	ΔZ (m)	ΔY (m)	ΔZ (m)	ΔY (m)	ΔZ (m)	ΔY (m)	ΔZ (m)
0.36	0.502	0.0095	0.474	0.0106	0.583	0.0020	0.369	0.0018
0.34	0.166	0.0007	0.121	0.0105	0.189	0.0001	0.121	0.0178
0.32	0.070	0.0100	0.051	0.0074	0.053	0.0075	0.014	0.0074
0.30	0.034	0.0089	0.043	0.0064	0.043	0.0020	0.010	0.0060
0.28	0.022	0.0078	0.025	0.0051	0.013	0.0053	0.008	0.0041
0.26	0.026	0.0061	0.009	0.0055	0.008	0.0043	0.006	0.0036
0.24	—	—	—	—	—	—	0.001	0.0028

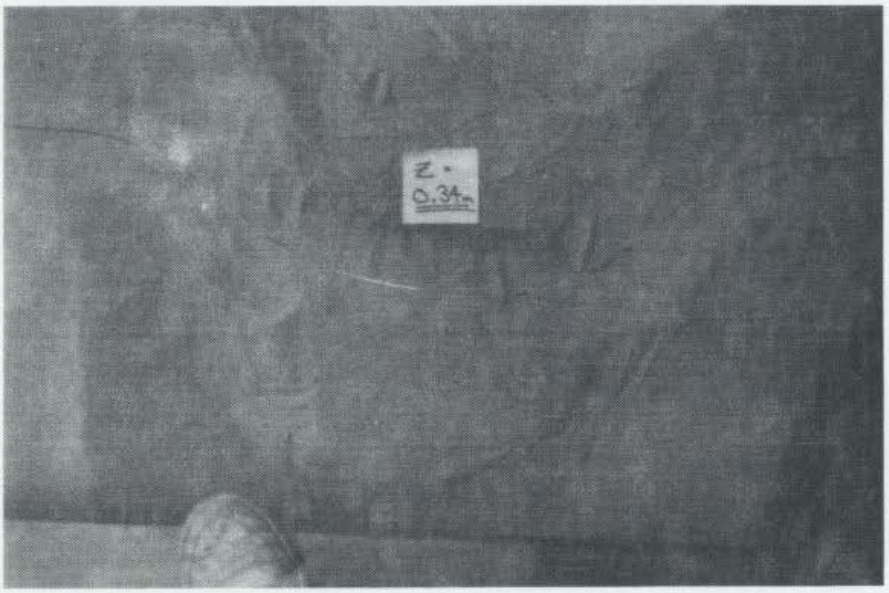

Figure 6.16: Displaced Solder Strand, Test 1, Z=0.34 m Plane.

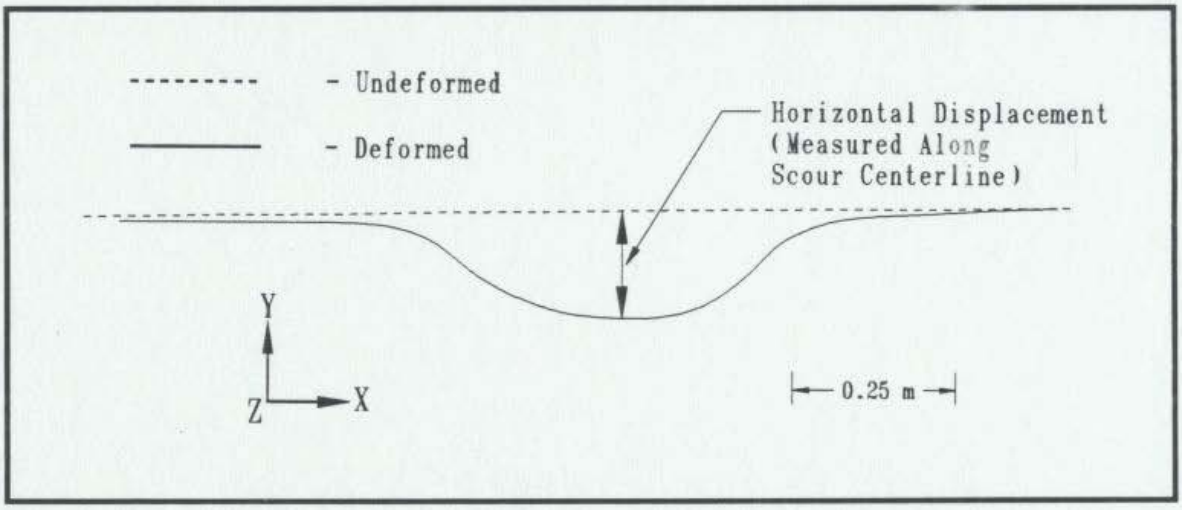

Figure 6.17: Displaced Solder Strand, Test 1, Z=0.34 m Plane.

6.10 Density Changes Across the Scour Profile

The nuclear densitometer used in Tests 1 and 2 could measure no differences in the density of the testbed across the scour profile. This was believed to be due to the measuring resolution of the device which was ± 32 kg/m^3. Penetrometer resistances across the scour profile and in various areas of the testbed are presented in Appendix B. No attempt has been made to try and quantify these penetration resistance values, rather they have been taken in a qualitative sense. Contoured plots of the results of these penetrations (with what points were available) are given in Figure 6.18 and Figure 6.19. The scour direction and model width outline are indicated on the figures.

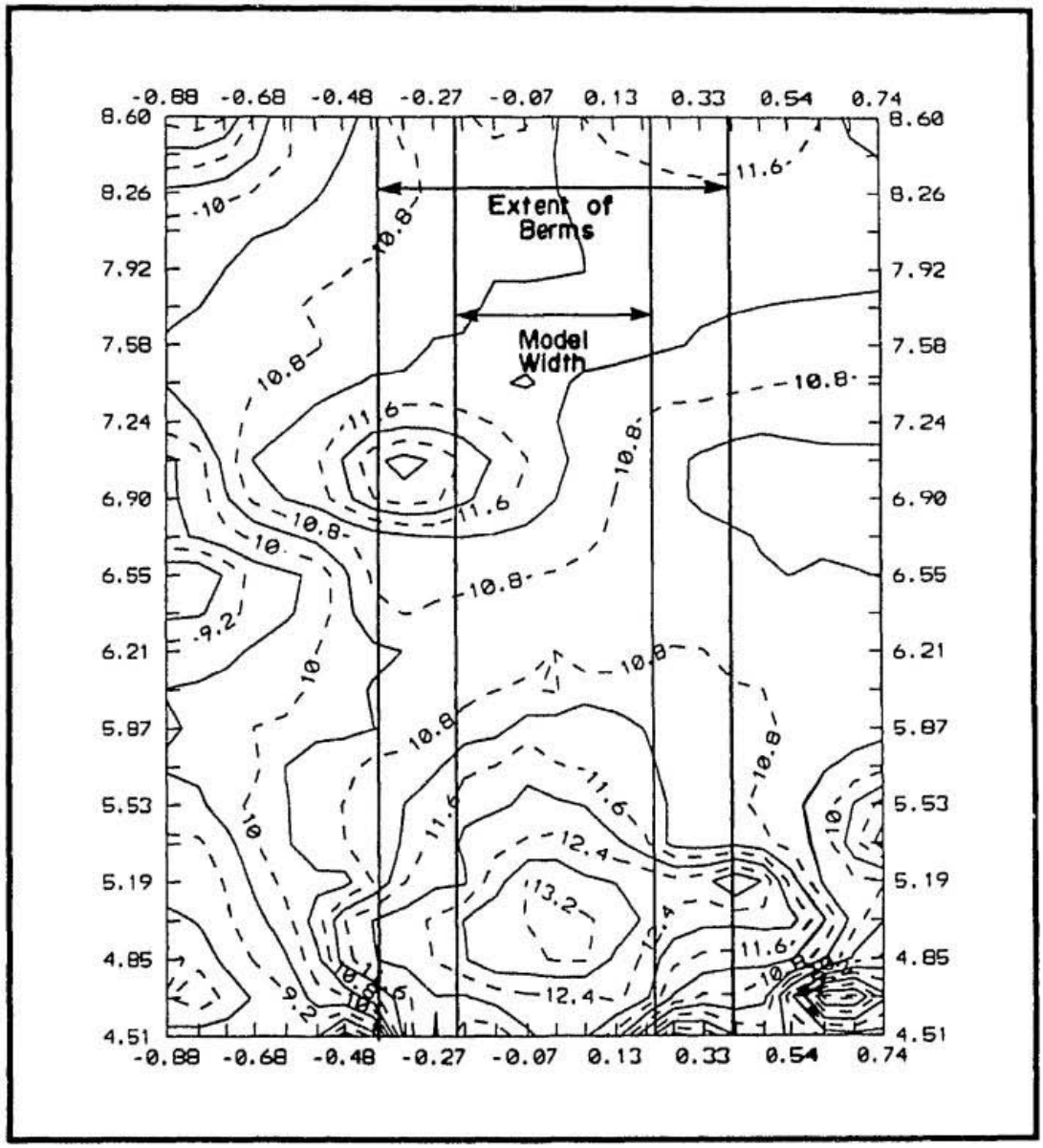

Figure 6.18: Penetration Resistance of the Testbed, Test 3.

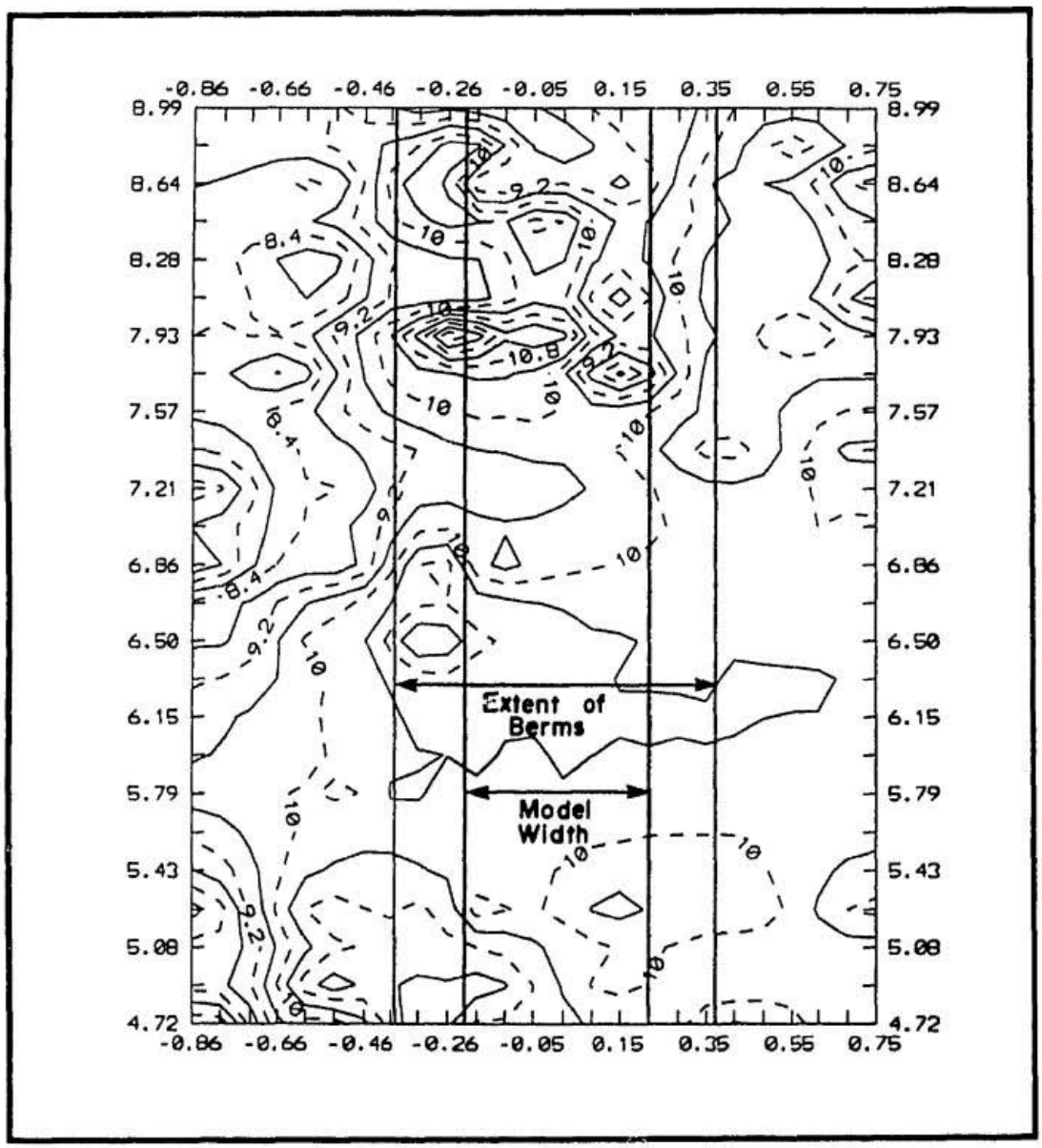

Figure 6.19: Penetration Resistance of the Testbed, Test 4.

Chapter 7

Analysis and Discussion of Results

7.1 Post-Scour Profiles

The average values for the post-scour profile measurements, as were described in Section 6.2, are presented in Table 7.1. The individual values measured for each test are presented in Appendix B. These average values were taken between the Y=5.0 m and the Y=8.0 m coordinate, omitting the values obtained from the start and finish of each scour where the testbed may have differed from test to test. The lower D_3 (see Figure 6.8) value for the submerged tests indicates lower berms for these tests. This, coupled with the lower W_1 values for the submerged tests, verifies that there was a greater amount of infilling behind the model as the scour took place. The corresponding values of α and β are also indicative of this fact. Similar values of W_3 for both the dry and submerged tests suggest that the disturbed portion of the testbed, or the portion of the testbed which has been influenced by scouring, was not dependant on whether or not the testbed was submerged.

The cross-sectional area of the berms (above the original testbed surface) should be equal to the cross-sectional area of the trough (below the original testbed surface) if neither densification nor dilation of the sand has taken place during scouring. The

Table 7.1: Post-Scour Measurements, Average Values (Y=5.0-8.0 m).

Test #	D_1 (m)	D_2 (m)	D_3 (m)	W_1 (m)	W_2 (m)	W_3 (m)	α (Deg.)	β (Deg.)
1	0.041	0.050	0.091	0.288	0.606	0.746	34.4	28.9
2	0.039	0.051	0.090	0.289	0.608	0.775	30.8	28.6
3	0.038	0.047	0.086	0.239	0.620	0.776	29.6	24.0
4	0.040	0.044	0.084	0.242	0.618	0.775	27.1	25.3

measured berm areas also included the cross-sectional areas of any rupture surfaces which extended out from the outer edge of the berms. The areas measured from the post-scour profiles at the Y=6.0 m coordinate for each test are shown in Figure 7.1. The measured values are presented in Table 7.2 where

$$A_B = A_{RB} + A_{LB} \tag{7.1}$$

and

$$Area\ Ratio = A_B/A_T. \tag{7.2}$$

The A_B and A_T values for the submerged tests are smaller than those values for the dry tests, again suggesting that there has been a greater amount of infilling behind the model. The greater amount of infilling, and therefore the smaller berms and smaller trough widths are to be expected because of the lower angle of repose for the submerged sand. The value of the Area Ratio for all tests is less than unity suggesting that some densification of the loose sand has taken place. Densification in turn suggests that some strain hardening of the soil has occurred during shearing.

Table 7.2: Post-Scour Profiles, Cross-Sectional Areas (Y=6.0 m).

Test #	A_{RB} (m^2)	A_{LB} (m^2)	A_B (m^2)	A_T (m^2)	Area Ratio
1	0.005558	0.005123	0.010681	0.014411	0.741
2	0.005993	0.005393	0.011386	0.013388	0.850
3	0.004835	0.005075	0.009910	0.012297	0.850
4	0.004803	0.004785	0.009588	0.009588	0.744

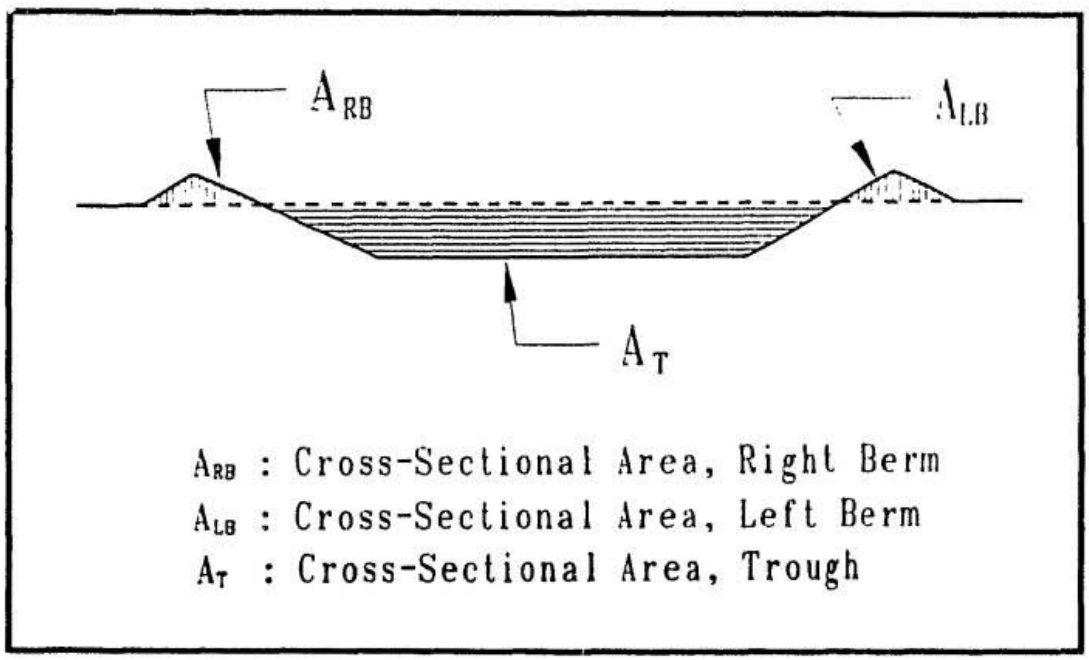

Figure 7.1: Scour Profile, Cross Sectional Area Measurements.

7.2 Forces and Pressures on the Iceberg Model

7.2.1 Pressures on the Model Faces

Green (1984) suggested that there might be no variation in face pressure across the width of the model. By comparing the results from FPC #3 (4 cm off the centerline of the model) to those obtained from FPC #5 (15 cm off the centerline), it can be seen that the pressures from FPC #5 vary as much as ±15 % from those values obtained from FPC #3. Therefore, some variation does exist across the face of the model and this should be taken into account during analysis.

The greatest pressures on the model were those measured on the inclined face of the model. The pressures measured on the horizontal face were very small as compared to those measured on the inclined face as was shown in Table 6.3. FPC #3 and FPC #5 were subjected to the highest pressures suggesting that the maximum pressures on the inclined face of the model are realized near the inflection line. Values recorded from FPC #4, located 195 mm up from FPC #3 and on the same vertical plane, were 30 to 50 % less than those values recorded from FPC #3. This pattern of response would be expected as there would be stress variation on the model face due depth differences below the testbed surface.

The response of the face pressure cells located on the inclined face of the model shows a cyclic pattern where there is an increase in load followed by a drop-off as was seen in Figure 6.11. This pattern suggests a build-up of force acting on the model followed by a failure of some sort relaxing the load. This type of pattern was also observed in records from the BLC's and HLC's.

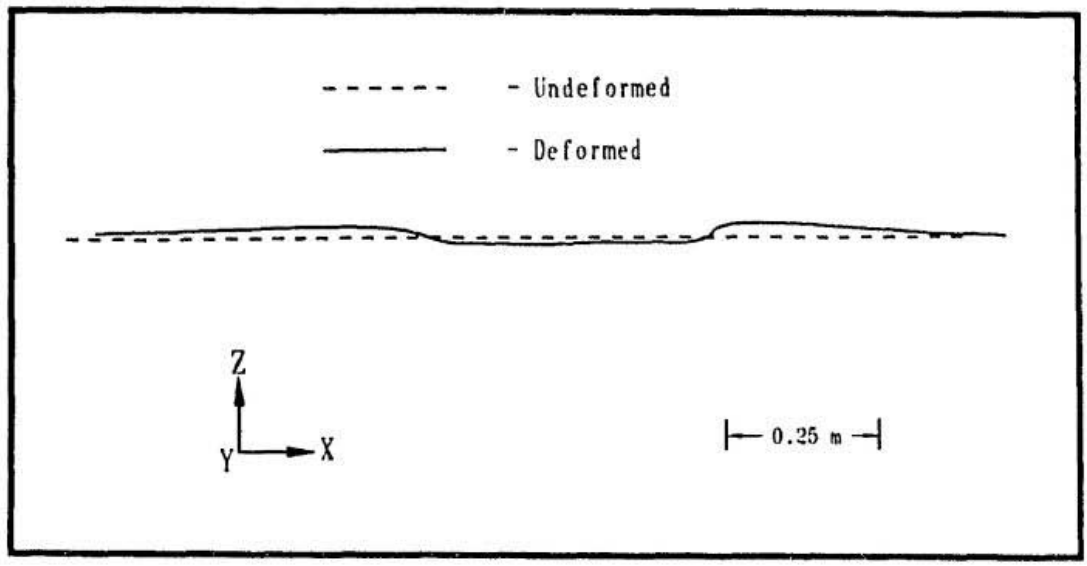

Figure 7.2: Deformed Solder Strand.

7.2.2 Vertical Forces on the Model

Figure 7.2 shows a frontal view of a solder strand which has been displaced during the scour process. It appears that some bearing capacity failure might have occurred as the solder strand is pushed down in the trough and uplifted to the sides. This failure might be like a Prandtl-type failure mechanism which was depicted in Figure 2.12. If vertical forces exerted on the testbed by the model were large enough, bearing capacity failure might have occurred, yielding the deformations shown in Figure 7.2.

The bearing capacity of the sand under the model keel can be analysed by considering the model as a shallow foundation. The four bearing capacity failure mechanisms presented in Figure 7.3 through Figure 7.6 seem like possible mechanisms for subscour deformation. The greatest pressures on the face of the model are located on the inclined face of the model as was previously mentioned. If a dead wedge of soil

under the model is considered, as was described by Palmer (1990), then vertical forces might be transmitted by the sloping model face through the dead wedge of soil and ultimately cause bearing capacity failure beneath the model as is shown in Figure 7.3 and Figure 7.4. In other words, the wedge is considered as a shallow foundation. The wedge is assumed to extend only to the original testbed surface and the surcharge from the frontal spoil is neglected. These assumptions will yield the lowest bearing capacities for the proposed mechanisms and indicate whether or not failure is possible. In Figure 7.3, the failure is assumed to occur in the longitudinal direction where the breadth of the foundation is taken as the length of the dead wedge, L_w, and the length of the foundation is taken as the width of the model, W. This potential failure mechanism has been termed Mechanism 1. The failure is assumed to occur normal to the scour track in Figure 7.4. In this case, the breadth of the foundation is equal to the width of the model and the length of the foundation is considered to be the length of the dead wedge. This mechanism has been labelled Mechanism 2. Alternatively, the failure could be assumed to occur by bearing capacity failure directly through the model loading as depicted in Figure 7.5 and Figure 7.6. The loading is considered to extend only to the original testbed surface and the frontal spoil surcharge is again neglected. The mechanism in Figure 7.5 assumes longitudinal failure with the breadth of the foundation equal to the length of the assumed soil/model interface, L_L, and the length of the foundation is taken to be equal to the width of the model. In Figure 7.6, the reverse is assumed. These potential failure mechanisms have been termed Mechanism 3 and Mechanism 4 respectively.

Terzaghi's Theory for general shear, Meyerhof's Theory, and Terzaghi's Theory for local shear were used to calculate the bearing capacity of the soil for the 4 mechanisms presented in Figures 7.3 to 7.6. The results of the calculations are presented

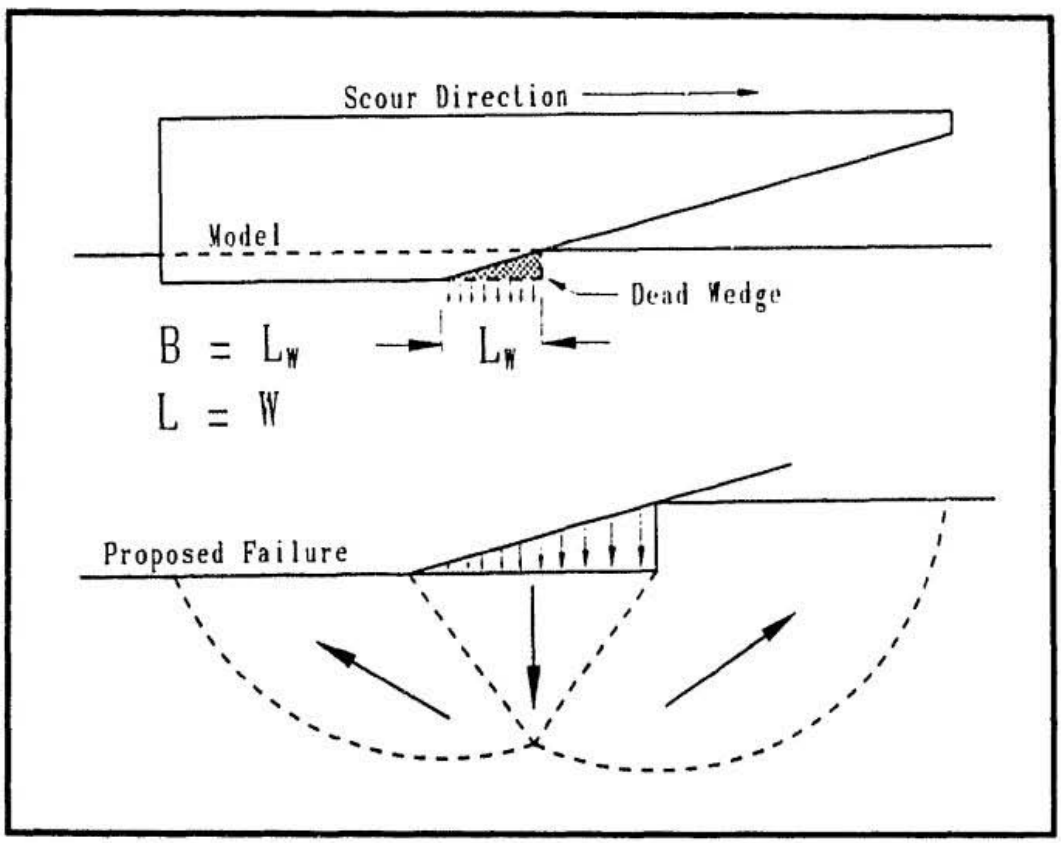

Figure 7.3: Potential Bearing Capacity Failure Beneath a Dead Wedge of Soil, Mechanism 1.

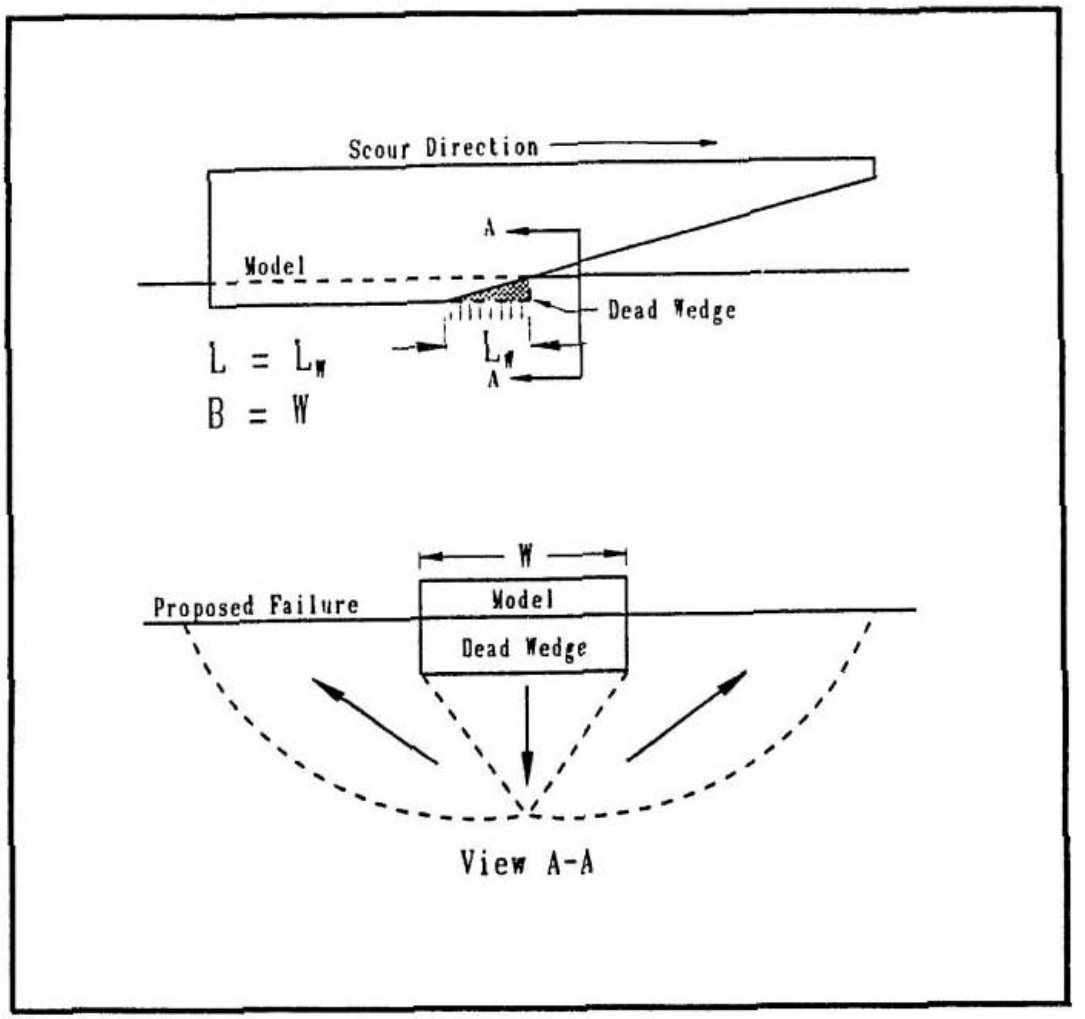

Figure 7.4: Potential Bearing Capacity Failure Beneath a Dead Wedge of Soil, Mechanism 2.

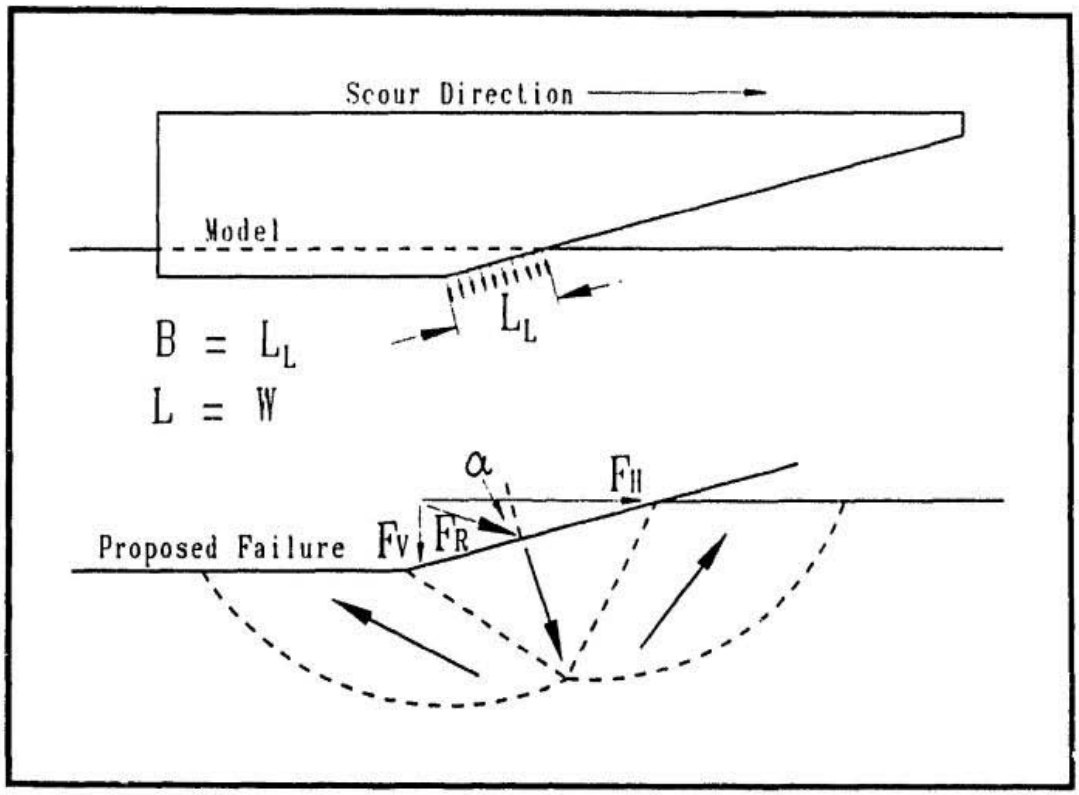

Figure 7.5: Potential Bearing Capacity Failure Through Direct Model Loading, Mechanism 3.

in Tables 7.3 to 7.6. In these tables the *Load on Soil* was calculated by considering that the total vertical load acting on the model acted perpendicular to the base of the equivalent footing as shown in Figures 7.3 to 7.6. The results in Table 7.3 indicate that bearing capacity failure by general shear failure has not occurred assuming this failure mechanism. However, values indicate that local shear failure might have occurred. When considering Mechanism 2, a term in the Terzaghi Equation becomes negative due to the considered loading pattern and failure mechanism (breadth of the foundation is larger than the width). This yields a factor of 10 between values obtained using Terzaghi's Theory and those obtained using Meyerhof's Theory as can be seen from Table 7.4. Therefore, low values are arrived at using Terzaghi's Theory and comparison with the values arrived at using Meyerhof's Theory suggest that bearing capacity failure had not occurred. Values suggest that local shear failure might have occurred. Mechanism 3 yields bearing capacity values which suggest that general shear or local shear bearing capacity failure below the model was possible. The negative term present in the analysis of the bearing capacity for Mechanism 4 yields negative bearing capacity, again due to the considered loading pattern and failure mechanism. However, Meyerhof's calculated values are close to measured values suggesting that general shear or at least local shear failure might have occurred and this failure could thus be responsible for the rupture surfaces to the sides of the model as well as for the displacement pattern of the solder strand shown in Figure 7.2.

The measurement of the vertical pressure on the face of the model should correspond with the total measured vertical force on the model during each test. If it is assumed that the pressures recorded from the FPC's are acting normal to the models inclined face, then the pressure can be resolved into vertical and horizontal

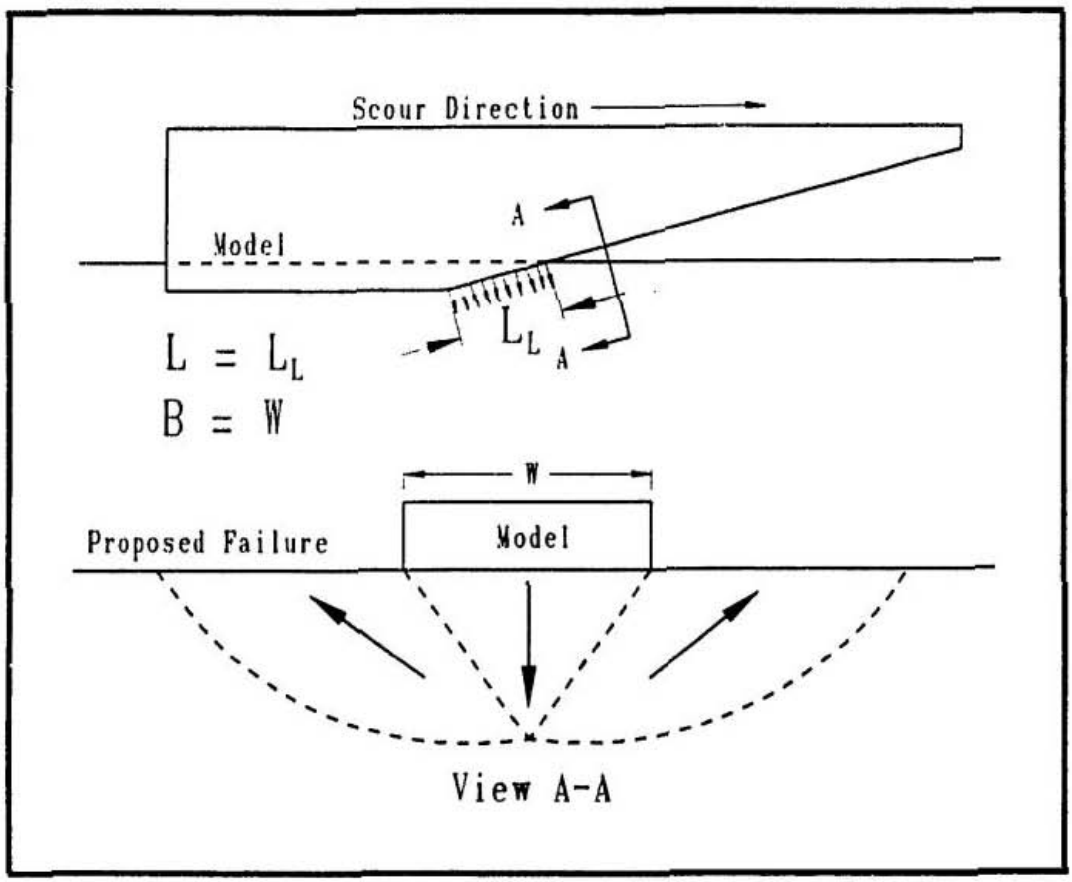

Figure 7.6: Potential Bearing Capacity Failure Through Direct Model Loading, Mechanism 4.

Table 7.3: Comparison of Calculated Bearing Capacity and Force Exerted on the Testbed, Mechanism 1, Dead Wedge.

Test Type	Analysis Method	Bearing Capacity (kN/m^2)	Load on Soil (kN/m^2)
Dry	Terzaghi (General Shear)	74.9	27.4
	Meyerhof	77.5	27.4
	Terzaghi (Local Shear)	17.9	27.4
Submerged	Terzaghi (General Shear)	45.7	15.1
	Meyerhof	47.7	15.1
	Terzaghi (Local Shear)	11.1	15.1

Table 7.4: Comparison of Calculated Bearing Capacity and Force Exerted on the Testbed, Mechanism 2, Dead Wedge.

Test Type	Analysis Method	Bearing Capacity (kN/m^2)	Load on Soil (kN/m^2)
Dry	Terzaghi (General Shear)	38.0	27.4
	Meyerhof	319.2	27.4
	Terzaghi (Local Shear)	9.6	27.4
Submerged	Terzaghi (General Shear)	23.5	15.1
	Meyerhof	196.8	15.1
	Terzaghi (Local Shear)	5.9	15.1

Table 7.5: Comparison of Calculated Bearing Capacity and Force Exerted on the Testbed, Mechanism 3, Direct Loading.

Test Type	Analysis Method	Bearing Capacity (kN/m^2)	Load on Soil (kN/m^2)
Dry	Terzaghi (General Shear)	8.5	33.3
	Meyerhof	7.2	33.3
	Terzaghi (Local Shear)	1.8	33.3
Submerged	Terzaghi (General Shear)	5.2	18.8
	Meyerhof	3.3	18.8
	Terzaghi (Local Shear)	1.1	18.8

Table 7.6: Comparison of Calculated Bearing Capacity and Force Exerted on the Testbed, Mechanism 4, Direct Loading.

Test Type	Analysis Method	Bearing Capacity (kN/m^2)	Load on Soil (kN/m^2)
Dry	Terzaghi (General Shear)	—	33.3
	Meyerhof	36.1	33.3
	Terzaghi (Local Shear)	—	33.3
Submerged	Terzaghi (General Shear)	—	18.8
	Meyerhof	16.4	18.8
	Terzaghi (Local Shear)	—	18.8

components by

$$p_H = p\sin(15°) \tag{7.3}$$

and

$$p_V = p\cos(15°). \tag{7.4}$$

The total vertical force on the model can then be expressed by

$$F_V = F_{V1} + F_{V2} \tag{7.5}$$

where F_{V1} is the vertical force acting on the horizontal face of the model and F_{V2} is the vertical force acting through the small dead wedge of soil considered earlier. Where L is length and W is width, F_{V1} and F_{V2} can be expressed as

$$F_{V1} = p_1 L_1 W \tag{7.6}$$

and

$$F_{V2} = p_2 L_2 W \tag{7.7}$$

where p_1 is the average pressure on the horizontal face of the model, p_2 is the vertical component of the average pressure on the inclined face of the model, L_1 is the length of the horizontal face of the model, L_2 is the length of the dead wedge of soil considered above, and W is the width of the model. The results of the calculations are presented in Table 7.7. Quite good agreement is obtained ($< \pm$ 10 %) between the values measured directly with the BLC'S and those values calculated from the measured face pressures.

7.2.3 Horizontal Forces on the Model

Successive failure surfaces were observed to appear in front of the model as the scour progressed as was shown in Figures 6.3 and 6.5. The same type of process was

Table 7.7: Comparison of Calculated and Measured Vertical Load.

Test #	Vertical Load (N)	F_{V1} (N)	F_{V2} (N)	F_V (N)	% Difference From Vertical Load
1	1754.9	423.5	1297.2	1720.7	-1.95 %
2	1629.0	424.7	1121.0	1121.0	-5.11 %
3	969.0	190.3	864.9	864.9	+8.88 %
4	826.3	174.9	585.1	585.1	-8.00 %

observed by Poorooshasb and Clark (1990), Prasad (1985), and Green (1984), all of whose tests were also conducted in sand. This type of failure is shown in Figure 7.7 and was described by Siemens (1963) in the analysis of model tillage tools. Selig and Nelson (1964) also conducted tests to observe soil deformations and failures for vertical and forward inclined blades as shown in Figure 7.8. Again, successive failure planes were present in front of the model.

As with calculation of the vertical forces acting on the model, a dead wedge of soil was considered as a first approach to the analysis of the horizontal forces acting on the model. This approach is depicted in Figure 7.9. If the front of the dead wedge carried by the model is assumed to have a vertical face, then several methods can be used to calculate the pressures required to cause passive earth pressure failure in front of the model. The reworked frontal spoil in front of the model is considered to be in the same state as the original sand in the testbed which was slumped into position. Therefore, no differentiation between the two materials is made and the measured horizontal force on the model should, in theory, equal the forces required to move the model through the testbed. The maximum horizontal forces (P_h) measured on the model were 1.358 kN and 0.7993 kN respectively for the dry and submerged

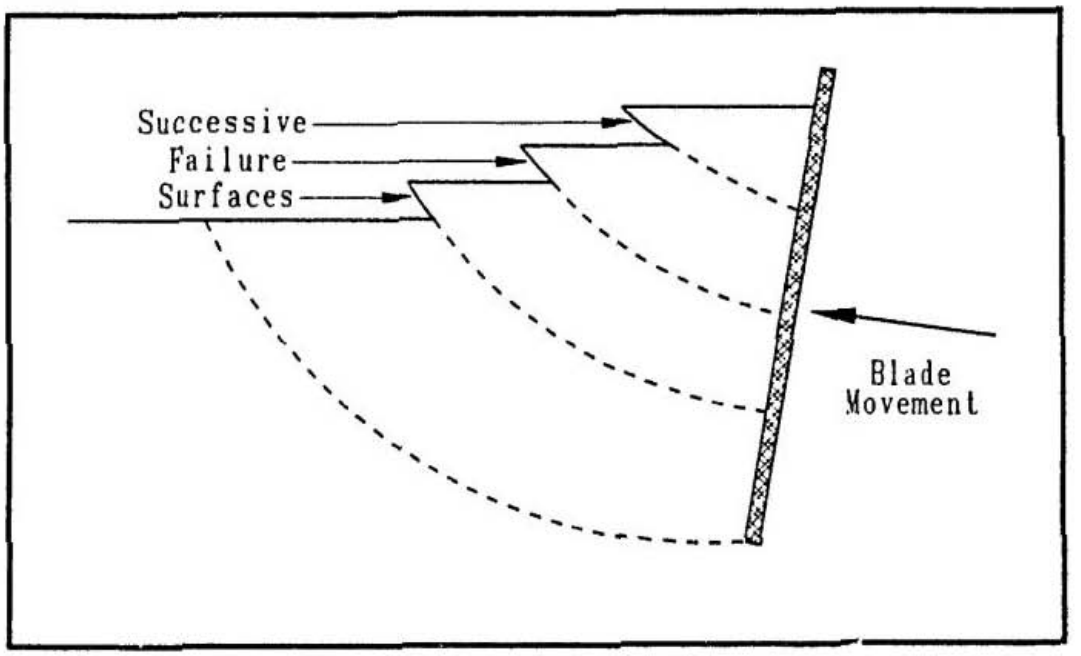

Figure 7.7: Successive Slip Surfaces in Front of Near-Vertical Model Tillage Tools (After Siemens, 1963).

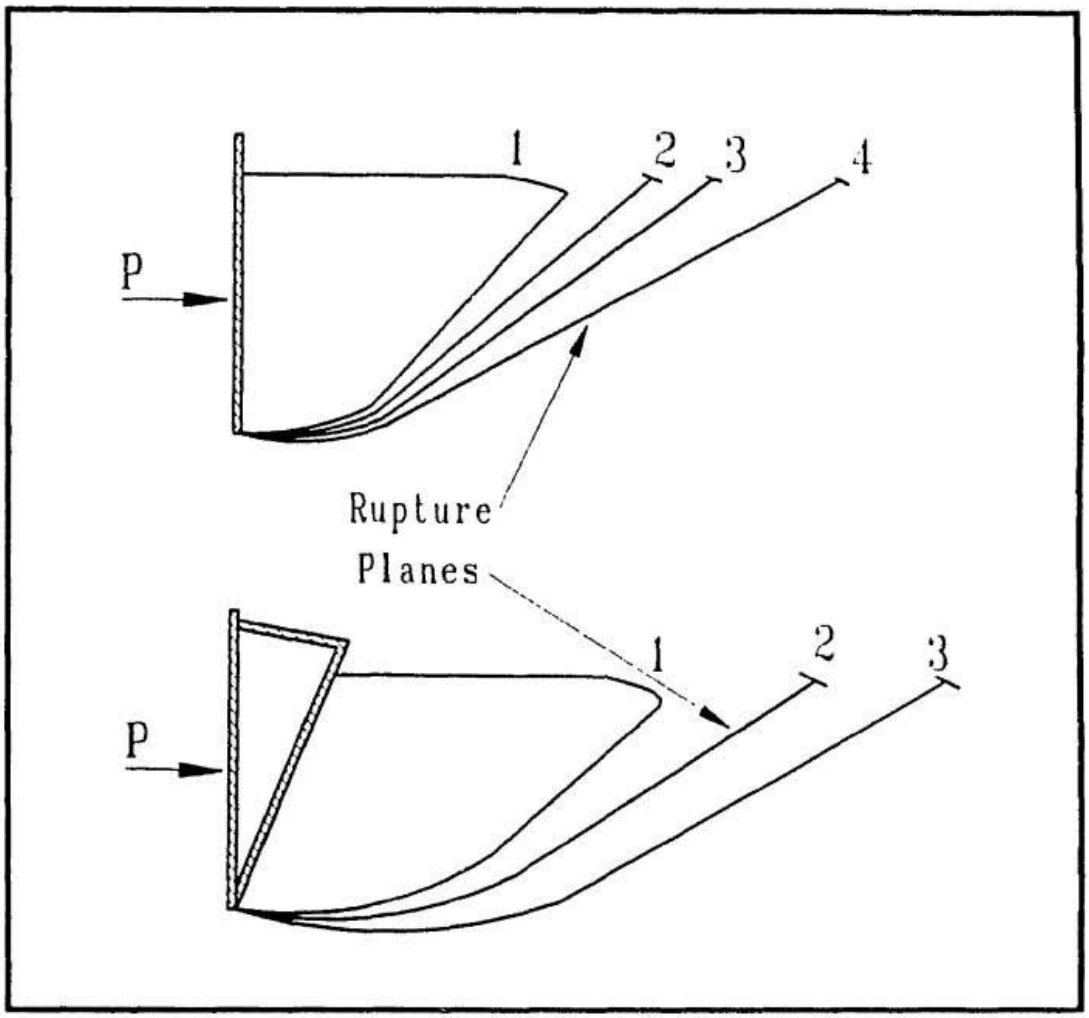

Figure 7.8: Failure Surfaces for Vertical and Forward-Inclined Blades in Medium-Dense Sand (After Selig and Nelson, 1964).

tests. These values are compared to passive earth pressure values calculated using Rankine's Theory, Coulomb's Theory, Terzaghi and Peck's Log Spiral Analysis, and Shields and Tolunay's method. Results are presented in Table 7.8.

Table 7.8: Results of Passive Earth Pressure Failure Calculations with the Inclusion of a Dead Wedge.

Test Type	Calculation Method	Maximum P_h (N)	P_p (N)
Dry	Rankine	1358.0	458.8
Dry	Coulomb	1358.0	3375.5
Dry	Terzaghi and Peck	1358.0	1053.9
Dry	Shields and Tolunay	1358.0	941.7
Submerged	Rankine	799.3	282.9
Submerged	Coulomb	799.3	2081.2
Submerged	Terzaghi and Peck	799.3	649.7
Submerged	Shields and Tolunay	799.3	580.5

Table 7.8 confirms several facts in the passive failure analysis assuming a dead wedge mechanism. The first is that by ignoring the effects of wall friction (Rankine's Theory), low passive earth pressure (P_p) resistance values are obtained. Also, Coulomb's Theory assumes that the failure surface is planar and thus overestimates the passive earth resistance as is seen in the table. The passive earth pressure resistance calculated using Coulomb's Theory indicates that passive failure would not have occurred when in reality some process similar to passive earth pressure failure has occurred. The last two calculation methods give results closest to values actually measured. Differences between calculated and measured values might be attributed to the fact that the dead wedge process might not be identical to the actual process or that the process might not be strictly attributed to passive earth pressure failure

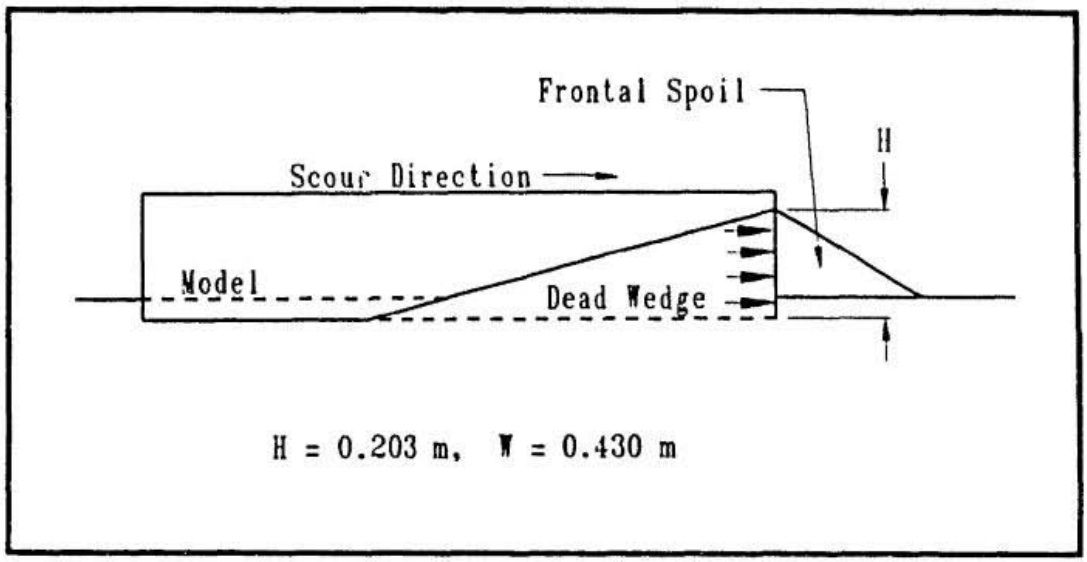

Figure 7.9: Horizontal Forces Acting on Dead Wedge of Soil in Front of the Model.

but that it might be coupled with some other failure mechanism.

If the dead wedge is not considered, then the horizontal forces acting on the model might be analysed by regarding the model as a retaining wall as shown in Figure 7.10 (with the same geometry as the model) and calculating the passive earth pressure resistance acting on the retaining wall. This retaining wall can be analysed using Coulomb's Theory or by Terzaghi and Peck's Log Spiral Analysis. An alternative means of analysis is to look at the problem from the point of view of Harrison's (1972) analysis of a single plate-grouser as was described earlier. The passive earth resistance has been calculated using these methods and is presented in Table 7.9.

As can be seen from Table 7.9, Coulomb's Theory again overestimates the passive resistance of the soil in front of the model. Terzaghi and Peck's Log Spiral Analysis yields results closest to those measured. P_p calculated using Harrison's method of analysis yielded values 43 to 56 % less than those measured. These values are com-

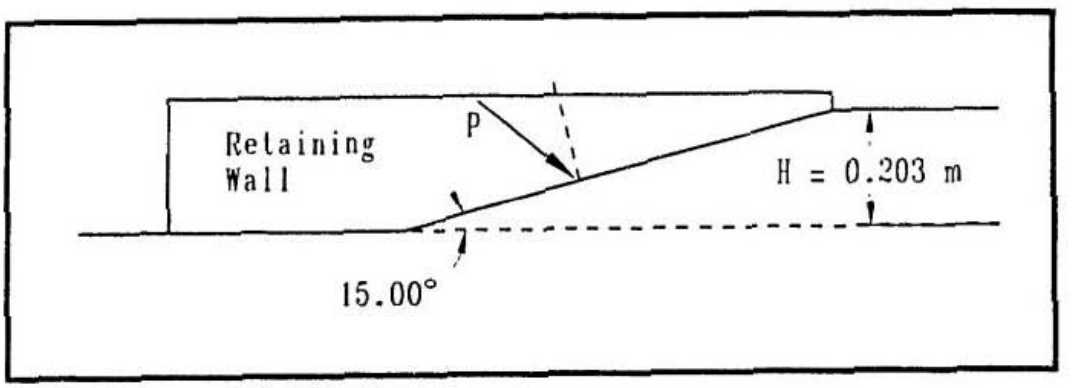

Figure 7.10: Retaining Wall with Model Geometry.

Table 7.9: Results of Passive Earth Pressure Calculations for a Sloped Retaining Wall as Shown in Figure 7.10.

Test Type	Calculation Method	Maximum P_h (N)	P_p (N)
Dry	Coulomb	1358.0	2906.8
Dry	Terzaghi and Peck	1358.0	958.0
Dry	Harrison	1358.0	597.7
Submerged	Coulomb	799.3	1793.1
Submerged	Terzaghi and Peck	799.3	590.8
Submerged	Harrison	799.3	434.3

parable to values measured by Prasad (1985) where P_p calculated using Harrison's method yielded values up to 53 % less than those values measured on a model inclined 30° from the horizontal. Differences in measured and calculated values might also be attributed to densification of the soil as it was remoulded in the frontal spoil.

The horizontal component of the pressure measured by the FPC's and acting on the face of the model was previously expressed as

$$p_H = p\sin(15°)$$

where p is the average pressure acting normal to the inclined face of the model. If the force is considered to be acting through the dead wedge of soil as shown in Figure 7.11a, then

$$F_{H1} = p_H HW \tag{7.8}$$

where H is the height of the dead wedge and W is the width of the model. The results of the calculations are presented in Table 7.10. Agreement is not very good between values measured directly and those calculated from the FPC measurements. Frictional forces were not considered between the soil and the horizontal base and sides of the model but even if this increase in horizontal force was to be taken into account, F_{H1} would not increase enough to make good agreement between it and the measured horizontal load. However, if the forces acting along the entire inclined face of the model are considered as shown in Figure 7.11b, then Eq. 7.8 becomes

$$F_{H2} = p_H L_F W \tag{7.9}$$

where L_F is the length of the inclined face of the model. This equation gives values which are greater than the measured values (see Table 7.10). The measured values are somewhere between the F_{H1} and F_{H2} calculated values and though it is not known

how to arrive at true values through calculation, if $F_{H(AVG)}$ is calculated by

$$F_{H(AVG)} = \frac{F_{H1} + F_{H2}}{2} \tag{7.10}$$

and the values are compared to measured loads, better results are obtained for 3 of the 4 tests.

Table 7.10: Comparison of Calculated and Measured Horizontal Load.

Test #	Hor. Load (N)	F_{H1} (N)	F_{H1} ÷ Hor. Load	F_{H2} (N)	F_{H2} ÷ Hor. Load	$F_{H(AVG)}$ (N)	$F_{H(AVG)}$ ÷ Hor. Load
1	1358.0	473.5	0.35	1828.8	1.35	1151.2	0.85
2	1123.5	409.1	0.36	1580.2	1.41	994.7	0.89
3	768.0	315.7	0.41	1219.4	1.59	767.6	1.00
4	799.3	213.6	0.27	825.0	1.03	519.3	0.65

7.3 Stresses and Pore Pressures in the Testbed

The maximum vertical loads exerted on the testbed through the small dead wedge of soil considered in Section 7.2, are presented in Table 7.11. The maximum stresses recorded by the TSC's are also presented in this table. The values indicate that the stresses in the soil are less than the load exerted on the testbed through the proposed dead wedge failure mechanism which is to be expected due to the dissipation of stress with depth. The limited number of data points collected does not give any indication of the dissipation pattern of stresses in the testbed with depth or distance off of model centerline. More data points would be needed to establish a relationship. Values close to what might be expected were recorded during Test 2, however, in Test 3 and Test 4, recorded values were much lower than what were expected. One

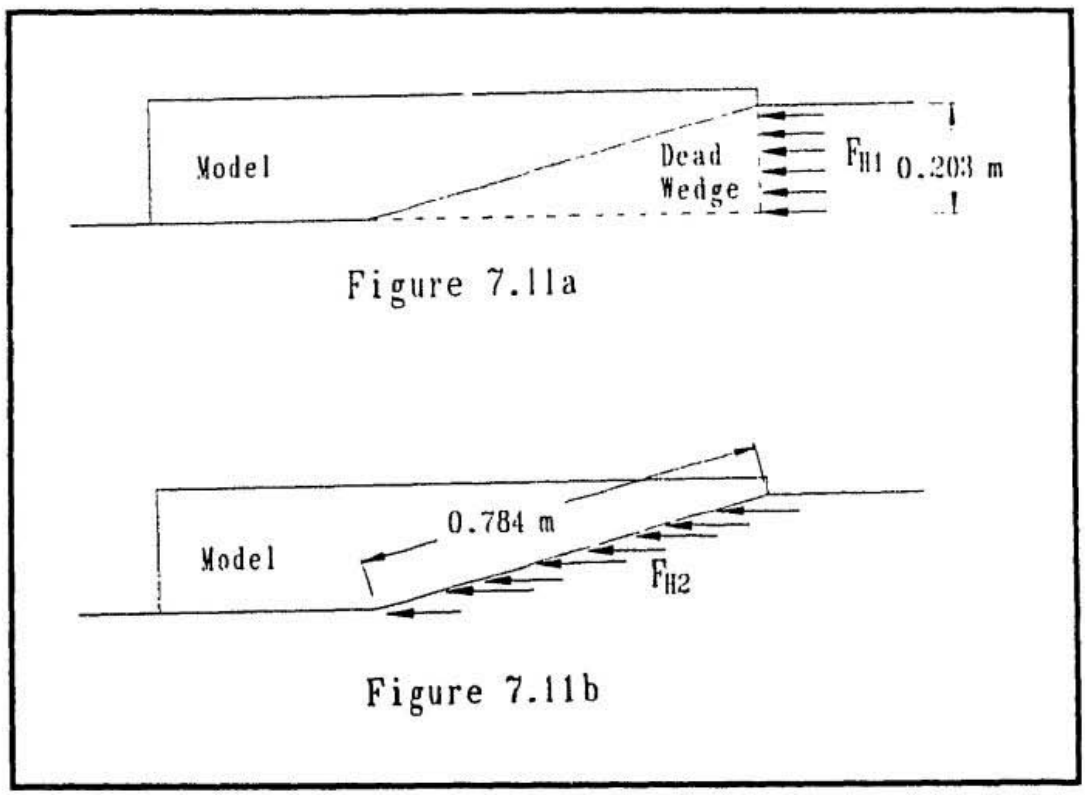

Figure 7.11: Assumed Horizontal Pressures Acting on the Inclined Model Face.

possibility for differing values might be that the dead wedge assumption is not totally correct.

Table 7.11: Comparison of Calculated and Measured Testbed Stresses, Dead Wedge.

Test #	Vertical Load (N)	Load on Testbed (kN/m^2)	TSC #1 Max. Stress (kN/m^2)	TSC #3 Max. Stress (kN/m^2)
1	1754.9	27.4	—	—
2	1629.0	25.4	20.1	15.1
3	969.1	15.1	3.2	5.9
4	826.3	12.9	4.5	3.3

Pore pressure increases in the testbed were small due to the type of the testbed material and also due to the relative density of the soil. However, the increases were definitely present as was demonstrated in Table 6.4. The greatest pore pressure increases were expected to be realized directly under the centerline of the scour. However, this was not the case as the largest increase was recorded almost immediately under the outside edge of the model (Test 3, PPT #6). Pore pressure response was measured to a depth of at least 0.06 m or 1.5 scour cut depths below the model which was the deepest point measured.

The variation of the maximum positive increase in pore pressure with depth below the iceberg model keel and distance off of centerline are plotted in Figure 7.12 and Figure 7.13. If the extreme value of 1.642 kPa on the plots is ignored, then there appears to be an increase in the positive change of pore pressure to a particular depth and distance off of centerline as can be seen from the figures. The variation of pore pressure increase with the straight line distance to the PPT is presented in Figure 7.14. Again, ignoring the extreme value, there appears to be an increase in the

positive change of pore pressure with increasing R up until approximately R=0.12 m. More points would be required to establish definite trends between these parameters.

It is not known how these results should apply to a full scale event or to what depth the pore pressures and stresses would be relevant. Depending on their magnitude, the full scale pore pressures and stresses would have to be taken into account especially where buried pipelines or other installations are concerned.

7.4 Displacements in the Testbed

Post-scour ball bearing positions from one of the tests are shown in Figure 7.15. Balls located above the scour cut depth tended to be caught up in the mound of spoil in front of the model and deposited in the berm as shown as shown in Zone A. Balls in Zone B tended to be pushed up and out with the rupture surfaces to the sides of the scour. Balls in Zone C, located on the scour interface were ridden over within a very short distance. Balls in Zone D, beneath the scour were pushed down and also pushed laterally in the scour direction, the magnitude of the movement depending on the original depth of the ball bearings below the model keel.

The variation of the vertical displacement of the solder strands with depth below the model keel is presented in Figure 7.16. These displacements were measured along the scour centerline as was described in Chapter 6. The figure shows that there is a general trend for the vertical displacement to decrease with the depth below the keel. Immediate settlement calculations based on elastic theory did not yield results similar to those measured during testing. Figure 7.17 presents maximum values of uplift for the Z=0.36 m solder strands. The uplift was caused by the rupture planes which surfaced to the sides of the model during scouring and which also tends to support the general or local shear bearing capacity failure theory presented earlier.

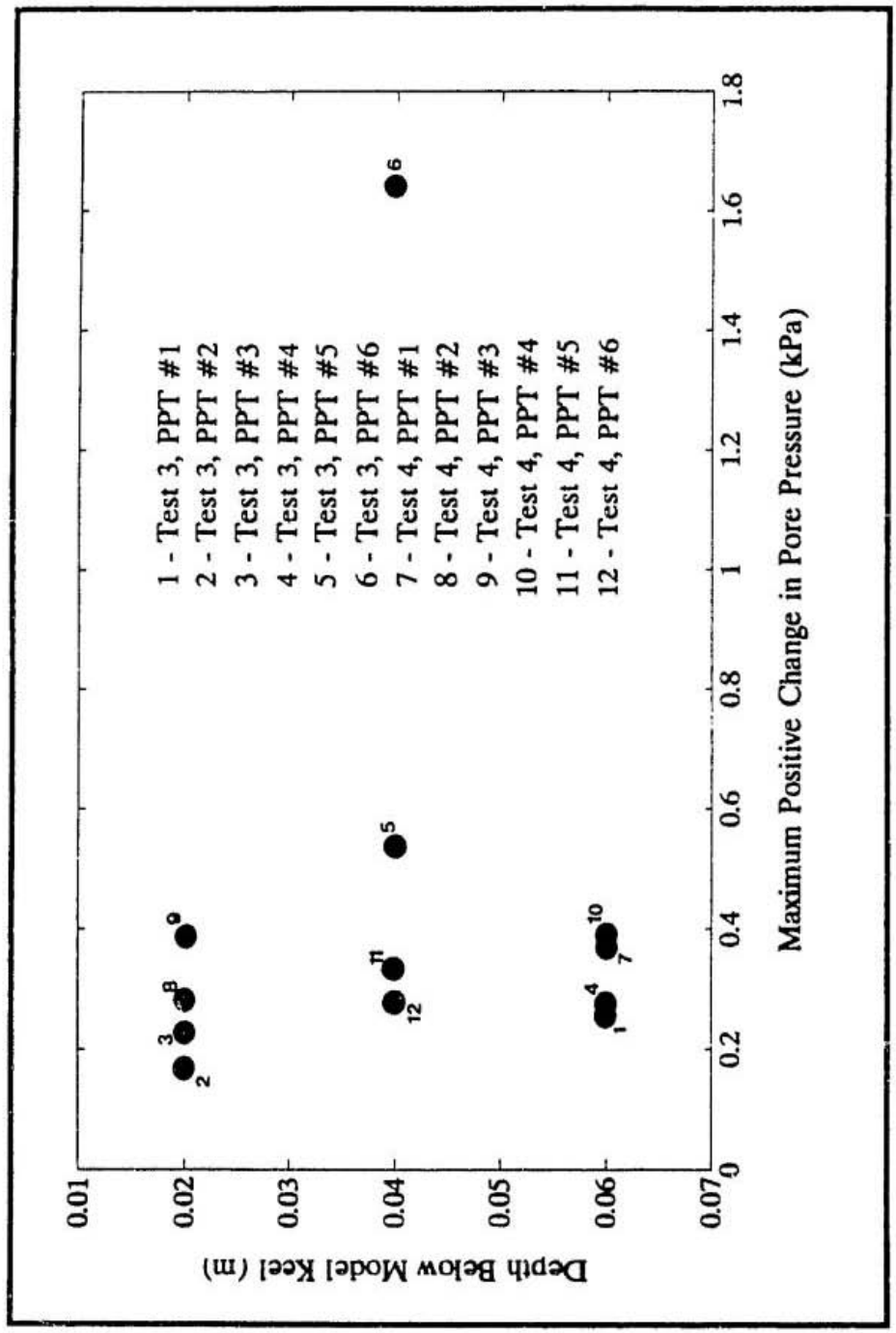

Figure 7.12: Variation of the Increase in Pore Pressure with Depth Below the Iceberg Model Keel.

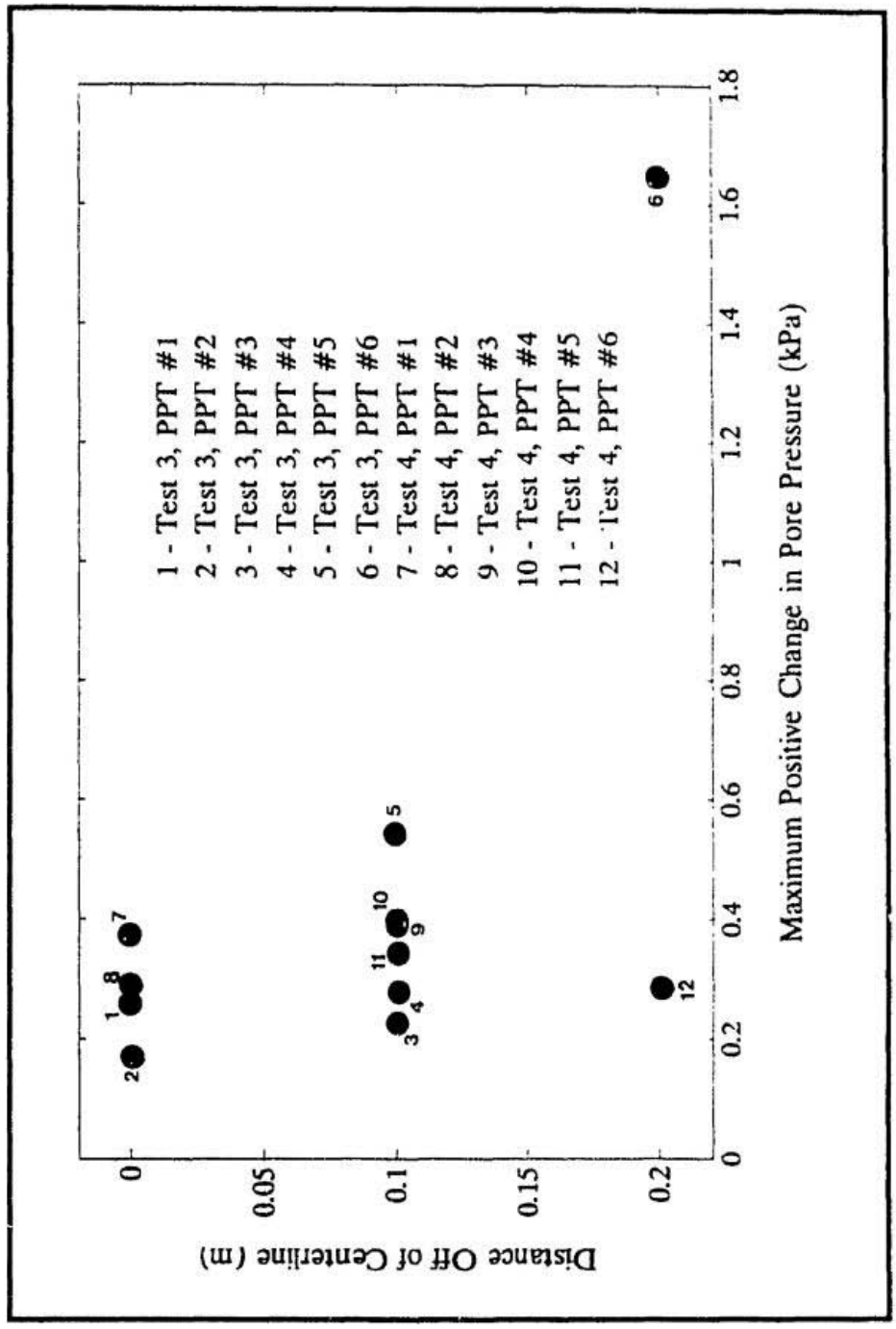

Figure 7.13: Variation of the Increase in Pore Pressure with Distance off of the Scour Centerline.

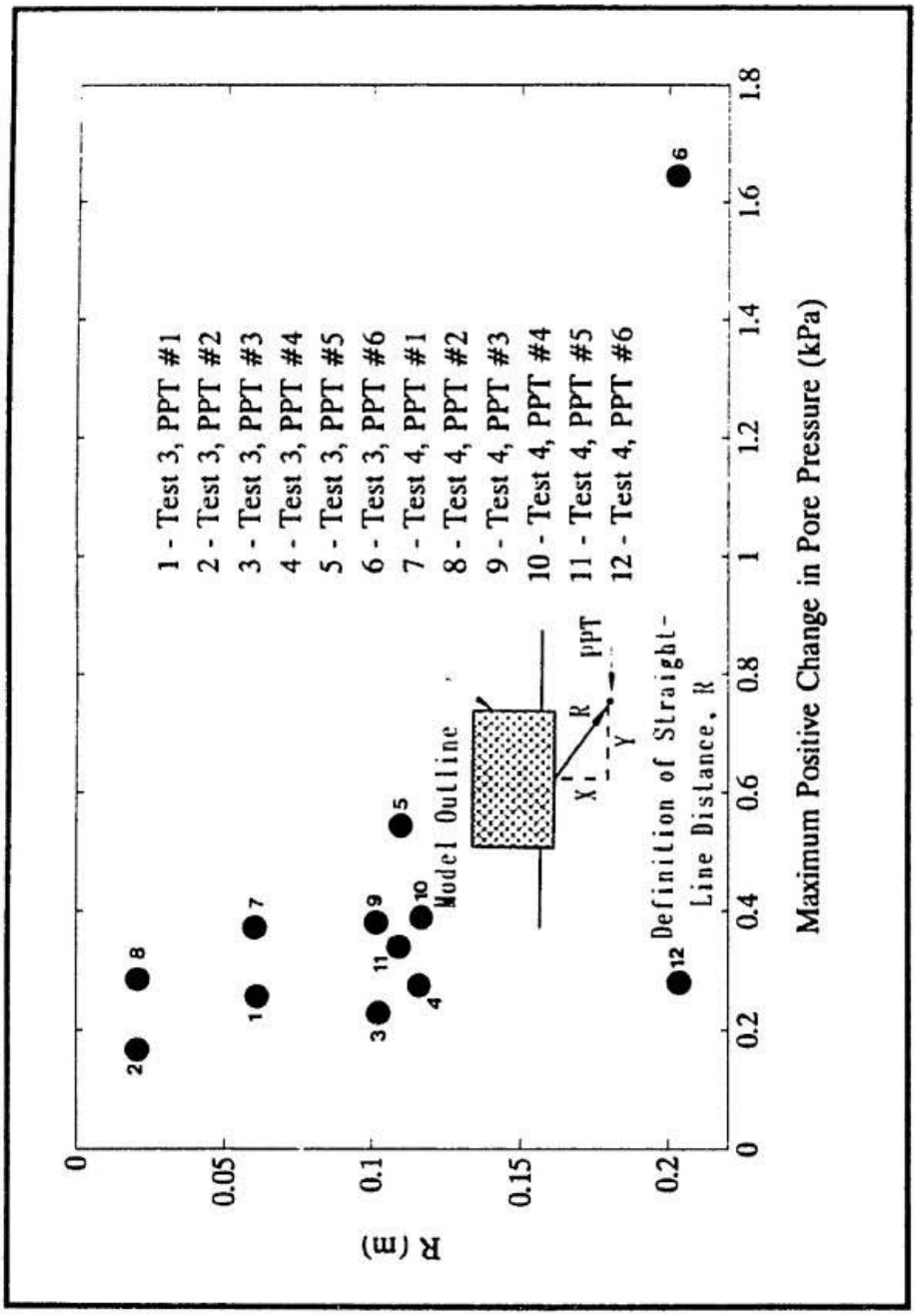

Figure 7.14: Variation of the Increase in Pore Pressure with Straight-Line Distance to the PPT.

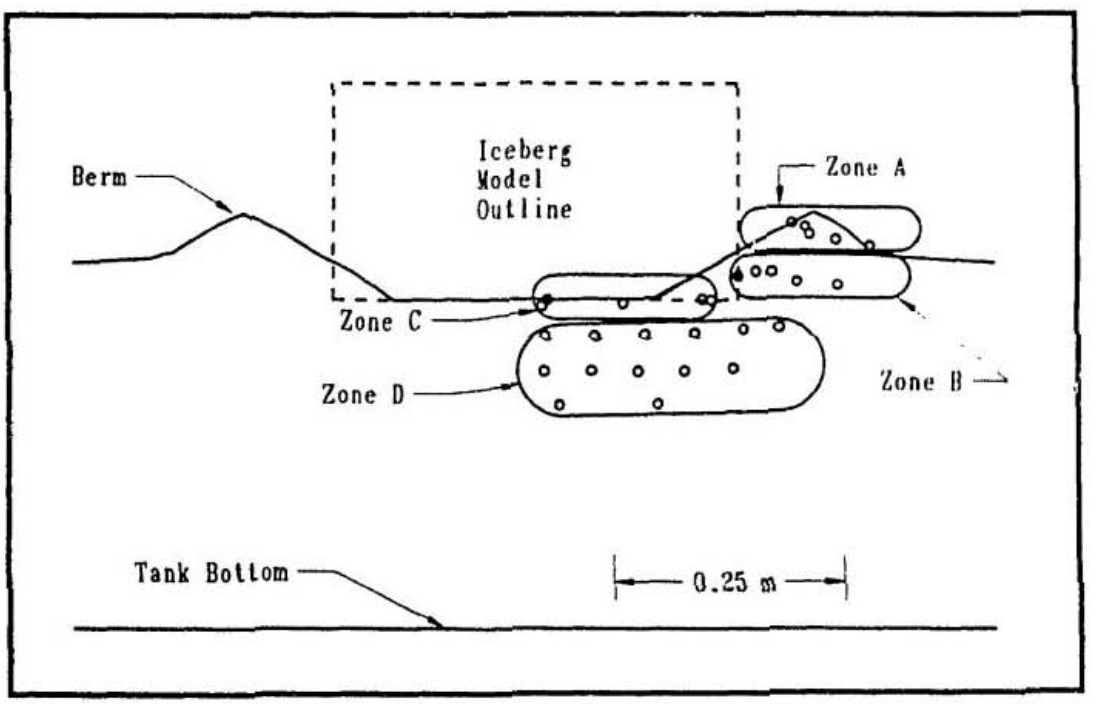

Figure 7.15: Post-Scour Zones of Ball Bearing Displacements.

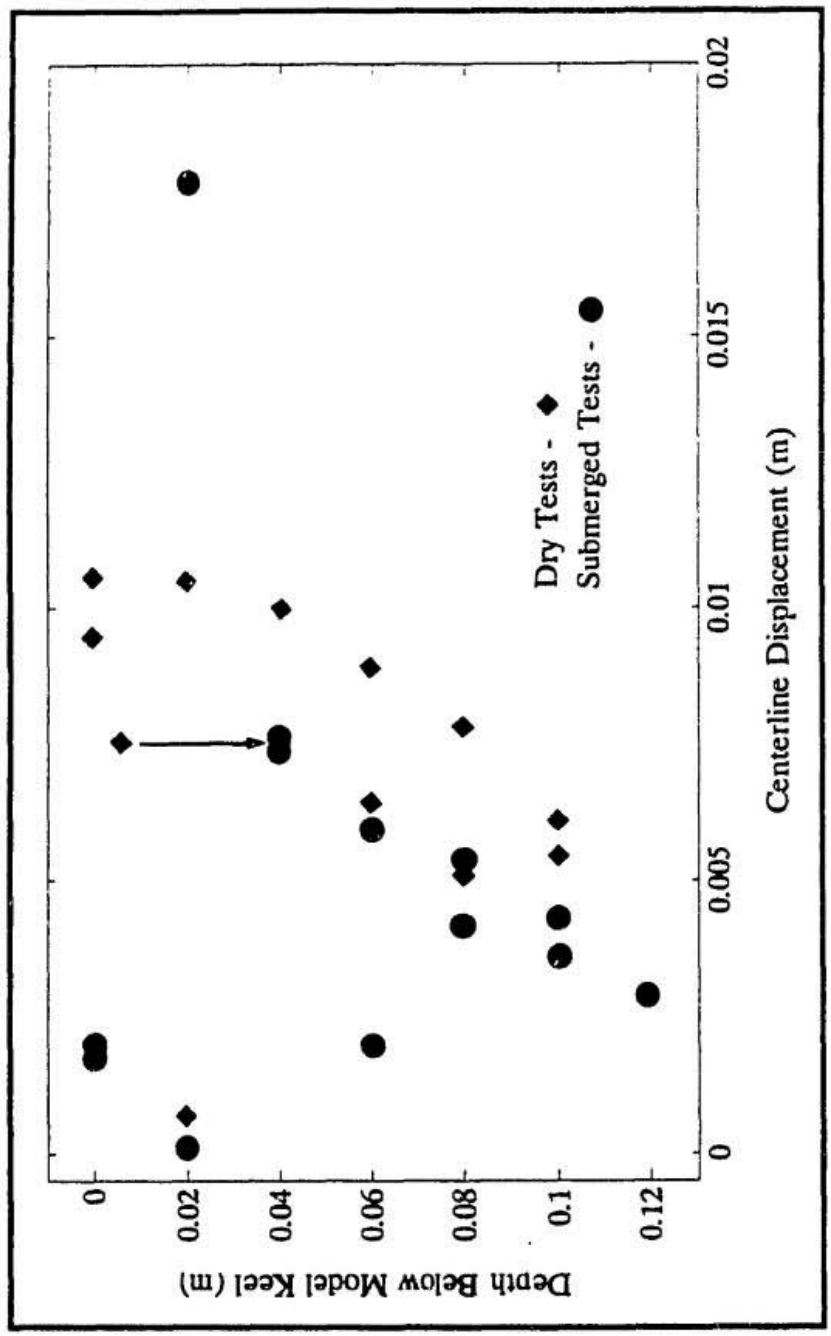

Figure 7.16: Variation of the Vertical Centerline Displacement of Solder Strands with Location Below the Scour.

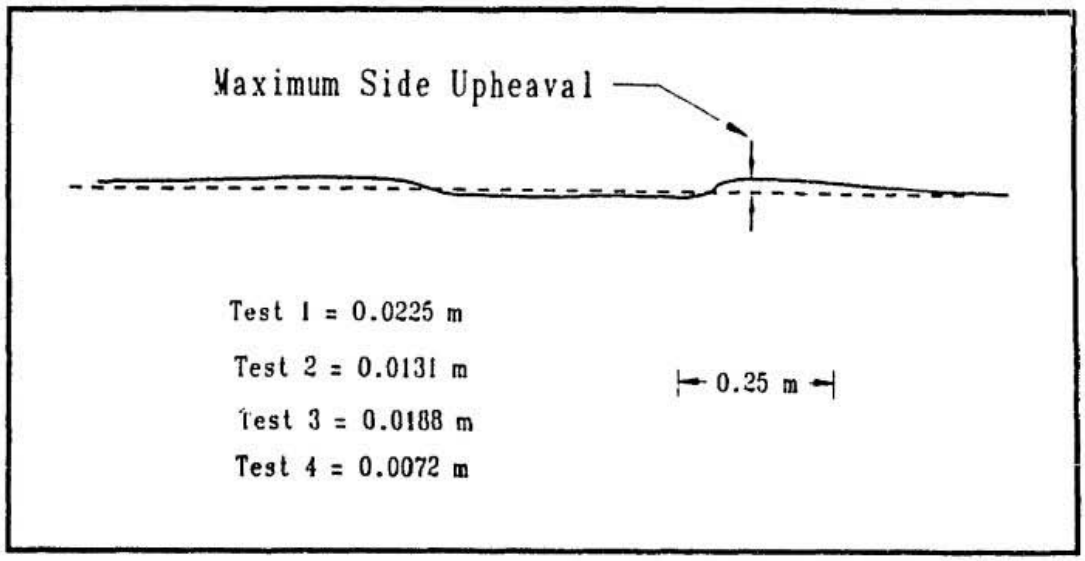

Figure 7.17: Side Upheaval Values for Z=0.36 m Solder Strands.

The variation of the horizontal displacement of the solder strands with depth below the model keel is presented in Figure 7.18. There is a definite pattern present; the horizontal displacement decreasing rapidly with depth. These horizontal displacements are attributed to the keel shear dragging mechanism (Been, 1990). Displacements were recorded up to 0.12 m below the model keel which was the extent to which measurements were taken. This is 3 scour cut depths below the model keel or 4 scour cut depths below the unscoured surface. Displacements of this type would have to be evaluated for a full scale event to determine how and to what depths they would affect a subsea installation such as pipeline.

7.5 Density Changes Across the Scour Profile

An observation of the contoured penetration resistance plots of Figure 6.18 and Figure 6.19 confirms that the soil has been disturbed in the area of influence of the

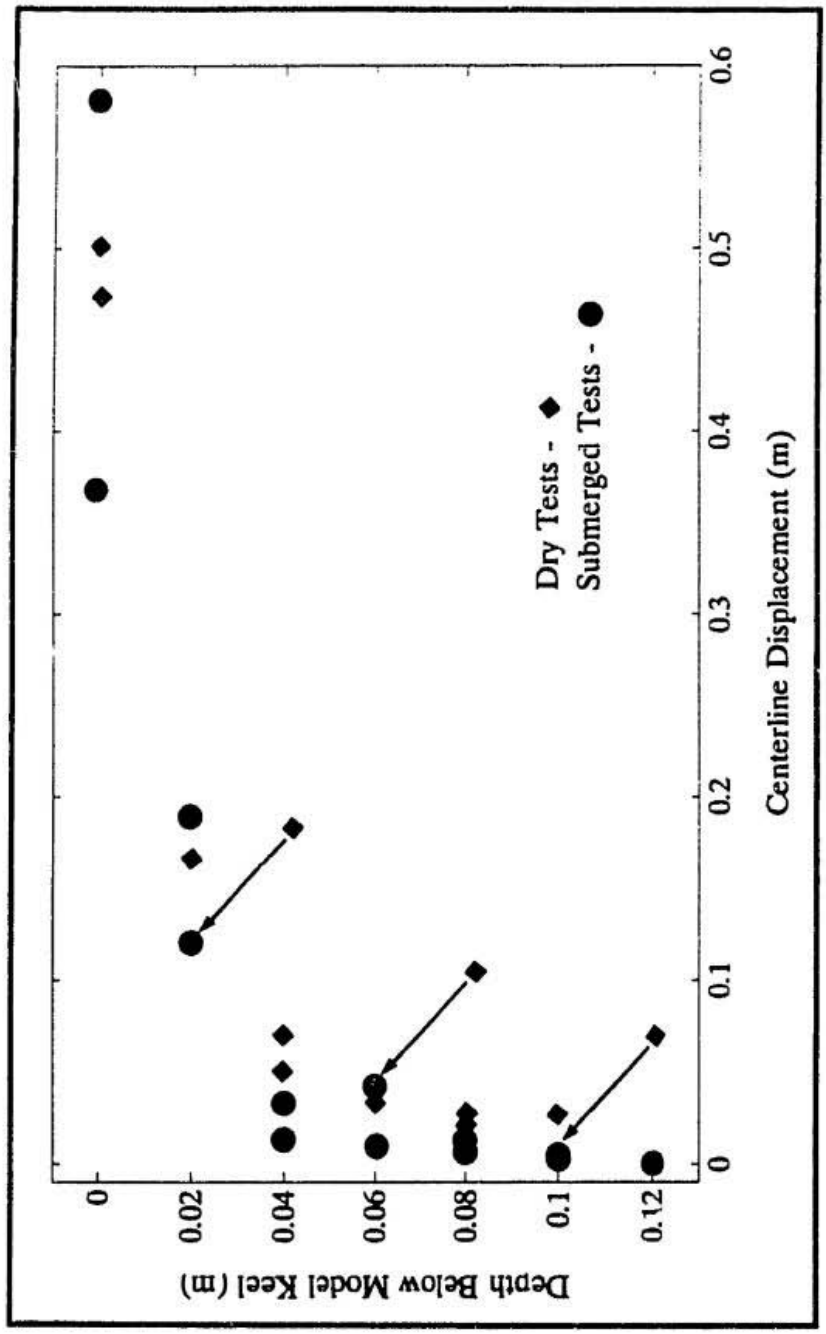

Figure 7.18: Variation of the Horizontal Centerline Displacement of Solder Strands with Location Below the Scour.

scour. These figures show that the areas of highest penetration resistance are within the trough of the scour and also show areas of high resistance within or adjacent to the berms. Strain hardening or densification of the soil in the trough may have been caused by the keel shear dragging mechanism below the model explaining the high penetration resistance values found in these areas. As for the areas of high penetration resistance under the berms, these were probably the result of the failure surfaces seen to the sides of the model, where, again, strain hardening has occurred along the failure surface rupture plane and within the wedge of soil displaced.

7.6 Comparison of Results with Previous Work

The post-scour profiles measured during this experimental program were similar to those recorded by Poorooshasb (1990), Prasad (1985), and Green (1984). Because of the sloping testbed used in the latter two tests, a steady-state scour profile was never reached during those experiments. Poorooshasb (1990) never reached a steady-state because of the scour cut depth and the length of run utilized.

A typical response from a total stress cell was presented in Figure 6.13. After the model had passed over the TSC, it was expected that the total stress below the scour would be at a lower-than-original steady-state due to the removal of 4 cm of overburden. However, greater drops than what were expected occurred. This was experienced with most of the TSC data which might suggest a data acquisition problem or a problem with the cells due to stress concentrations or some other factor such as differential stiffness. The results of Poorooshasb's (1990) tests, which utilized the same TSC's, with the exception of one or two anomalous results, corresponded fairly well with expected drops in total stress due to the removal of sand. Stresses were measured by Poorooshasb (1990) from 3.9 to 12.4 cm under the model and stress

increases varied from 5 to 15 kPa. Stresses measured by Green (1984) in the testbed varied from an increase of 2 to 20 kPa at depths of 1.2 to 11.7 cm below the scouring model keel.

No literature encountered during the research for this thesis revealed any values for the increase in pore pressures in sand during a model test as most tests were conducted in a dry state. However, Poorooshasb et al (1990) conducted tests in a saturated silt and recorded pore pressure increases of 0.5 to 6 kPa in depths from 5 to 20 cm below the scour trough. No attempt is made to try and directly compare these values with those obtained from the present tests; they are presented to illustrate the zone within which pore pressure changes have been recorded.

The relative magnitude of the face pressure in Poorooshasb's (1990) sand tests was greater than that of the present tests primarily because of the denser sand used in all areas of the testbed. The face pressures recorded on Green's (1984) and Prasad's (1985) models when they were at a scour cut depth of 0.04 m were interpolated from presented results for the models with a 60° and 30° angle of attack. The values obtained were 13.6 kPa (5 cm above the base) and 9.94 kPa (10 cm above the base) respectively which are smaller than those measured with the present 15° attack angle model.

Table 7.12 shows measured maximum vertical and horizontal forces exerted on the model during scouring for both the present tests and Poorooshasb's (1990) tests. The relative magnitude of the forces in Poorooshasb's tests is greater because of the denser sand used in those tests. If the vertical force is divided by the horizontal, ratio values typically range from 1.1 to 1.5 with the exception of Poorooshasb's Test 3 (ratio $\approx$0.9) which was the only test which used a model with a 30° angle of attack. Variations in force ratios indicate that the vertical force is dominant for small attack angles,

while for large attack angles the horizontal force is dominant. Horizontal force also decreases with increasing attack angle as was shown by Poorooshasb (1990), Prasad (1985), and Green (1984).

Table 7.12: Comparison of Vertical Force to Horizontal Force Ratios; Poorooshasb's (1990) Tests Compared to the Present Study.

Test Series	Test #	Max. Vertical Force (N)	Max. Horizontal Force (N)	Vertical Force ÷ Horizontal Force
Poorooshasb (1990)	1	6100	5100	1.196
	2	8900	8000	1.113
	3	7600	8500	0.894
	4	12,500	9500	1.316
Present Study	1	1755	1358	1.292
	2	1629	1124	1.449
	3	969	768	1.262
	4	826	799	1.034

Displacements in the testbed were also measured by Poorooshasb (1990) using metal ball bearings and solder strands as displacement markers. The greatest horizontal displacements were measured in loose sand, while in dense sand, displacements were restricted to immediately below the model keel. This same variation of displacement was also reported by Been (1990). Measurements of horizontal displacement in loose and medium sand for all three test programs are presented in Figure 7.19. Poorooshasb's loose sand was slightly more dense than the sand used in the present tests and models with different attack angles were used. Few details on the experimental program were given by Been (1990), however, the sand was slightly denser ($\approx$ +4 % for the data presented in Figure 7.19) than the sand used for the present tests. The figure shows great variation by using differing testbed materials and different

models. Further similar tests would be needed to identify the most critical model parameters.

7.7 Discussion

The results obtained during this experimental program can be explained by various theories and these are summarized in Table 7.13. This table indicates (Y = yes, N = no, or N/A = not applicable) whether or not the measured results could be predicted by the listed theories or previous test results.

The results from Poorooshasb's (1990) tests best predict the test results from the present series as would be expected due to the similarity of the test programs. Bearing capacity calculations, passive earth pressure calculations, and the keel shear dragging mechanism all predict various aspects of the experimental results, but no one theory predicts all of the results measured. Therefore, the results are attributed to the potential combination of mechanisms; bearing capacity failure, passive earth pressure failure, and the keel shear dragging mechanism proposed by Been (1990).

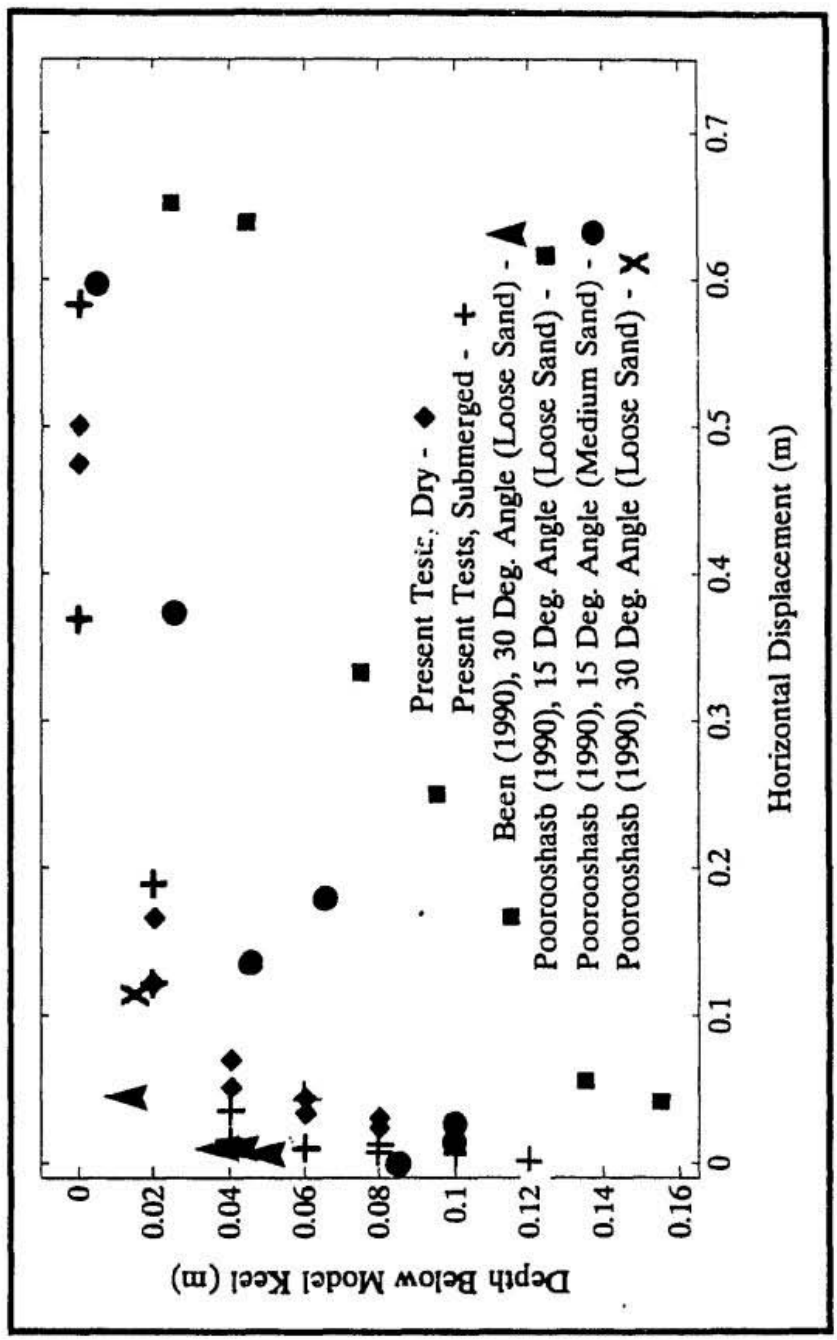

Figure 7.19: Variation of Horizontal Displacement with Depth Below Model Keel.

Table 7.13: Comparison of Experimental Results and Various Soil Failure Mechanisms.

Theory	Model Face Pressures	Vertical Forces	Horizontal Forces	Total Stresses	Pore Pressures	Sub-Scour Ball Bearing Displacements	Sub-Scour Solder Strand Displacements	Densification
Terzaghi's Bearing Capacity Theory	Y	Y	N	Y	Y	Y	Y	Y
Meyerhof's Bearing Capacity Theory	Y	Y	N	Y	Y	Y	Y	Y
Rankine's Passive Earth Pressure Theory	Y	N	Y	N	N	N	N	Y
Coulomb's Passive Earth Pressure Theory	Y	N	Y	N	N	N	N	Y
Terzaghi's Passive Earth Pressure Theory	Y	N	Y	N	N	Y	Y	Y
Shields and Tolunay's Passive Earth Pressure Theory	Y	N	Y	N	N	Y	Y	Y
Harrison's Plate-Grouser Analysis	Y	N	Y	N	N	N	N	Y
Poorooshasb's (1990) Test Results	Y	Y	Y	Y	N	Y	Y	Y
Been's (1990) Test Results	?	?	?	?	?	Y	Y	?
Been's (1990) Keel Shear Dragging Mechanism	N/A	N/A	Y	Y	N	Y	Y	Y

Chapter 8

Summary and Conclusions

In order to further understand the ice scour process, an experimental program was conducted as part of this thesis work in an attempt to observe and monitor a scouring event under controlled conditions. Soil displacements and stress response in the soil were measured; forces and pressures on the model were monitored; and the effects of the inclusion of pore fluids were studied during the test series.

The model tests were conducted in a testbed of controlled density which was prepared in a tank by raining silica sand from a hopper. As the testbed was built-up layer by layer, the raining was stopped and instrumentation or displacement markers placed in the testbed at predetermined locations. The model iceberg was instrumented and attached to a gantry spanning the tank. The face of the model was inclined 15° from the horizontal. The model was driven through the testbed at a scour cut depth of 0.04 m, each run covering a distance of approximately 5 m.

Displacement markers and instrumentation in the testbed were located and excavated after each test. Post-scour positions were then recorded and displacements calculated. Scour profiles and density changes across the scour profile were also measured.

Results and observations allow several conclusions to be made:

1. There was a greater amount of infilling of sand behind the moving model during the tests in which the testbed was submerged as compared to the dry tests.

2. According to the scour profile measurements, some densification of the sand occurred during the scour process. Since the sand was so loose initially, this was to be expected during the scour process.

3. The greatest pressures on the model occurred on the inclined face.

4. The vertical forces exerted on the testbed by the model were large enough in some cases to create a general shear bearing capacity failure. At the very least, it appears that a local shear bearing capacity failure occurred. This was determined by comparing calculated bearing capacity values to measured vertical loads and by observing the displacement (uplift) of the solder strands to the sides of the scour.

5. Maximum vertical loads exerted on the testbed by the model were 40 to 57 % less for the submerged tests. Maximum horizontal loads exerted on the testbed by the model were 29 to 43 % less for the submerged tests. Vertical forces acting on the model were typically 1 to 1.5 times the horizontal forces acting on the model (F_V = 1 to 1.5 F_H).

6. The successive failure surfaces observed during scouring are believed to have been caused by passive earth pressure failure of the soil in front of the model. Calculations of the passive earth resistance of the soil indicate that this process was feasible.

7. Stress and pore pressure increases beneath the scouring model were measured to a depth of 0.06 m or 1.5 scour cut depths below the model keel which was

to the extent of the measurements.

8. Displacements of markers in the testbed were measured up to 0.12 m below the model keel which was to the extent to which the measurements were taken. Horizontal displacements were much greater than the vertical displacements and the horizontal movements were attributed to the keel shear dragging mechanism as described by Been (1990).

Some of the results obtained from this testing program are similar to those obtained from other testing programs and comparisons were made with these previous results. Similarities and general trends were observed between experimental programs.

The results from this testing program cannot be directly scaled to a full scale event due to the problems with geotechnical modelling in the laboratory as were described earlier. If these results were scaled to a prototype event, using relations to the critical-state or steady-state, the full scale prototype may or may not be realistic. Then, further analysis would have to be done to determine to what extent stresses, pore pressures, and displacements would be relevant to a full scale event.

Further research must be conducted in order to fully explore the ice scour process. Tests could be conducted at a centrifuge facility in order to correctly model the geotechnical process of scouring. If resources were unlimited, a great many tests could be conducted in which iceberg geometry, scour depths, pipeline burial depths (if model pipelines were included), and soil conditions along with many other parameters could be varied. This physical modelling could then be verified through an extensive field program in which the same parameters could be varied. However, due to physical and economical restraints, this type of extensive program would not be feasible and

a smaller scale field program would have to be conducted.

A limited number of centrifuge tests are currently being conducted on Cambridge University's beam centrifuge at an acceleration of 100 gravities (1:100 scale) and in kaolin clay. Data is being obtained on the effects of scouring, including changes in pore water pressure, soil deformations, and model pipeline deformations. This data will help to verify full scale subscour deformations. A numerical model is also being designed to analyse an ice/pipe/soil system. The results from the centrifuge modelling will be used to help calibrate this finite element model and then this model should be able to be used to hindcast the results of the 1-g tests, the centrifuge tests, and full scale field programs. The analytical model could then be used to determine safe trenching depths, backfilling methods, and the ice response to the same. With the proper inputs, the analytical model should then be able to predict the seabed and pipeline response in the field, making this model an invaluable and much-needed tool in the design of subsea installations for a cold ocean environment.

References

Abdelnour, R., Lapp, D., Haider, S., Shinde, S.B., and Wright, B. (1981). "Model Tests of Sea Bottom Scouring," *Proceedings, 6th International Conference on Port and Ocean Engineering under Arctic Conditions*, Québec City, Québec, pp. 688-705.

Abdelnour, R., and Graham, B. (1984). "Small Scale Tests of Sea Bottom Ice Scouring," *Proceedings, Ice Symposium*, International Association for Hydraulic Research, Hamburg, West Germany, pp. 267-279.

Andrier, B. (1981). "E.T.P.M. in Pipelaying and Burying Activities," *Proceedings, Symposium on Production and Transportation Systems for the Hibernia Discovery*, St. John's, Newfoundland, pp. 270-278.

Barnes, P.W., McDowell, D.M., and Reimnitz, E. (1978). *Ice Gouging Characteristics: Their Changing Patterns From 1975-1977, Beaufort Sea, Alaska*, United States Geological Survey Open-File Report 78-730, 42 p.

Barrie, J.V. (1980). "Iceberg-Seabed Interaction (Northern Labrador Sea)," *Annals of Glaciology*, Vol. 1, pp. 71-76.

Barrie, J.V., and Woodworth-Lynas, C.M.T. (1982). "Ice Scour: Methods of Analysis," *A Short Course on the Sediment Stability of Canadian Shelves*, ed. J.V. Barrie, C-CORE Publication 82-10, pp. 83-97.

Barrie, J.V., Collins, W.T., Clark, J.I., Lewis, C.F.M., and Parrott, D.R. (1986). "Submersible Observations and Origin of an Iceberg Pit on the Grand Banks of Newfoundland," *Current Research, Part A*, Geological Survey of Canada, Paper 86-1A, pp. 251-258.

Bass, D.W., and Peters, G.R. (1984). "Computer Simulations of Iceberg Instability," *Cold Regions Science and Technology*, Vol. 9, pp. 163-169.

Bass, D.W., and Woodworth-Lynas, C.M.T. (1988). "Iceberg Crater Marks on the Sea Floor, Labrador Shelf," *Marine Geology*, Vol. 79, pp. 243-260.

Been, K. (1990). "Mechanisms of Failure and Soil Deformation During Scouring," *Proceedings, Workshop on Ice Scouring and the Design of Offshore Pipelines*, Canada Oil and Gas Lands Administration, Calgary, Alberta, pp. 179-192.

Been, K., Kosar, K., Hachey, J., Rogers, B.T., and Palmer, A.C. (1990a). "Ice Scour Models," *Proceedings, 9th International Conference on Offshore Mechanics and Arctic Engineering*, Houston, Texas, Vol. V, pp. 179-188.

Been, K., Palmer, A., and Comfort, G. (1990b). *Analysis of Subscour Stresses and Probability of Ice Scour-Induced Damage for Buried Submarine Pipelines, Volume II, Deterministic Model of Ice-Soil-Pipe Interaction*, Report Prepared by Golder Associates Ltd., Andrew Palmer and Associates Ltd, and Fleet Technology Limited for Canada Oil and Gas Lands Administration, 204 p.

Bowles, J.E. (1977). *Foundation Analysis and Design*, Second Edition, McGraw-Hill Book Company, New York, New York, 750 p.

Brown, R.J., and Palmer, A.C. (1985). "Submarine Pipeline Trenching by Multipass Ploughs," *Proceedings, 17th Offshore Technology Conference*, Houston, Texas, Vol. 2, pp. 283-288.

Chari, T.R. (1975). "Some Geotechnical Aspects of Iceberg Grounding," *Ph.D. thesis*, Memorial University of Newfoundland, St. John's, Newfoundland, 181 p.

Chari, T.R., and Muthukrishaiah, K. (1975). "Iceberg Threat to Ocean Floor Structures," *Proceedings, Symposium on Ice Problems*, International Association for Hydraulic Research, Luleå, Sweden, pp. 421-435.

Chari, T.R., and Green, H.P. (1981). "Iceberg Scour Studies in Medium Dense Sands," *Proceedings, 6th International Conference on Port and Ocean Engineering under Arctic Conditions*, Québec City, Québec, Vol. 2, pp. 1012-1019.

Chen, W.F., and Scawthorn, C.R. (1970). "Limit Analysis and Limit Equilibrium Solutions in Soil Mechanics," *Soils and Foundations*, Vol. 10, No. 3, pp. 13-49.

Clark, J.I., and Landva, J. (1986). "The Controlling Factors of Ice-Created Seabed Features Related to Production Systems in Canadian Cold Oceans," *Proceedings, Polartech '86, International Offshore and Navigation Conference and Exhibition*, Espoo, Finland, Vol. 2, pp. 565-582.

Clark, J.I., and Landva, J. (1988). "Geotechnical Aspects of Seabed Pits in the Grand Banks Area," *Canadian Geotechnical Journal*, Vol. 25, pp. 448-454.

Comfort, G., Abdelnour, R., Trak, B., Menon, B., and Graham, B. (1982). "Lake Erie Ice Scour Investigation," *Proceedings, Workshop on Ice Scouring*, National Research Council, Montebello, Québec, pp. 55-99.

Comfort, G., and Graham, B. (1986). *Evaluation of Sea-Bottom Ice Scour Models*, Environmental Studies Revolving Funds Report No. 037, Ottawa, Ontario, 71 p.

Craig, R.F. (1987). *Soil Mechanics*, Fourth Edition, Van Nostrand Reinhold (International), London, England, 410 p.

d'Apollonia, S.J., and Lewis, C.F.M. (1981). *Iceberg Scour Data Maps for the Grand Banks of Newfoundland Between 46° N and 48° N*, Geological Survey of Canada, Open-File Report.

Darwin, C. (1855). "On the Power of Icebergs to Make Rectilinear, Uniformly-Directed Grooves Across a Submarine Undulatory Surface," *London, Edinburgh, and Dublin Philosophical Magazine and Journal of Science*, Vol. 10, pp. 96-98.

Das, B.M. (1985). *Principles of Geotechnical Engineering*, PWS-Kent Publishing Company, Boston, Massachusetts, 571 p.

deVries, J. (1981). "An Offshore Seabottom Excavation System," *Proceedings, Symposium on Production and Transportation Systems for the Hibernia Discovery*, St. John's, Newfoundland, pp. 212-222.

Dinsmore, R.P. (1972). "Ice and Its Drift Into the North Atlantic Ocean," *Proceedings, Symposium on Environmental Conditions in the Northwest Atlantic, 1960-1969*, ICNAF Special Publication No. 8, pp. 89-128.

Dredge, L.A. (1982). "Relict Ice-Scour Marks and Late Phases of Lake Agassiz in Northernmost Manitoba," *Canadian Journal of Earth Science*, Vol. 19, pp. 1079-1087.

Dunwoody, A.B., Losch, J.A., and Been, K. (1984). "Ice/Berm Interactions," *Proceedings, 16th Annual Offshore Technology Conference*, Houston, Texas, pp. 223-229.

Fader, G.B., and King, L.H. (1981). "A Reconnaissance Study of the Surficial Geology of the Grand Banks of Newfoundland," *Current Research, Part A*, Geological Survey of Canada, Paper 81-1A, pp. 45-56.

FENCO - Foundation of Canada Engineering Corporation Limited (1975). *An Analytical Study of Ice Scour on the Sea Bottom,* Report for the Arctic Petroleum Operators Association, APOA Project No. 69, 241 p.

Gaskill, H., and Lewis, C.F.M. (1988). "On the Spatial Frequency of Linear Ice Scours on the Seabed," *Cold Regions Science and Technology*, No. 15, pp. 107-130.

Gibson, C.E. (1981). "Underwater Trench Production Systems," *Proceedings, Symposium on Production and Transportation Systems for the Hibernia Discovery*, St. John's, Newfoundland, pp. 223-237.

Grass, J.D. (1982). "Lake Erie Cable Crossing - Ice Scour Study," *Proceedings, Workshop on Ice Scouring*, National Research Council, Montebello, Québec, pp. 1-10.

Green, H.P. (1984). "Geotechnical Modelling of Iceberg-Seabed Interaction," *M.Eng. thesis*, Memorial University of Newfoundland, St. John's, Newfoundland, 165 p.

Gustajtis, K.A. (1979). *Iceberg Population Distribution Study in the Labrador Sea*, C-CORE Data Report 79-8, 41 p.

Harris, I. McK. (1974). "Iceberg Marks on the Labrador Shelf," *Offshore Geology of Eastern Canada*, Geological Survey of Canada, Paper No. 74-30, Vol. 1, pp. 97-101.

Harrison, W.L. (1972). *Soil Failure Under Inclined Loads*, Cold Regions Research & Engineering Laboratory, Hanover, New Hampshire, DA Proj. 1T062112A130.

Hnatiuk, J., and Wright, B.D. (1983). "Sea Bottom Scouring in the Canadian Beaufort Sea," *Proceedings, 15th Annual Offshore Technology Conference*, Houston, Texas, Vol. 3, pp. 35-40.

King, E.L., and Gillespie, R.T. (1982). "Regional Iceberg Scour Distribution and Variability on the Eastern Canadian Continental Shelf," *Ice Scour and Seabed Engineering*, Environmental Studies Revolving Funds Report, No. 049, eds. C.F.M. Lewis, D.R. Parrott, P.G. Simpkin, and J.T. Buckley, Ottawa, Ontario, pp. 172-181.

King, L.H. (1976). "Relict Iceberg Furrows on the Laurentian Channel and Western Grand Banks," *Canadian Journal of Earth Sciences*, Vol. 13, pp. 1082-1092.

Kovacs, A., and Mellor, M. (1974). "Sea Ice Morphology and Ice as a Geological Agent in the Southern Beaufort Sea," *The Coast and Shelf of the Beaufort Sea*, eds. J.C. Reed, and J.E. Sater, Arctic Institute of North America, Arlington, Virgina, Vol. 2, pp. 113-161.

Lewis, C.F.M. (1977). "The Frequency and Magnitude of Drift Ice Groundings from Ice-Scour Tracks in the Canadian Beaufort Sea," *Proceedings, 4th International Conference on Port and Ocean Engineering under Arctic Conditions*, St. John's, Newfoundland, Vol. 1, pp. 568-576.

Lewis, C.F.M., and Barrie, J.V. (1981). "Geological Evidence of Iceberg Groundings and Related Seafloor Process in the Hibernia Discovery Area of Grand Bank, Newfoundland," *Proceedings, Symposium on Production and Transportation Systems for the Hibernia Discovery*, St. John's, Newfoundland, pp. 146-177.

Lewis, C.F.M., and Blasco, S.M. (1990). "Character and Distribution of Sea-Ice and Iceberg Scours," *Proceedings, Workshop on Ice Scouring and the Design of Offshore Pipelines*, Canada Oil and Gas Lands Administration, Calgary, Alberta, pp. 57-101.

Meyerhof, G.G. (1951). "The Ultimate Bearing Capacity of Foundations," *Géotechnique*, Vol. 2, pp. 301-332.

Meyerhof, G.G. (1963). "Some Recent Research on the Bearing Capacity of Foundations," *Canadian Geotechnical Journal*, Vol. 1, No. 1, pp. 16-26.

Morgenstern, N.R., and Sterne, K. (1980). *Soil Stabilization for Protection of Sea-Bed Structures from Ice Scour,* Report for Boreal Institute for Northern Studies, University of Alberta, Edmonton, Alberta, 35 p.

Murray, J.E. (1969). "The Drift, Deterioration and Distribution of Icebergs in the North Atlantic Ocean," *Proceedings, Ice Seminar*. Canadian Institute of Mining and Metallurgy, Special Vol. 10, pp. 3-18.

Nadreau, T.P. (1986). "Survey of Physical and Mechanical Properties of Icebergs," *Proceedings, Workshop on Extreme Ice Features*, National Research Council of Canada, Banff, Alberta, pp. 155-192.

Nessim, M.A., and Jordan, I.J. (1985). "Protection of Arctic Submarine Pipelines against Ice Scour," *Proceedings, 4th International Offshore Mechanics and Arctic Engineering Symposium*, Dallas, Texas, Vol. 1, pp. 610-617.

Noble, P.G., and Comfort, G. (1980). "Damage to an Underwater Pipeline by Ice Ridges," *Proceedings, 1st Workshop on Sea Ice Ridging and Pile-Up*, National Research Council, Calgary, Alberta, pp. 248-284.

NORDCO (1975). *Icebergs: A Brief Outline*, St. John's, Newfoundland, 23 p.

O'Donnell, J.P. (1976). "Polar Gas Tunnels Designed to Protect Arctic Pipelines from Ice Scours," *Offshore*, Vol. 36, No. 8, pp. 72-75.

Palmer, A.C., Brown, R.T., and Baudais, D.J. (1979). "Design and Installation of an Offshore Flowline for the Canadian Arctic Islands," *Proceedings, 11th Offshore Technology Conference*, Houston, Texas, pp. 765-772.

Palmer, A. (1990). "Design of Marine Pipelines in Seabed Vulnerable to Ice Scour," *Proceedings, Workshop on Ice Scouring and the Design of Offshore Pipelines*, Canada Oil and Gas Lands Administration, Calgary, Alberta, pp. 167-178.

Pelletier, B.R., and Shearer, J.M. (1972). "Sea Bottom Scouring in the Beaufort Sea of the Arctic Ocean," *Proceedings, 24th International Geological Congress*, Montreal, Québec, Section 8, pp. 251-261.

Poorooshasb, F., Clark, J.I., and Woodworth-Lynas, C.M.T. (1989). "Small Scale Modelling of Iceberg Scouring of the Seabed," *Proceedings, 10th International Conference on Port and Ocean Engineering under Arctic Conditions*, Luleå, Sweden, Vol. I, pp. 133-145.

Poorooshasb, F. (1990). *Analysis of Subscour Stresses and Probability of Ice Scour-Induced Damage for Buried Submarine Pipelines, Volume IV, Large Scale Laboratory Test of Seabed Scour*, Report Prepared by the Centre for Cold Ocean Resources Engineering (C-CORE) for Canada Oil and Gas Lands Administration, 168 p.

Poorooshasb, F., and Clark, J.I. (1990). "On Small Scale Ice Scour Modelling," *Proceedings, Workshop on Ice Scouring and the Design of Offshore Pipelines*, Canada Oil and Gas Lands Administration, Calgary, Alberta, pp. 193-235.

Prasad, K.S.R. (1985). "Analytical and Experimental Modelling of Iceberg Scours," *M.Eng. thesis*, Memorial University of Newfoundland, St. John's, Newfoundland, 170 p.

Rearic, D.M. (1982). *Temporal and Spatial Character of Newly Formed Ice Gouges in Harrison Bay, Alaska, 1977-1982*, United States Department of the Interior Geological Survey, Open-File Report 86-391, 52 p.

Reimnitz, E., and Barnes, P.W. (1974). "Sea Ice as a Geologic Agent on the Beaufort Sea Shelf of Alaska," *The Coast and Shelf of the Beaufort Sea*, eds. J.C. Reed, and J.E. Sater, Arctic Institute of North America, Arlington, Virgina, pp. 301-351.

Selig, E.T., and Nelson, R.D. (1964). "Observations of Soil Cutting with Blades," *Journal of Terramechanics*, Vol. 1, No. 3, pp. 32-53.

Shearer, J., and Blasco, S. (1975). "Further Observations of the Scouring Phenomena in the Beaufort Sea," *Report of Activities, Part A*, Geological Survey of Canada, Paper 75-1A, pp. 483-493.

Shields, D.H., and Tolunay, A.Z. (1973). "Passive Pressure Coefficients by Method of Slices," *Journal of the Soil Mechanics and Foundations Division*, ASCE, Vol. 99, No. SM12, pp. 1043-1053.

Siemens, J.C. (1963). "Mechanics of Soil Under the Influence of Model Tillage Tools," *Ph.D. thesis*, University of Illinois at Urbana, 139 p.

Terzaghi, K., and Peck, R.B. (1967). *Soil Mechanics in Engineering Practice*, Second Edition, John Wiley and Sons, New York, New York, 729 p.

Timmermans, W.J. (1981). "Design, Installation and Operation of Gathering and Transmission Pipelines for the Hibernia Field," *Proceedings, Symposium on Production and Transportation Systems for the Hibernia Discovery*, St. John's, Newfoundland, pp. 238-252.

Venkatesh, S., and El-Tahan, M. (1988). "Iceberg Life Expectancies in the Grand Banks and Labrador Sea," *Cold Regions Science and Technology*, No. 15, pp. 1-11.

Vesić, A.S. (1973). "Analysis of Ultimate Loads of Shallow Foundations," *Journal of the Soil Mechanics and Foundations Division*, ASCE, Vol. 99, No. SM1, pp. 45-73.

Vesić, A.S. (1975). "Bearing Capacity of Shallow Foundations," *Foundation Engineering Handbook*, eds. H.F. Winterkorn and H.Y. Fang, Van Nostrand Reinhold, New York, pp. 121-147.

Wadhams, P. (1975). *Sea Ice Morphology in the Beaufort Sea*, Beaufort Sea Project, Technical Report No. 36, Department of the Environment, Victoria, British Colombia, 66 p.

Weber, J.N. (1958). "Recent Grooving in Lake Bottom Sediments at Great Slave Lake, Northwest Territories," *Journal of Sedimentary Petrology*, Vol. 28, No. 3, pp. 333-341.

Weeks, W.F., Barnes, P.W., Rearic, D.M., and Reimnitz, E. (1983). *Statistical Aspects of Ice Gouging on the Alaskan Shelf of the Beaufort Sea*, CRREL Report 83-21, Cold Regions Research and Engineering Laboratory, Hanover, New Hampshire, 34 p.

Wheeler, J.D., and Wang, A.T. (1985). "Sea Ice Gouge Statistics," *Proceedings, 8th International Conference on Port and Ocean Engineering Under Arctic Conditions*, Narssarssuaq, Greenland, Vol. 1, pp. 408-418.

Woodworth-Lynas, C.M.T. (1983). *The Relative Age of Ice Scours Using Cross-Cutting Relationships*, Technical Report, C-CORE Publication No. 83-3, 54 p.

Woodworth-Lynas, C.M.T., and Barrie, J.V. (1985). "Iceberg Scouring Frequencies and Scour Degradation on Canada's Eastern Shelf Areas Using Sidescan Mosaic Remapping Techniques," *Proceedings, 8th International Conference on Port and Ocean Engineering Under Arctic Conditions*, Narssarssuaq, Greenland, Vol. 1, pp. 419-442.

Woodworth-Lynas, C.M.T., Day, T.E., Christian, D., and Seidel, M. (1985). "Surveying and Trenching an Iceberg Scour, King William Island, Arctic Canada," *Iceberg Research*, No. 10, pp. 3-8.

Woodworth-Lynas, C.M.T., Bass, D.W., and Bobbitt, J. (1986). *Inventory of Upslope and Downslope Iceberg Scouring*, Environmental Studies Revolving Funds Report No. 039, Ottawa, Ontario, 103 p.

Woodworth-Lynas, C.M.T., and Guigné, J.Y. (1990). "Iceberg Scours in the Geological Record: Examples From Glacial Lake Agassiz," *Glacimarine Environments: Processes and Sediments*, eds. J.A. Dowdeswell, and J.D. Scourse, Geological Society Special Publication No. 53, pp. 217-233.

Wright, B., Hnatiuk, J., and Kovacs, A. (1978). "Sea Ice Pressure Ridges in the Beaufort Sea," *Proceedings, 4th Symposium on Ice Problems*, International Association for Hydraulic Research, Luleå, Sweden, Part I, pp. 249-271.

Appendix A

Instrumentation Specifications and Calibrations

Total Stress Cells

Measurement	:	4 Strain Gauges
Configuration	:	Wheatstone Bridge
Range	:	0-400 kPa

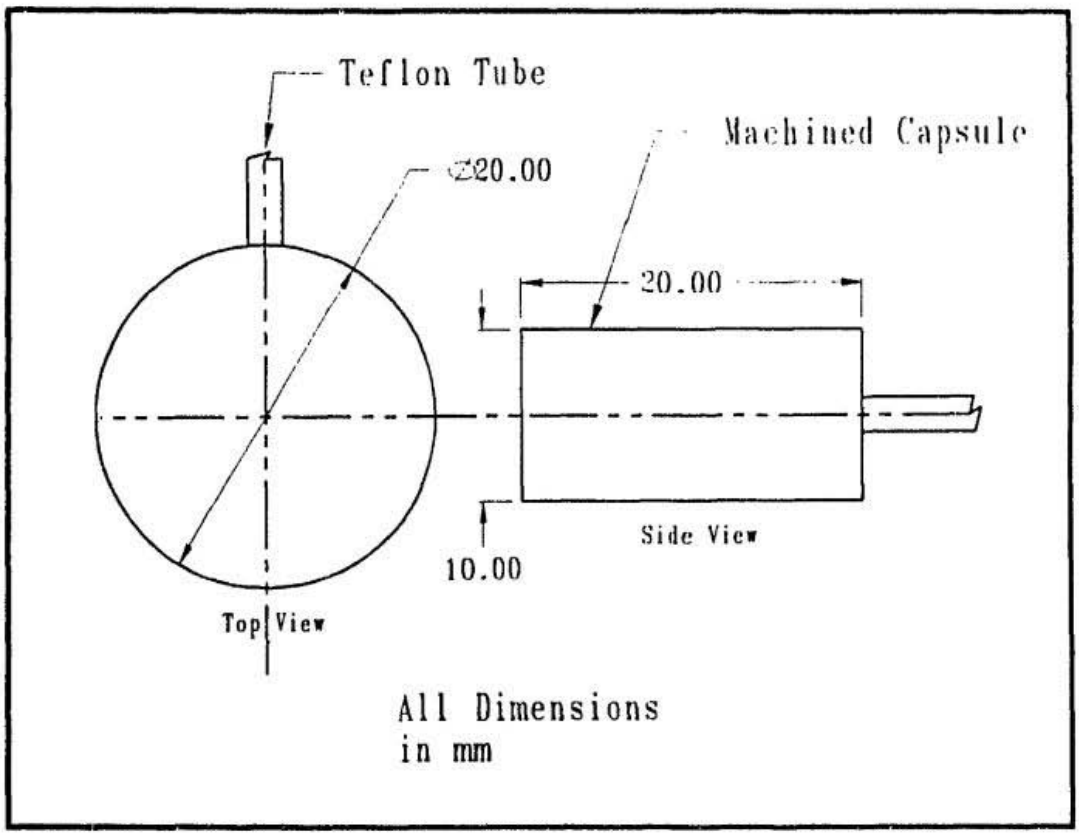

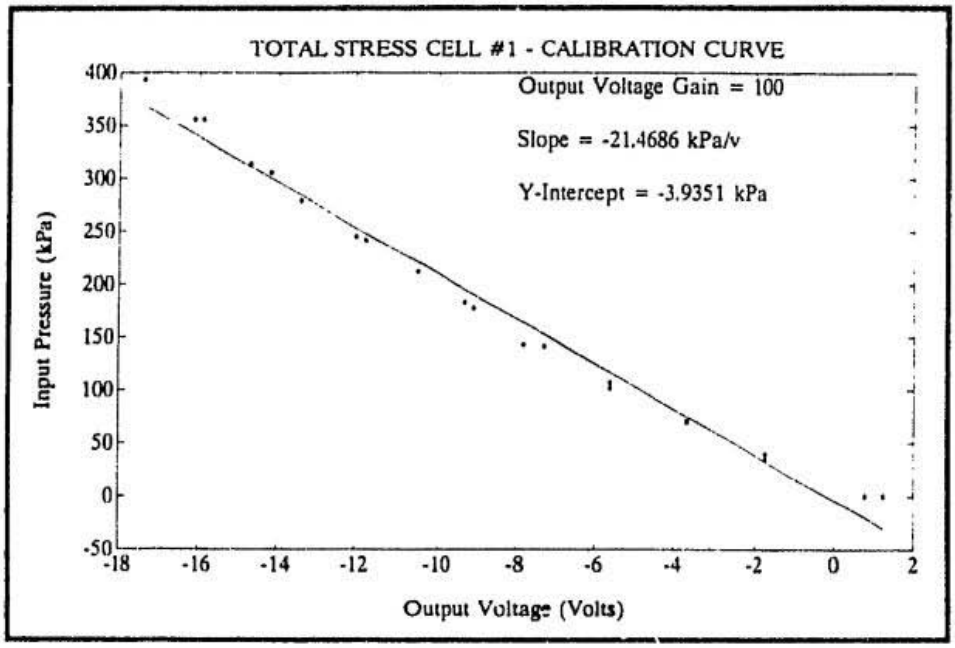
TOTAL STRESS CELL #1 - CALIBRATION CURVE
Output Voltage Gain = 100
Slope = -21.4686 kPa/v
Y-Intercept = -3.9351 kPa
Input Pressure (kPa)
400
350
300
250
200
150
100
50
0
-50
-18
-16
-14
-12
-10
-8
-6
-4
-2
0
2
Output Voltage (Volts)

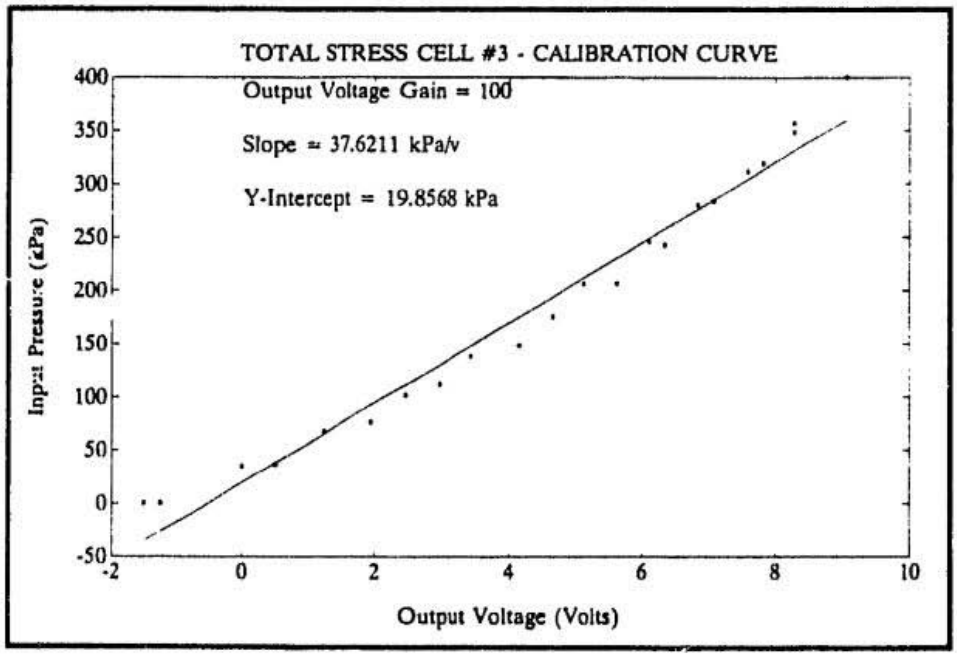
TOTAL STRESS CELL #3 - CALIBRATION CURVE
Output Voltage Gain = 100
Slope = 37.6211 kPa/v
Y-Intercept = 19.8568 kPa
Input Pressure (kPa)
400
350
300
250
200
150
100
50
0
-50
-2
0
2
4
6
8
10
Output Voltage (Volts)

Druck PDCR 81
Miniature Pore Pressure Transducer

Operating Pressure Ranges	:	0-35 and 0-105 kPa
Non-Linearity & Hysterisis	:	±0.2 % B.S.L.
Resolution	:	Infinite
Transduction Principle	:	Integrated Strain Gauge Bridge
Excitation Voltage	:	5 V DC or AC
Input Impedance	:	1000 ohms nominal
Output Voltage	:	35 and 50 mV
Output Impedance	:	1000 ohms nominal
Zero Offset	:	< ±10 mV standard
Operating Temperature Range	:	-20 to +120 °C
Weight, with cable	:	30 grams

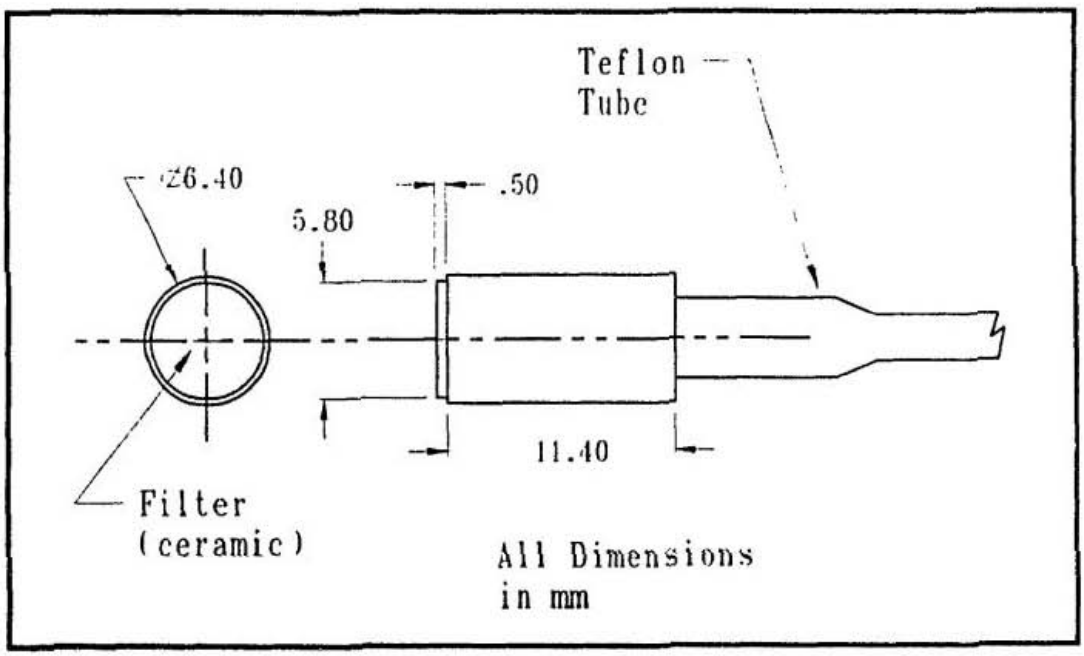

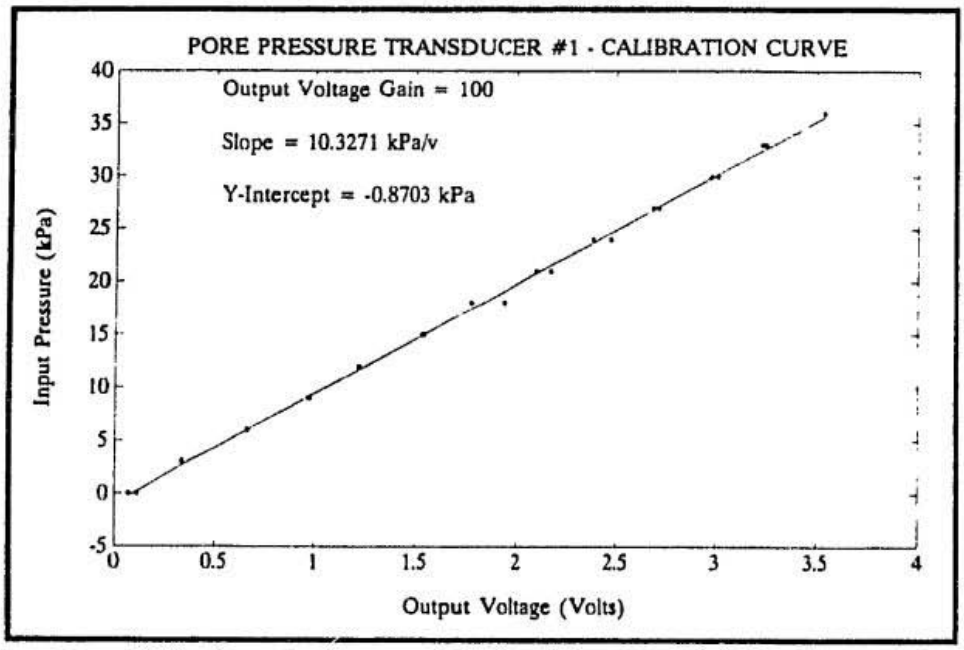
PORE PRESSURE TRANSDUCER #1 - CALIBRATION CURVE
Output Voltage Gain = 100
Slope = 10.3271 kPa/v
Y-Intercept = -0.8703 kPa
Input Pressure (kPa)
Output Voltage (Volts)
40
35
30
25
20
15
10
5
0
-5
0
0.5
1
1.5
2
2.5
3
3.5
4

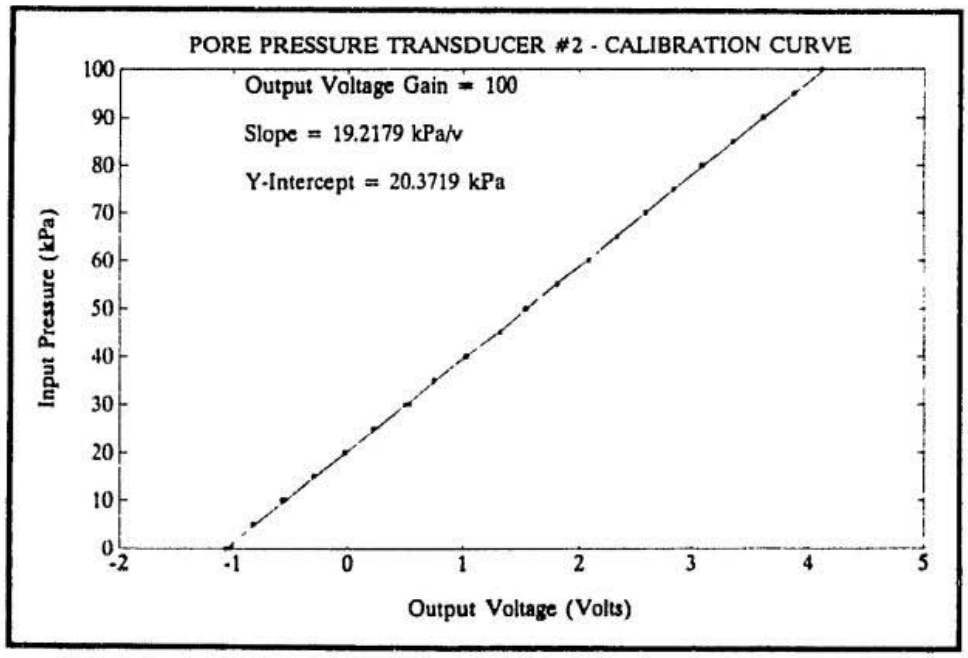
PORE PRESSURE TRANSDUCER #2 - CALIBRATION CURVE
Output Voltage Gain = 100
Slope = 19.2179 kPa/v
Y-Intercept = 20.3719 kPa
Input Pressure (kPa)
Output Voltage (Volts)
100
90
80
70
60
50
40
30
20
10
0
-2
-1
0
1
2
3
4
5

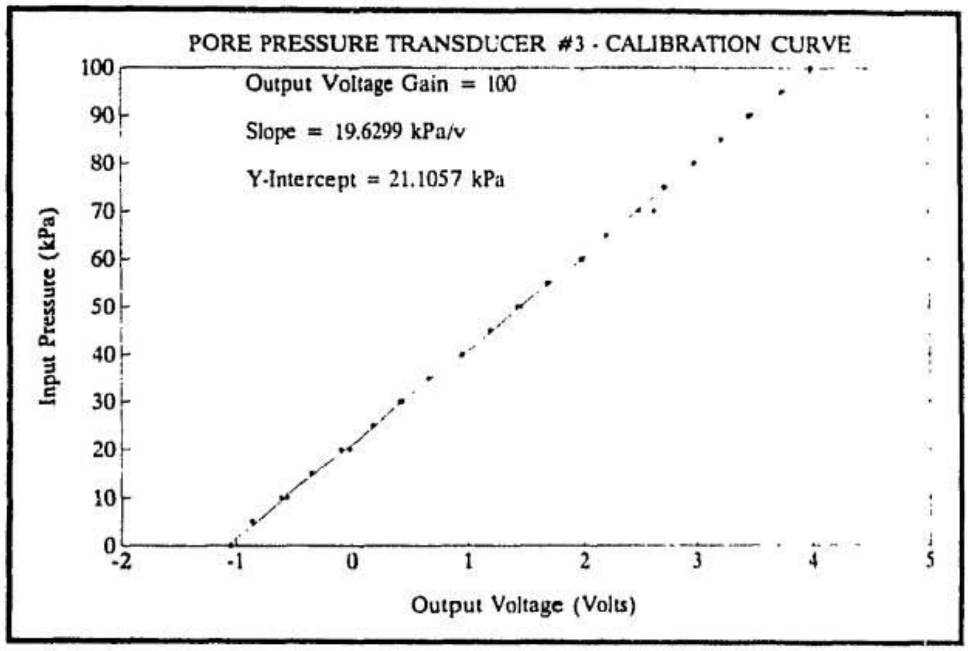
PORE PRESSURE TRANSDUCER #3 - CALIBRATION CURVE
Output Voltage Gain = 100
Slope = 19.6299 kPa/v
Y-Intercept = 21.1057 kPa
Input Pressure (kPa)
Output Voltage (Volts)
100
90
80
70
60
50
40
30
20
10
0
-2
-1
0
1
2
3
4
5

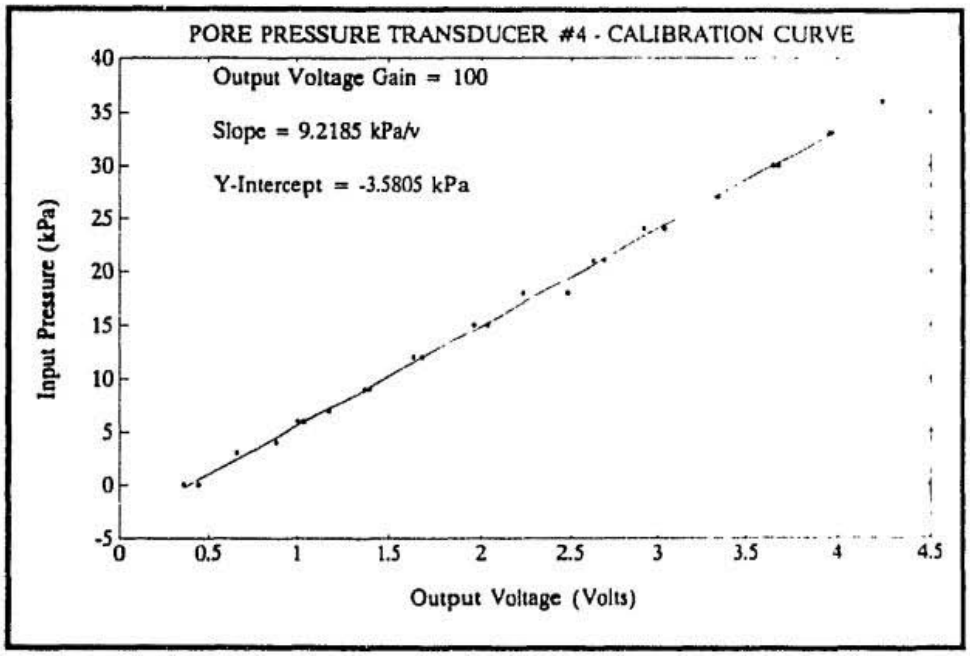
PORE PRESSURE TRANSDUCER #4 - CALIBRATION CURVE
Output Voltage Gain = 100
Slope = 9.2185 kPa/v
Y-Intercept = -3.5805 kPa
Input Pressure (kPa)
Output Voltage (Volts)
40
35
30
25
20
15
10
5
0
-5
0
0.5
1
1.5
2
2.5
3
3.5
4
4.5

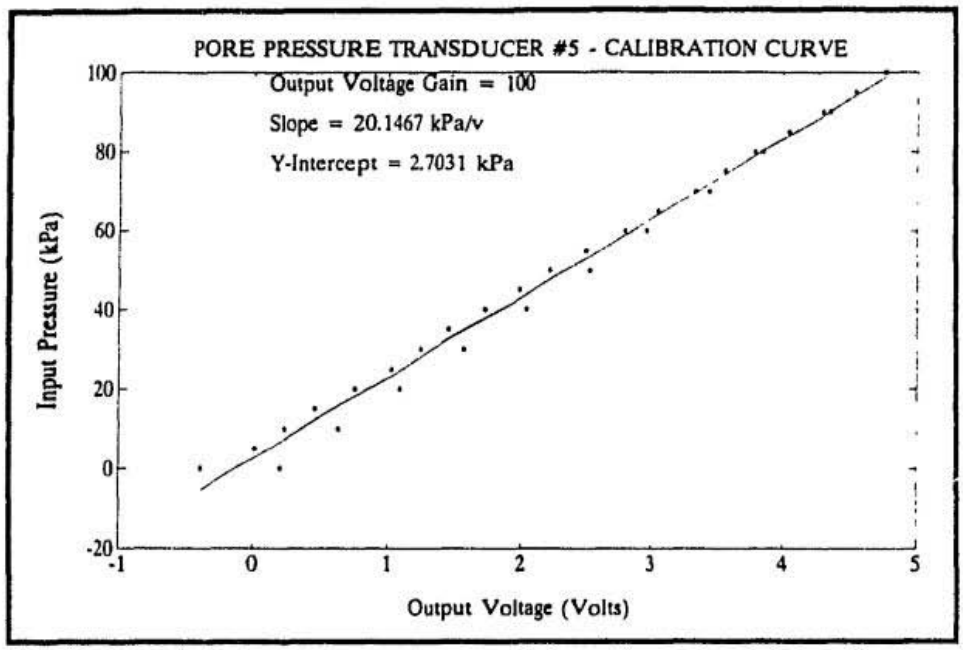
PORE PRESSURE TRANSDUCER #5 - CALIBRATION CURVE
Output Voltage Gain = 100
Slope = 20.1467 kPa/v
Y-Intercept = 2.7031 kPa
Input Pressure (kPa)
Output Voltage (Volts)
100
80
60
40
20
0
-20
-1
0
1
2
3
4
5

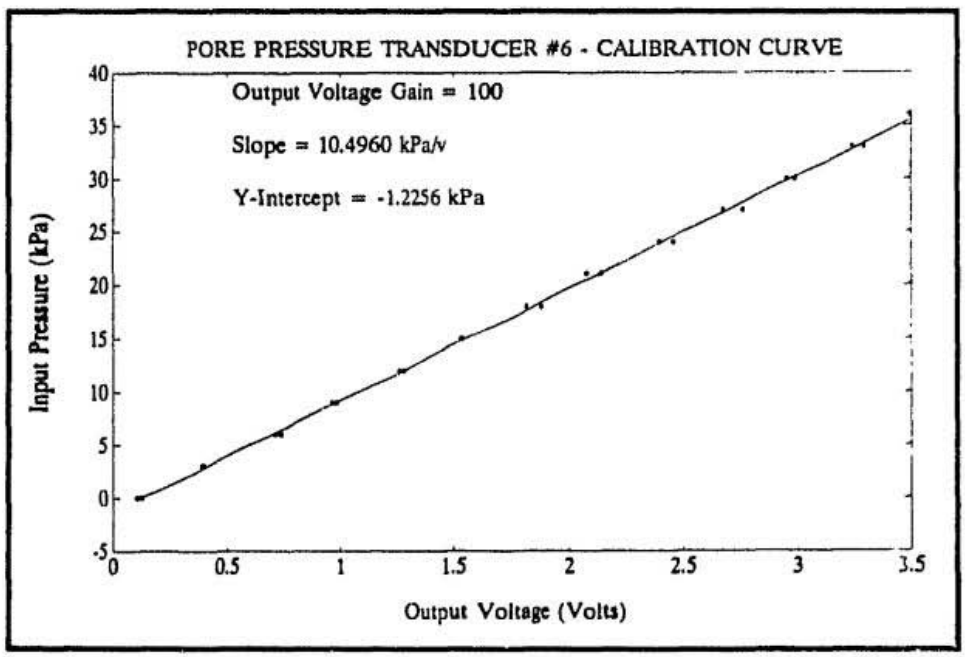
PORE PRESSURE TRANSDUCER #6 - CALIBRATION CURVE
Output Voltage Gain = 100
Slope = 10.4960 kPa/v
Y-Intercept = -1.2256 kPa
Input Pressure (kPa)
Output Voltage (Volts)
40
35
30
25
20
15
10
5
0
-5
0
0.5
1
1.5
2
2.5
3
3.5

Kistler Model 912
Quartz Dynamic Load Cell

Range: compression	:	5000 lbs
Range: tension	:	100 lbs
Resolution	:	0.002 lb
Overload	:	20 %
Sensitivity (nominal)	:	50 picocoulombs/lb
Linearity	:	±1 %
Capacitance (nominal)	:	58 picofarads
Temperature Range	:	-100 to +300 °F
Weight (approximate)	:	17 grams

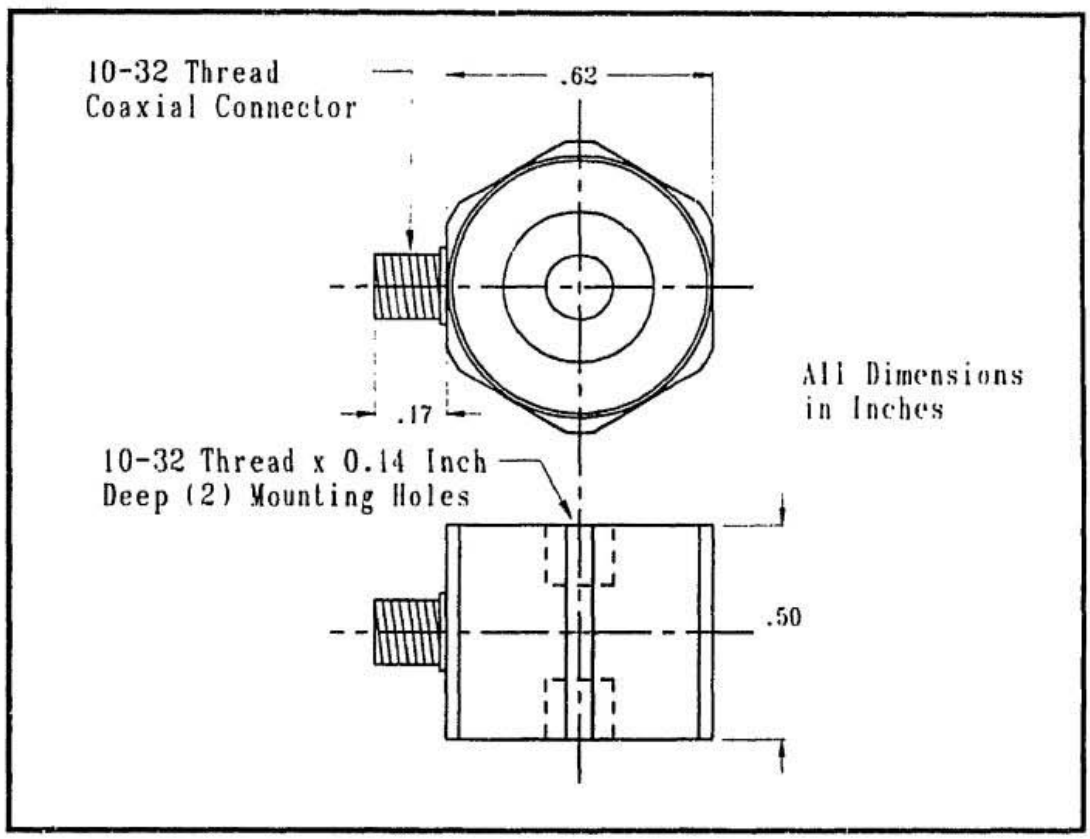

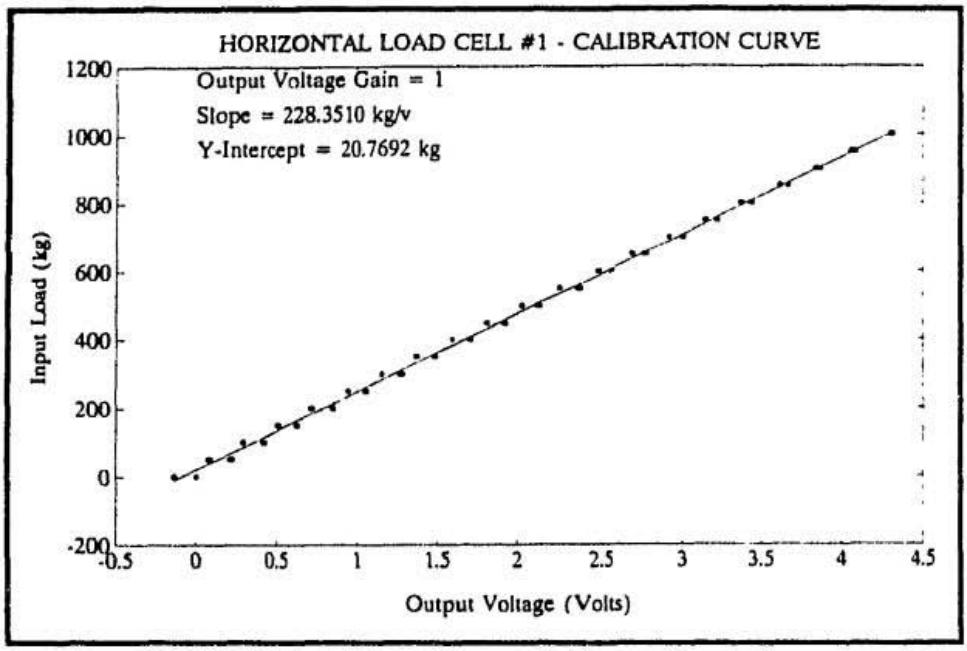
HORIZONTAL LOAD CELL #1 - CALIBRATION CURVE
Output Voltage Gain = 1
Slope = 228.3510 kg/v
Y-Intercept = 20.7692 kg
Input Load (kg)
1200
1000
800
600
400
200
0
-200
-0.5
0
0.5
1
1.5
2
2.5
3
3.5
4
4.5
Output Voltage (Volts)

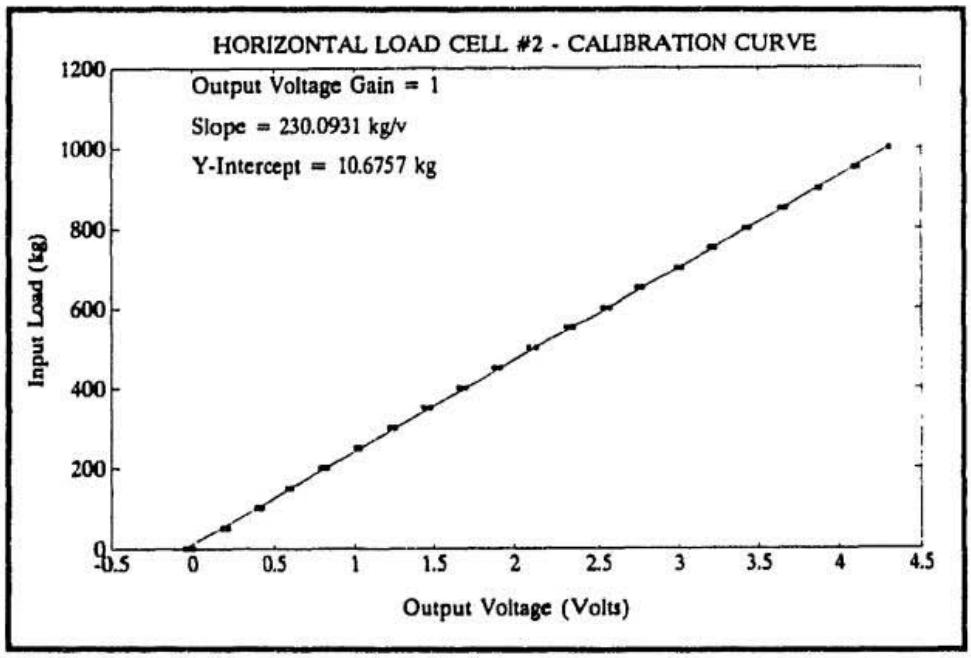
HORIZONTAL LOAD CELL #2 - CALIBRATION CURVE
Output Voltage Gain = 1
Slope = 230.0931 kg/v
Y-Intercept = 10.6757 kg
Input Load (kg)
1200
1000
800
600
400
200
0
-0.5
0
0.5
1
1.5
2
2.5
3
3.5
4
4.5
Output Voltage (Volts)

HBM 2.5K
Beam Load Cell

Rated Capacity	:	2500 lbs
Rated Output	:	3.0 ± 0.003 mV/V
Non-Linearity	:	0.03 %
Hysteresis	:	0.05 %
Non-Repeatability	:	0.01 %
Input Terminal Resistance	:	1000 ohms min.
Output Terminal Resistance	:	1000 ± 10 ohms
Excitation Voltage	:	15 V DC or AC rms max.
Maximum Load, Safe	:	150 %
Weight	:	2 lbs

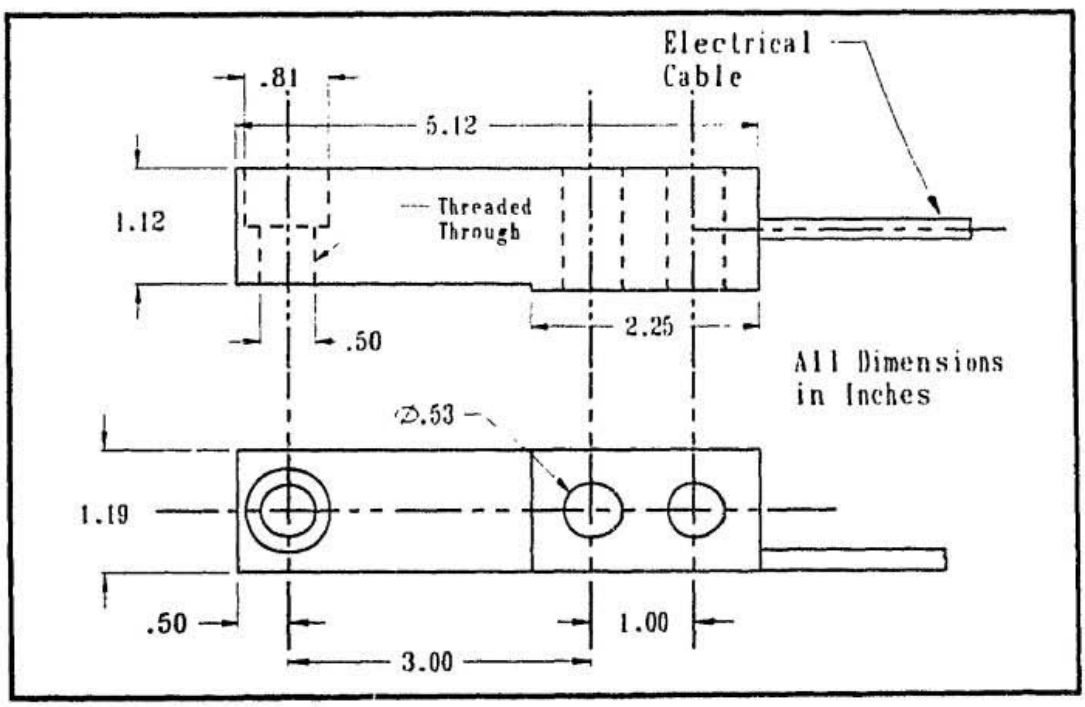

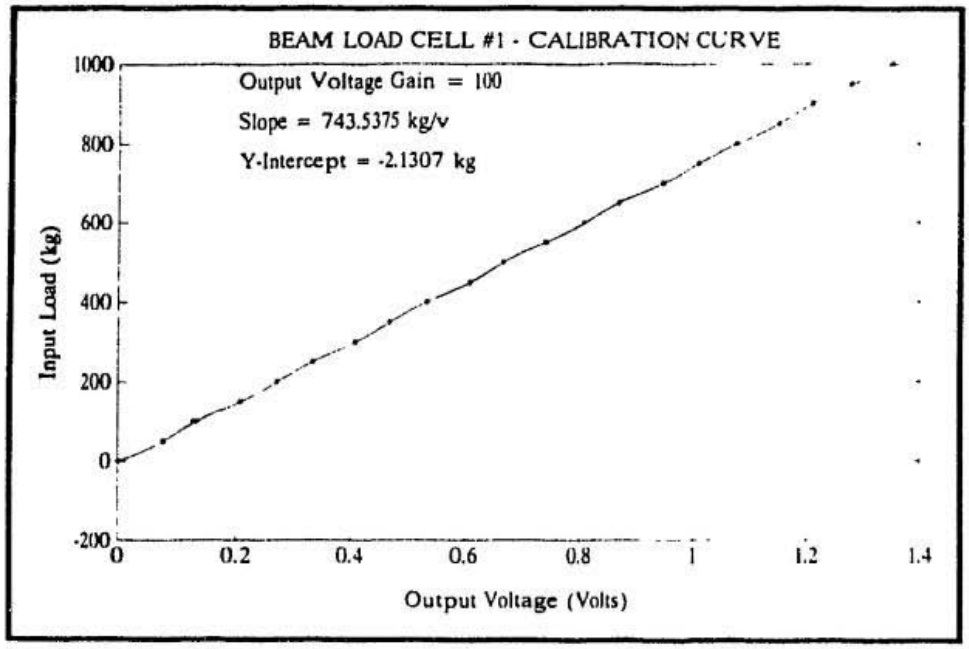
BEAM LOAD CELL #1 - CALIBRATION CURVE
Output Voltage Gain = 100
Slope = 743.5375 kg/v
Y-Intercept = -2.1307 kg
Input Load (kg)
1000
800
600
400
200
0
-200
0
0.2
0.4
0.6
0.8
1
1.2
1.4
Output Voltage (Volts)

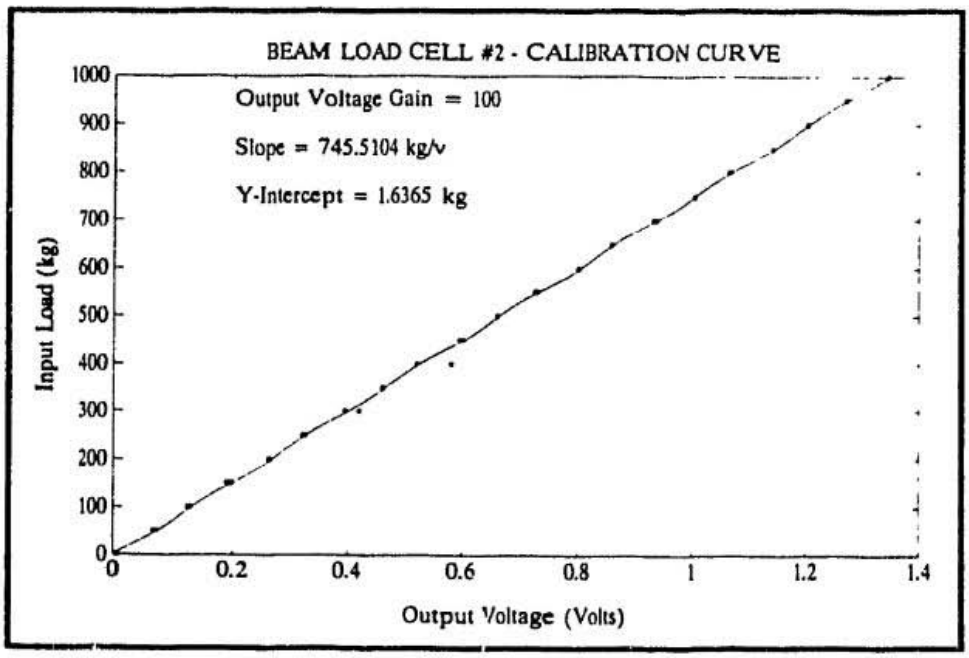
BEAM LOAD CELL #2 - CALIBRATION CURVE
Output Voltage Gain = 100
Slope = 745.5104 kg/v
Y-Intercept = 1.6365 kg
Input Load (kg)
1000
900
800
700
600
500
400
300
200
100
0
0
0.2
0.4
0.6
0.8
1
1.2
1.4
Output Voltage (Volts)

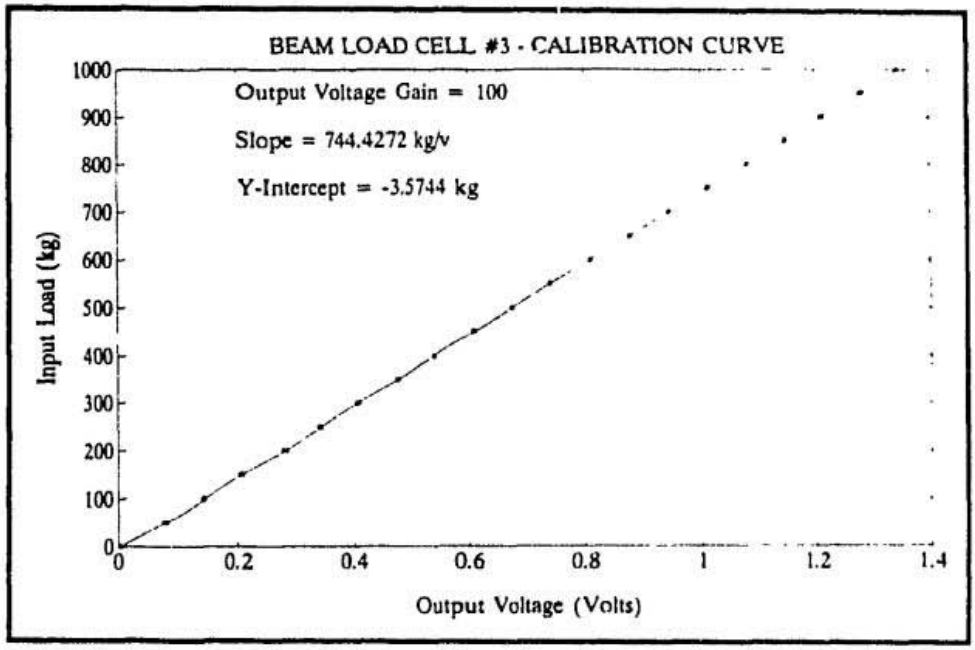
BEAM LOAD CELL #3 - CALIBRATION CURVE
Output Voltage Gain = 100
Slope = 744.4272 kg/v
Y-Intercept = -3.5744 kg
Input Load (kg)
1000
900
800
700
600
500
400
300
200
100
0
0
0.2
0.4
0.6
0.8
1
1.2
1.4
Output Voltage (Volts)

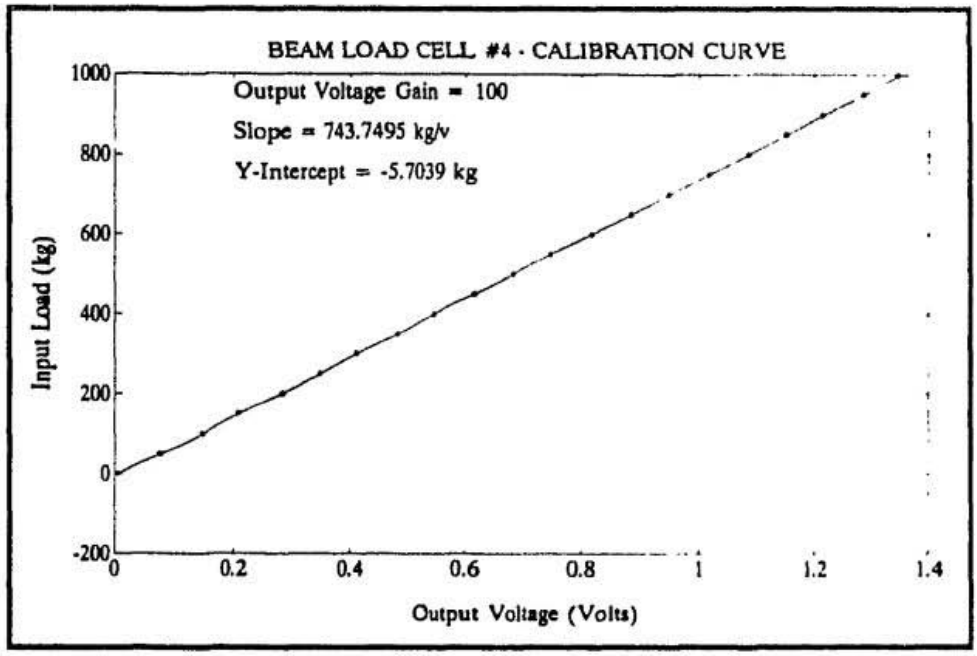
BEAM LOAD CELL #4 - CALIBRATION CURVE
Output Voltage Gain = 100
Slope = 743.7495 kg/v
Y-Intercept = -5.7039 kg
Input Load (kg)
1000
800
600
400
200
0
-200
0
0.2
0.4
0.6
0.8
1
1.2
1.4
Output Voltage (Volts)

HBM P11
Inductive Pressure Transducer

Measuring Range	:	0-5 bar
Natural Frequency of the Diaphragm	:	3.6 kHz
Nominal Sensitivity	:	8 mV/V
Linearity Error	:	$\leq \pm 1$ %
Nominal Energising Voltage	:	2.5 ± 5% V
Input Resistance	:	54 ohms
Input Inductance	:	14 mH
Nominal Temperature Range	:	-10° C to 80° C
Weight	:	105 g

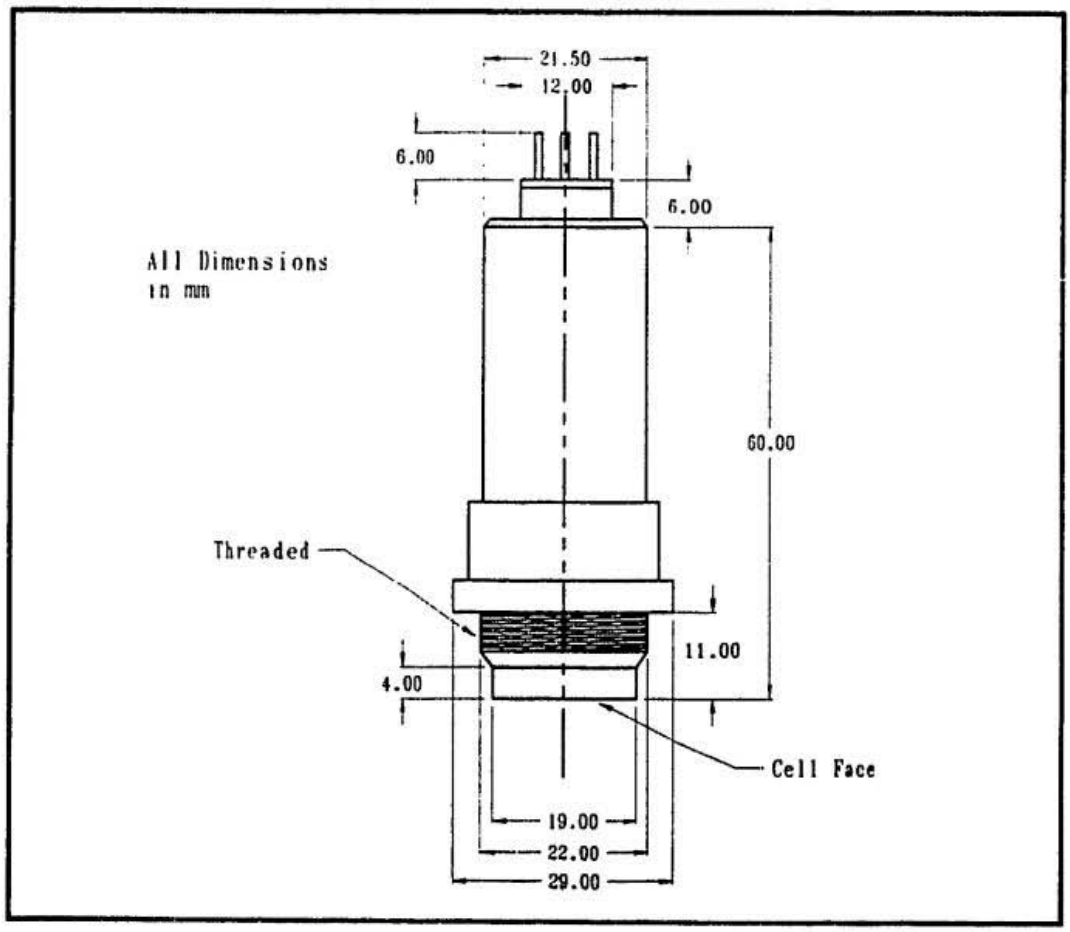

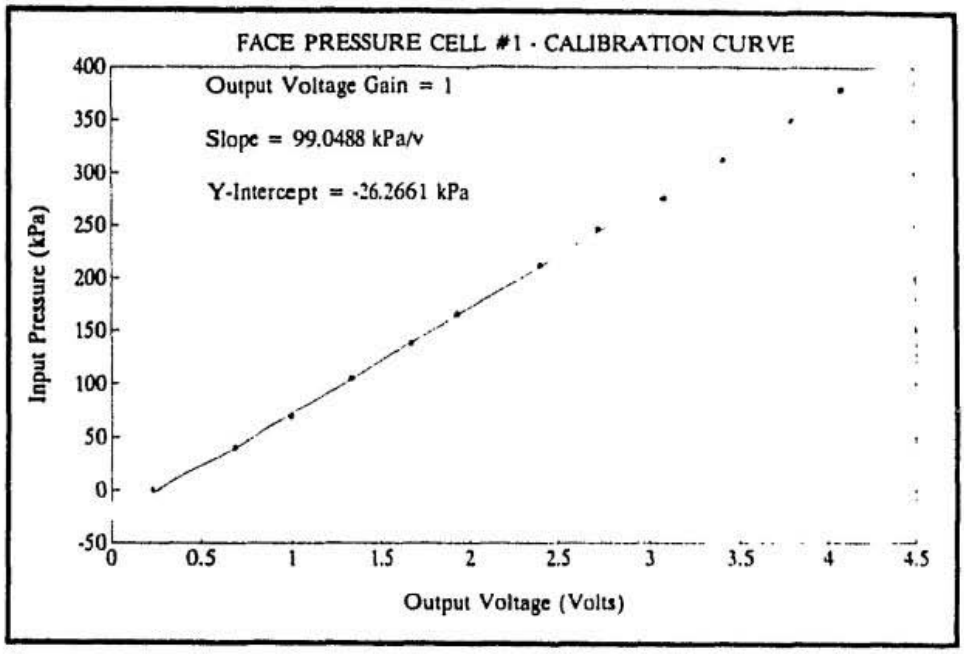
FACE PRESSURE CELL #1 - CALIBRATION CURVE
Output Voltage Gain = 1
Slope = 99.0488 kPa/v
Y-Intercept = -26.2661 kPa
Input Pressure (kPa)
400
350
300
250
200
150
100
50
0
-50
0
0.5
1
1.5
2
2.5
3
3.5
4
4.5
Output Voltage (Volts)

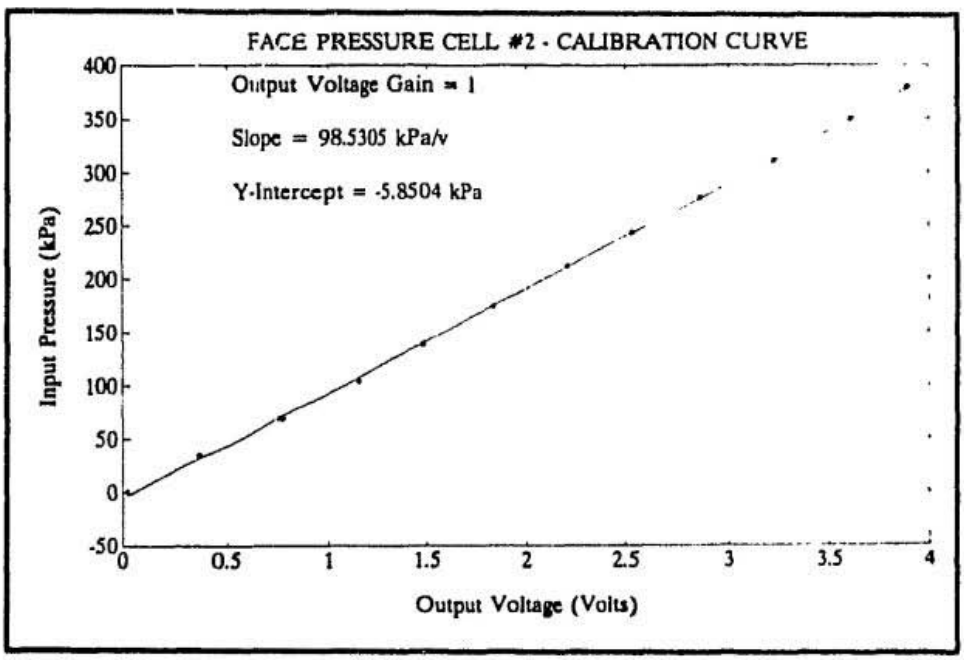
FACE PRESSURE CELL #2 - CALIBRATION CURVE
Output Voltage Gain = 1
Slope = 98.5305 kPa/v
Y-Intercept = -5.8504 kPa
Input Pressure (kPa)
400
350
300
250
200
150
100
50
0
-50
0
0.5
1
1.5
2
2.5
3
3.5
4
Output Voltage (Volts)

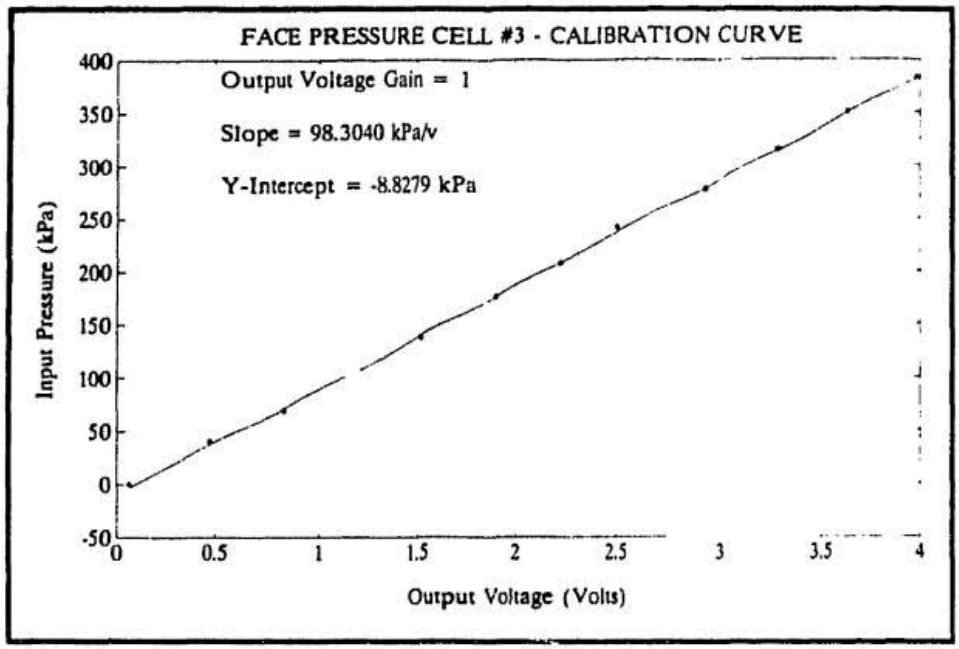
FACE PRESSURE CELL #3 - CALIBRATION CURVE
Output Voltage Gain = 1
Slope = 98.3040 kPa/v
Y-Intercept = -8.8279 kPa
Input Pressure (kPa)
400
350
300
250
200
150
100
50
0
-50
0
0.5
1
1.5
2
2.5
3
3.5
4
Output Voltage (Volts)

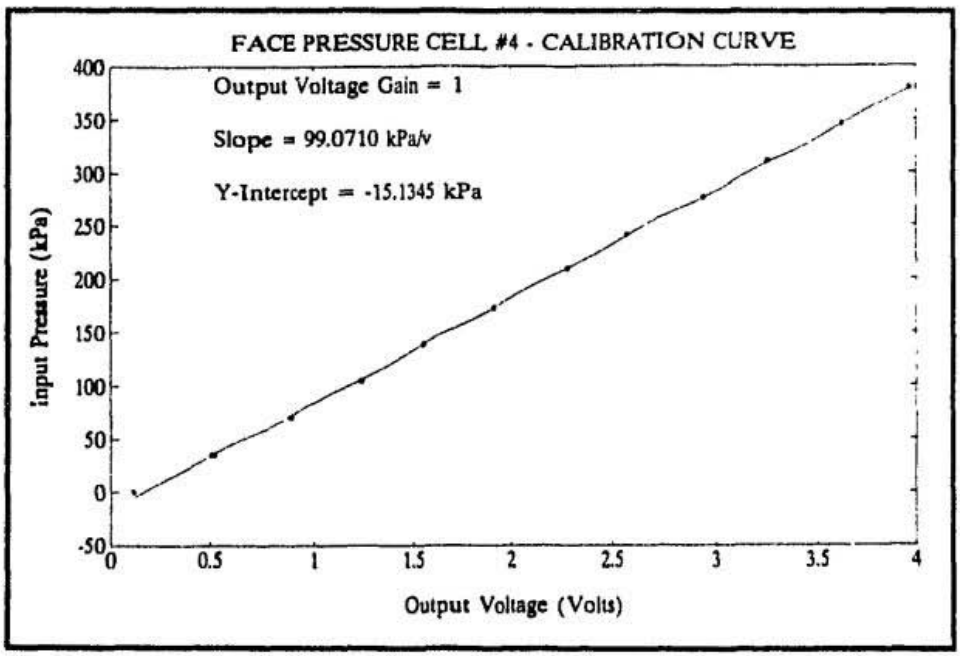
FACE PRESSURE CELL #4 - CALIBRATION CURVE
Output Voltage Gain = 1
Slope = 99.0710 kPa/v
Y-Intercept = -15.1345 kPa
Input Pressure (kPa)
400
350
300
250
200
150
100
50
0
-50
0
0.5
1
1.5
2
2.5
3
3.5
4
Output Voltage (Volts)

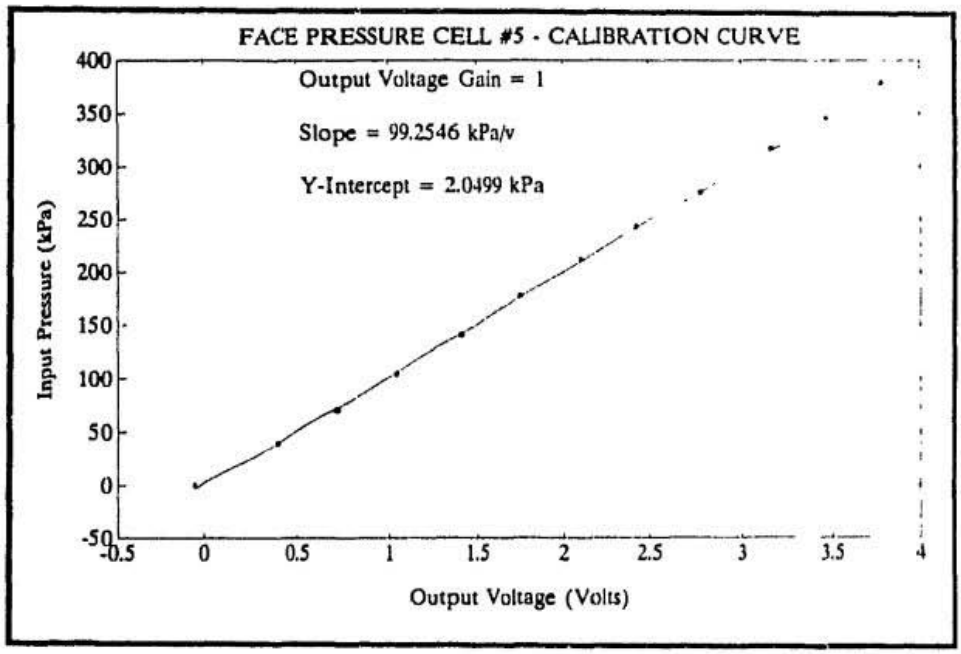
FACE PRESSURE CELL #5 - CALIBRATION CURVE
Output Voltage Gain = 1
Slope = 99.2546 kPa/v
Y-Intercept = 2.0499 kPa
Input Pressure (kPa)
400
350
300
250
200
150
100
50
0
-50
-0.5
0
0.5
1
1.5
2
2.5
3
3.5
4
Output Voltage (Volts)

Celesco PT101
Linear Position Displacement Transducer

GENERAL		
Range	:	0-2 to 0-750 inches
Weight	:	20 ounces (to 50 inch range)
Case Material	:	Aluminum
Sensing System	:	Precision Potentiometer
ELECTRICAL		
Input Resistance	:	500 ohms std.
Output Resistance	:	138 ohms max. std.
Excitation Voltage	:	25 volts max., AC or DC
PERFORMANCE		
Accuracy	:	±0.1 % F.S. typical
Resolution	:	0.008 % F.S. max.
Temperature Range	:	0° F to +200° F

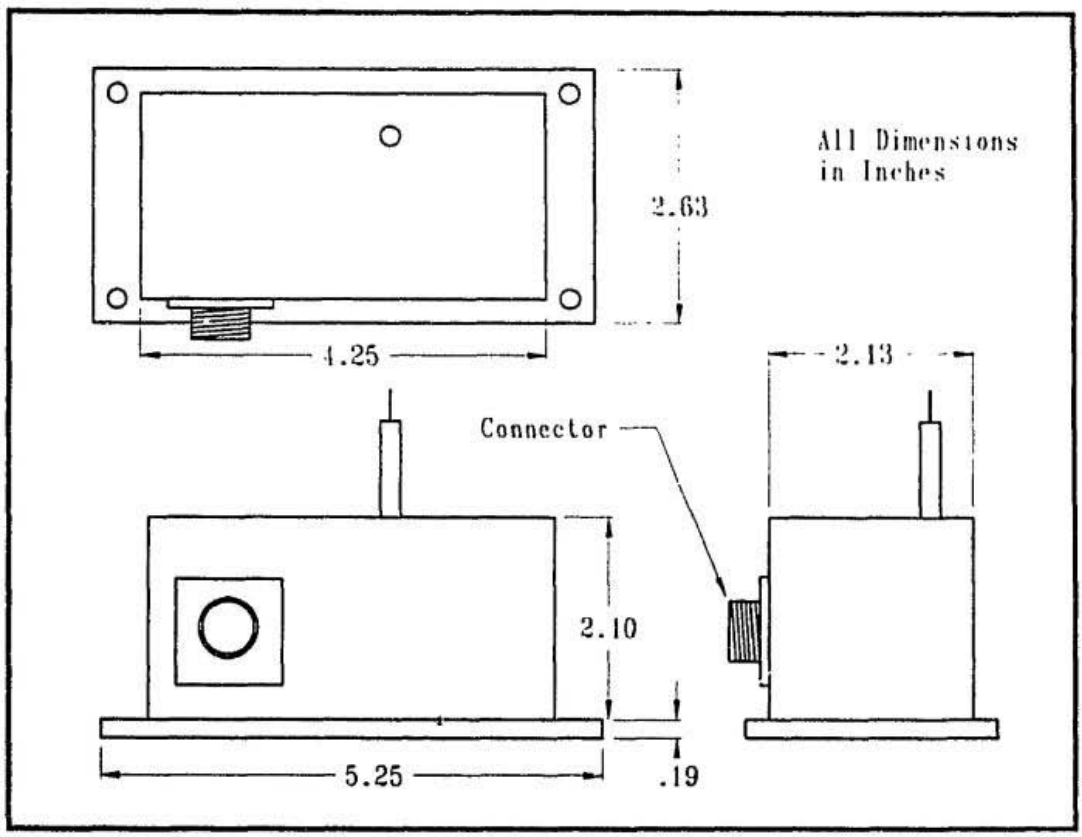
All Dimensions
in Inches
2.63
4.25
2.13
Connector
2.10
5.25
.19

MetraByte DAS-8 Data Acquisition and Control Interface Board

POWER CONSUMPTION		
+5 V supply	:	107 mA typical / 180 mA max.
+12 V supply	:	6 mA typical / 10 mA max.
-12 V supply	:	10 mA typical / 16 mA max.
ANALOG INPUTS		
Number of Channels	:	8, single ended
Resolution	:	12 bits (2.4 mV/bit)
Accuracy	:	0.01% of reading ±1 bit
Full Scale	:	±5 volts
Coding	:	Offset binary
A/D SPECIFICATION		
Type	:	Successive approximation
Resolution	:	12 bits
Linearity	:	±1 bit
Acquisition time	:	15 mSec

MetraByte EXP-16 Universal Expansion Interface

POWER CONSUMPTION		
+5 V current	:	20 mA typical, 30 mA max.
+12/+15 V current	:	8 mA typical, 10 mA max.
-12/-15 V current	:	8 mA typical, 10 mA max.
ANALOG DATA SPECIFICATIONS		
Analog Output Voltage	:	±5 Volts max.
Analog Output Current	:	20 mA max.
Gains	:	1000, 100, 10, 1
Non-Linearity	:	0.005 - 0.015 %
ENVIRONMENTAL		
Operating Temperature Range	:	0 to 60 Deg. C

Appendix B

Testbed Measurements

Testbed Density Measurements

Density Measurements - Test 1

Density Cup No.	X Coordinate (m)	Y Coordinate (m)	Z Coordinate (m)	Density ρ_d (kg/m^3)
1	0.0000	5.0000	0.0200	1366.4
2	0.7500	6.0000	0.0200	1367.0
3	0.0000	7.0000	0.0200	1359.0
4	-0.7500	8.0000	0.0200	1353.0
5	-0.2500	6.0000	0.0500	1360.9
6	0.0057	6.3224	0.2444	1390.6
7	-0.0019	6.3039	0.2848	1384.4
8	-0.1565	6.5906	0.3655	1381.7

Density Measurements - Test 2

Density Cup No.	X Coordinate (m)	Y Coordinate (m)	Z Coordinate (m)	Density ρ_d (kg/m^3)
1	0.2500	5.0000	0.0200	1372.1
2	0.0000	6.0000	0.0200	1354.7
3	-0.2500	7.0000	0.0200	1359.2
4	0.0000	8.0000	0.0200	1364.2
5	0.0000	5.5000	0.2600	1372.3
6	-0.1000	7.5000	0.2900	1380.1
7	0.0000	7.0000	0.3700	1367.4

Density Measurements - Test 3

Density Cup No.	X Coordinate (m)	Y Coordinate (m)	Z Coordinate (m)	Density ρ_d (kg/m^3)
1	-0.2500	5.0000	0.0200	1364.9
2	0.0000	6.0000	0.2000	1359.7
3	0.2500	7.0000	0.2000	1368.1
4	0.0000	8.0000	0.2000	1372.9
5	0.2500	6.0000	0.2500	1377.7
6	-0.2500	7.0000	0.2500	1376.3
7	-0.2500	5.6800	0.2700	1382.1
8	0.0000	6.5000	0.2900	1369.6
9	-0.5000	5.5000	0.2900	1378.1
10	0.0000	8.0000	0.3300	1350.2
11	-0.2500	5.0000	0.3300	1353.6
12	0.4829	5.5032	0.3641	1349.5
13	-0.7353	7.5219	0.3633	1348.7

Density Measurements - Test 4

Density Cup No.	X Coordinate (m)	Y Coordinate (m)	Z Coordinate (m)	Density ρ_d (kg/m^3)
1	0.0000	5.0000	0.0200	1385.2
2	-0.7500	6.0000	0.0200	1380.2
3	0.7500	7.0000	0.0200	1394.3
4	0.0000	8.0000	0.0200	1379.0
5	0.2500	5.0000	0.2500	1343.9
6	0.0000	7.0000	0.2500	1329.5
7	0.5000	5.5000	0.2900	1371.1
8	-0.5000	7.5000	0.2900	1350.7
9	-0.2500	5.5000	0.3400	1374.6
10	-0.2500	7.5000	0.3400	1362.5
11	-0.2500	5.5000	0.3700	1347.5
12	-0.2500	7.5000	0.3700	1348.3

Density Cup Positions

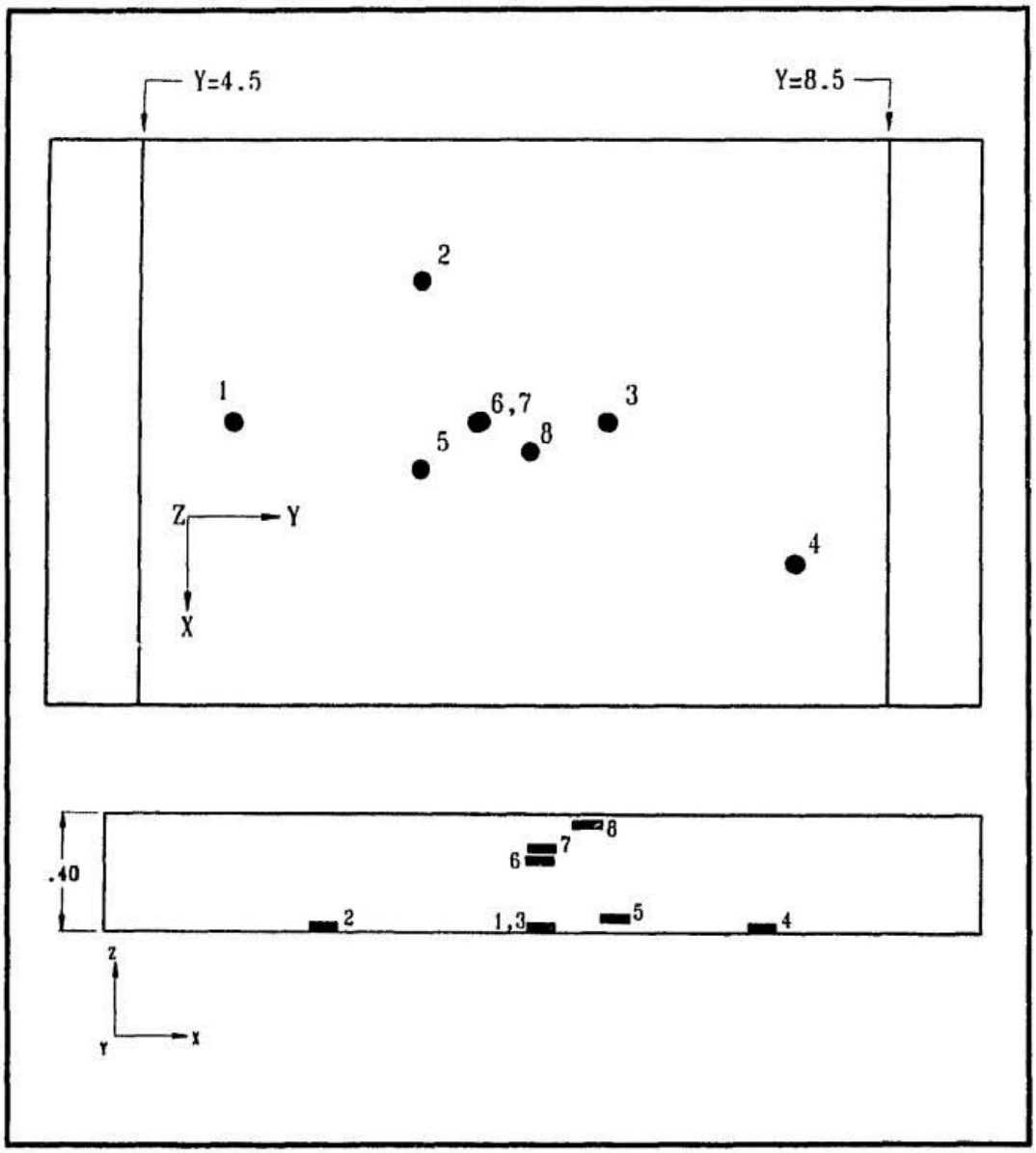

Density Cup Positions - Test 1

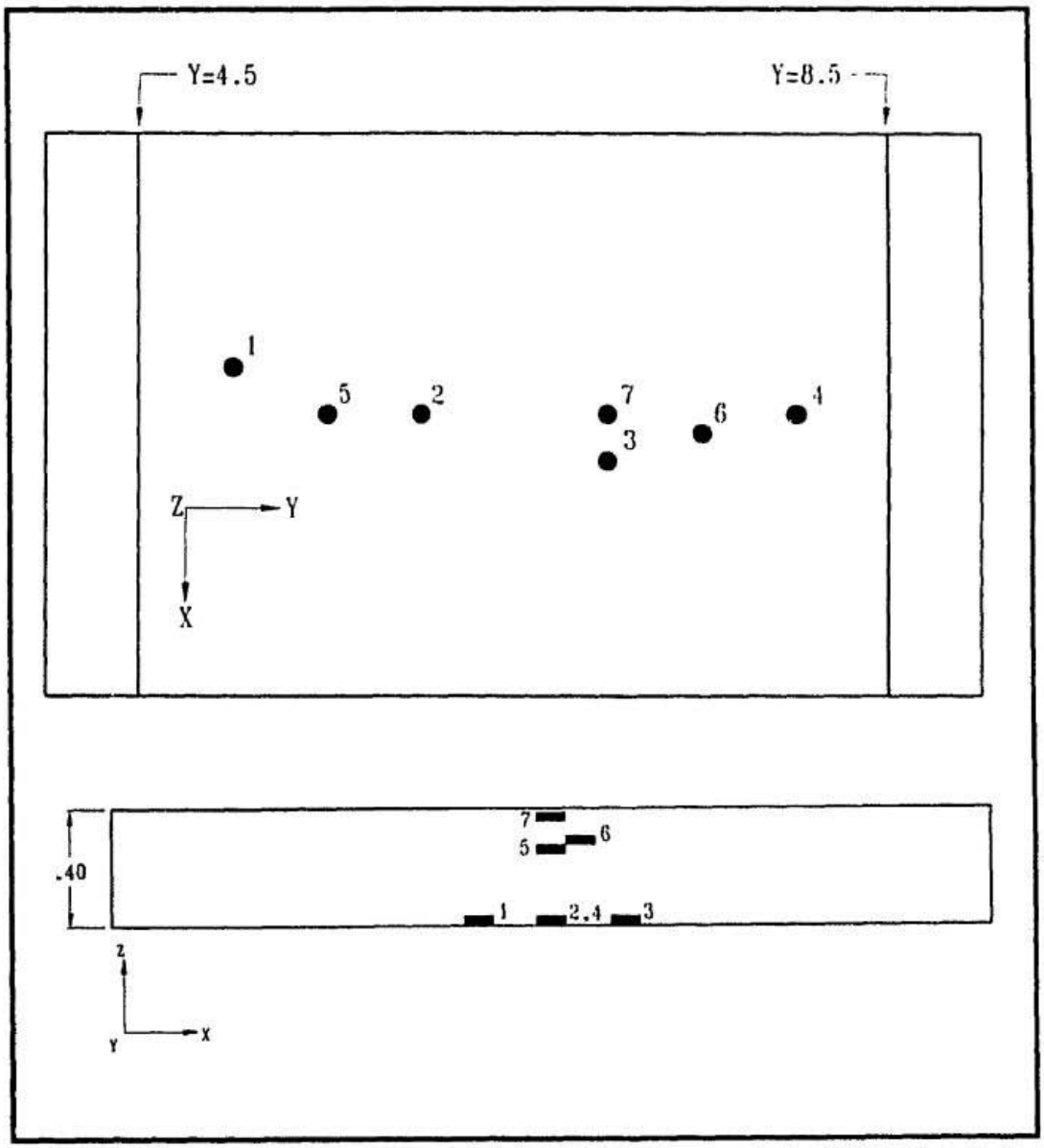

Density Cup Positions - Test 2

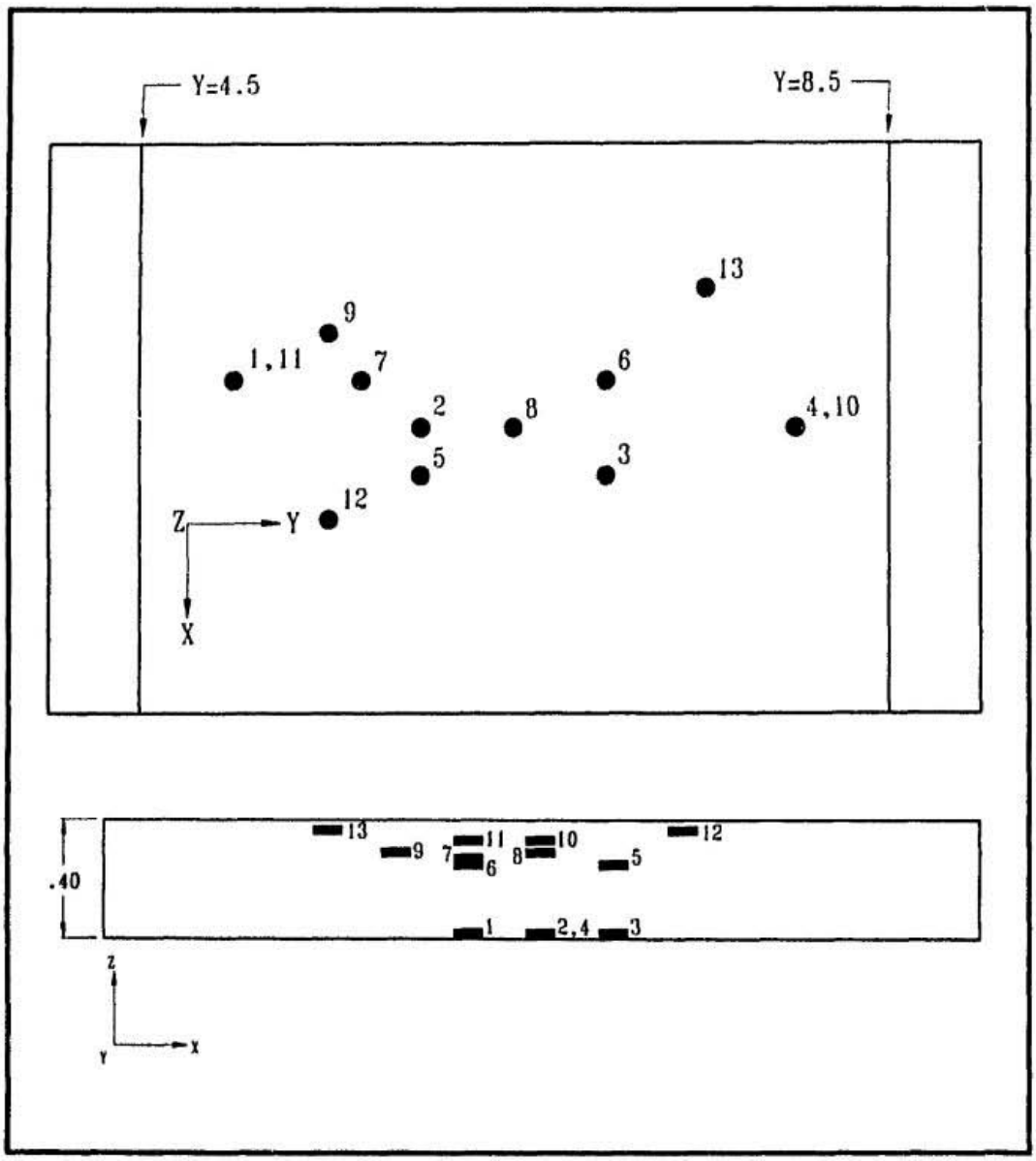

Density Cup Positions - Test 3

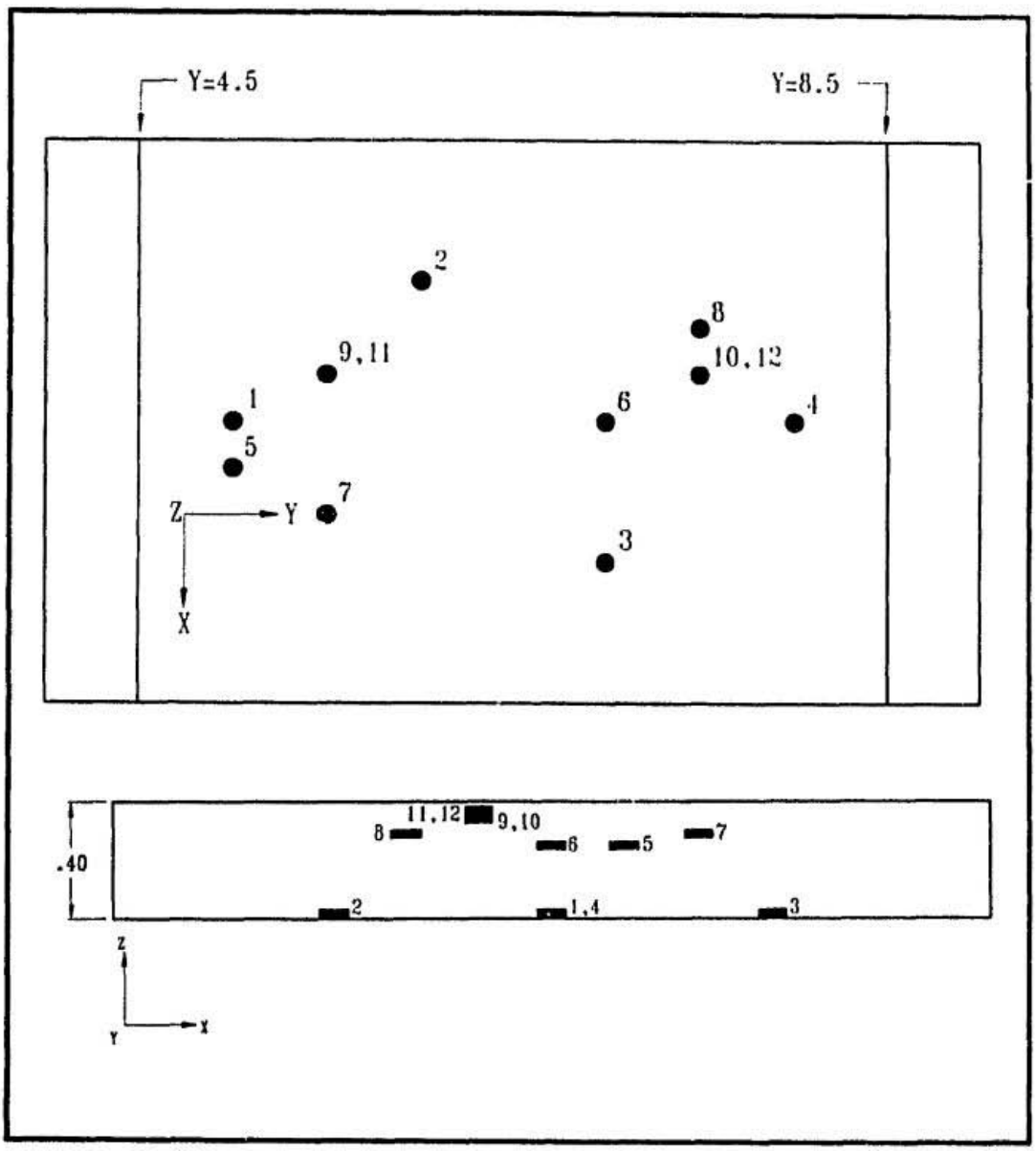

Density Cup Positions - Test 4

Scour Profile Measurements - Test 1

Y (m)	D_1 (m)	D_2 (m)	D_3 (m)	W_1 (m)	W_2 (m)	W_3 (m)	α (Deg.)	β (Deg.)
4.5	0.043	0.030	0.073	0.323	0.575	0.770	34.6	28.2
5.0	0.042	0.055	0.097	0.276	0.611	0.753	30.2	29.3
5.5	0.042	0.054	0.096	0.278	0.614	0.768	30.0	30.4
6.0	0.040	0.054	0.094	0.282	0.615	0.770	31.8	28.8
6.5	0.041	0.051	0.092	---	---	---	39.1	26.9
7.0	0.042	0.052	0.094	0.291	0.611	0.744	37.8	27.4
7.5	0.042	0.044	0.086	0.296	0.596	0.713	37.3	30.2
8.0	0.040	0.038	0.078	0.306	0.586	0.730	34.9	29.9
8.5	0.044	0.020	0.064	0.330	0.550	0.654	22.9	27.1

Scour Profile Measurements - Test 2

Y (m)	D_1 (m)	D_2 (m)	D_3 (m)	W_1 (m)	W_2 (m)	W_3 (m)	α (Deg.)	β (Deg.)
5.0	0.040	0.057	0.097	0.274	0.617	0.787	33.2	27.9
5.5	0.039	0.056	0.095	0.282	0.617	0.774	30.4	28.8
6.0	0.038	0.055	0.093	0.282	0.609	0.786	28.3	28.9
6.5	0.039	0.055	0.094	0.285	0.620	0.791	30.5	28.3
7.0	0.039	0.052	0.091	0.290	0.611	0.777	30.7	29.2
7.5	0.039	0.064	0.085	0.298	0.600	0.808	29.1	29.3
8.0	0.039	0.038	0.077	0.314	0.584	0.702	33.1	27.5
8.5	0.041	0.020	0.061	0.344	0.546	0.660	10.6	27.7

Scour Profile Measurements

Scour Profile Measurements - Test 3

Y (m)	D_1 (m)	D_2 (m)	D_3 (m)	W_1 (m)	W_2 (m)	W_3 (m)	α (Deg.)	β (Deg.)
4.5	0.043	0.039	0.082	0.262	0.600	0.726	31.4	26.2
5.0	0.038	0.057	0.095	0.230	0.628	0.797	31.9	24.4
5.5	0.037	0.052	0.089	0.228	0.627	0.781	31.1	23.7
6.0	0.039	0.047	0.086	0.232	0.617	0.780	32.6	25.1
6.5	0.038	0.051	0.089	0.245	0.628	0.783	29.2	25.6
7.0	0.039	0.048	0.087	0.238	0.627	0.786	23.8	23.9
7.5	0.038	0.043	0.081	0.244	0.608	0.745	30.1	21.9
8.0	0.040	0.037	0.077	0.256	0.602	0.764	28.3	23.6
8.5	0.039	0.027	0.066	0.283	0.577	0.728	16.2	24.0

Scour Profile Measurements - Test 4

Y (m)	D_1 (m)	D_2 (m)	D_3 (m)	W_1 (m)	W_2 (m)	W_3 (m)	α (Deg.)	β (Deg.)
4.5	0.023	0.053	0.076	0.268	0.601	0.730	30.4	24.7
5.0	0.038	0.045	0.083	0.247	0.606	0.803	26.8	26.7
5.5	0.040	0.046	0.086	0.239	0.623	0.793	31.2	24.7
6.0	0.040	0.047	0.087	0.233	0.625	0.788	26.4	25.7
6.5	0.040	0.046	0.086	0.242	0.622	0.789	26.3	23.7
7.0	0.040	0.045	0.085	0.240	0.624	0.765	23.2	24.7
7.5	0.400	0.040	0.080	0.240	0.613	0.748	26.1	27.5
8.0	0.042	0.040	0.082	0.251	0.610	0.742	29.7	24.3
8.5	0.042	0.032	0.074	0.260	0.600	0.726	32.0	25.2
9.0	0.042	0.019	0.061	0.304	0.564	0.714	15.5	25.8

Testbed Penetration Resistance Values

Penetration Resistances - Test 3

Reading No.	X Coordinate	Y Coordinate	Penetration Resistance
1-0	0.2875	4.5112	8.53
1-1	0.0000	4.5058	12.30
1-2	-0.1745	4.5132	11.20
1-3	-0.2950	4.5225	12.23
1-4	-0.4525	4.5179	7.50
1-5	-0.6546	4.6546	8.80
2-1	0.6328	4.6894	6.27
2-2	0.4184	4.6940	10.80
2-3	0.1347	4.7014	12.56
2-4	-0.0550	4.7167	12.34
2-5	-0.2741	4.7171	12.09
2-6	-0.5189	4.7187	9.94
2-7	-0.7969	4.7107	8.00
3-1	0.7296	4.9286	8.78
3-2	0.5294	4.9439	13.21
3-3	0.3178	4.9159	11.52
3-4	0.0304	4.9225	13.91
3-5	-0.1499	4.9188	13.73
3-6	-0.2789	4.9142	12.33
3-7	-0.4326	4.9179	12.86
3-8	-0.6489	4.9101	9.19
3-9	-0.8775	4.9182	7.99
4-1	0.6480	5.1585	9.96
4-2	0.4203	5.1491	13.62
4-3	0.1404	5.1605	12.79
4-4	-0.0531	5.1652	13.31
4-5	-0.2362	5.1865	11.88
4-6	-0.4886	5.1859	10.24
4-7	-0.8102	5.1598	9.02

Penetration Resistances - Test 3 (Cont.)

Reading No.	X Coordinate	Y Coordinate	Penetration Resistance
5-1	0.7372	5.4182	8.08
5-2	0.5275	5.4235	10.61
5-3	0.3065	5.3981	10.80
5-4	-0.4743	5.3975	10.79
5-5	-0.8472	5.3794	9.08
6-1	0.7277	6.9934	10.32
6-2	0.4554	6.9987	10.21
6-3	-0.3519	6.9941	13.29
6-4	-0.6128	7.0068	11.53
6-5	-0.8804	6.9847	9.24
7-1	-0.3851	6.4826	11.15
7-2	-0.5777	6.4826	9.33
7-3	-0.8339	6.4973	8.18
8-1	0.7267	8.5803	10.89
8-2	0.5247	8.5756	11.92
8-3	0.3302	8.5716	11.99
8-4	0.1528	8.5909	11.88
8-5	-0.1195	8.5983	10.62
8-6	-0.2874	8.5996	11.15
8-7	-0.5037	8.6026	10.20
8-8	-0.8121	8.5990	8.08

Penetration Resistances - Test 4

Reading No.	X Coordinate	Y Coordinate	Penetration Resistance
1-1	0.7419	4.7292	10.29
1-2	0.4355	4.7375	9.54
1-3	0.1310	4.7375	10.33
1-4	-0.1622	4.7382	10.68
1-5	-0.3030	4.7335	11.51
1-6	-0.5379	4.7235	9.79
1-7	-0.8282	4.7346	7.18
2-1	0.7524	5.0043	10.16
2-2	0.4175	4.9556	10.44
2-3	0.1272	4.9362	9.80
2-4	-0.1745	4.8942	11.43
2-5	-0.3140	4.9296	11.31
2-6	-0.5331	4.9345	11.58
2-7	-0.7893	5.0103	8.18
3-1	0.7362	5.2795	10.93
3-2	0.4203	5.2708	9.71
3-3	0.1347	5.2982	9.39
3-4	-0.1764	5.2661	9.82
3-5	-0.3045	5.2494	10.91
3-6	-0.5388	5.2735	11.01
3-7	-0.8595	5.2735	7.81
4-1	-0.1612	6.5517	10.73
4-2	-0.2912	6.5474	11.94
4-3	-0.5312	6.5497	10.26
4-4	-0.8102	6.5524	8.66
5-1	-0.1584	6.9133	8.99
5-2	-0.2722	6.9087	11.63
5-3	-0.5123	6.9147	8.24
5-4	-0.8548	6.9066	6.64
6-1	-0.1679	7.2152	9.29
6-2	-0.2855	7.2119	9.40
6-3	-0.5322	7.2119	8.39
6-4	-0.8424	7.2072	6.58

Penetration Resistances - Test 4 (Cont.)

Reading No.	X Coordinate	Y Coordinate	Penetration Resistance
7-1	0.7210	7.4275	9.43
7-2	0.3862	7.4229	11.01
8-1	0.7315	7.7799	10.48
8-2	0.4061	7.7939	10.88
8-3	0.1480	7.7932	7.45
8-4	-0.1318	7.7912	10.46
8-5	-0.3197	7.7779	10.27
8-6	-0.6432	7.7832	7.48
9-1	0.7400	8.1455	9.16
9-2	0.3691	8.1742	10.78
9-3	0.1376	8.1662	7.79
9-4	-0.1793	8.1909	8.13
9-5	-0.2950	8.1909	8.29
9-6	-0.5597	8.2051	7.08
10-1	0.7239	8.5785	8.72
10-2	0.3909	8.5891	10.57
10-3	0.1547	8.5838	8.40
10-4	-0.1612	8.5931	8.09
10-5	-0.2960	8.5847	11.28
10-6	-0.5682	8.5951	8.19
11-1	0.5664	8.9909	10.19
11-2	0.1518	8.9915	9.31
11-3	-0.1394	8.9922	8.37
11-4	-0.3064	8.9922	8.59
12-1	0.5512	8.7718	11.20
12-2	0.0000	8.7818	8.31
12-3	-0.2239	8.7818	11.00
13-1	0.5484	8.3674	11.28
13-2	-0.0332	8.3825	12.29
13-3	-0.2315	8.3827	11.39
14-1	0.5749	7.9783	11.50
14-2	-0.0275	7.9742	12.20
14-3	-0.2352	7.9409	12.99

Testbed Penetration Locations

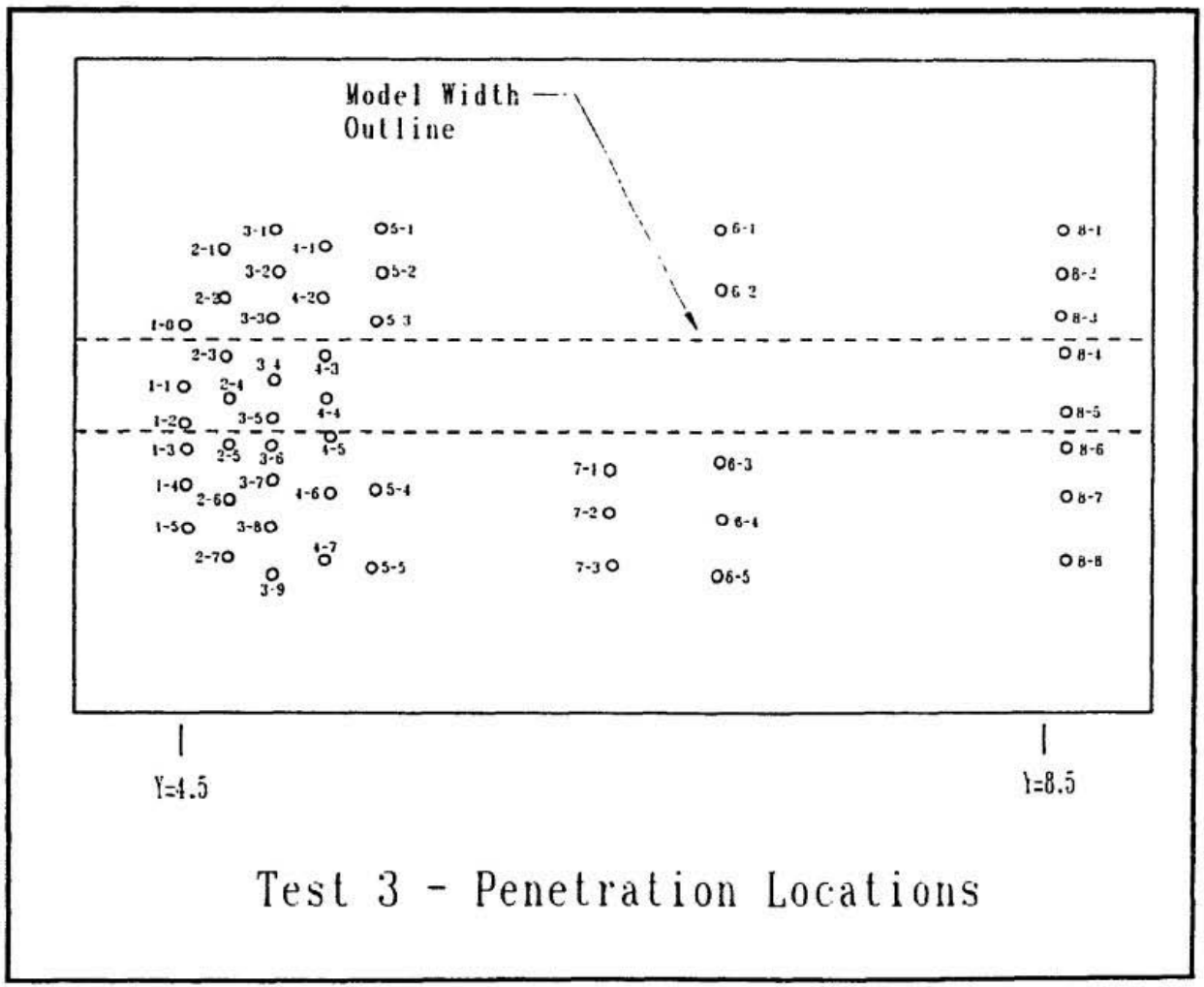

Test 3 - Penetration Locations

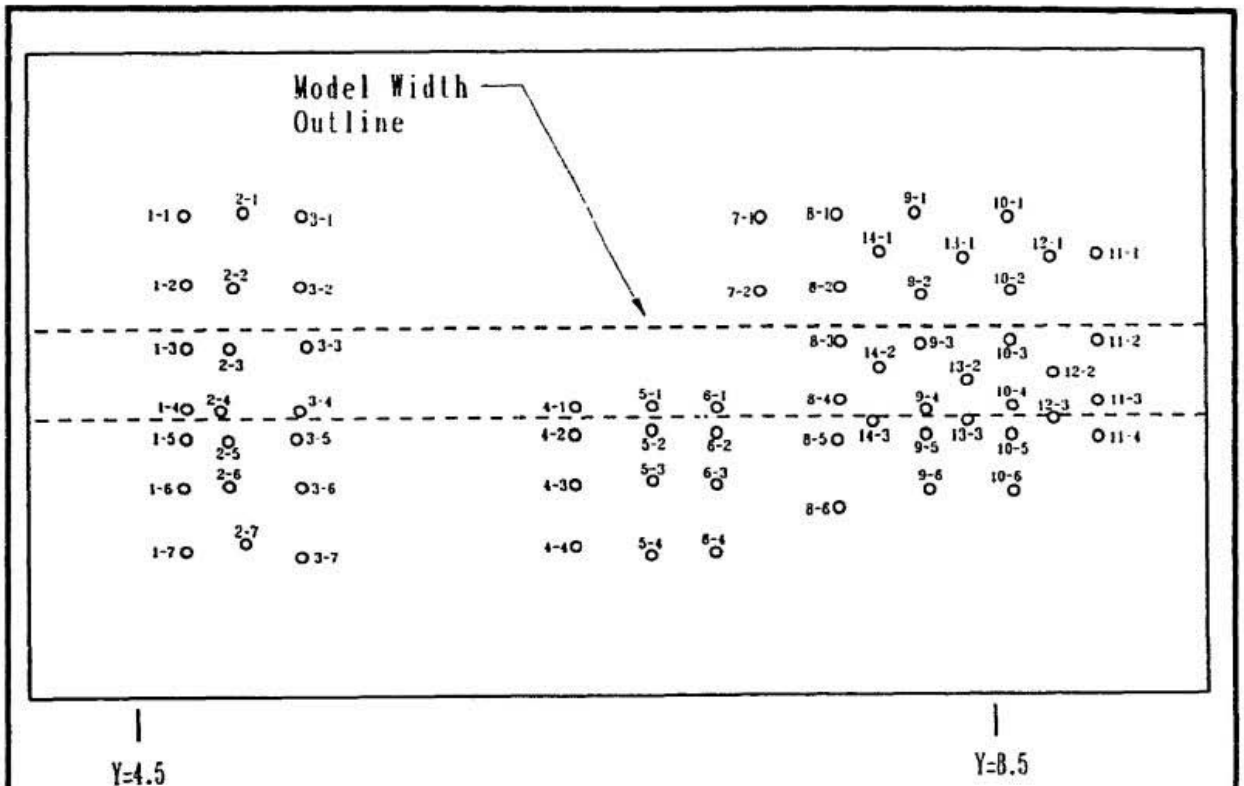

Test 4 - Penetration Locations

Appendix C

Test 1 Results

Instrumentation Output

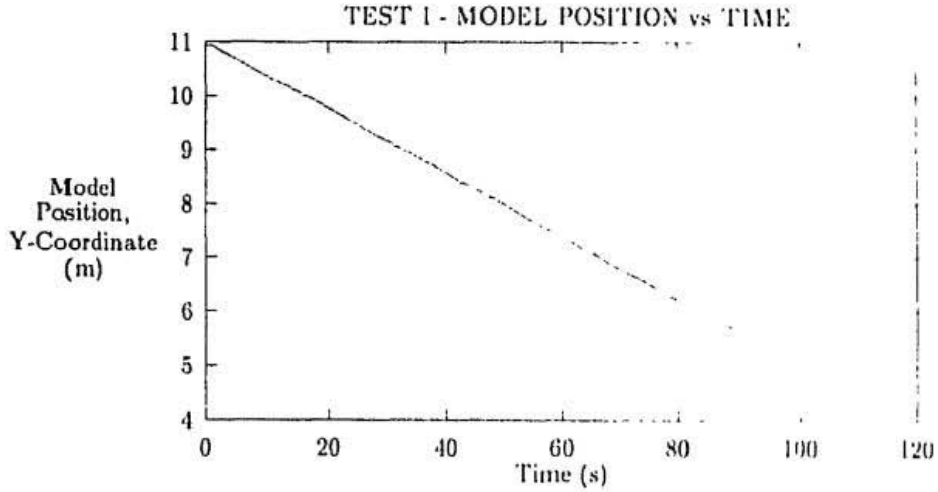
TEST 1 - MODEL POSITION vs TIME
Model Position, Y-Coordinate (m)
11
10
9
8
7
6
5
4
0
20
40
60
80
100
120
Time (s)

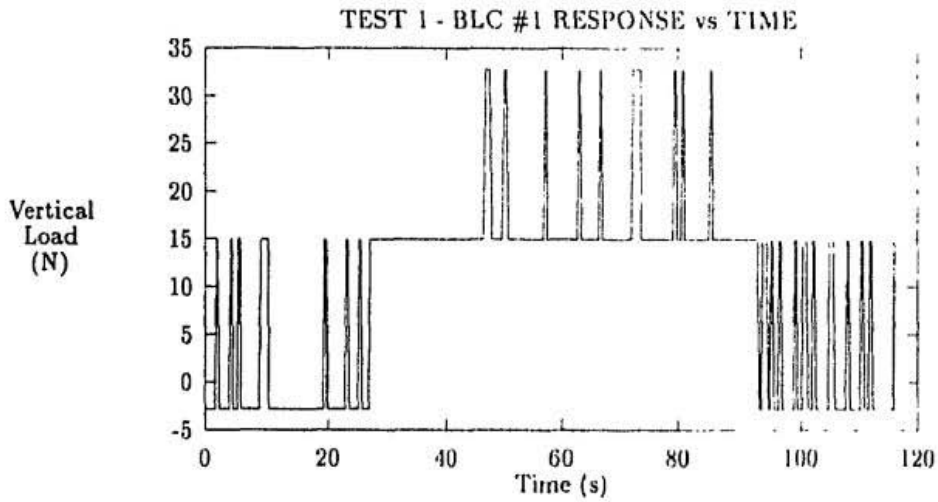
TEST 1 - BLC #1 RESPONSE vs TIME
Vertical Load (N)
35
30
25
20
15
10
5
0
-5
0
20
40
60
80
100
120
Time (s)

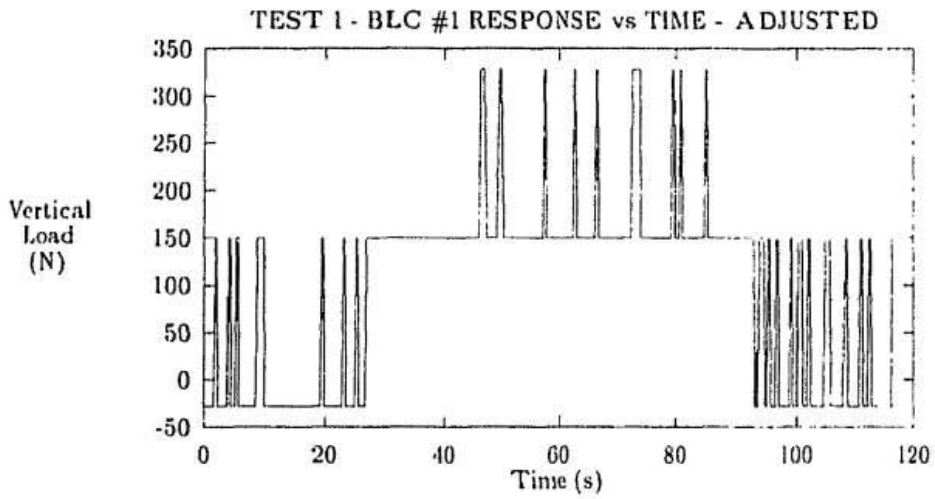
TEST 1 - BLC #1 RESPONSE vs TIME - ADJUSTED
Vertical Load (N)
350
300
250
200
150
100
50
0
-50
0
20
40
60
80
100
120
Time (s)

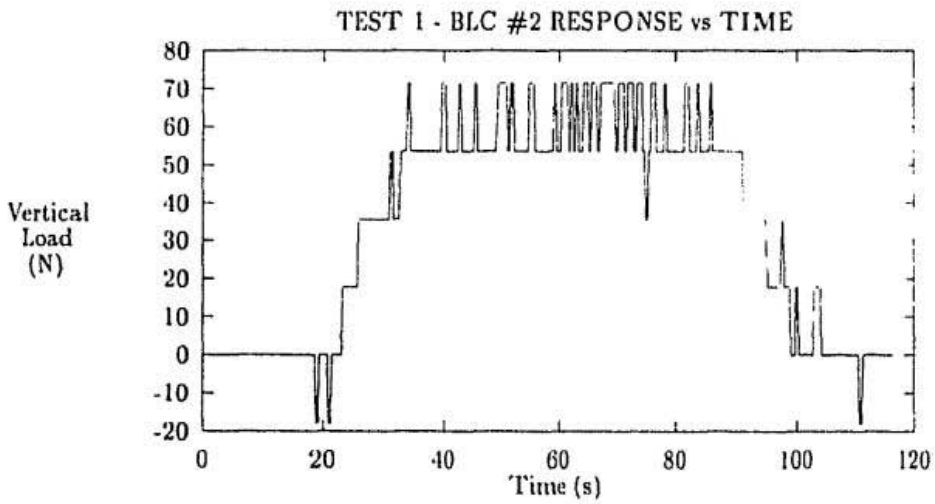
TEST 1 - BLC #2 RESPONSE vs TIME
Vertical Load (N)
80
70
60
50
40
30
20
10
0
-10
-20
0
20
40
60
80
100
120
Time (s)

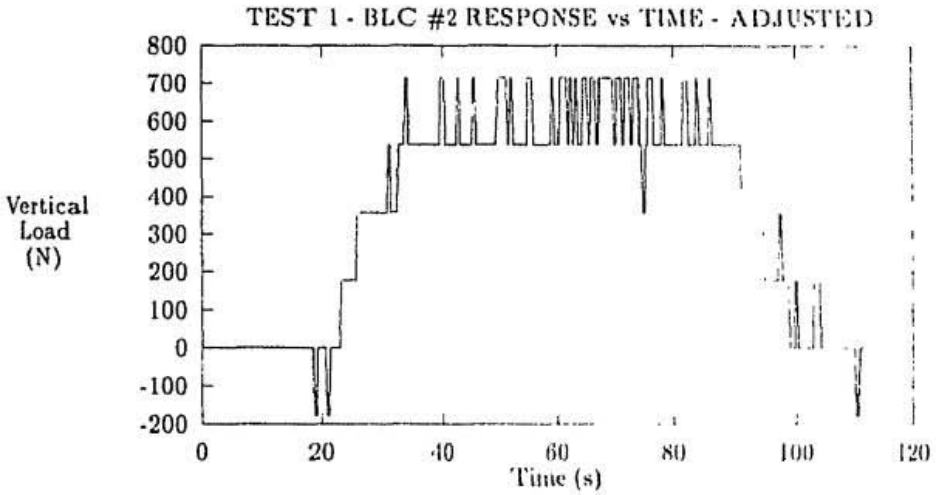
TEST 1 - BLC #2 RESPONSE vs TIME - ADJUSTED
Vertical Load (N)
800
700
600
500
400
300
200
100
0
-100
-200
0
20
40
60
80
100
120
Time (s)

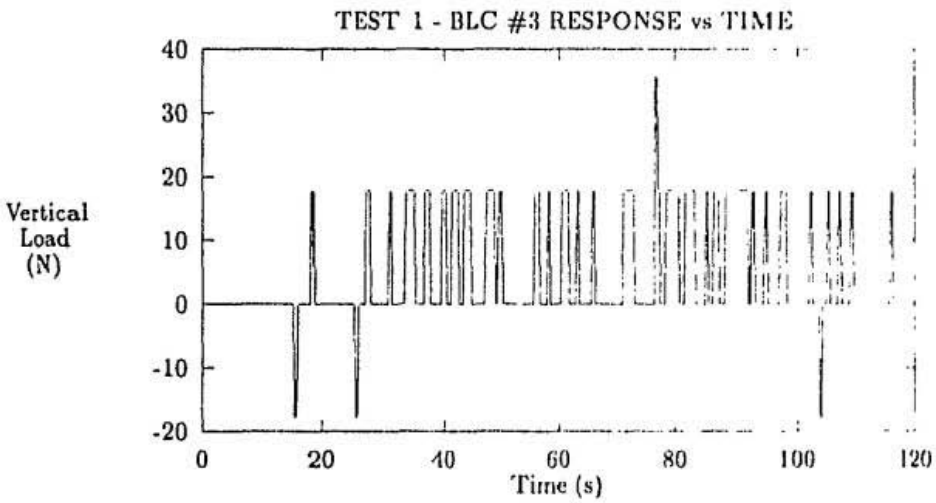
TEST 1 - BLC #3 RESPONSE vs TIME
Vertical Load (N)
40
30
20
10
0
-10
-20
0
20
40
60
80
100
120
Time (s)

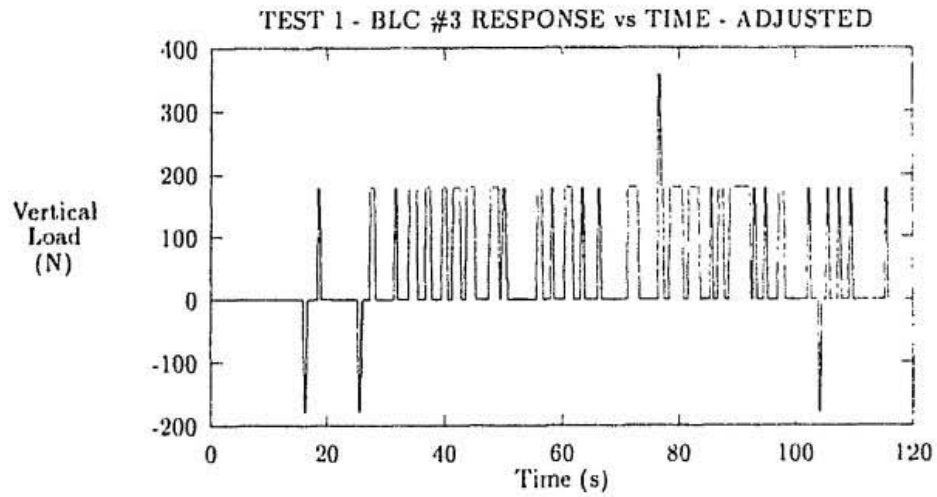
TEST 1 - BLC #3 RESPONSE vs TIME - ADJUSTED
Vertical Load (N)
400
300
200
100
0
-100
-200
0
20
40
60
80
100
120
Time (s)

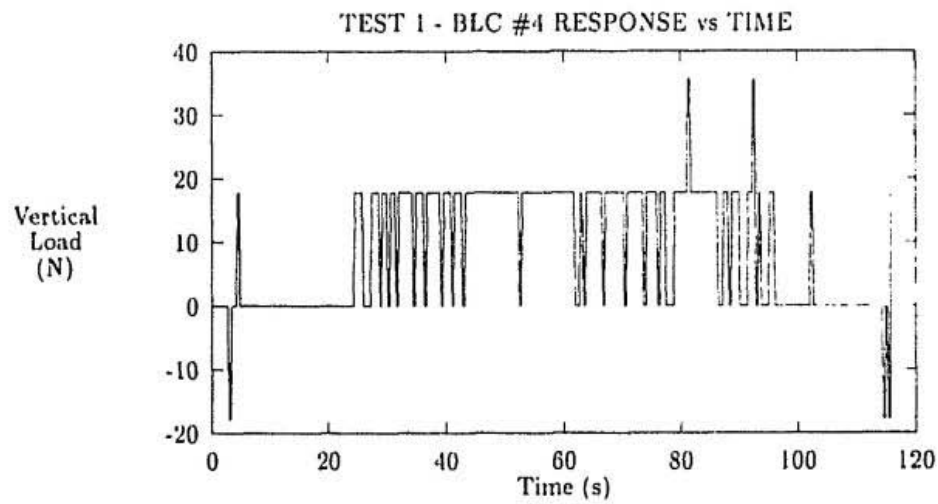
TEST 1 - BLC #4 RESPONSE vs TIME
Vertical Load (N)
40
30
20
10
0
-10
-20
0
20
40
60
80
100
120
Time (s)

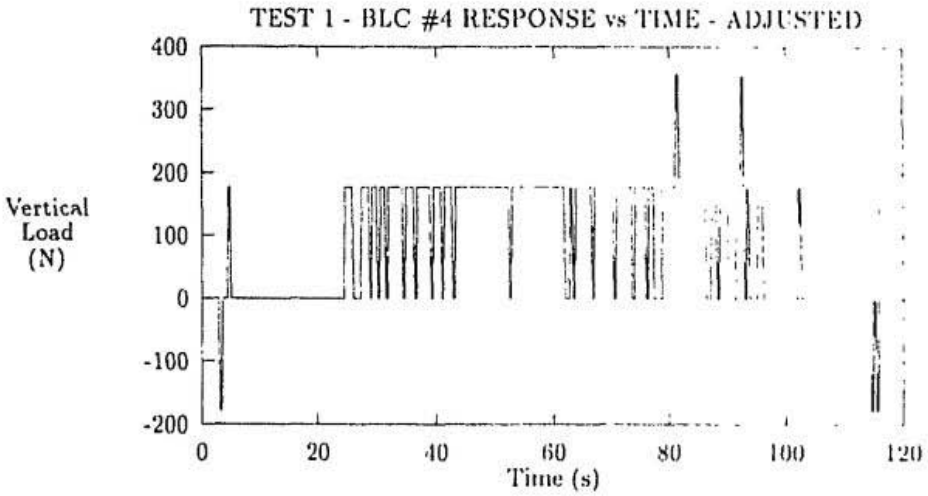
TEST 1 - BLC #4 RESPONSE vs TIME - ADJUSTED
Vertical Load (N)
400
300
200
100
0
-100
-200
0
20
40
60
80
100
120
Time (s)

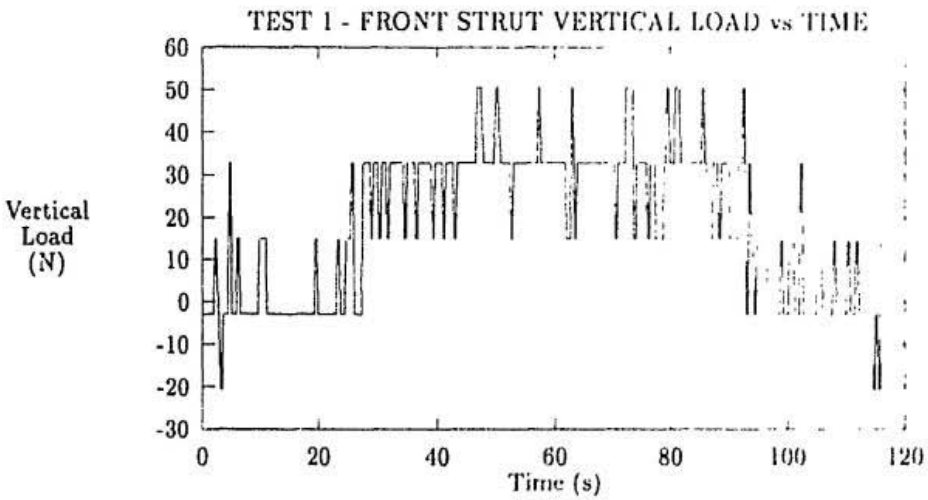
TEST 1 - FRONT STRUT VERTICAL LOAD vs TIME
Vertical Load (N)
60
50
40
30
20
10
0
-10
-20
-30
0
20
40
60
80
100
120
Time (s)

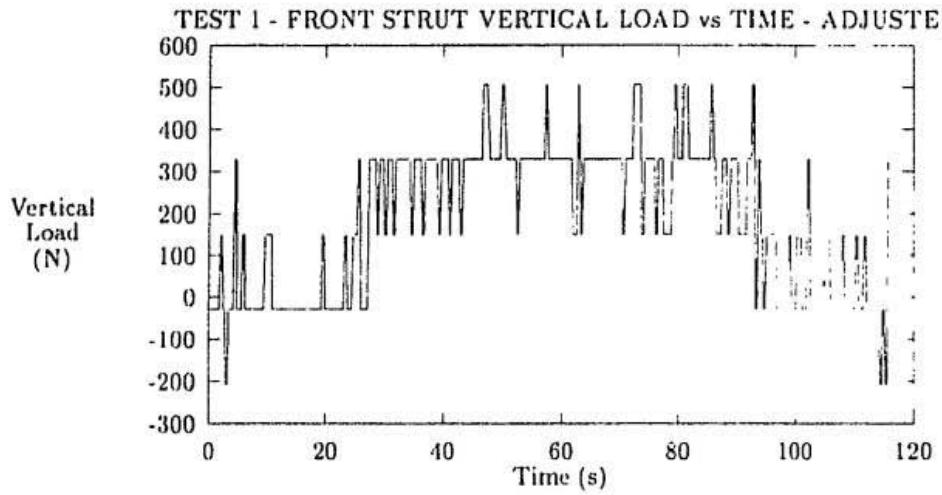
TEST 1 - FRONT STRUT VERTICAL LOAD vs TIME - ADJUSTED
Vertical Load (N)
600
500
400
300
200
100
0
-100
-200
-300
0
20
40
60
80
100
120
Time (s)

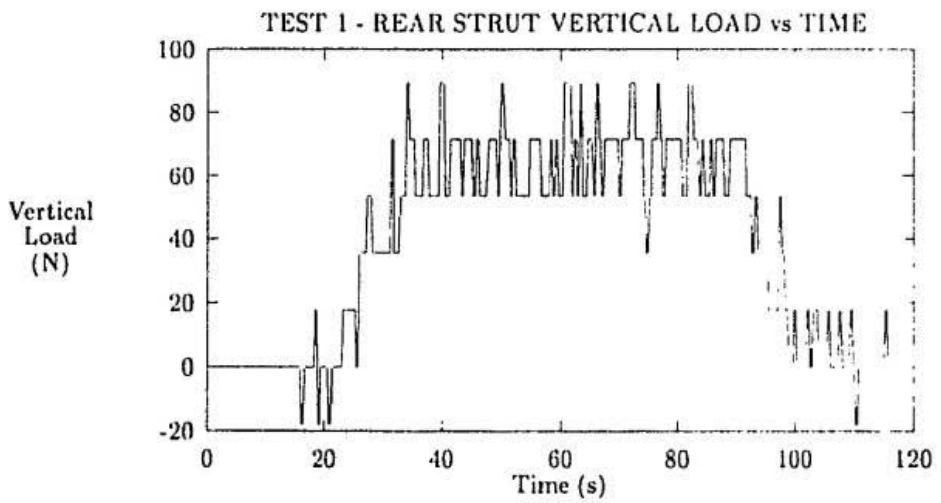
TEST 1 - REAR STRUT VERTICAL LOAD vs TIME
Vertical Load (N)
100
80
60
40
20
0
-20
0
20
40
60
80
100
120
Time (s)

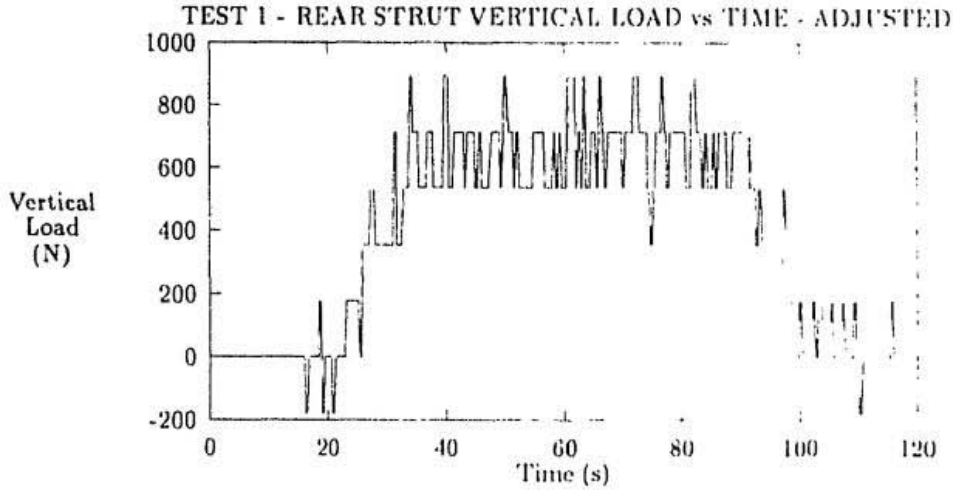
TEST 1 - REAR STRUT VERTICAL LOAD vs TIME - ADJUSTED
Vertical Load (N)
1000
800
600
400
200
0
-200
0
20
40
60
80
100
120
Time (s)

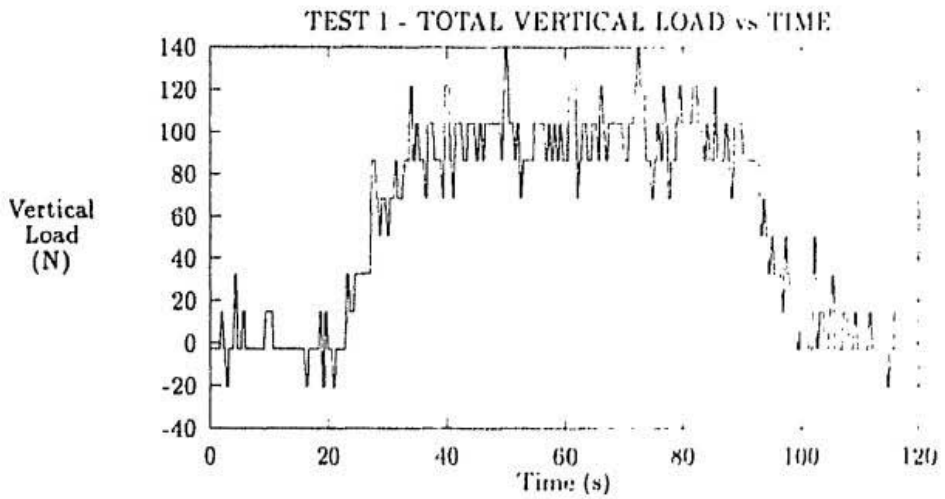
TEST 1 - TOTAL VERTICAL LOAD vs TIME
Vertical Load (N)
140
120
100
80
60
40
20
0
-20
-40
0
20
40
60
80
100
120
Time (s)

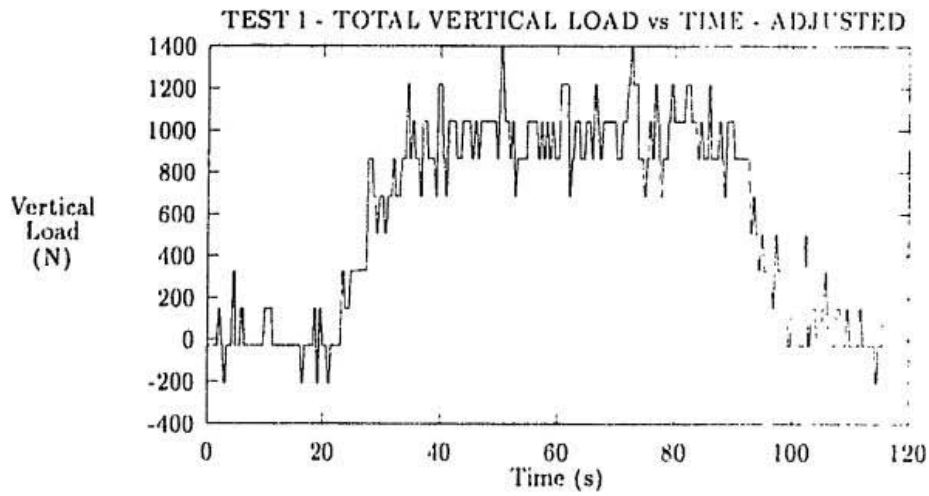
TEST 1 - TOTAL VERTICAL LOAD vs TIME - ADJUSTED
Vertical Load (N)
1400
1200
1000
800
600
400
200
0
-200
-400
0
20
40
60
80
100
120
Time (s)

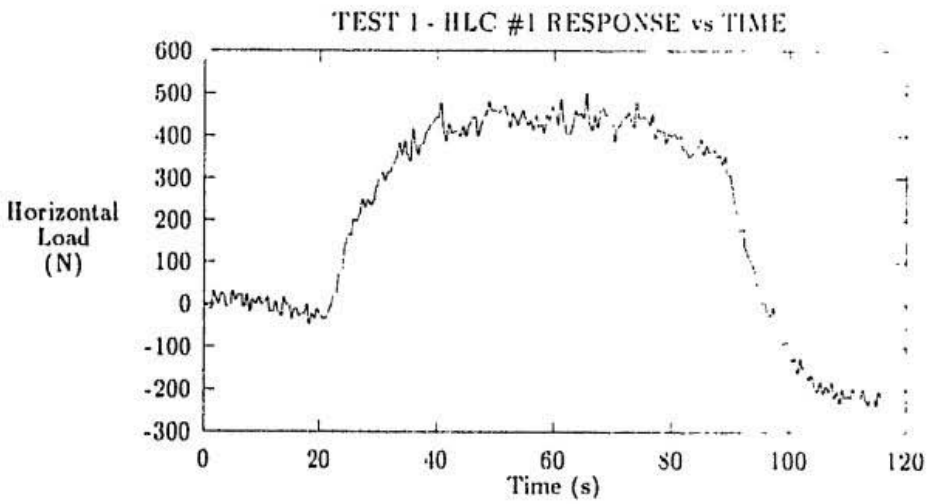
TEST 1 - HLC #1 RESPONSE vs TIME
Horizontal Load (N)
600
500
400
300
200
100
0
-100
-200
-300
0
20
40
60
80
100
120
Time (s)

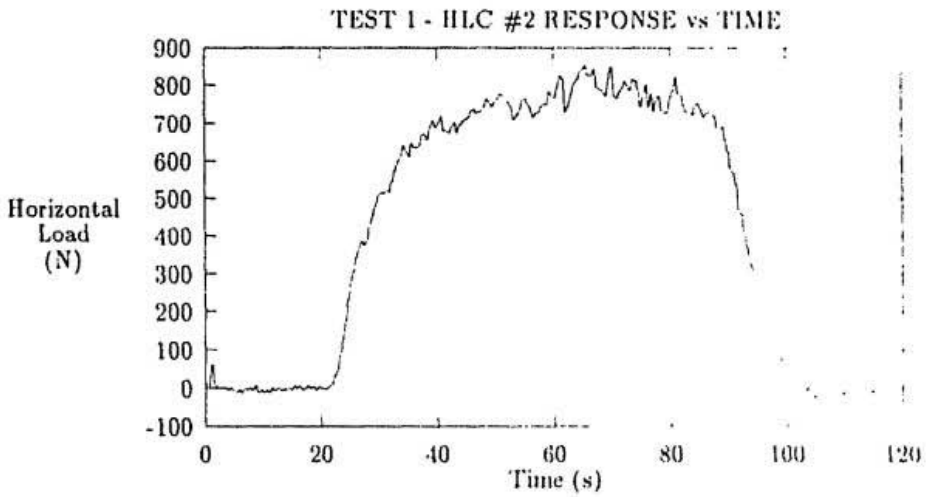
TEST 1 - HLC #2 RESPONSE vs TIME
Horizontal Load (N)
900
800
700
600
500
400
300
200
100
0
-100
0
20
40
60
80
100
120
Time (s)

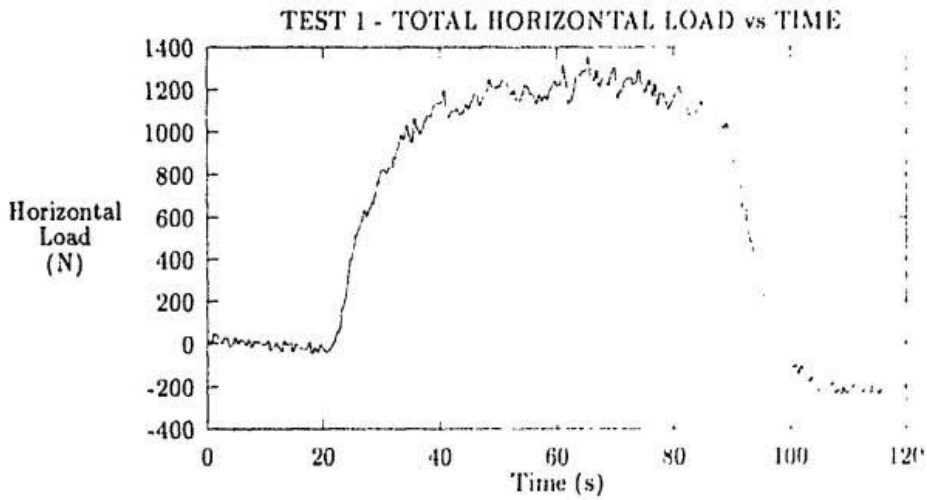
TEST 1 - TOTAL HORIZONTAL LOAD vs TIME
Horizontal Load (N)
1400
1200
1000
800
600
400
200
0
-200
-400
0
20
40
60
80
100
120
Time (s)

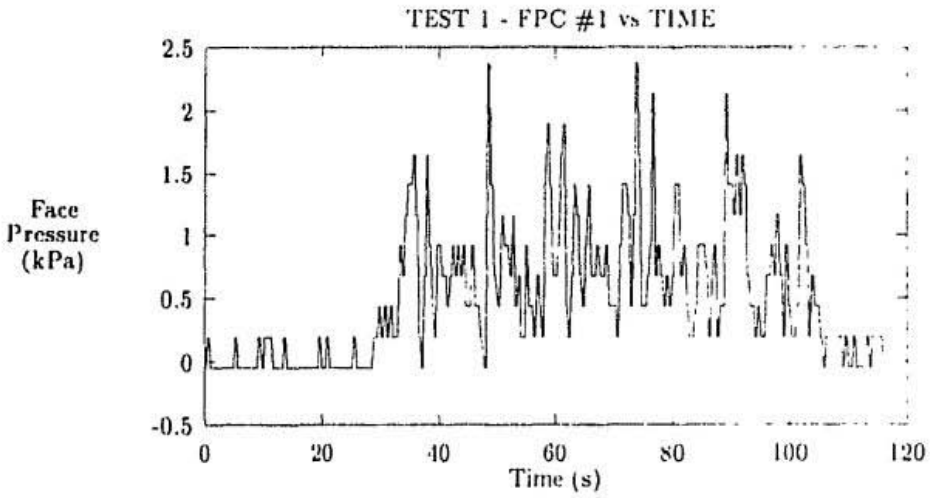
TEST 1 - FPC #1 vs TIME
Face Pressure (kPa)
2.5
2
1.5
1
0.5
0
-0.5
0
20
40
60
80
100
120
Time (s)

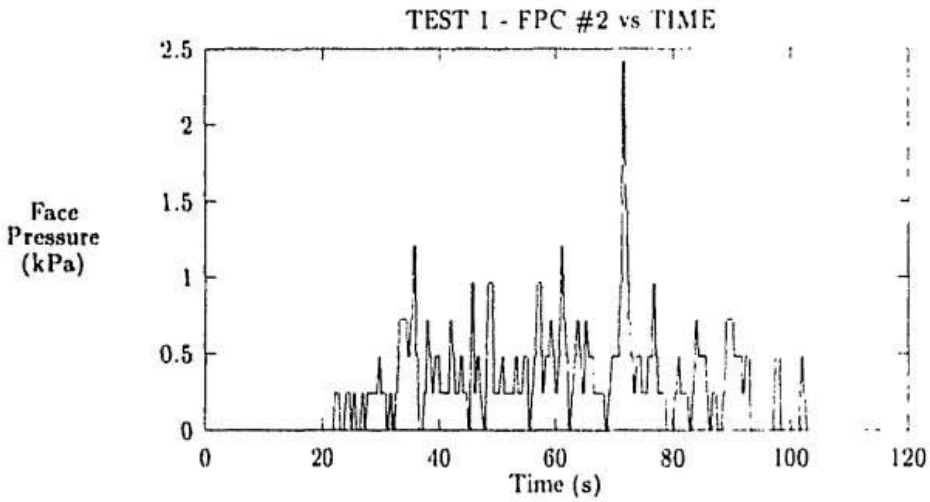
TEST 1 - FPC #2 vs TIME
Face Pressure (kPa)
2.5
2
1.5
1
0.5
0
0
20
40
60
80
100
120
Time (s)

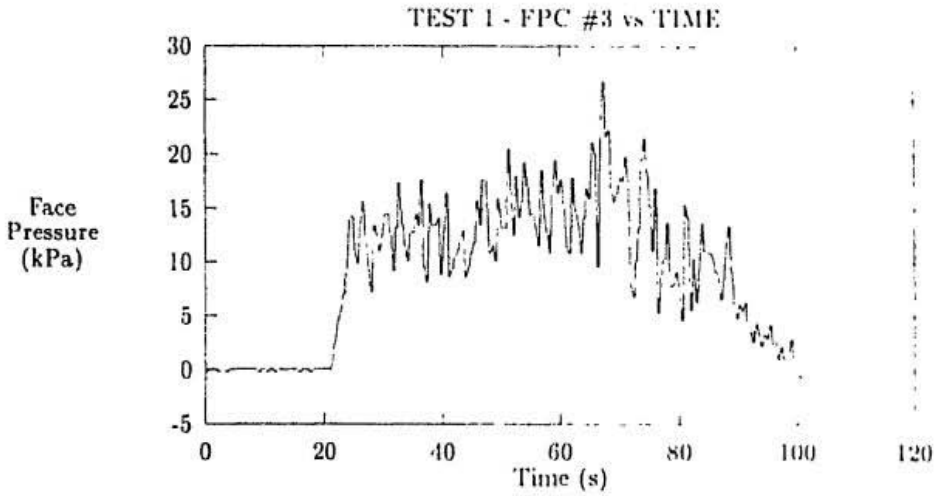
TEST 1 - FPC #3 vs TIME
Face Pressure (kPa)
30
25
20
15
10
5
0
-5
0
20
40
60
80
100
120
Time (s)

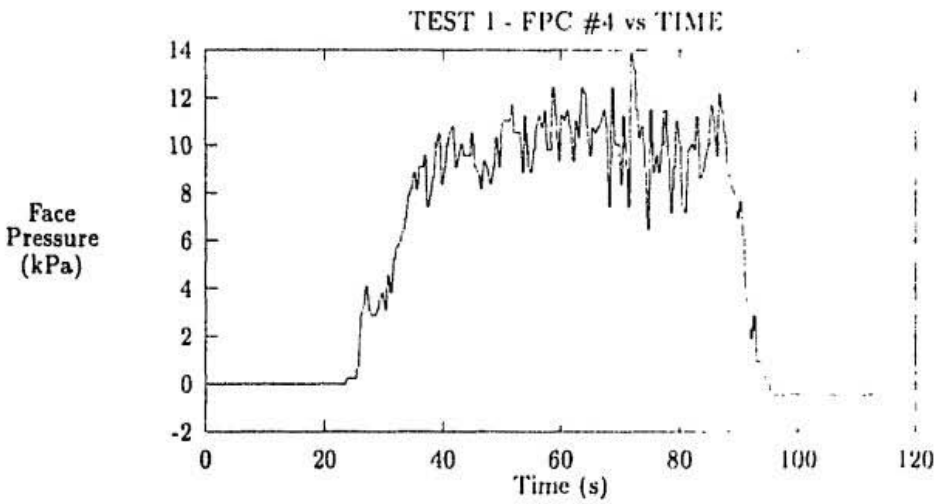
TEST 1 - FPC #4 vs TIME
Face Pressure (kPa)
14
12
10
8
6
4
2
0
-2
0
20
40
60
80
100
120
Time (s)

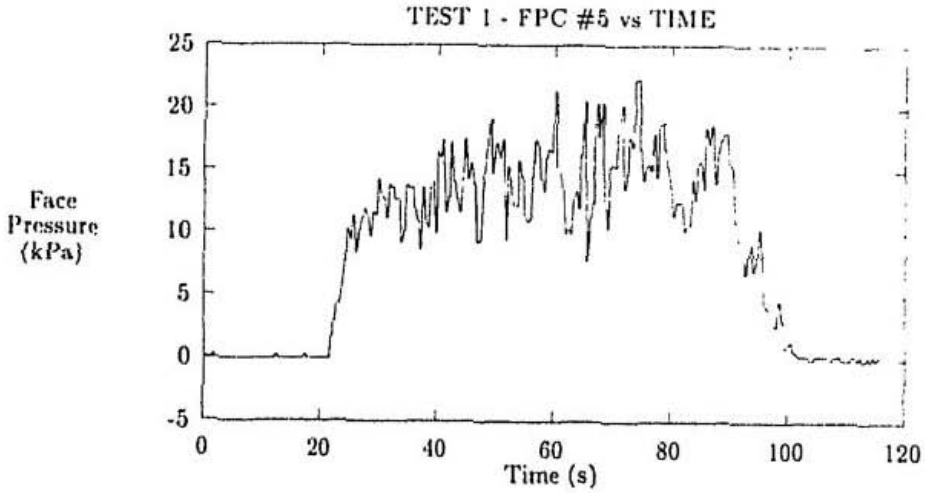
TEST 1 - FPC #5 vs TIME
Face Pressure (kPa)
25
20
15
10
5
0
-5
0
20
40
60
80
100
120
Time (s)

Scour Profiles

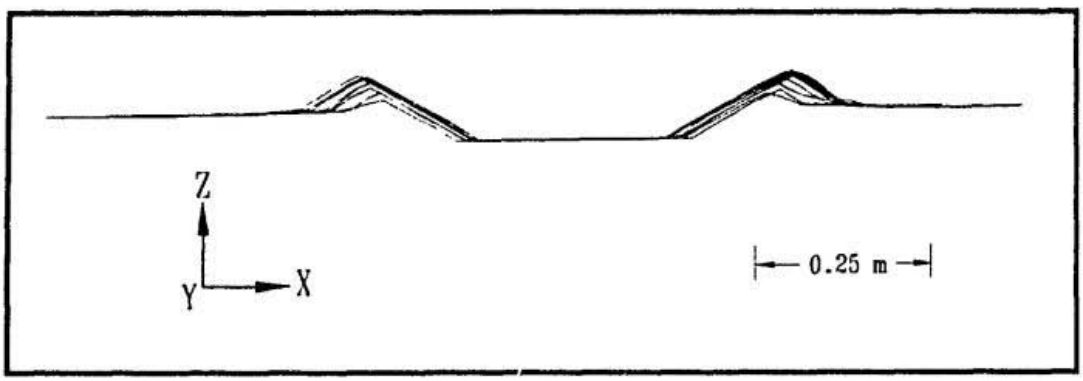
Z
Y
X
0.25 m

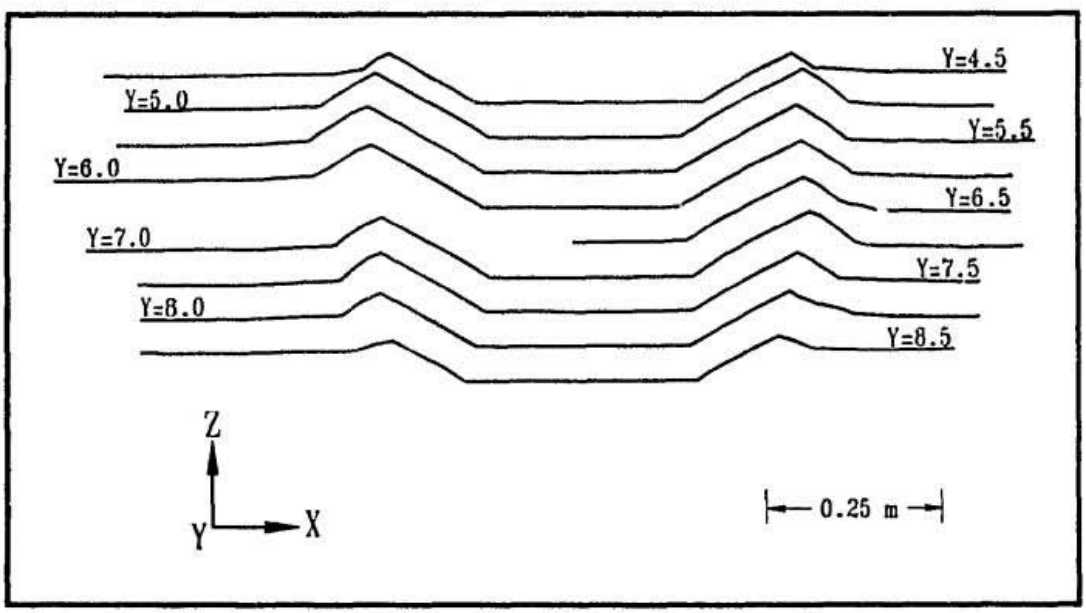
Y=4.5
Y=5.0
Y=5.5
Y=6.0
Y=6.5
Y=7.0
Y=7.5
Y=8.0
Y=8.5
Z
Y
X
0.25 m

Ball Bearing Displacements

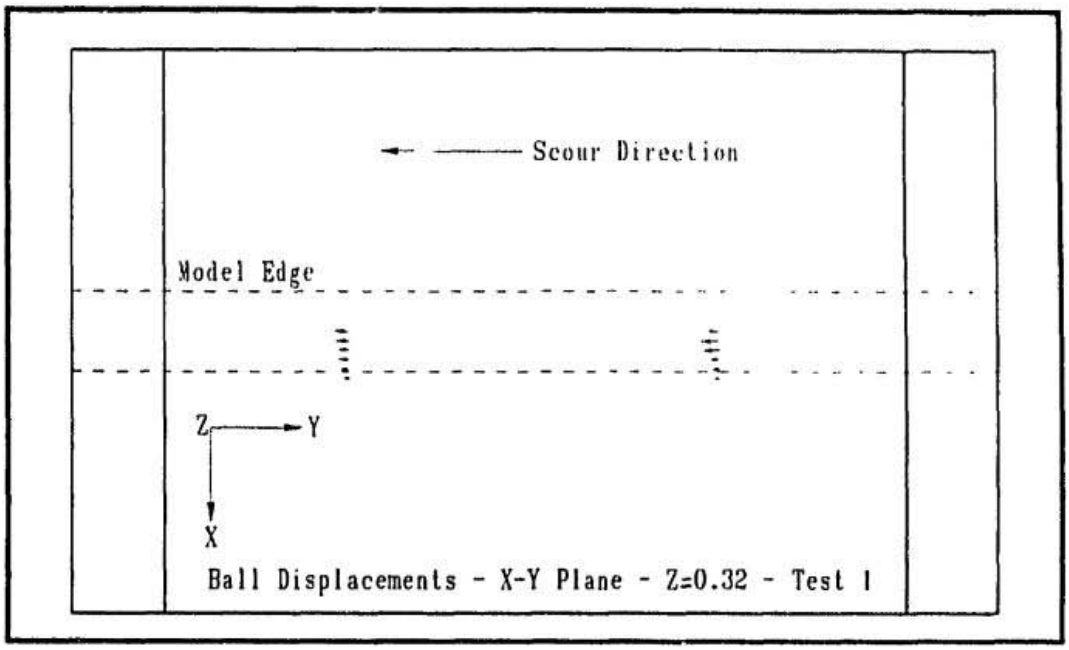
Scour Direction
Model Edge
Z
Y
X
Ball Displacements - X-Y Plane - Z=0.32 - Test 1

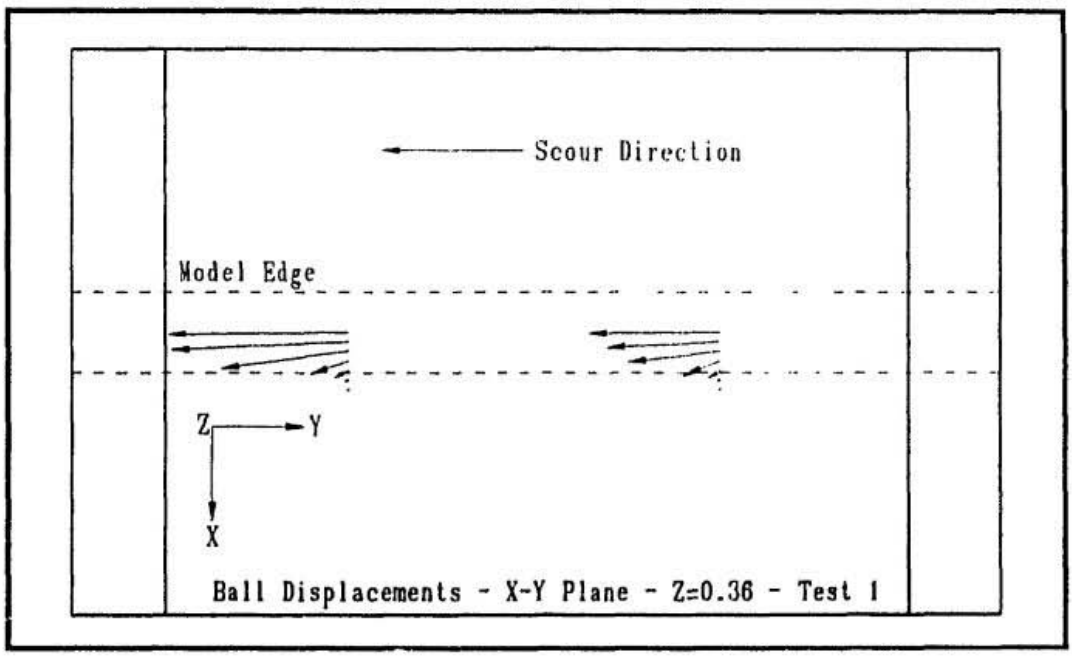
Scour Direction
Model Edge
Z
Y
X
Ball Displacements - X-Y Plane - Z=0.36 - Test 1

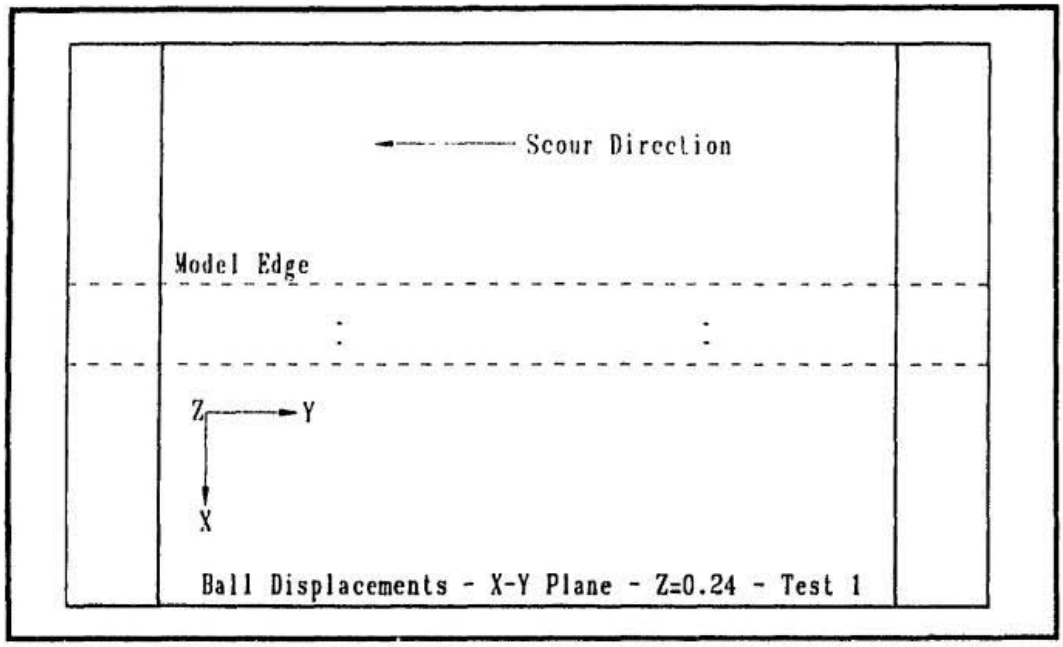
Scour Direction
Model Edge
Z
Y
X
Ball Displacements - X-Y Plane - Z=0.24 - Test 1

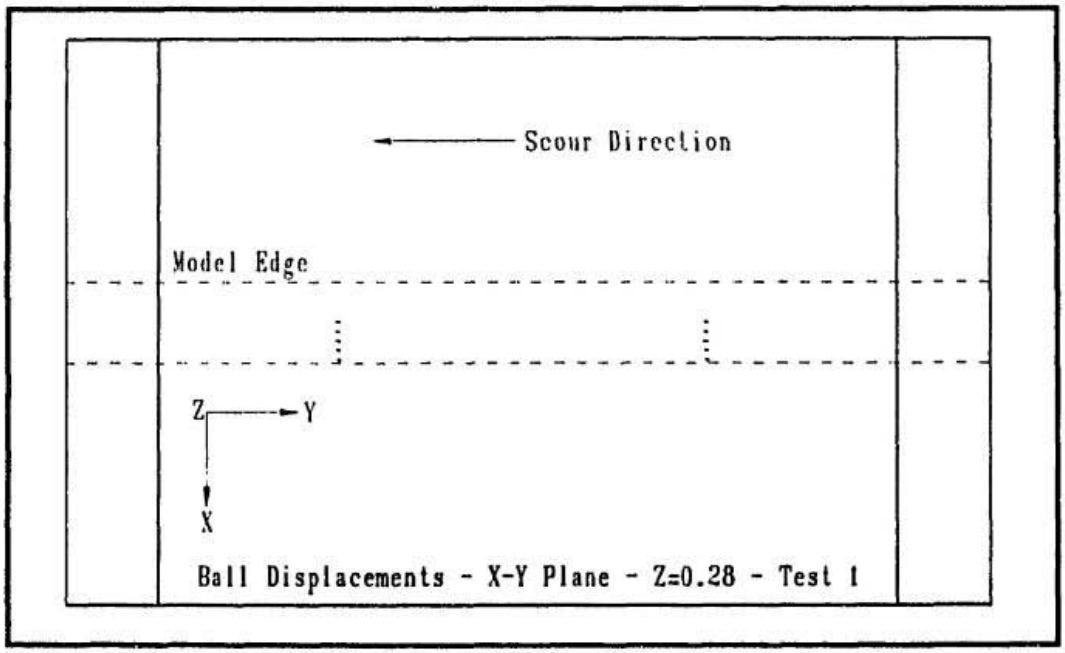
Scour Direction
Model Edge
Z
Y
X
Ball Displacements - X-Y Plane - Z=0.28 - Test 1

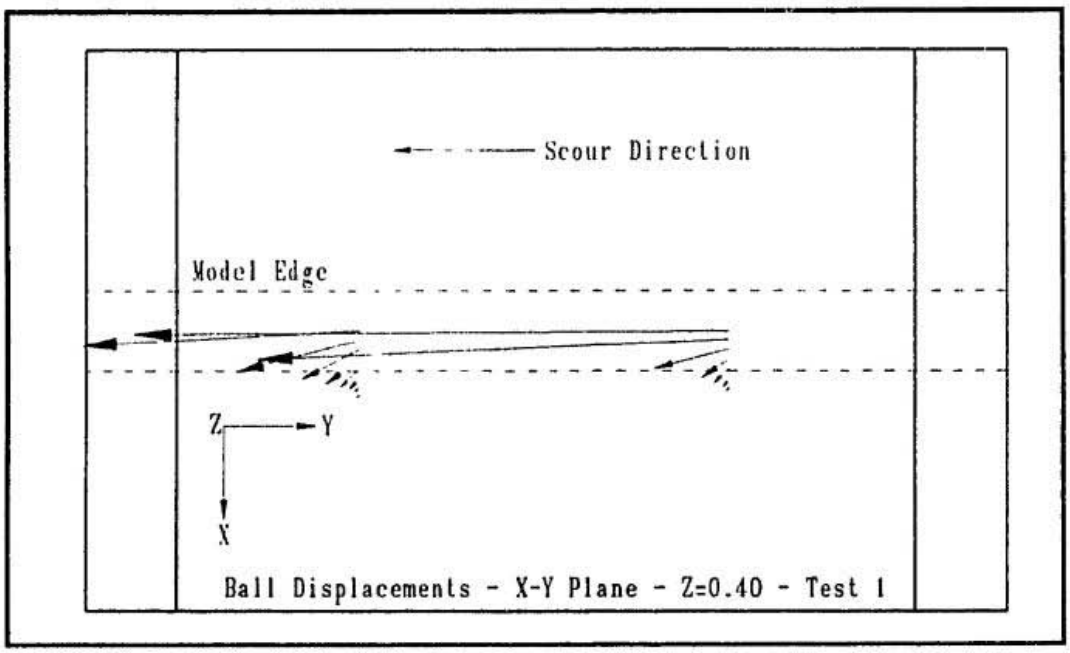
Scour Direction
Model Edge
Z
Y
X
Ball Displacements - X-Y Plane - Z=0.40 - Test 1

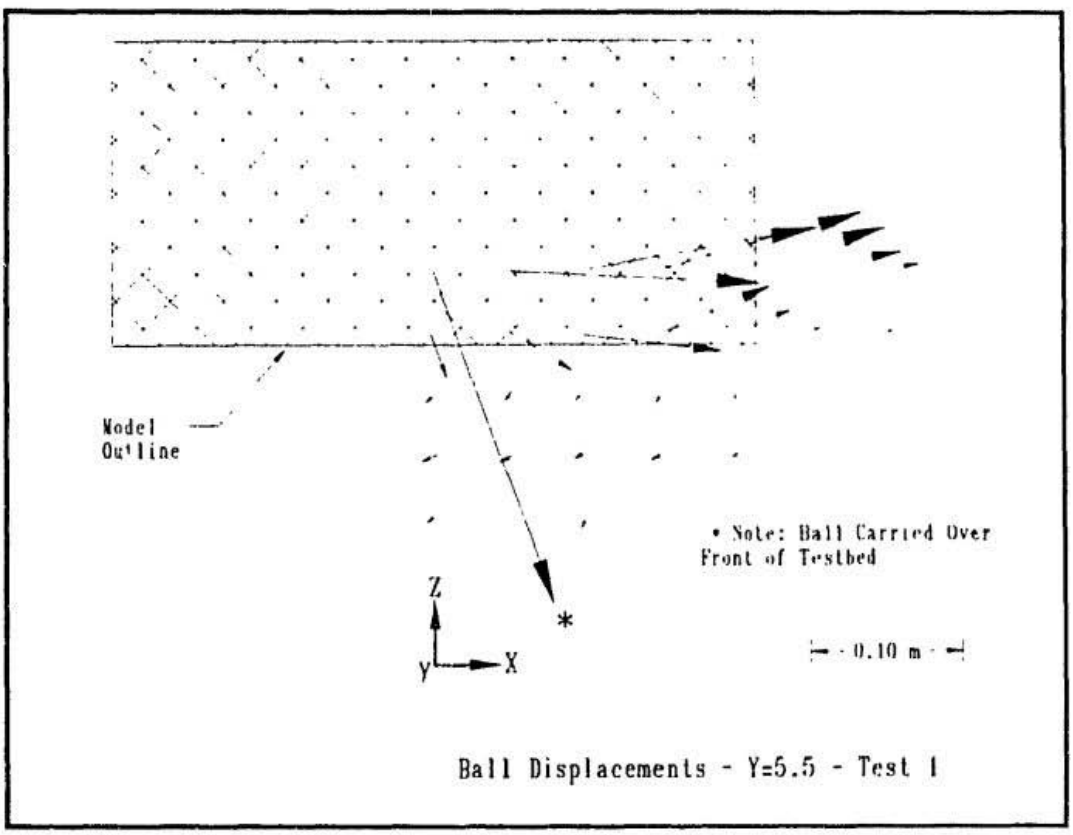

Ball Displacements - Y=5.5 - Test 1

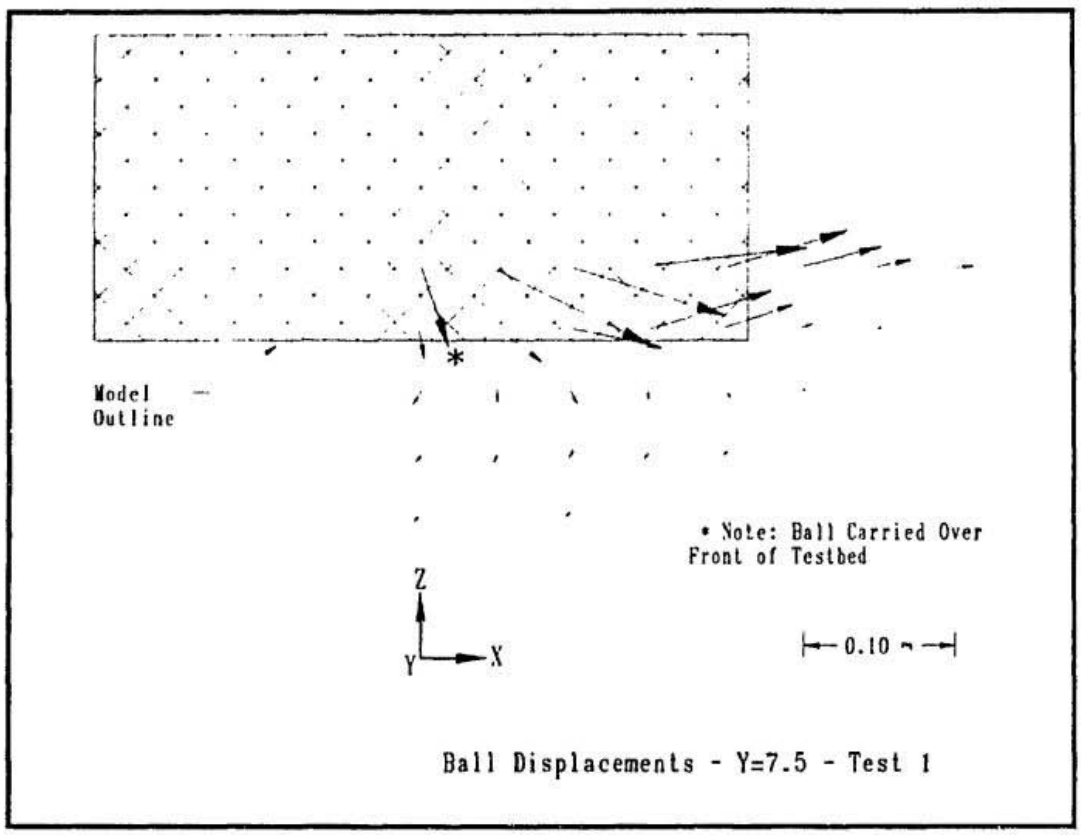

Ball Displacements - Y=7.5 - Test 1

Solder Strand Displacements

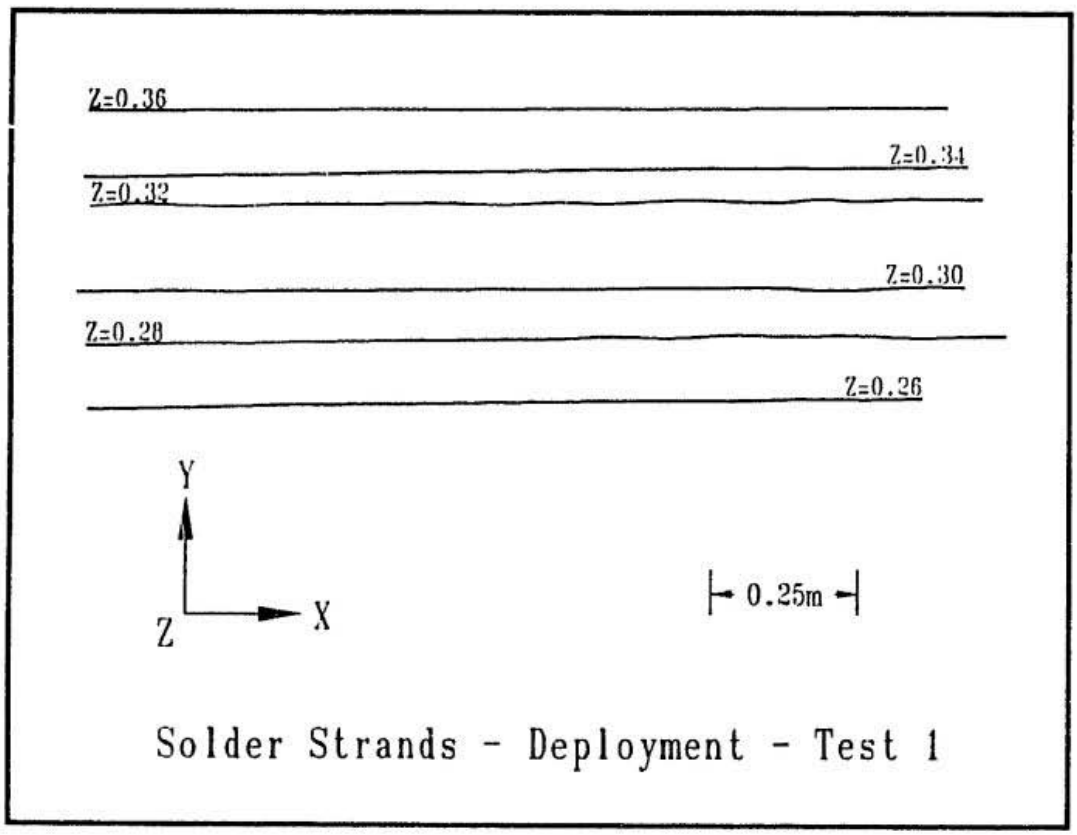

Solder Strands - Deployment - Test 1

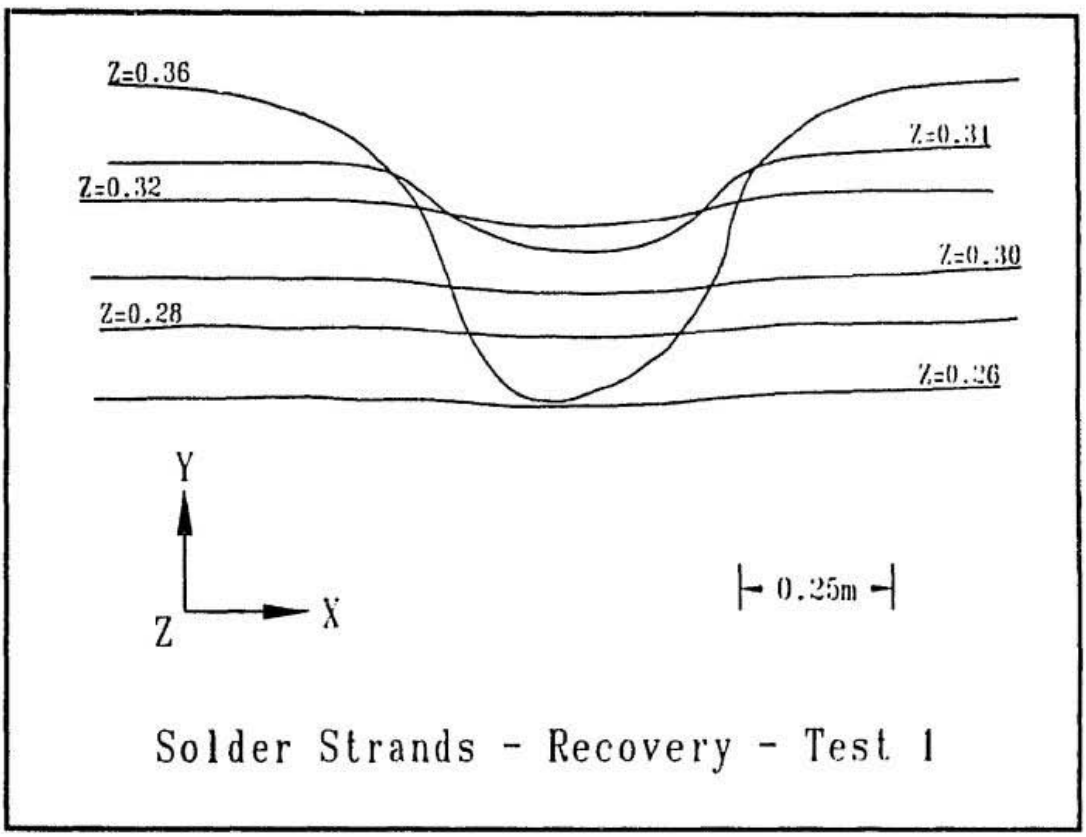

Solder Strands - Recovery - Test 1

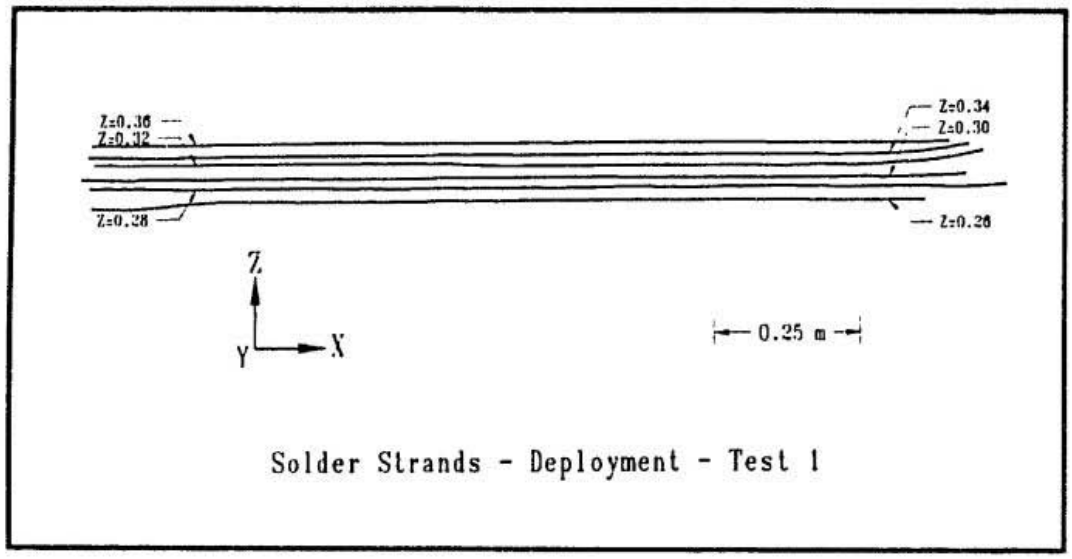

Solder Strands - Deployment - Test 1

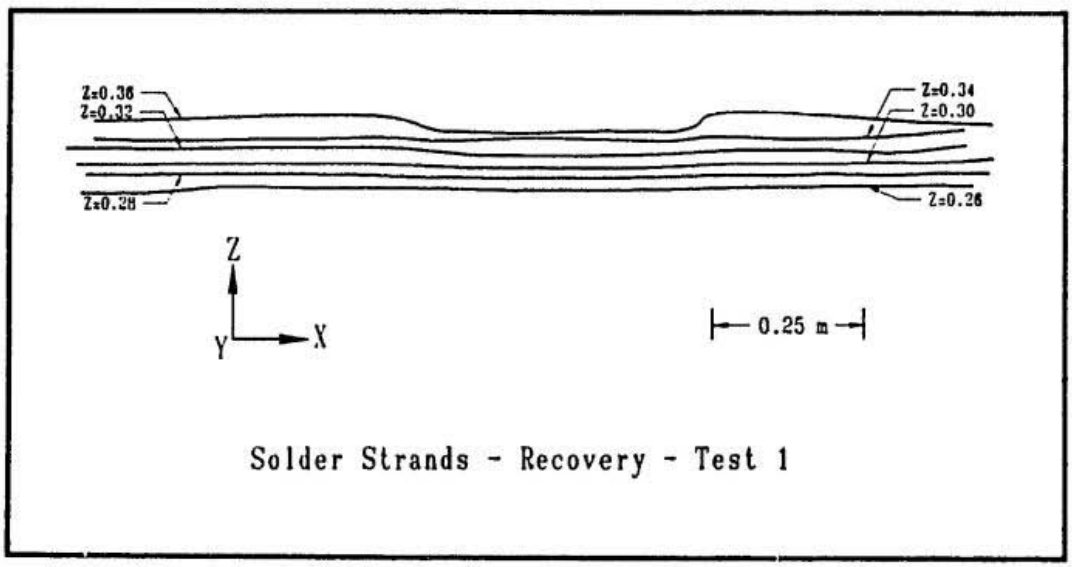

Solder Strands - Recovery - Test 1

Appendix D

Test 2 Results

Instrumentation Output

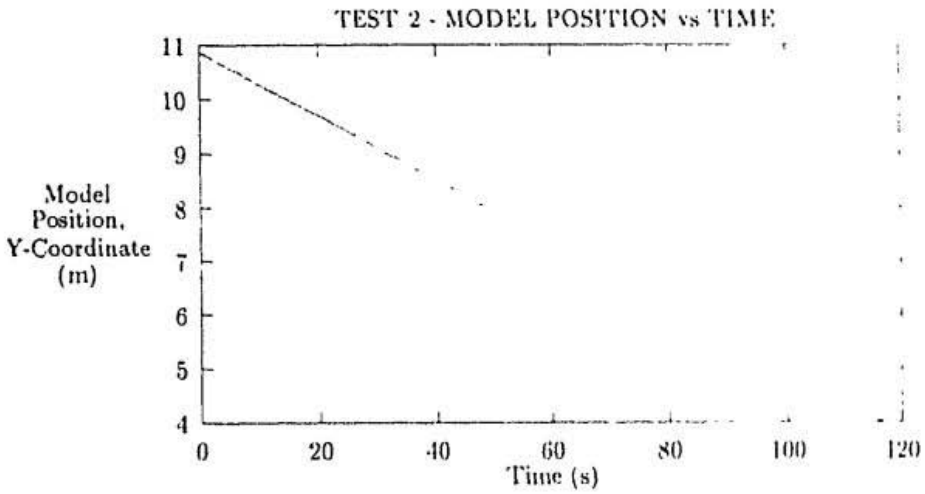
TEST 2 - MODEL POSITION vs TIME
Model Position, Y-Coordinate (m)
11
10
9
8
7
6
5
4
0
20
40
60
80
100
120
Time (s)

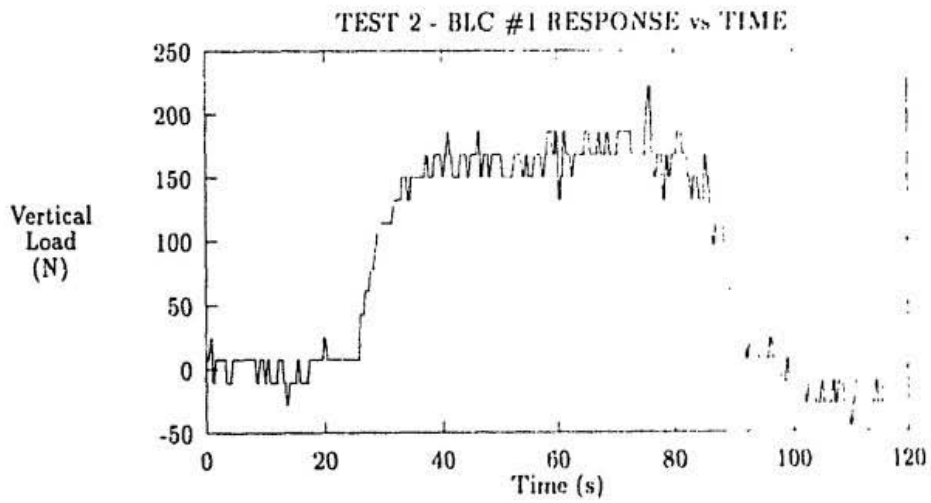
TEST 2 - BLC #1 RESPONSE vs TIME
Vertical Load (N)
250
200
150
100
50
0
-50
0
20
40
60
80
100
120
Time (s)

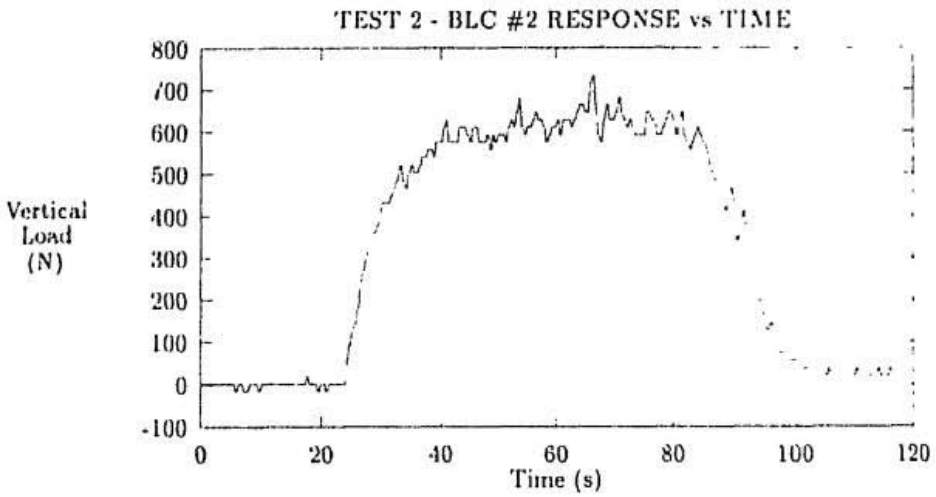
TEST 2 - BLC #2 RESPONSE vs TIME
Vertical Load (N)
800
700
600
500
400
300
200
100
0
-100
0
20
40
60
80
100
120
Time (s)

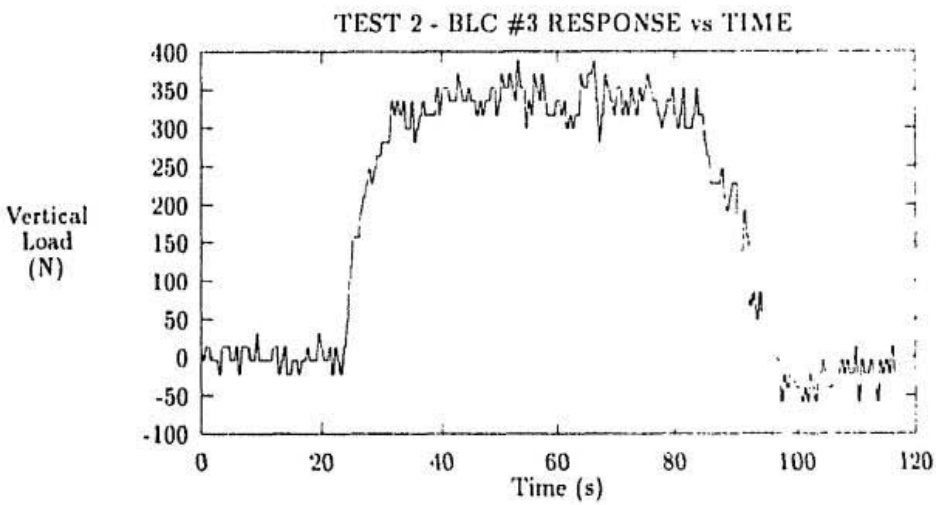
TEST 2 - BLC #3 RESPONSE vs TIME
Vertical Load (N)
400
350
300
250
200
150
100
50
0
-50
-100
0
20
40
60
80
100
120
Time (s)

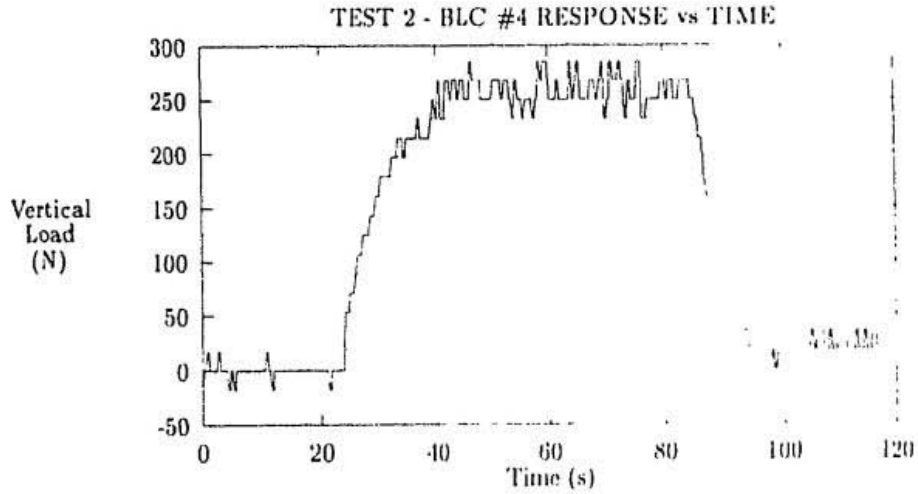
TEST 2 - BLC #4 RESPONSE vs TIME
Vertical Load (N)
300
250
200
150
100
50
0
-50
0
20
40
60
80
100
120
Time (s)

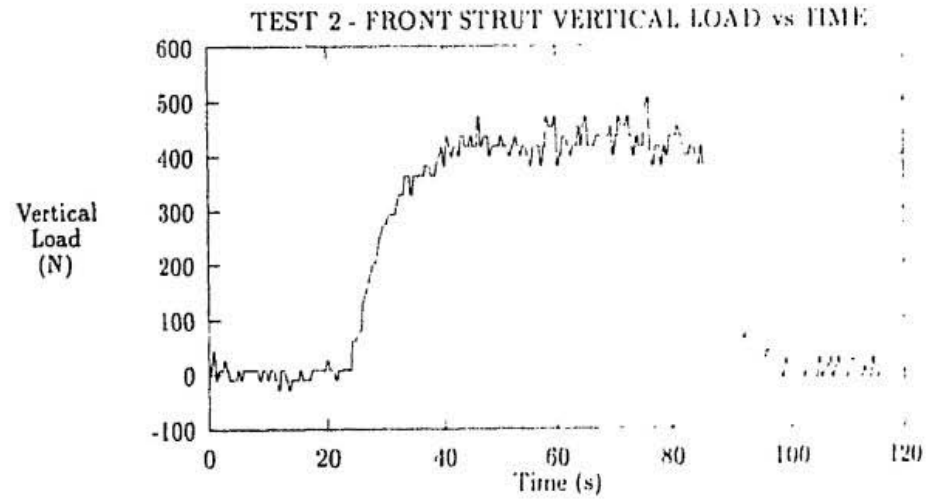
TEST 2 - FRONT STRUT VERTICAL LOAD vs TIME
Vertical Load (N)
600
500
400
300
200
100
0
-100
0
20
40
60
80
100
120
Time (s)

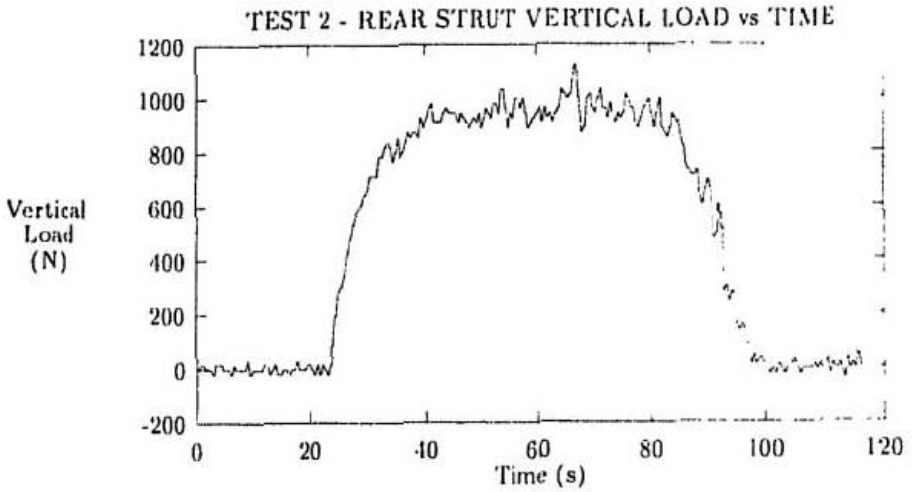
TEST 2 - REAR STRUT VERTICAL LOAD vs TIME
Vertical Load (N)
1200
1000
800
600
400
200
0
-200
0
20
40
60
80
100
120
Time (s)

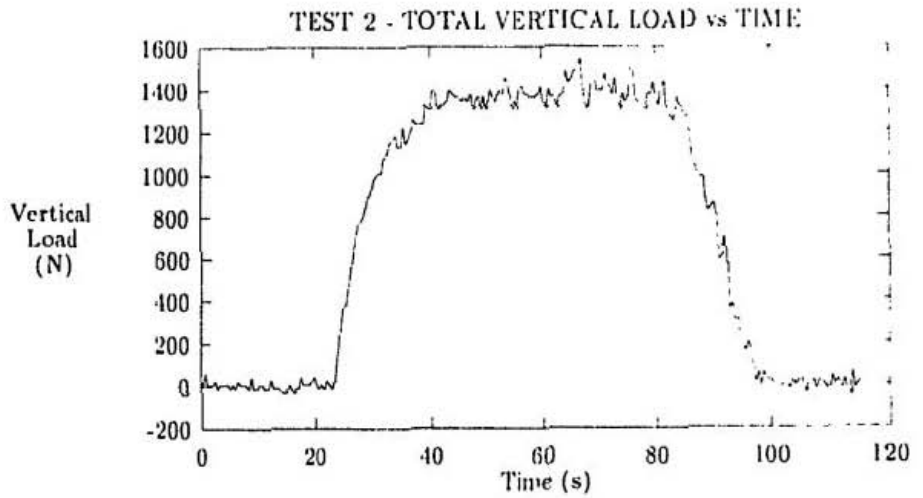
TEST 2 - TOTAL VERTICAL LOAD vs TIME
Vertical Load (N)
1600
1400
1200
1000
800
600
400
200
0
-200
0
20
40
60
80
100
120
Time (s)

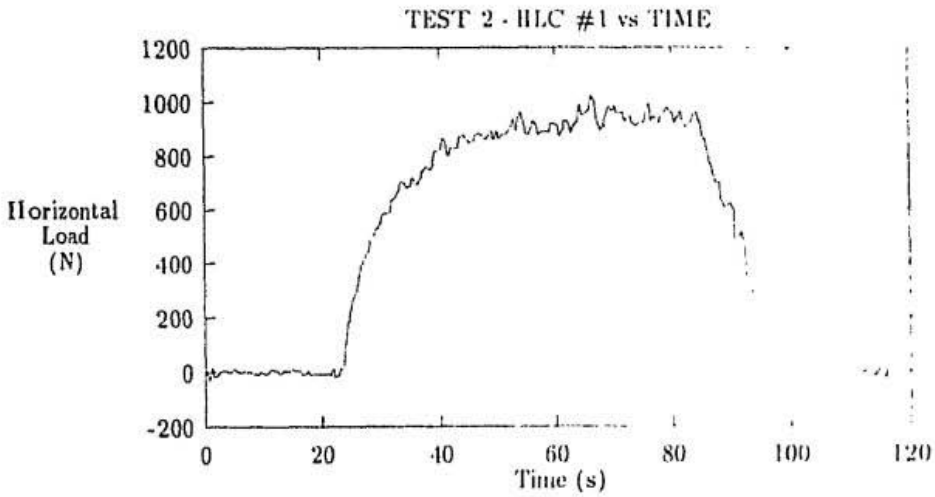
TEST 2 - HLC #1 vs TIME
Horizontal Load (N)
1200
1000
800
600
400
200
0
-200
0
20
40
60
80
100
120
Time (s)

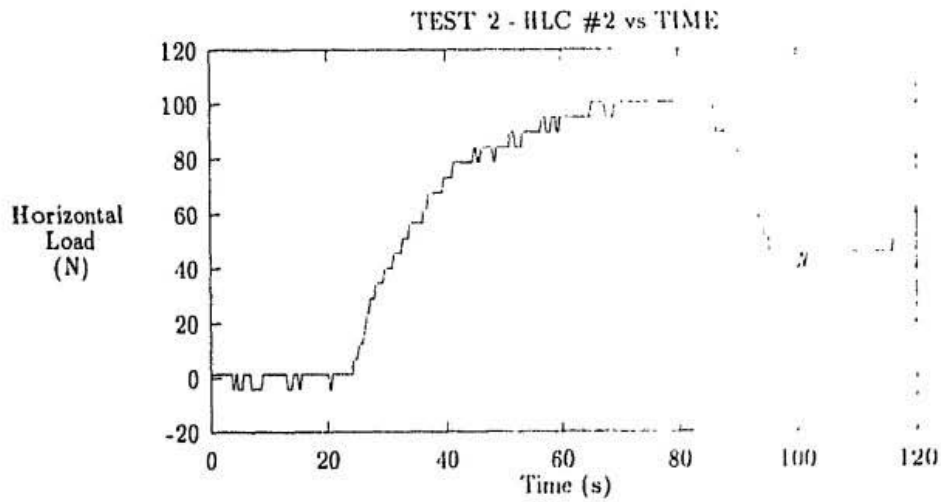
TEST 2 - HLC #2 vs TIME
Horizontal Load (N)
120
100
80
60
40
20
0
-20
0
20
40
60
80
100
120
Time (s)

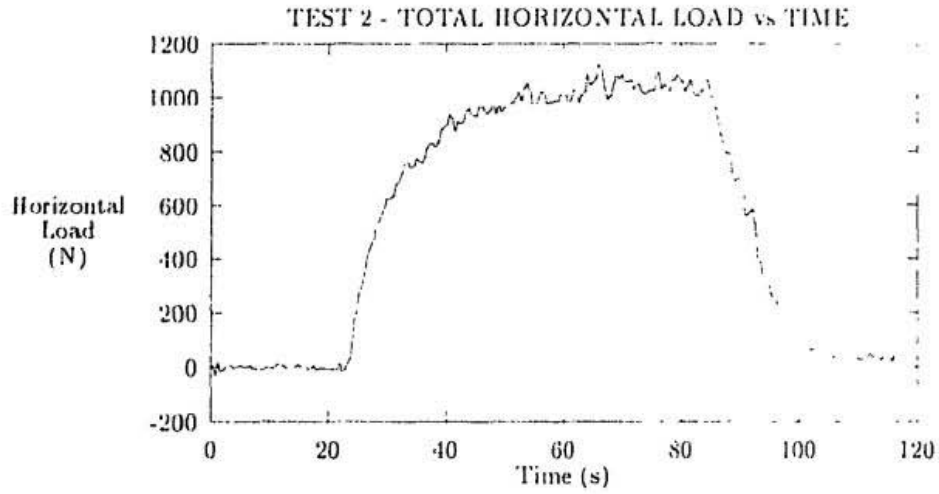
TEST 2 - TOTAL HORIZONTAL LOAD vs TIME
Horizontal Load (N)
1200
1000
800
600
400
200
0
-200
0
20
40
60
80
100
120
Time (s)

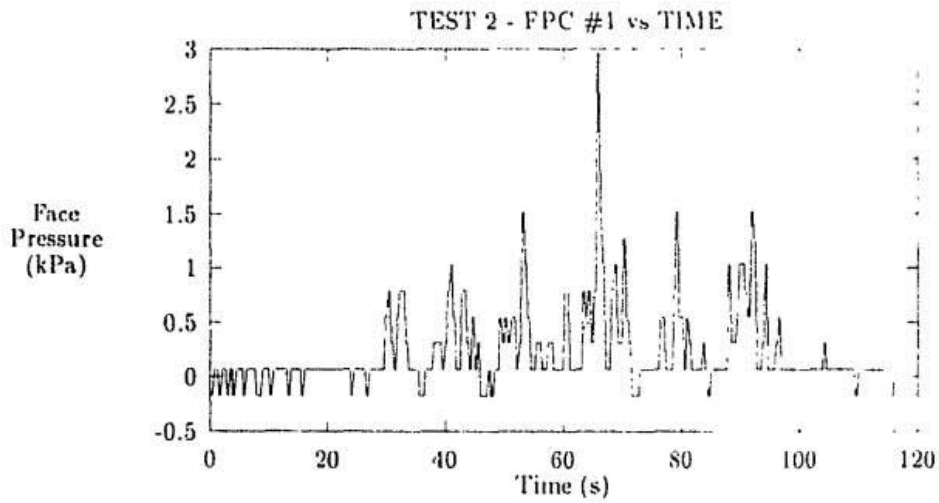
TEST 2 - FPC #1 vs TIME
Face Pressure (kPa)
3
2.5
2
1.5
1
0.5
0
-0.5
0
20
40
60
80
100
120
Time (s)

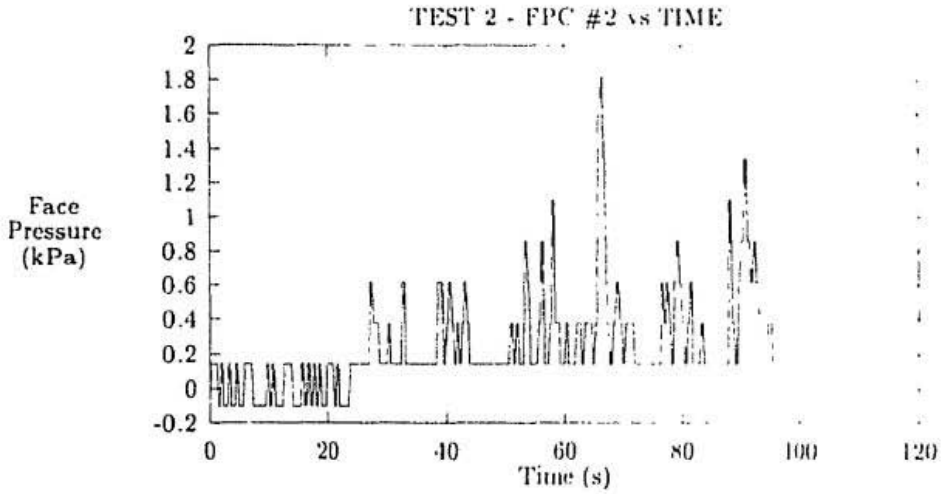
TEST 2 - FPC #2 vs TIME
Face Pressure (kPa)
2
1.8
1.6
1.4
1.2
1
0.8
0.6
0.4
0.2
0
-0.2
0
20
40
60
80
100
120
Time (s)

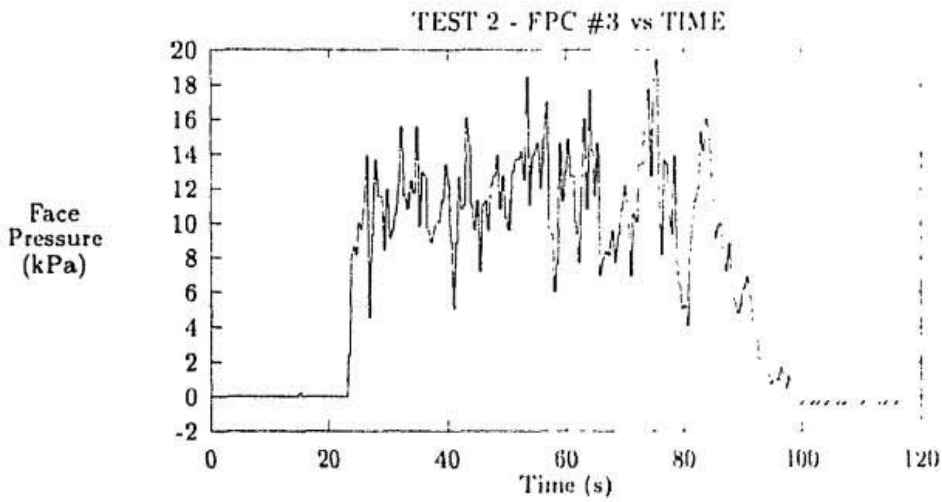
TEST 2 - FPC #3 vs TIME
Face Pressure (kPa)
20
18
16
14
12
10
8
6
4
2
0
-2
0
20
40
60
80
100
120
Time (s)

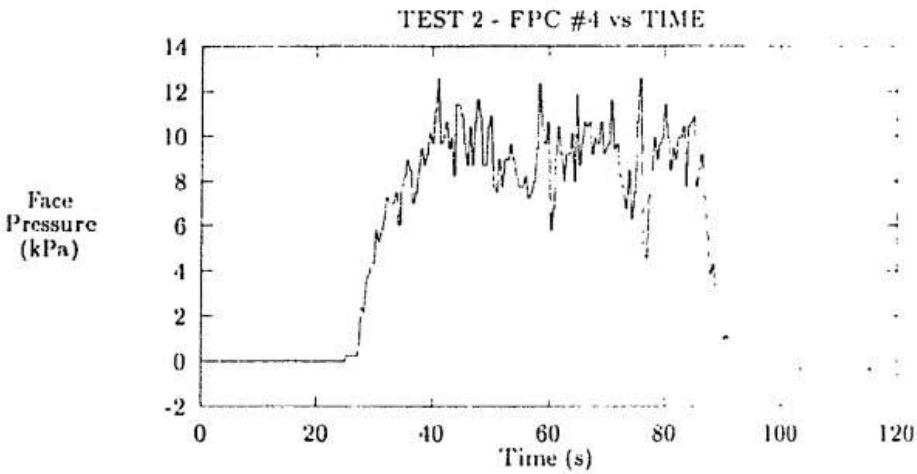
TEST 2 - FPC #4 vs TIME
Face Pressure (kPa)
14
12
10
8
6
4
2
0
-2
0
20
40
60
80
100
120
Time (s)

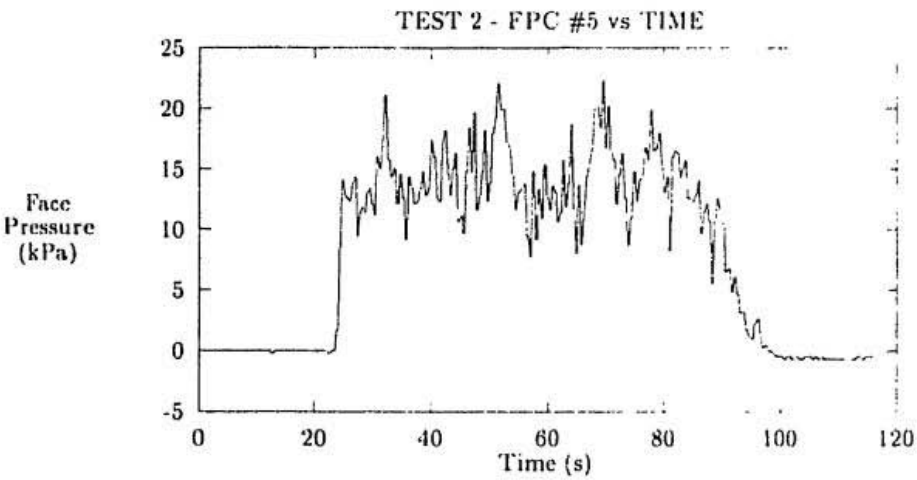
TEST 2 - FPC #5 vs TIME
Face Pressure (kPa)
25
20
15
10
5
0
-5
0
20
40
60
80
100
120
Time (s)

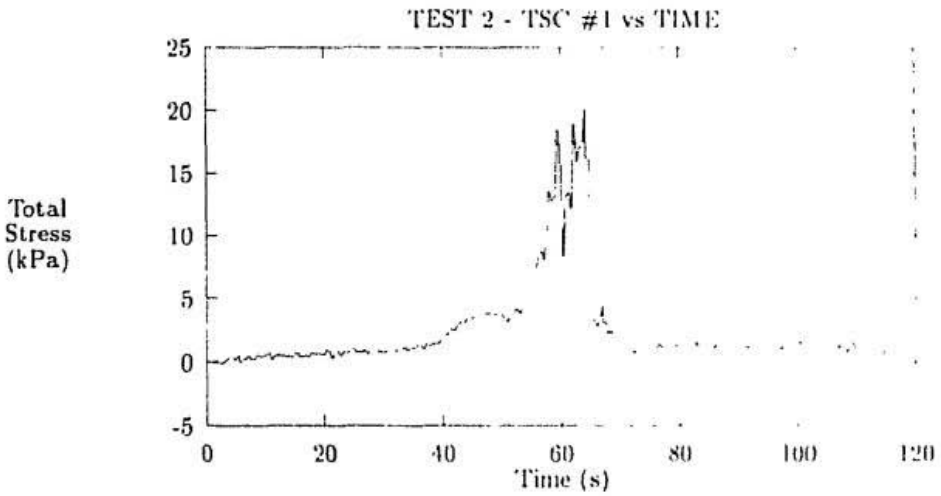
TEST 2 - TSC #1 vs TIME
Total Stress (kPa)
25
20
15
10
5
0
-5
0
20
40
60
80
100
120
Time (s)

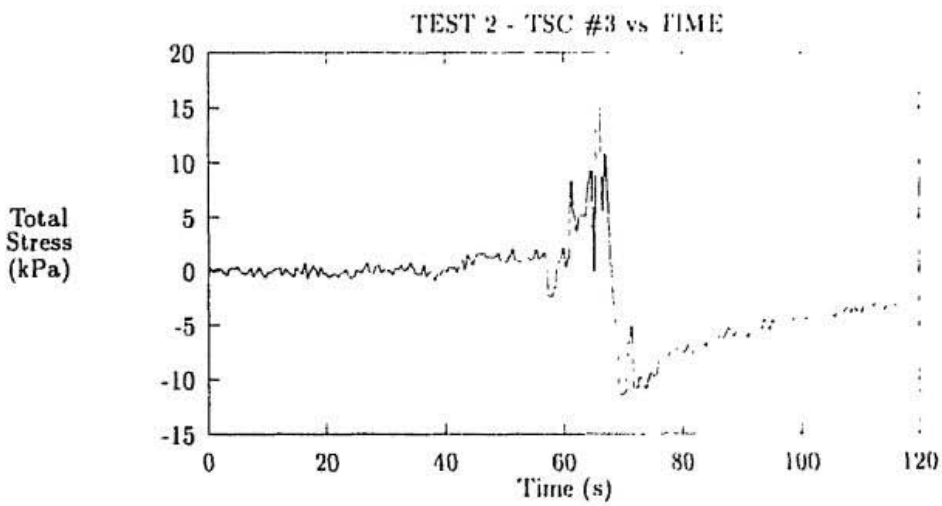
TEST 2 - TSC #3 vs TIME
Total Stress (kPa)
20
15
10
5
0
-5
-10
-15
0
20
40
60
80
100
120
Time (s)

Scour Profiles

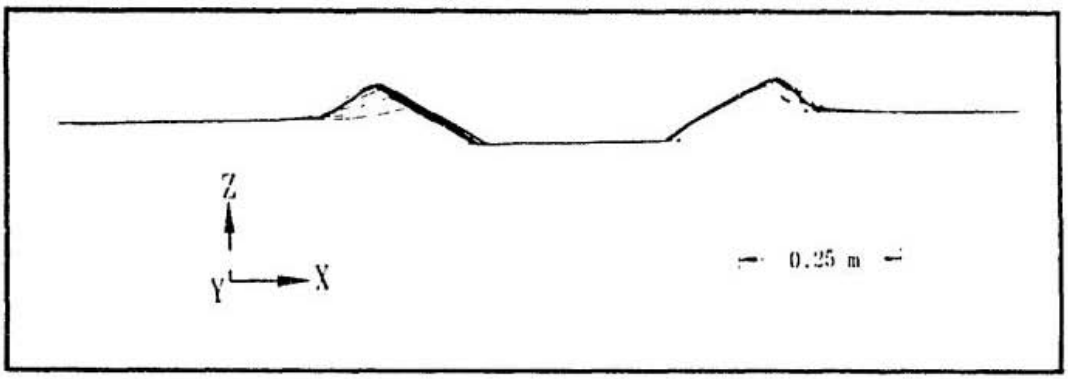
Z
Y
X
0.25 m

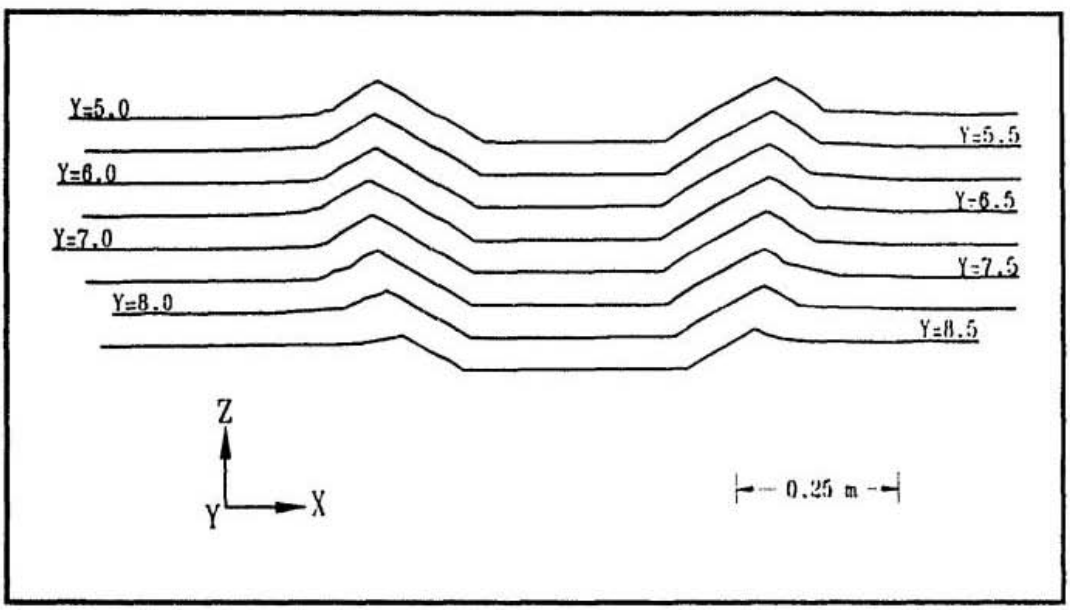
Y=5.0
Y=5.5
Y=6.0
Y=6.5
Y=7.0
Y=7.5
Y=8.0
Y=8.5
Z
Y
X
0.25 m

Ball Bearing Displacements

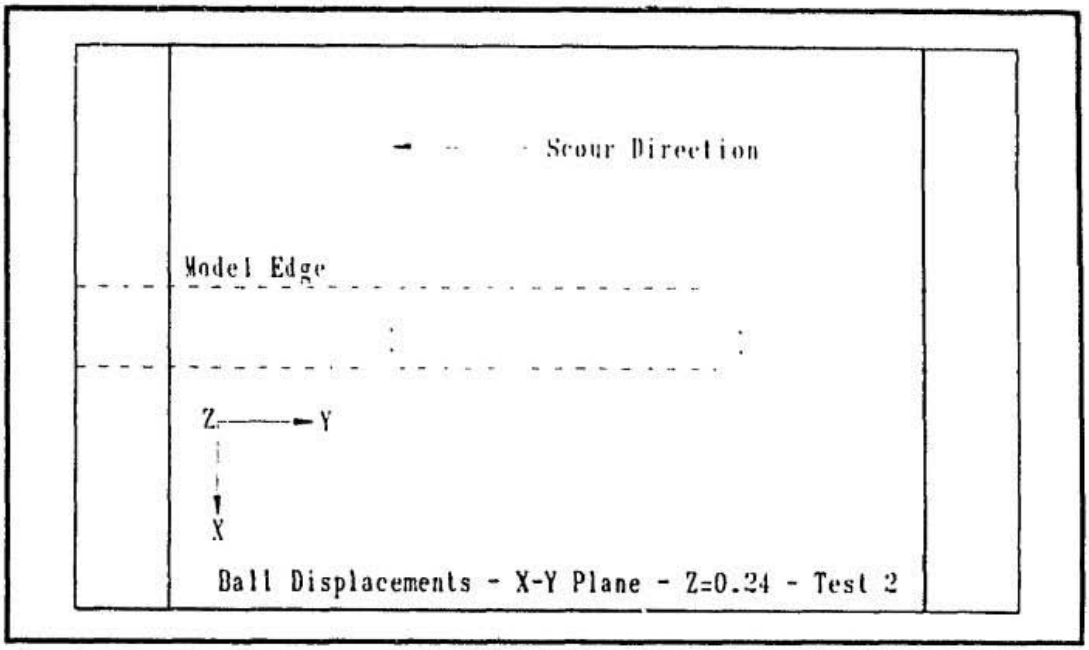
Scour Direction
Model Edge
Z
Y
X
Ball Displacements - X-Y Plane - Z=0.24 - Test 2

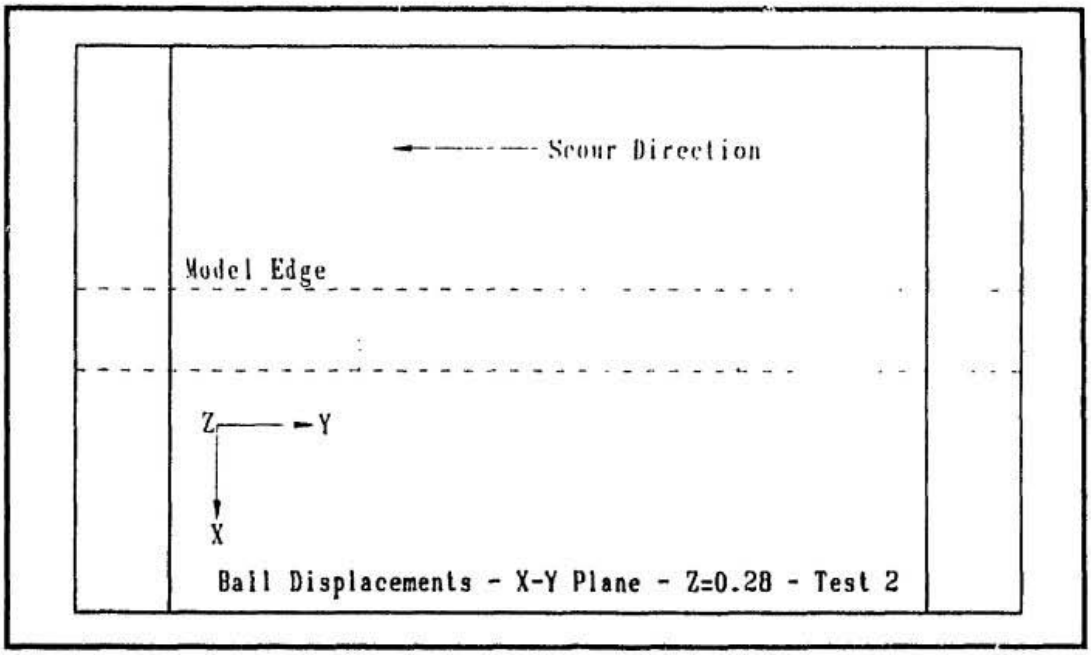
Scour Direction
Model Edge
Z
Y
X
Ball Displacements - X-Y Plane - Z=0.28 - Test 2

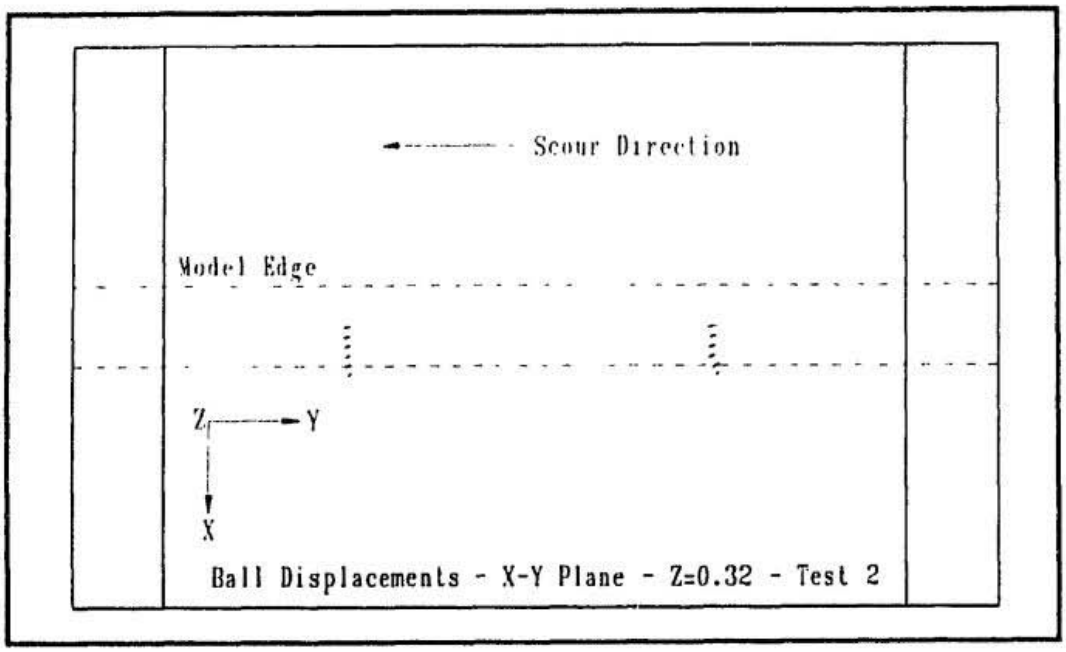
Scour Direction
Model Edge
Z
Y
X
Ball Displacements - X-Y Plane - Z=0.32 - Test 2

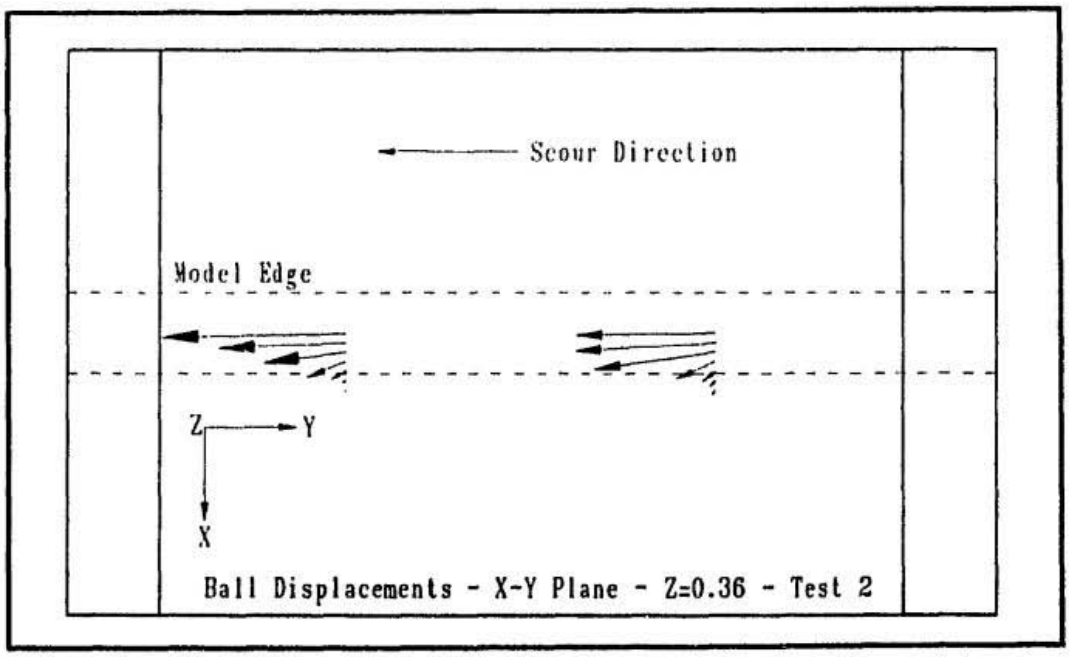
Scour Direction
Model Edge
Z
Y
X
Ball Displacements - X-Y Plane - Z=0.36 - Test 2

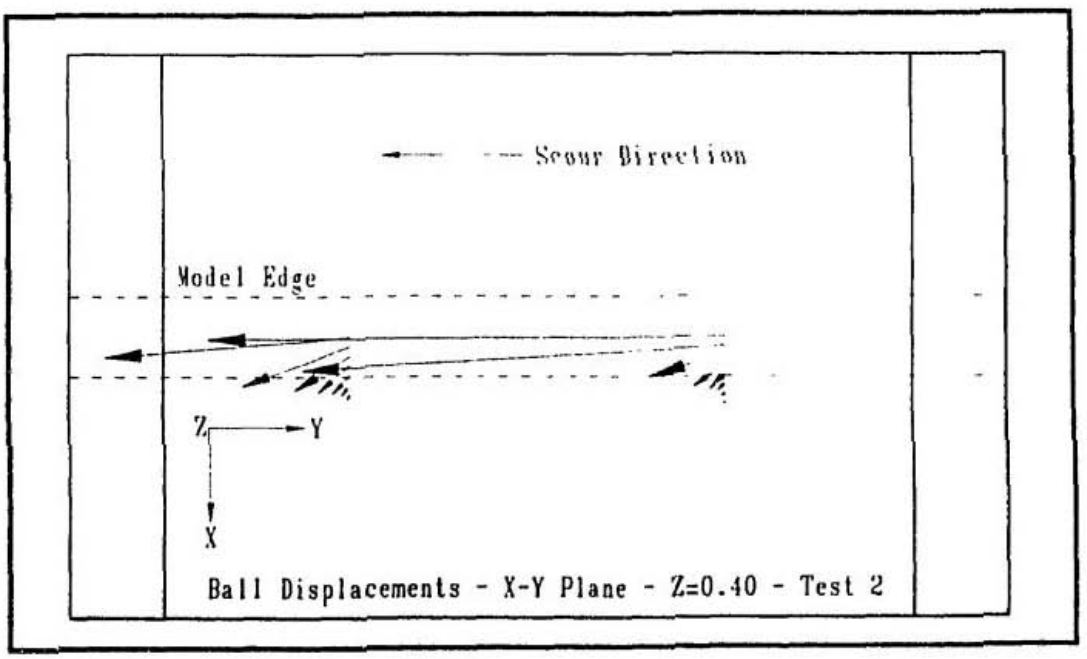
Scour Direction
Model Edge
Z
Y
X
Ball Displacements - X-Y Plane - Z=0.40 - Test 2

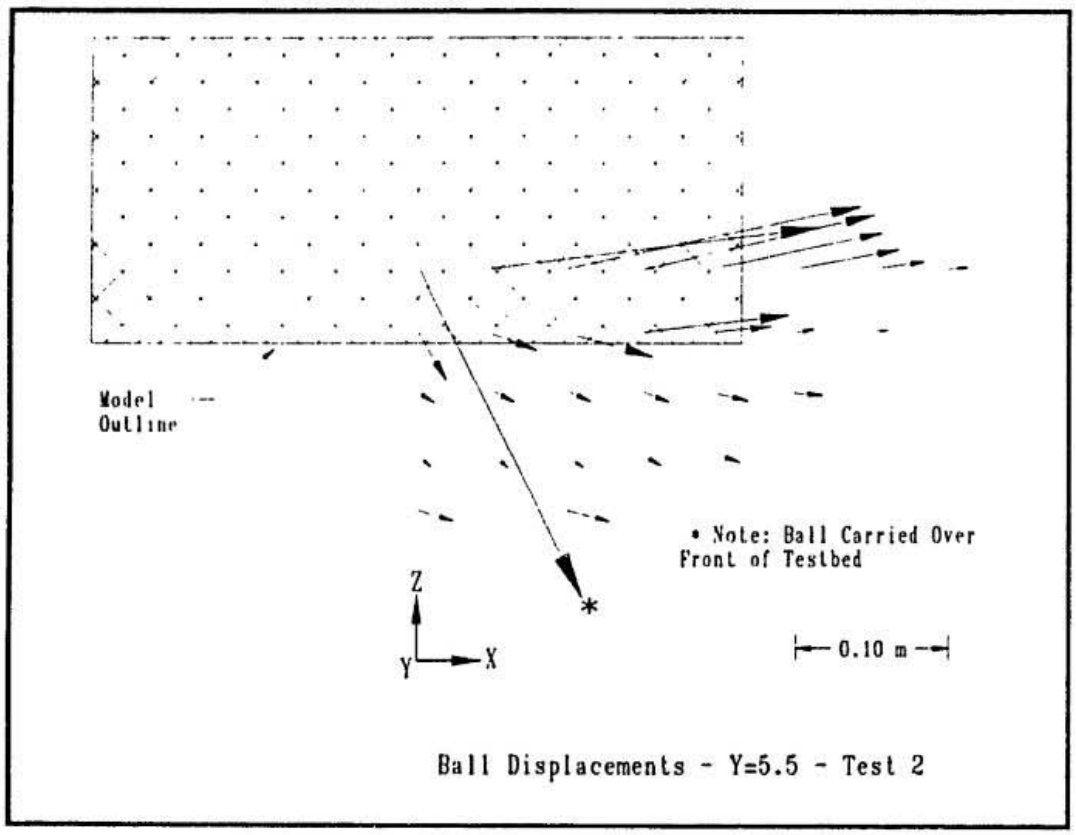

Ball Displacements - Y=5.5 - Test 2

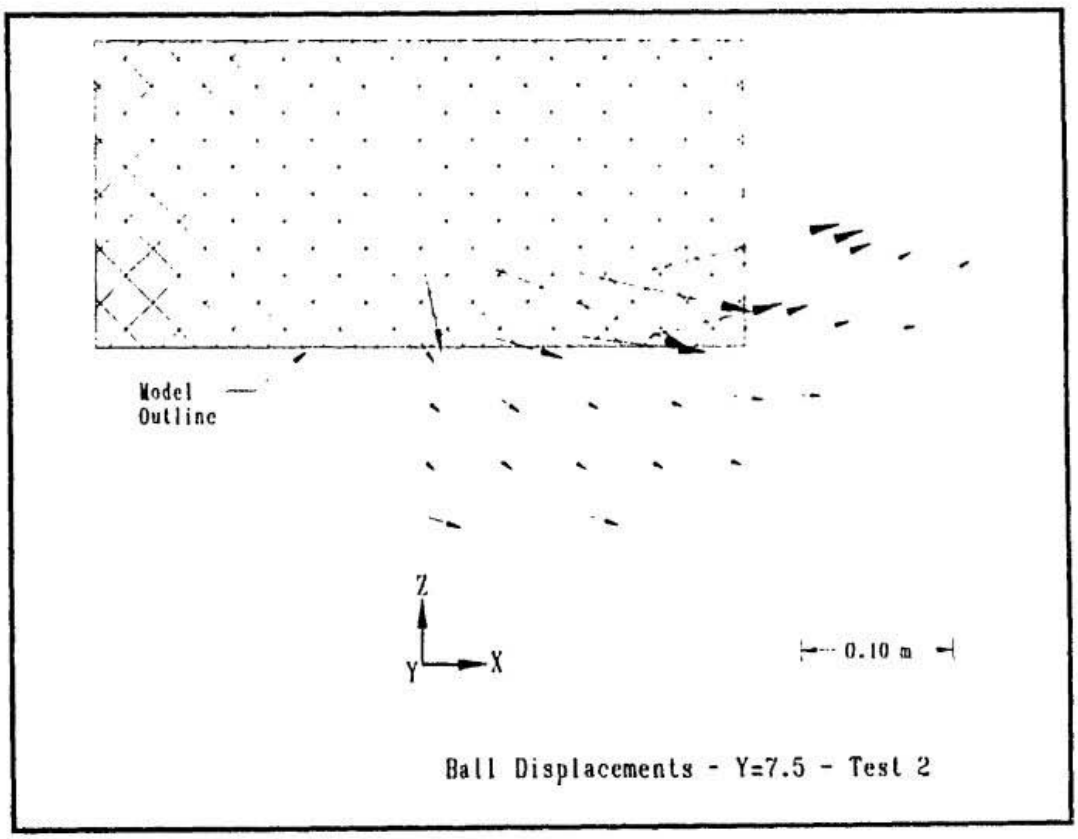

Ball Displacements - Y=7.5 - Test 2

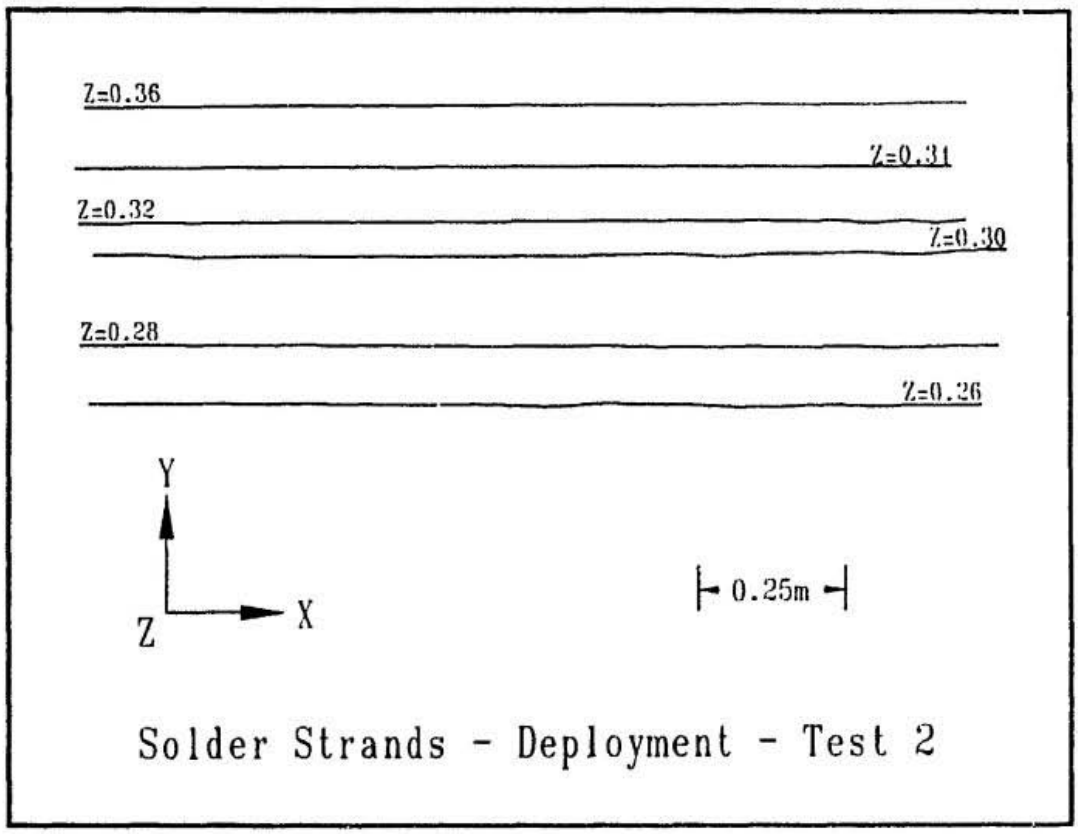

Solder Strands - Deployment - Test 2

Solder Strand Displacements

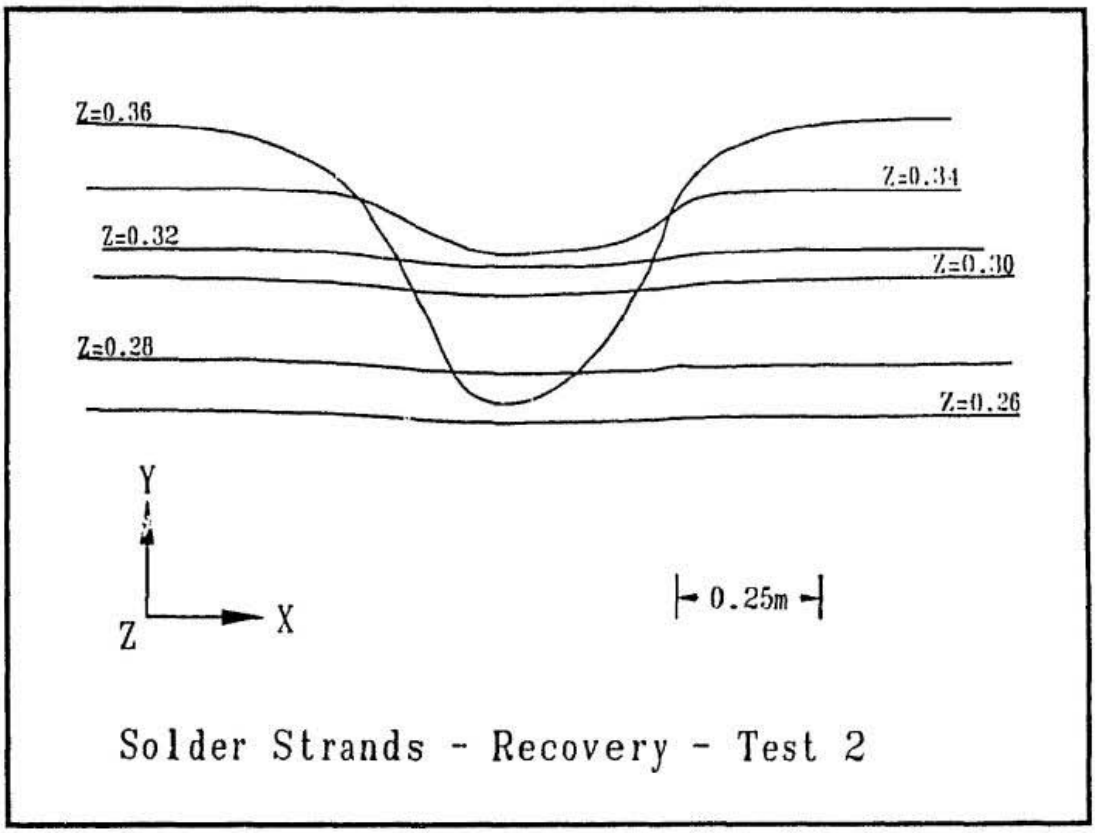

Solder Strands - Recovery - Test 2

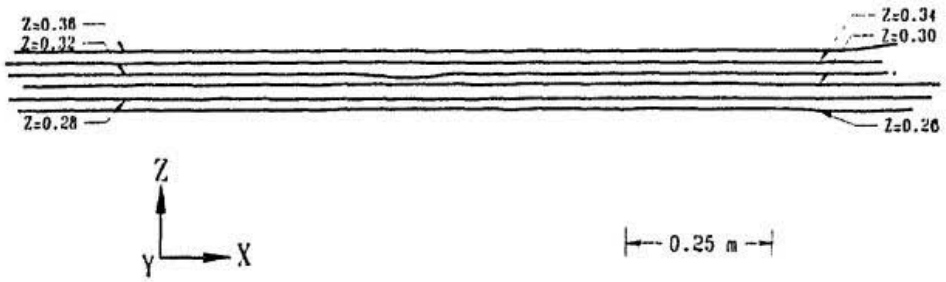

Solder Strands - Deployment - Test 2

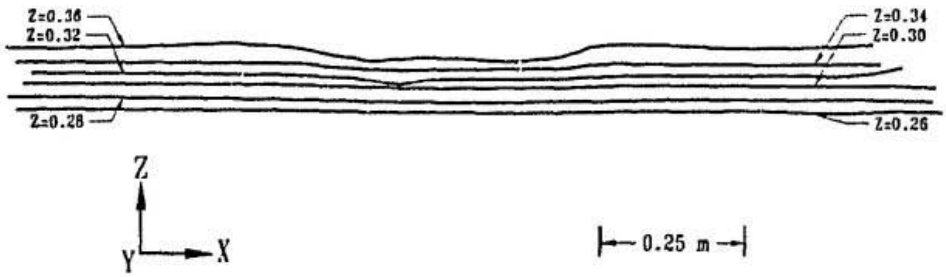

Solder Strands - Recovery - Test 2

Appendix E

Test 3 Results

Instrumentation Output

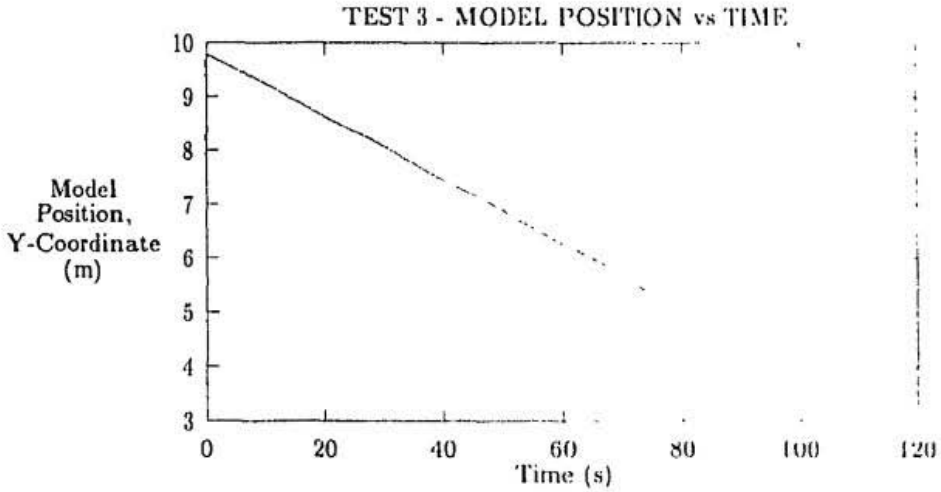
TEST 3 - MODEL POSITION vs TIME
Model Position, Y-Coordinate (m)
10
9
8
7
6
5
4
3
0
20
40
60
80
100
120
Time (s)

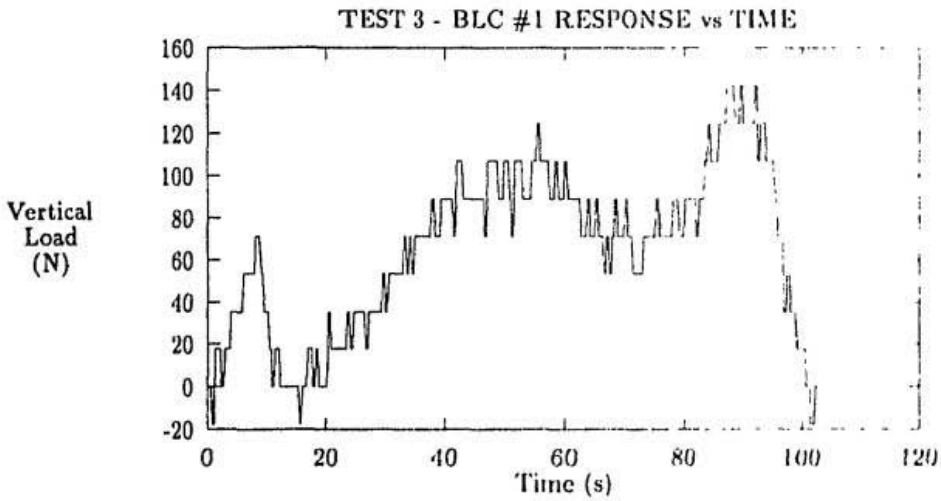
TEST 3 - BLC #1 RESPONSE vs TIME
Vertical Load (N)
160
140
120
100
80
60
40
20
0
-20
0
20
40
60
80
100
120
Time (s)

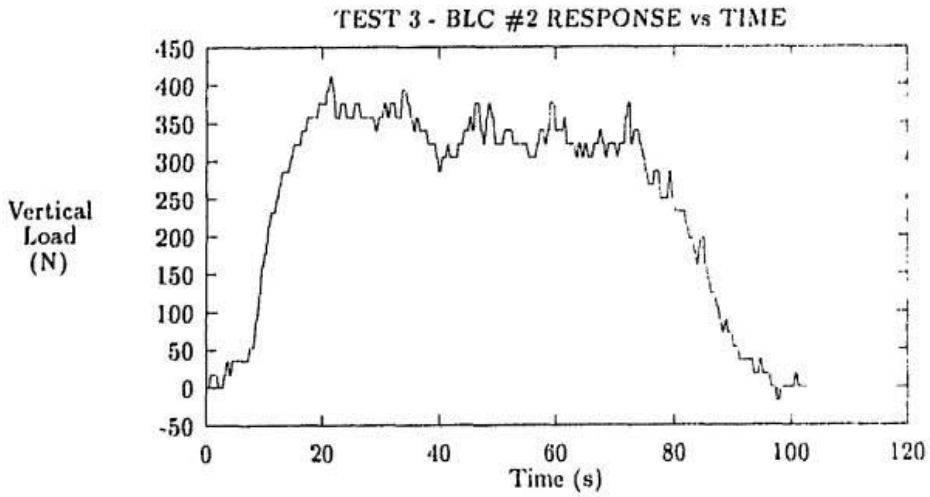
TEST 3 - BLC #2 RESPONSE vs TIME
Vertical Load (N)
450
400
350
300
250
200
150
100
50
0
-50
0
20
40
60
80
100
120
Time (s)

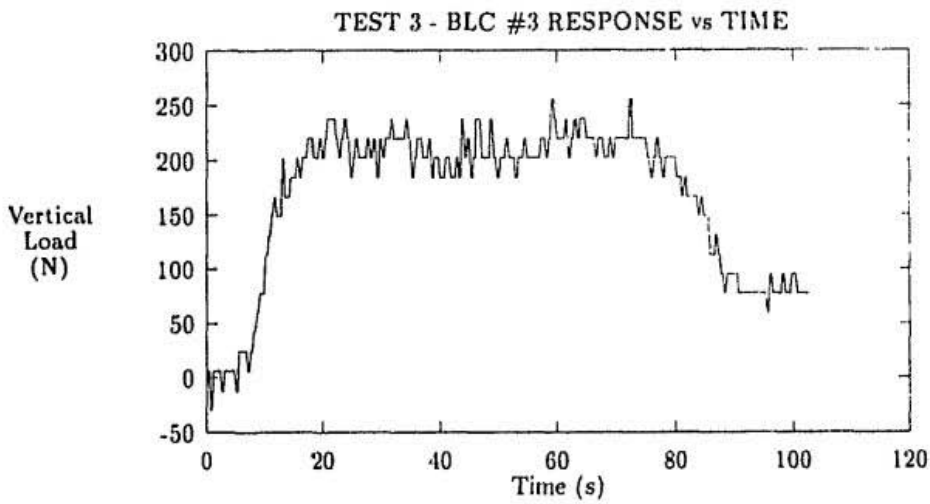
TEST 3 - BLC #3 RESPONSE vs TIME
Vertical Load (N)
300
250
200
150
100
50
0
-50
0
20
40
60
80
100
120
Time (s)

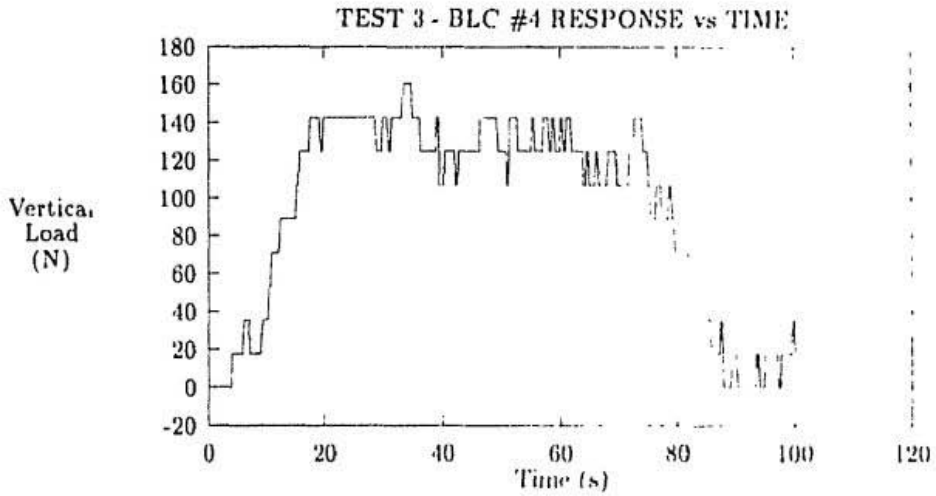
TEST 3 - BLC #4 RESPONSE vs TIME
Vertical Load (N)
180
160
140
120
100
80
60
40
20
0
-20
0
20
40
60
80
100
120
Time (s)

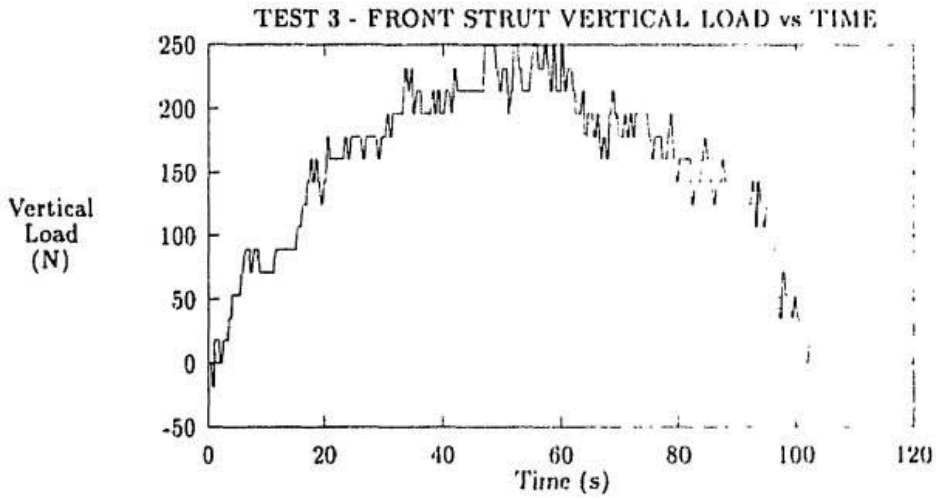
TEST 3 - FRONT STRUT VERTICAL LOAD vs TIME
Vertical Load (N)
250
200
150
100
50
0
-50
0
20
40
60
80
100
120
Time (s)

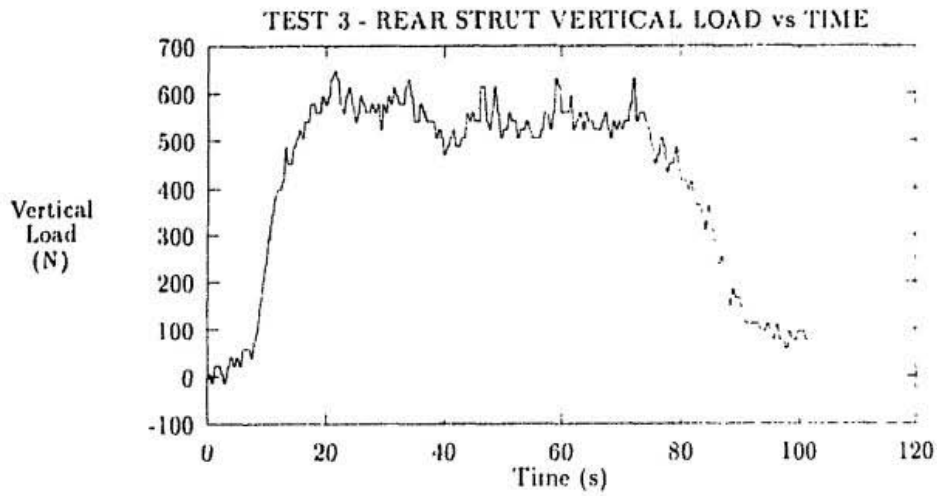
TEST 3 - REAR STRUT VERTICAL LOAD vs TIME
Vertical Load (N)
700
600
500
400
300
200
100
0
-100
0
20
40
60
80
100
120
Time (s)

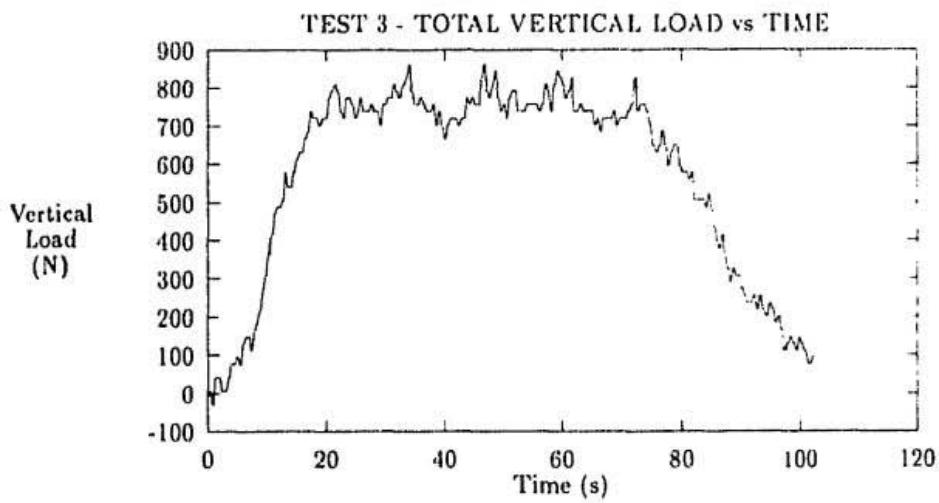
TEST 3 - TOTAL VERTICAL LOAD vs TIME
Vertical Load (N)
900
800
700
600
500
400
300
200
100
0
-100
0
20
40
60
80
100
120
Time (s)

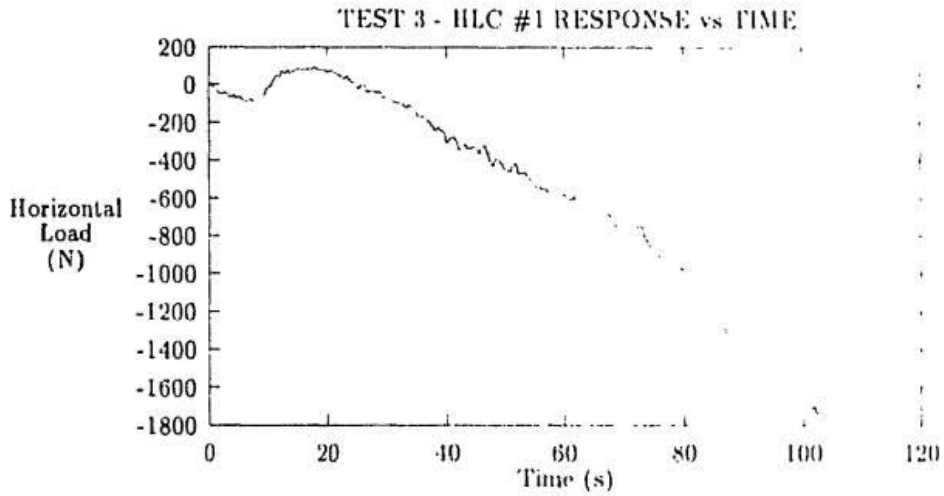
TEST 3 - HLC #1 RESPONSE vs TIME
Horizontal Load (N)
200
0
-200
-400
-600
-800
-1000
-1200
-1400
-1600
-1800
0
20
40
60
80
100
120
Time (s)

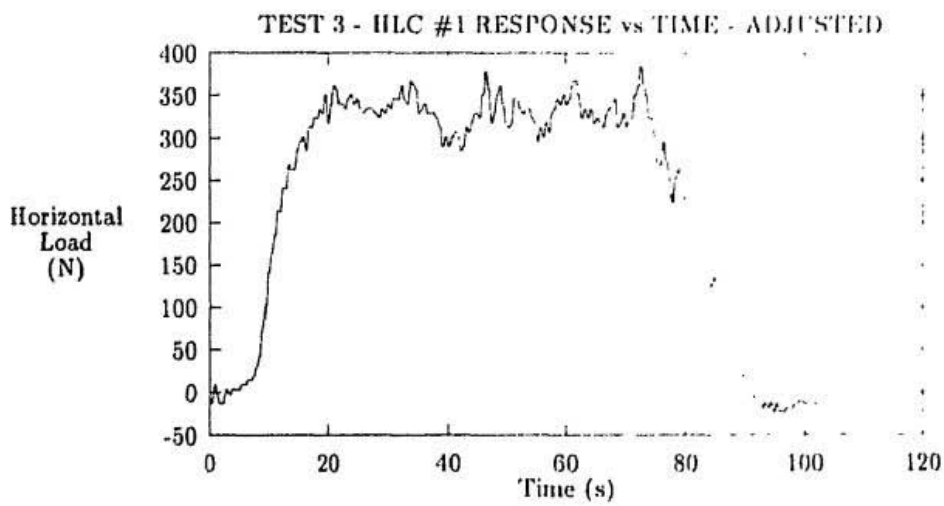
TEST 3 - HLC #1 RESPONSE vs TIME - ADJUSTED
Horizontal Load (N)
400
350
300
250
200
150
100
50
0
-50
0
20
40
60
80
100
120
Time (s)

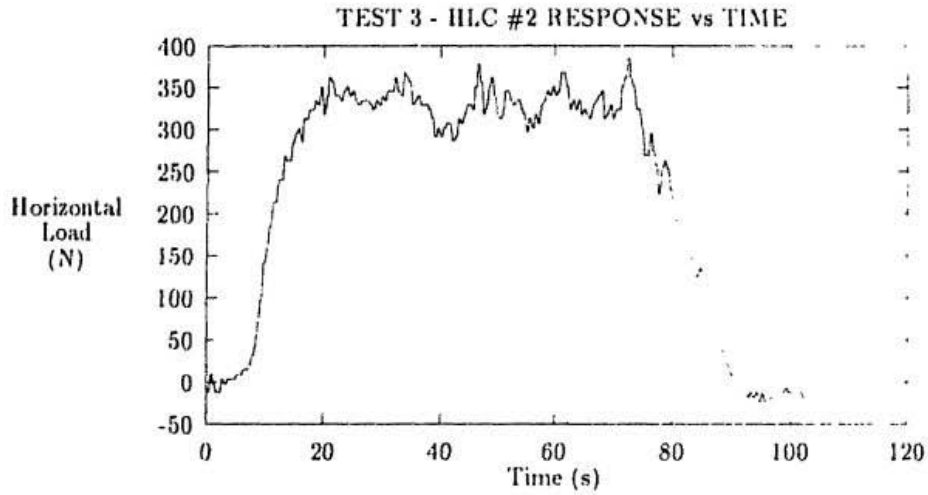
TEST 3 - HLC #2 RESPONSE vs TIME
Horizontal Load (N)
400
350
300
250
200
150
100
50
0
-50
0
20
40
60
80
100
120
Time (s)

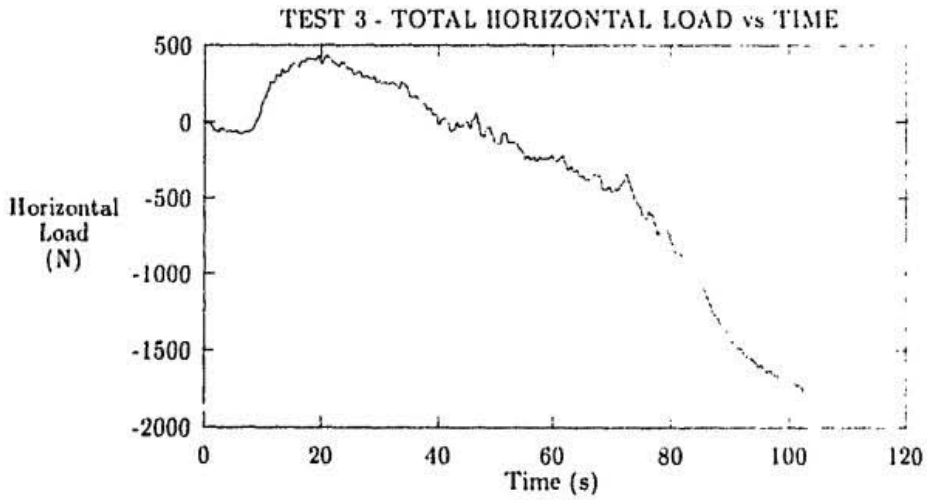
TEST 3 - TOTAL HORIZONTAL LOAD vs TIME
Horizontal Load (N)
500
0
-500
-1000
-1500
-2000
0
20
40
60
80
100
120
Time (s)

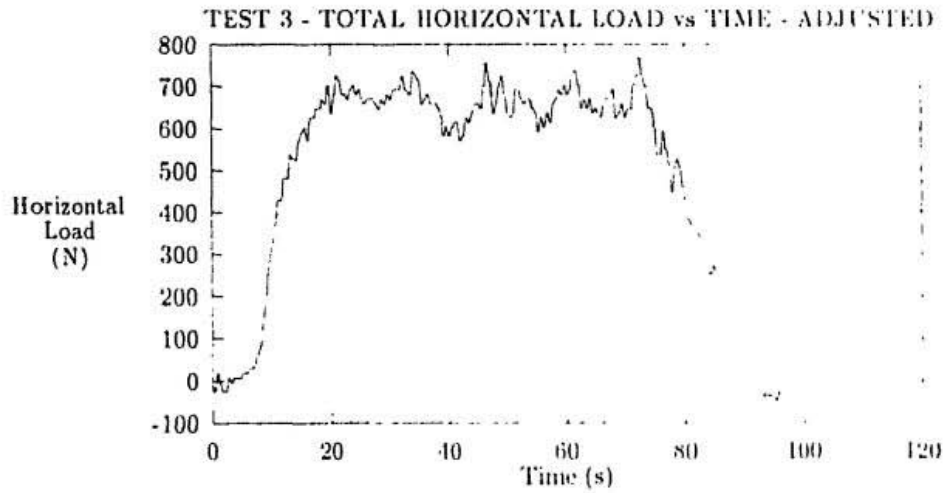
TEST 3 - TOTAL HORIZONTAL LOAD vs TIME - ADJUSTED
Horizontal Load (N)
800
700
600
500
400
300
200
100
0
-100
0
20
40
60
80
100
120
Time (s)

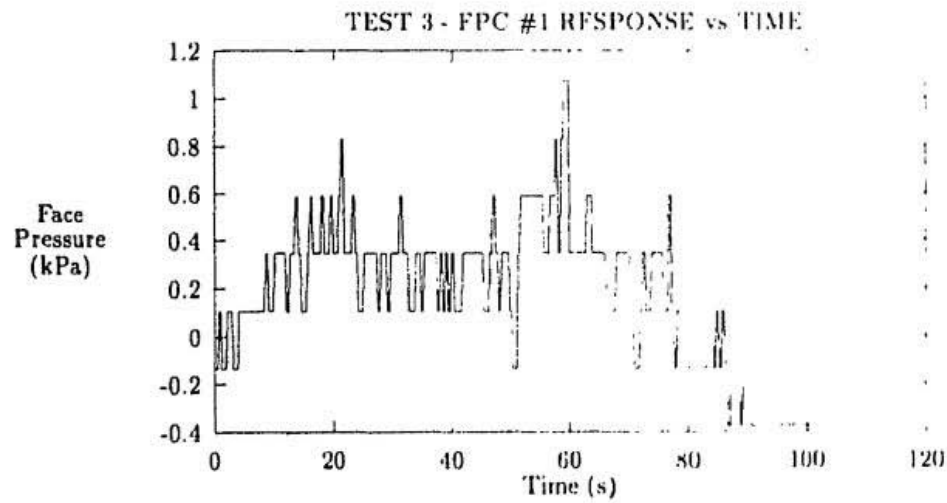
TEST 3 - FPC #1 RESPONSE vs TIME
Face Pressure (kPa)
1.2
1
0.8
0.6
0.4
0.2
0
-0.2
-0.4
0
20
40
60
80
100
120
Time (s)

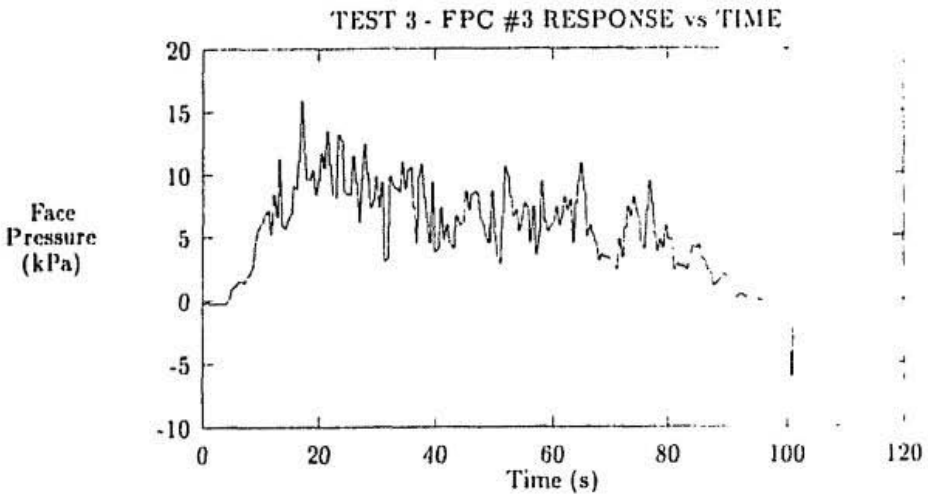
TEST 3 - FPC #3 RESPONSE vs TIME
Face Pressure (kPa)
20
15
10
5
0
-5
-10
0
20
40
60
80
100
120
Time (s)

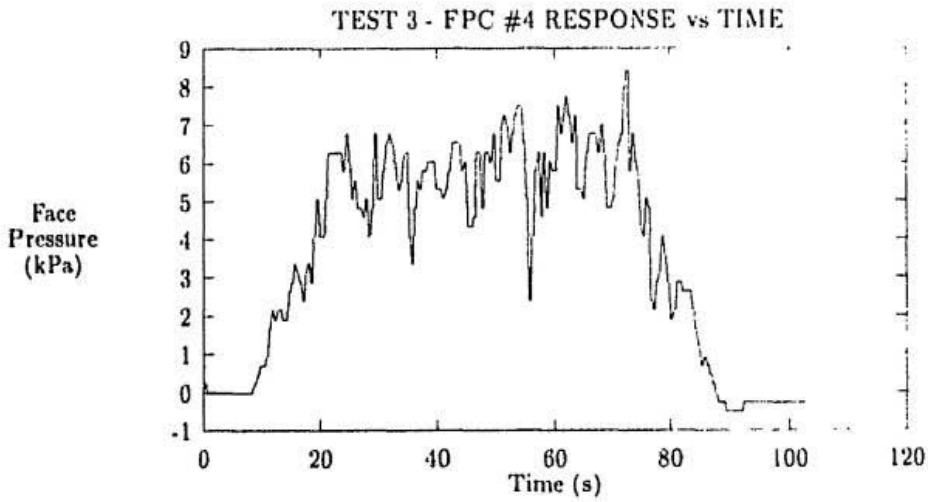
TEST 3 - FPC #4 RESPONSE vs TIME
Face Pressure (kPa)
9
8
7
6
5
4
3
2
1
0
-1
0
20
40
60
80
100
120
Time (s)

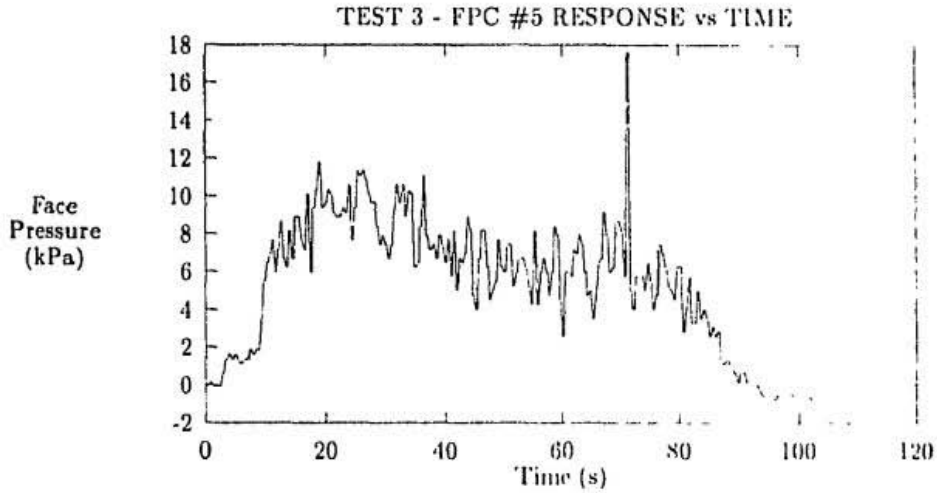
TEST 3 - FPC #5 RESPONSE vs TIME
Face Pressure (kPa)
18
16
14
12
10
8
6
4
2
0
-2
0
20
40
60
80
100
120
Time (s)

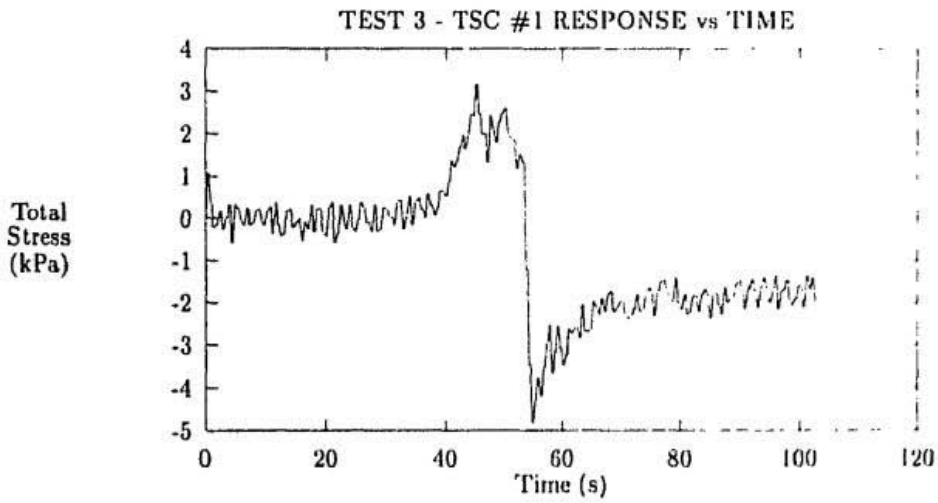
TEST 3 - TSC #1 RESPONSE vs TIME
Total Stress (kPa)
4
3
2
1
0
-1
-2
-3
-4
-5
0
20
40
60
80
100
120
Time (s)

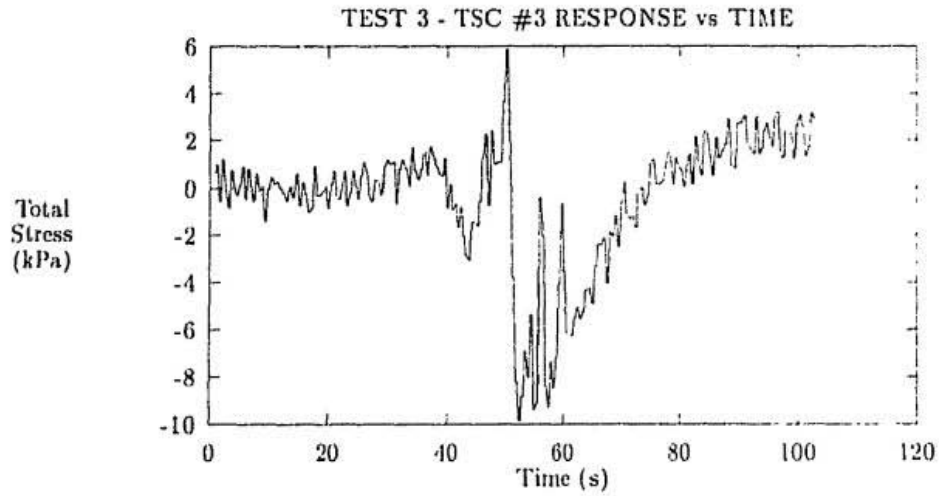
TEST 3 - TSC #3 RESPONSE vs TIME
Total Stress (kPa)
6
4
2
0
-2
-4
-6
-8
-10
0
20
40
60
80
100
120
Time (s)

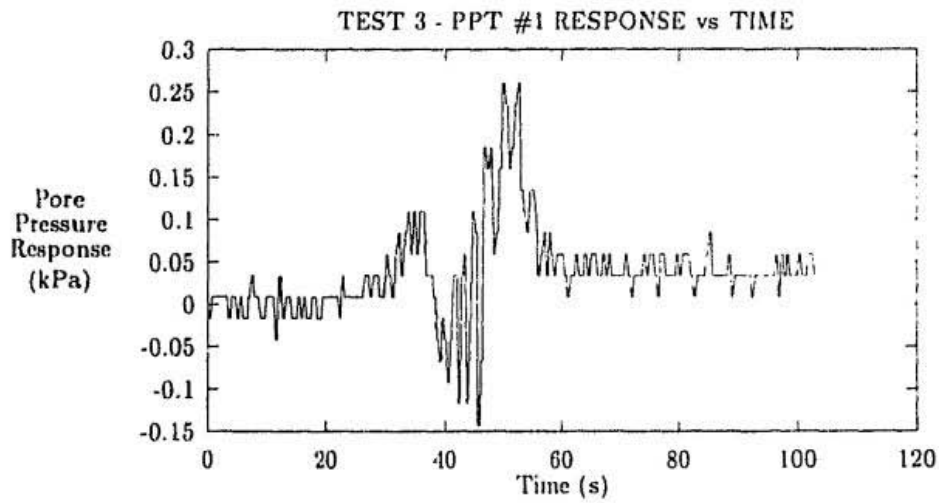
TEST 3 - PPT #1 RESPONSE vs TIME
Pore Pressure Response (kPa)
0.3
0.25
0.2
0.15
0.1
0.05
0
-0.05
-0.1
-0.15
0
20
40
60
80
100
120
Time (s)

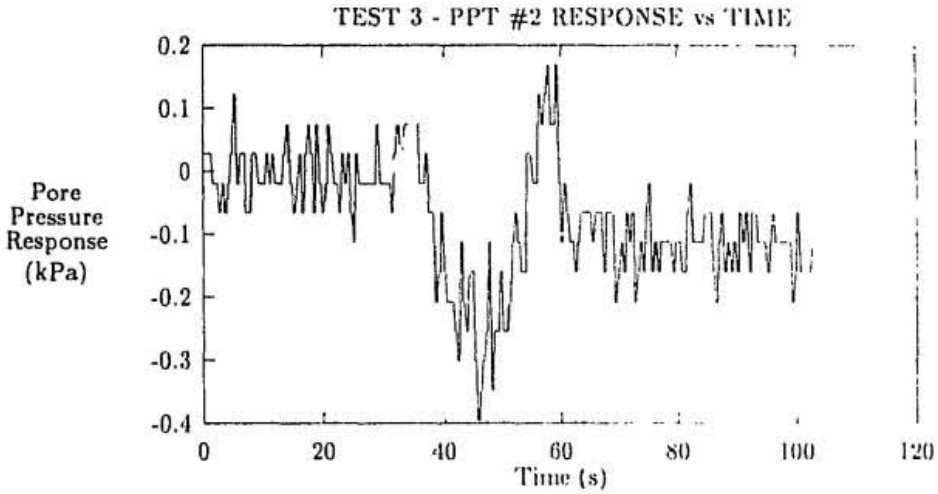
TEST 3 - PPT #2 RESPONSE vs TIME
Pore Pressure Response (kPa)
0.2
0.1
0
-0.1
-0.2
-0.3
-0.4
0
20
40
60
80
100
120
Time (s)

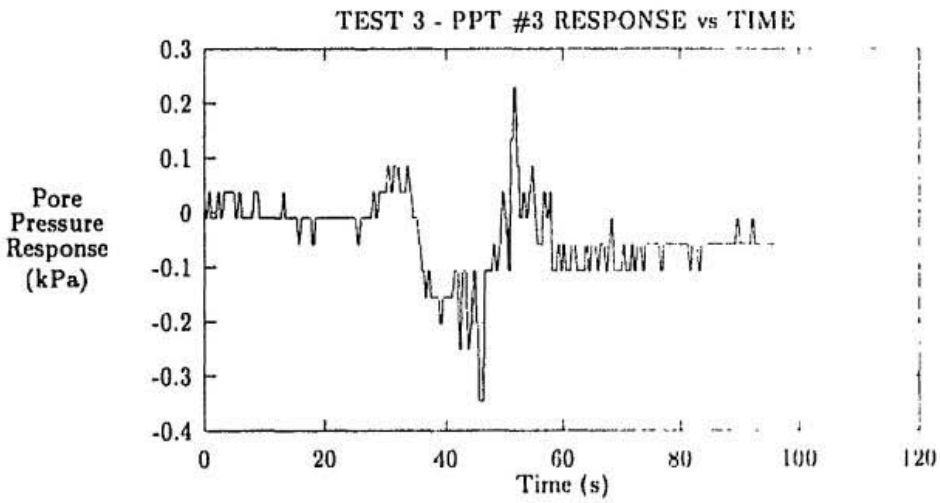
TEST 3 - PPT #3 RESPONSE vs TIME
Pore Pressure Response (kPa)
0.3
0.2
0.1
0
-0.1
-0.2
-0.3
-0.4
0
20
40
60
80
100
120
Time (s)

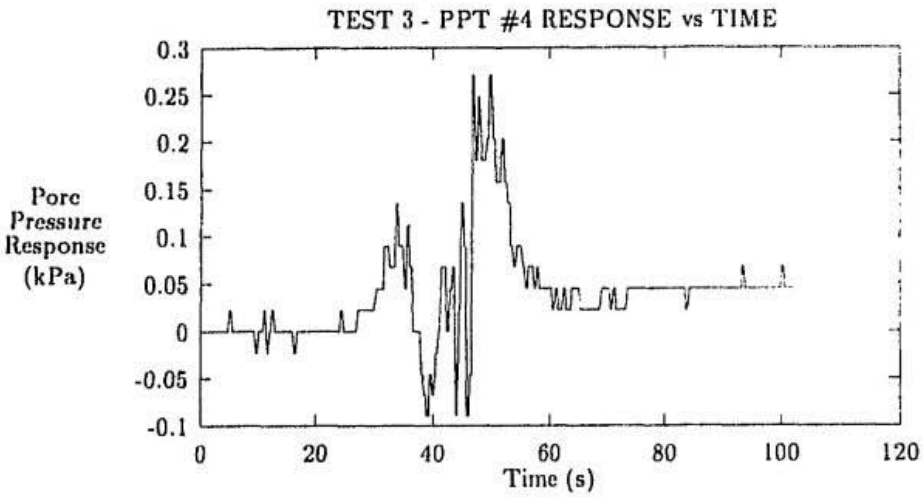
TEST 3 - PPT #4 RESPONSE vs TIME
Pore Pressure Response (kPa)
0.3
0.25
0.2
0.15
0.1
0.05
0
-0.05
-0.1
0
20
40
60
80
100
120
Time (s)

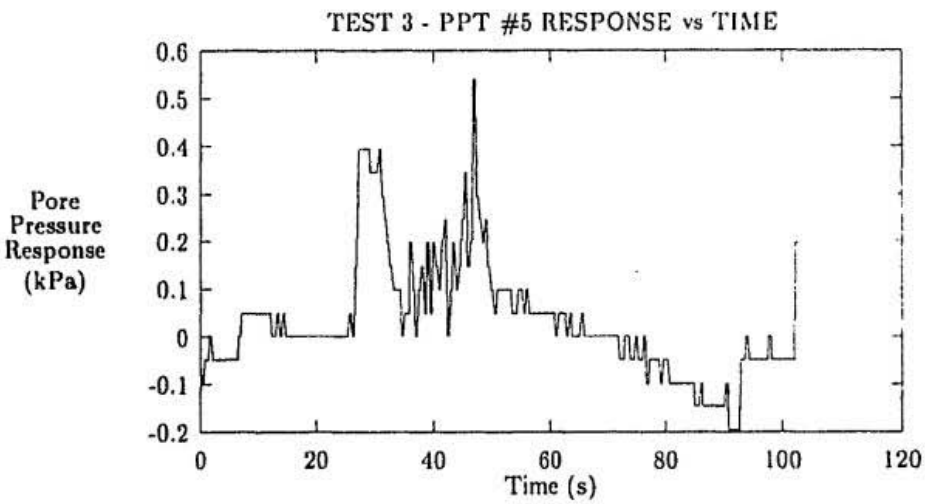
TEST 3 - PPT #5 RESPONSE vs TIME
Pore Pressure Response (kPa)
0.6
0.5
0.4
0.3
0.2
0.1
0
-0.1
-0.2
0
20
40
60
80
100
120
Time (s)

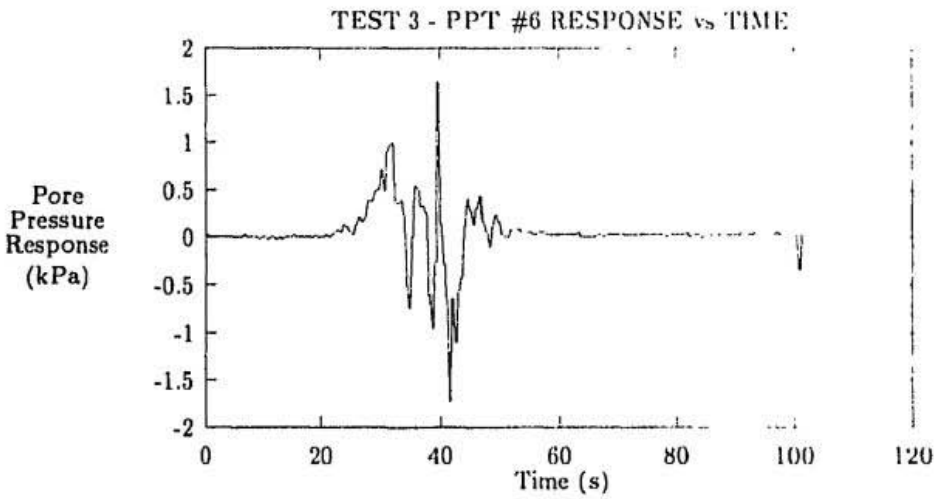
TEST 3 - PPT #6 RESPONSE vs TIME
Pore Pressure Response (kPa)
2
1.5
1
0.5
0
-0.5
-1
-1.5
-2
0
20
40
60
80
100
120
Time (s)

Scour Profiles

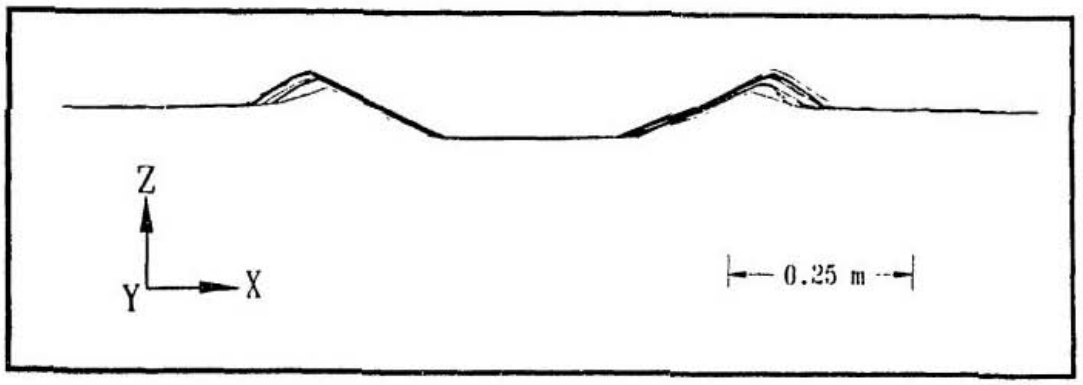
Z
Y
X
0.25 m

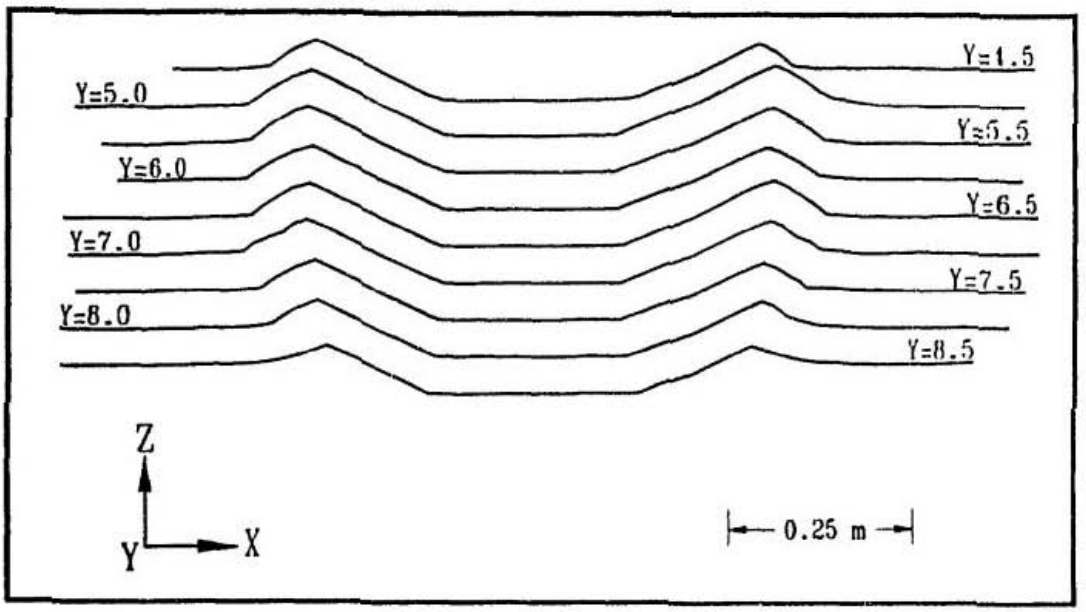
Y=1.5
Y=5.0
Y=5.5
Y=6.0
Y=6.5
Y=7.0
Y=7.5
Y=8.0
Y=8.5
Z
Y
X
0.25 m

Ball Bearing Displacements

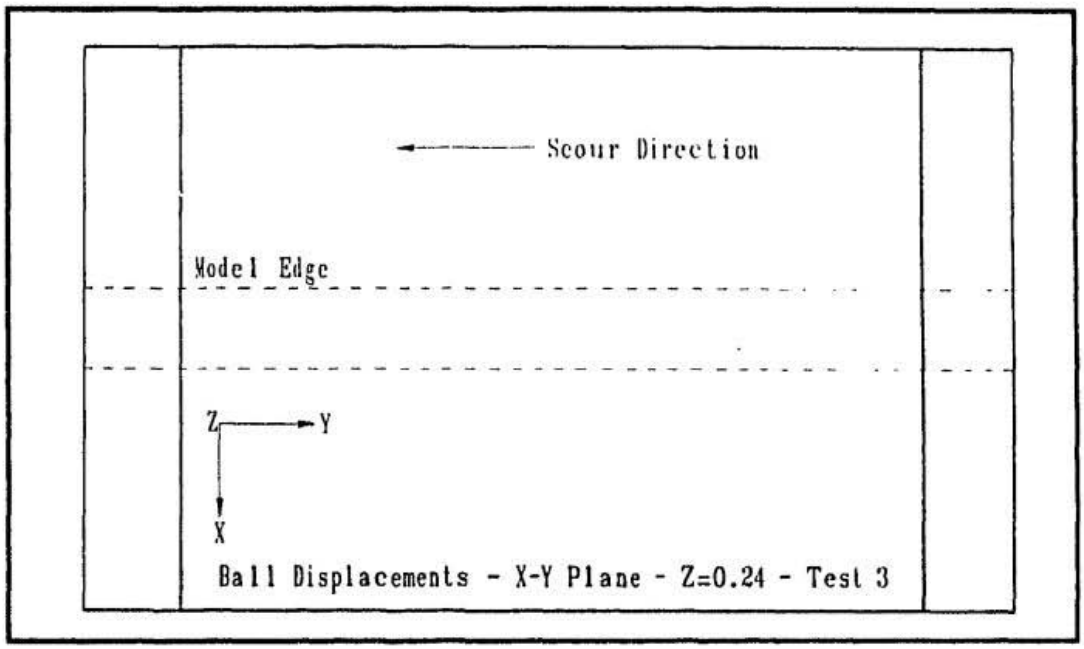
Scour Direction
Model Edge
Z
Y
X
Ball Displacements - X-Y Plane - Z=0.24 - Test 3

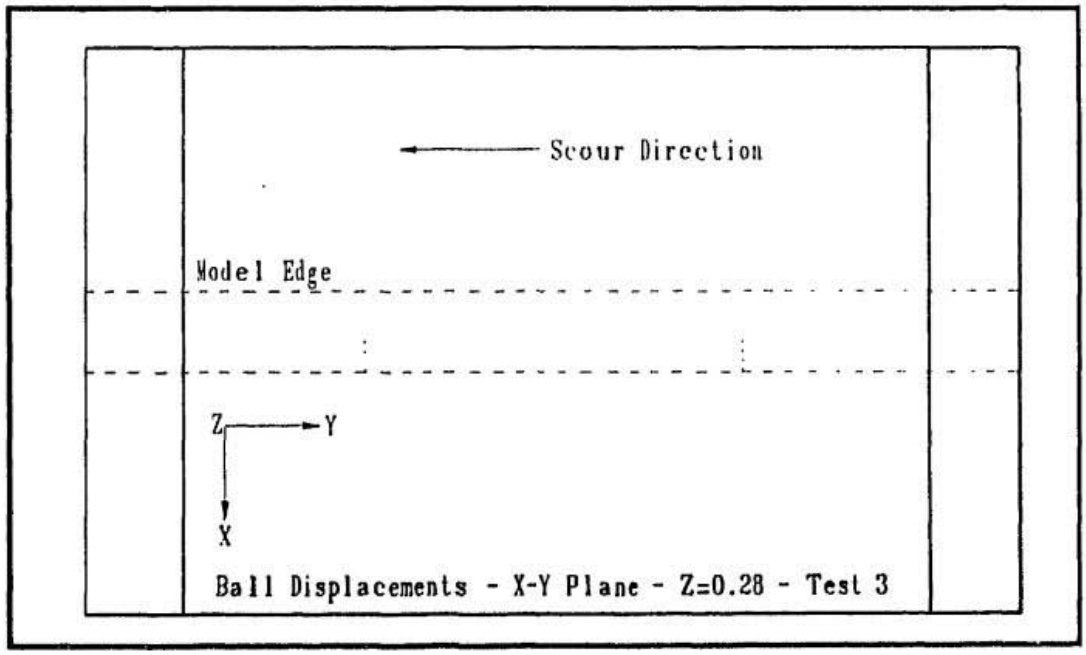
Scour Direction
Model Edge
Z
Y
X
Ball Displacements - X-Y Plane - Z=0.28 - Test 3

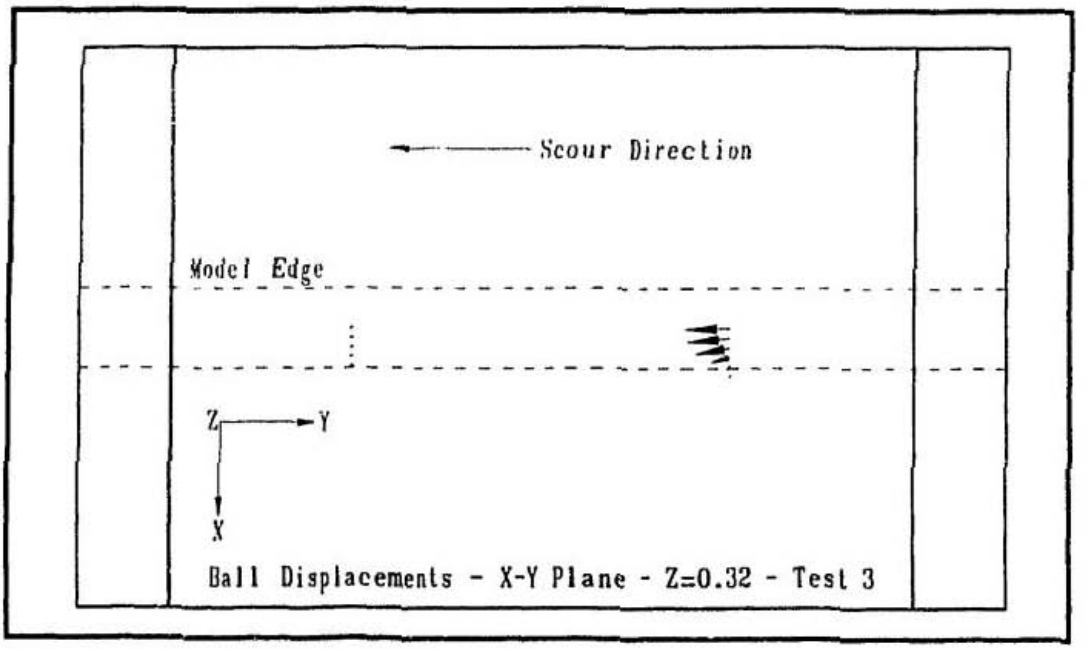
Scour Direction
Model Edge
Z
Y
X
Ball Displacements - X-Y Plane - Z=0.32 - Test 3

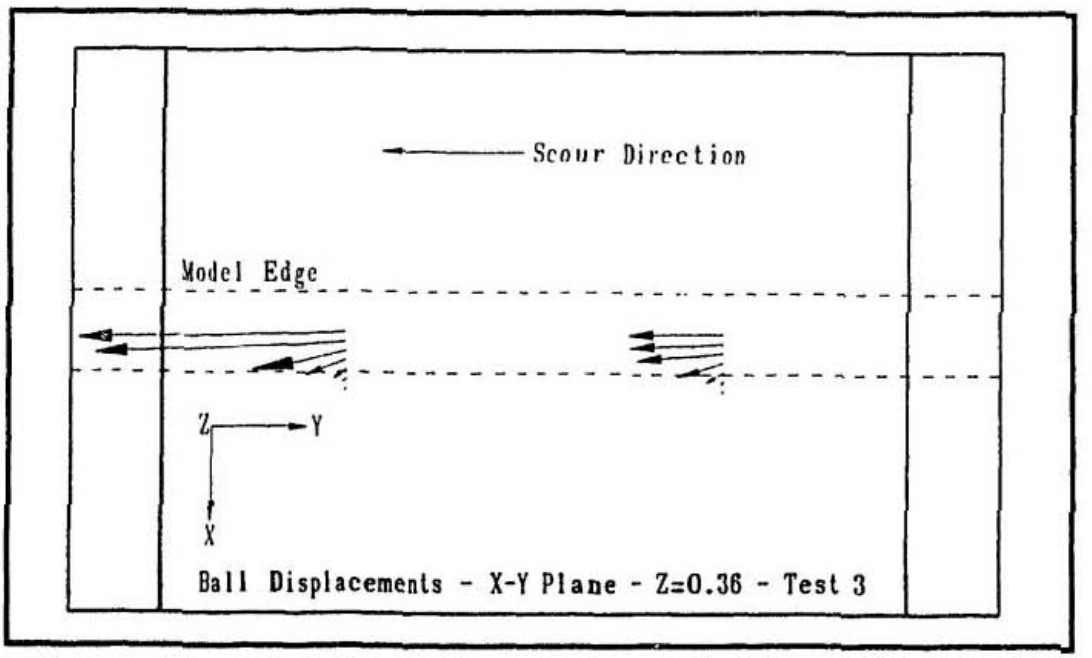
Scour Direction
Model Edge
Z
Y
X
Ball Displacements - X-Y Plane - Z=0.36 - Test 3

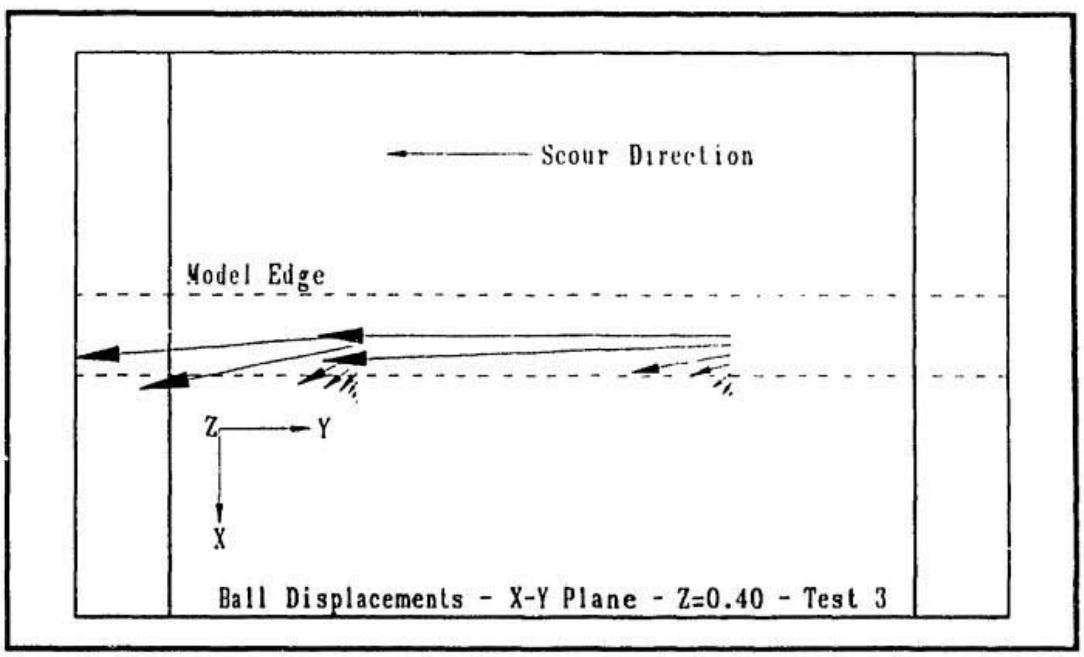
Scour Direction
Model Edge
Z
Y
X
Ball Displacements - X-Y Plane - Z=0.40 - Test 3

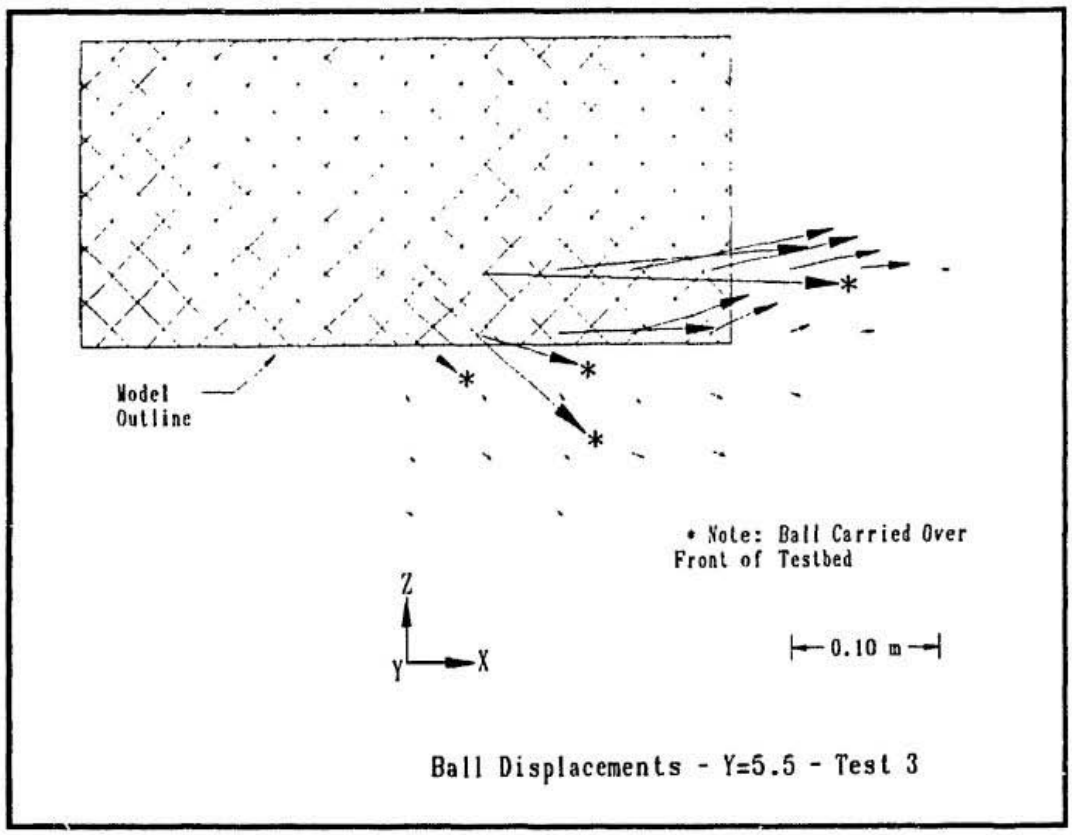

Ball Displacements - Y=5.5 - Test 3

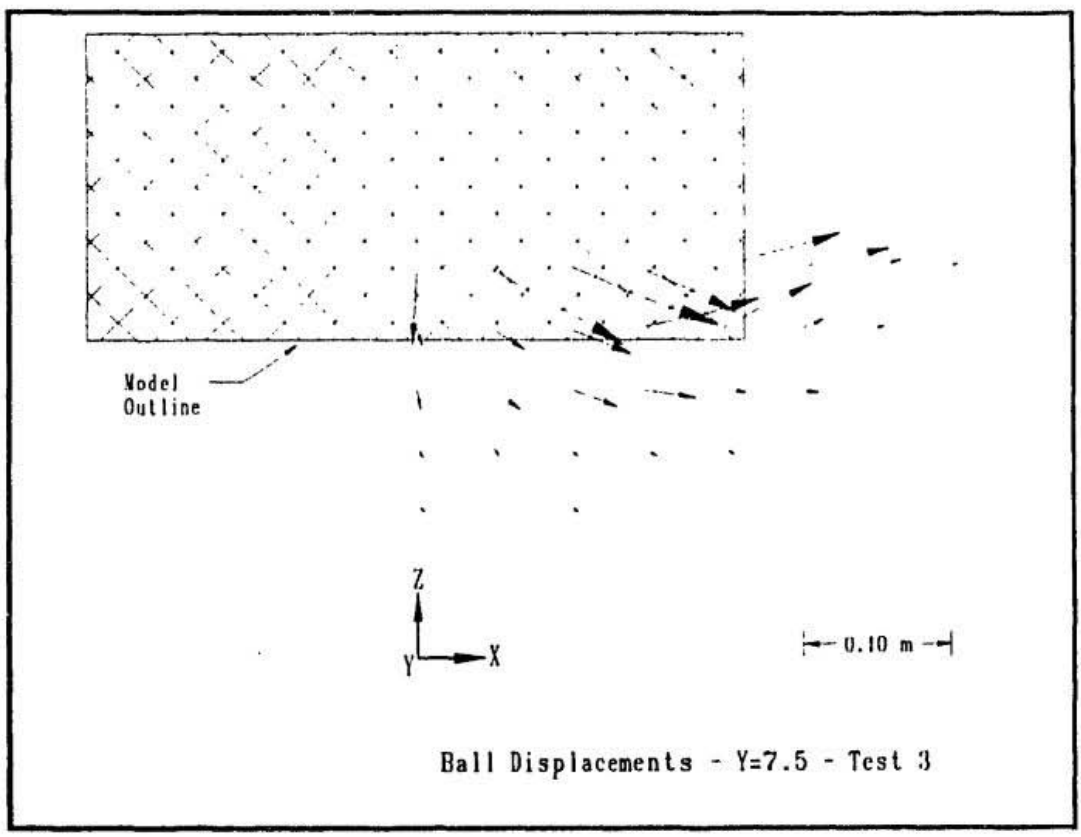

Ball Displacements - Y=7.5 - Test 3

Solder Strand Displacements

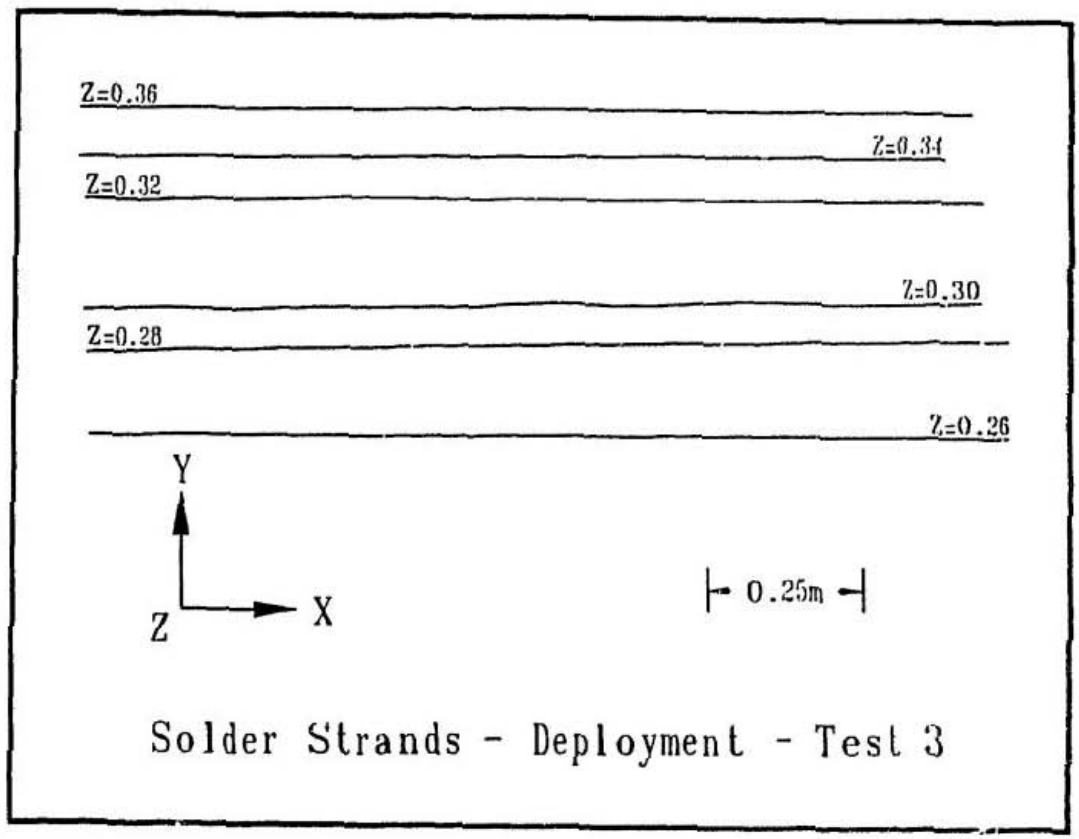

Solder Strands - Deployment - Test 3

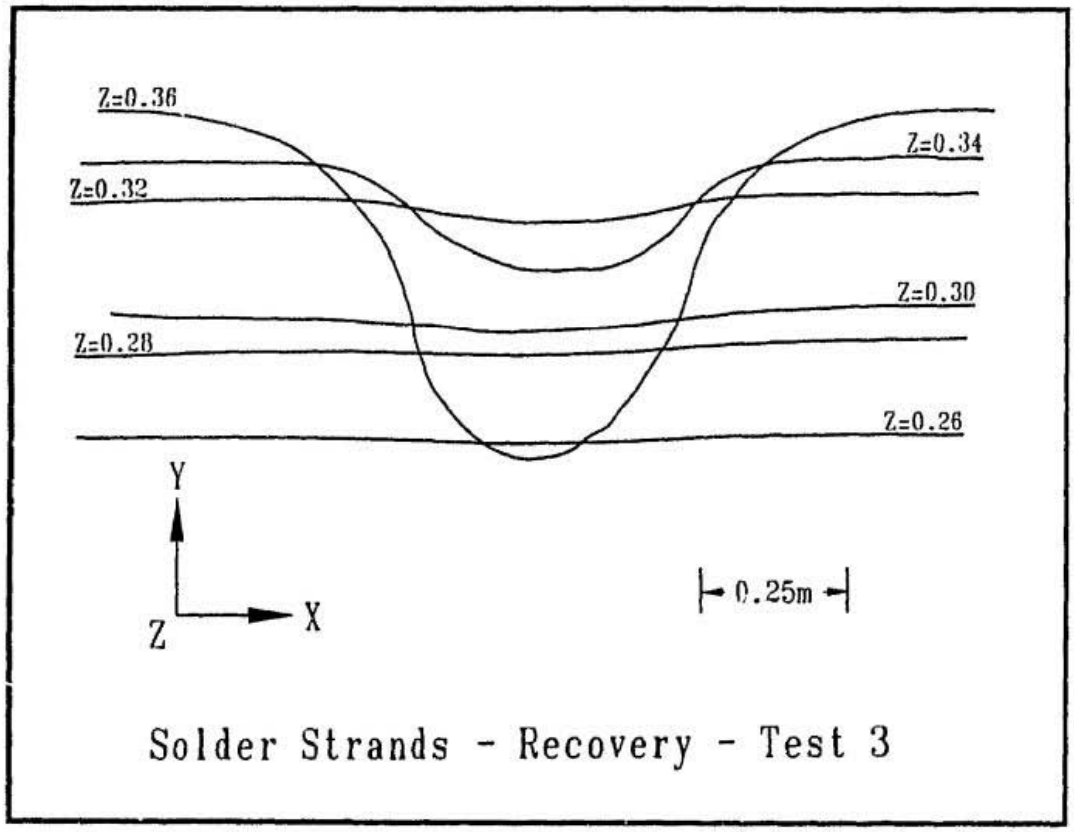

Solder Strands - Recovery - Test 3

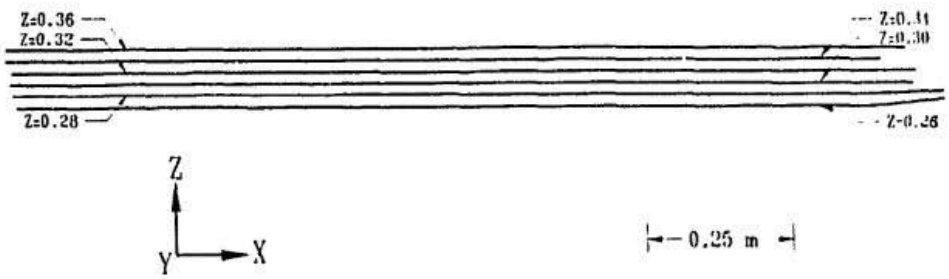

Solder Strands - Deployment - Test 3

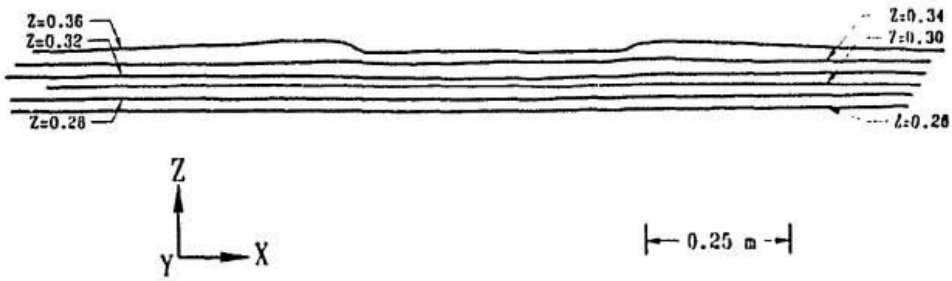

Solder Strands - Recovery - Test 3

Appendix F

Test 4 Results

Instrumentation Output

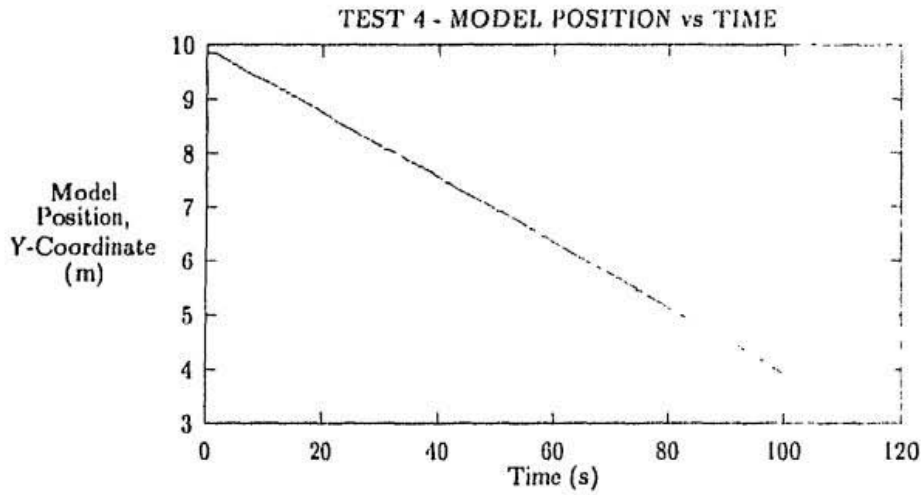
TEST 4 - MODEL POSITION vs TIME
Model Position, Y-Coordinate (m)
10
9
8
7
6
5
4
3
0
20
40
60
80
100
120
Time (s)

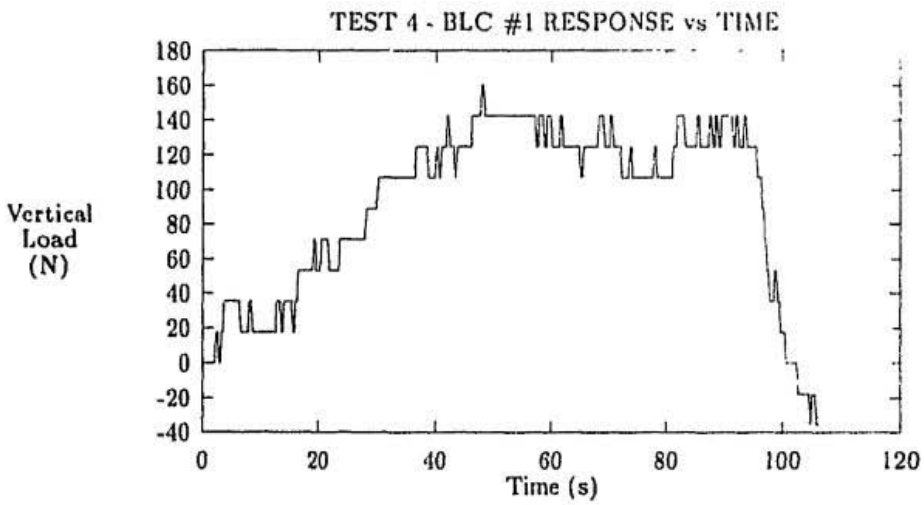
TEST 4 - BLC #1 RESPONSE vs TIME
Vertical Load (N)
180
160
140
120
100
80
60
40
20
0
-20
-40
0
20
40
60
80
100
120
Time (s)

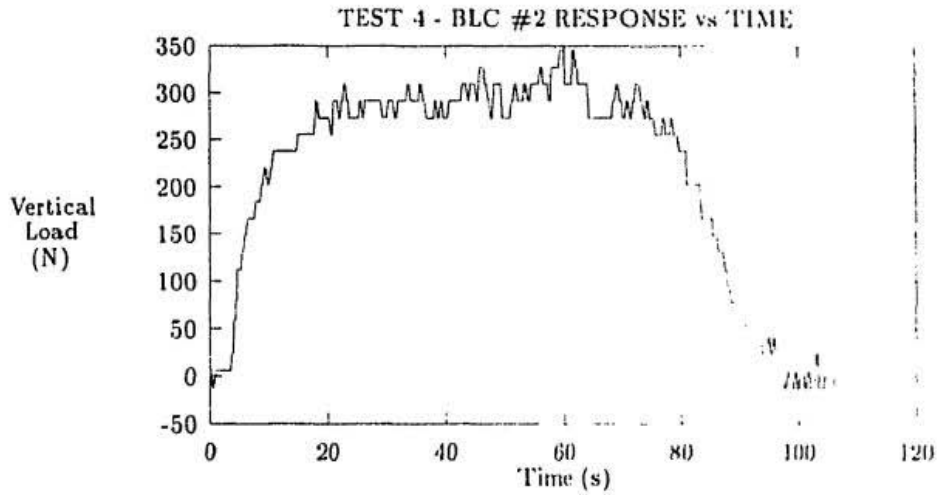
TEST 4 - BLC #2 RESPONSE vs TIME
Vertical Load (N)
350
300
250
200
150
100
50
0
-50
0
20
40
60
80
100
120
Time (s)

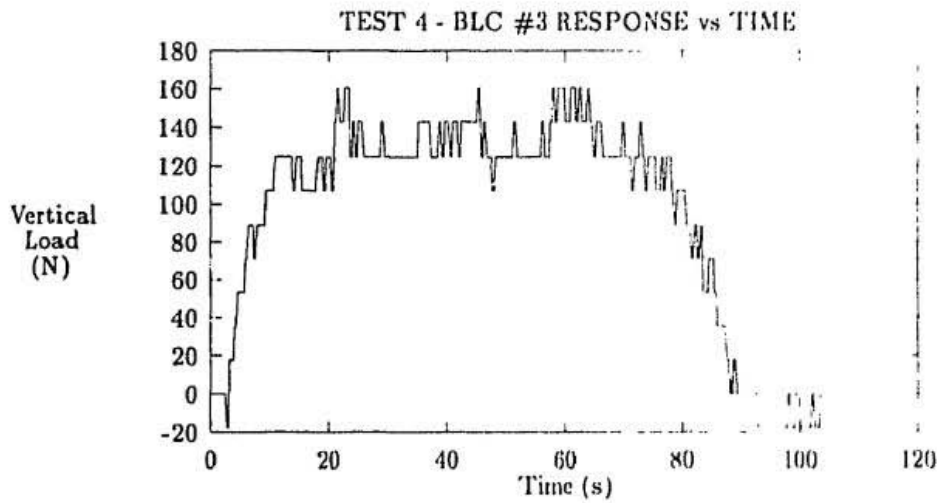
TEST 4 - BLC #3 RESPONSE vs TIME
Vertical Load (N)
180
160
140
120
100
80
60
40
20
0
-20
0
20
40
60
80
100
120
Time (s)

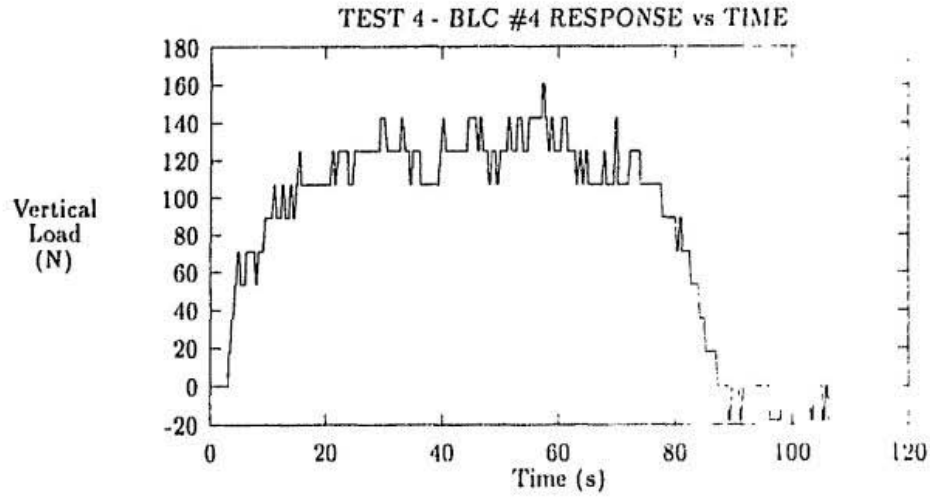
TEST 4 - BLC #4 RESPONSE vs TIME
Vertical Load (N)
180
160
140
120
100
80
60
40
20
0
-20
0
20
40
60
80
100
120
Time (s)

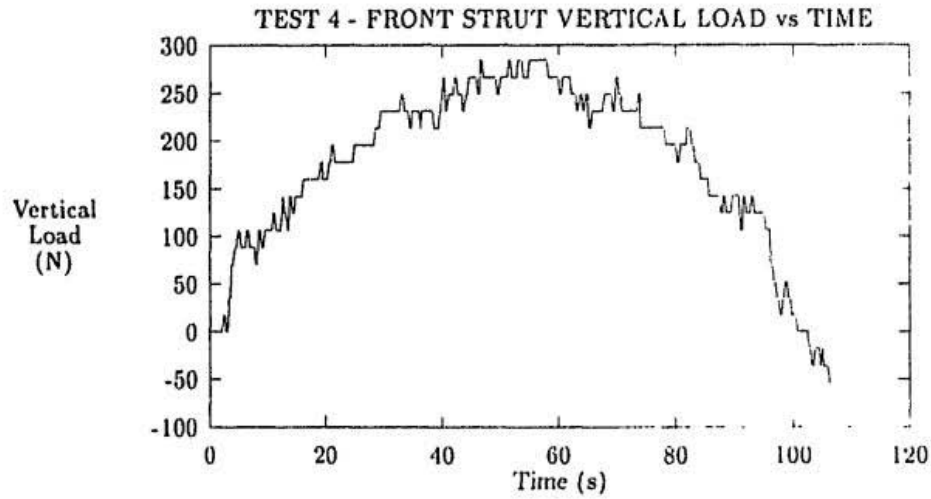
TEST 4 - FRONT STRUT VERTICAL LOAD vs TIME
Vertical Load (N)
300
250
200
150
100
50
0
-50
-100
0
20
40
60
80
100
120
Time (s)

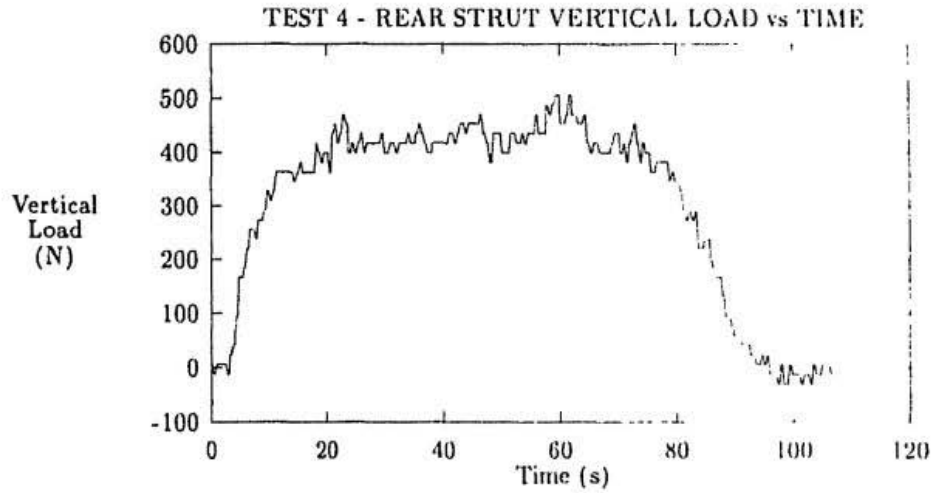
TEST 4 - REAR STRUT VERTICAL LOAD vs TIME
Vertical Load (N)
600
500
400
300
200
100
0
-100
0
20
40
60
80
100
120
Time (s)

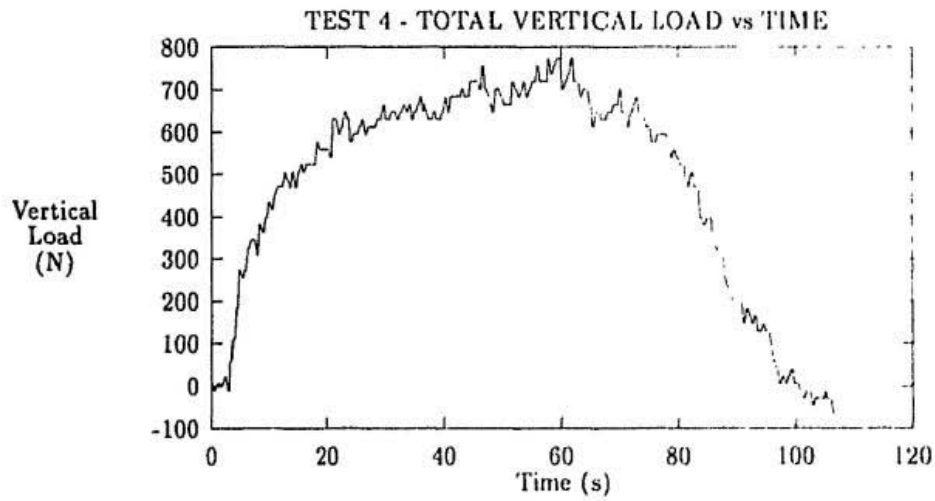
TEST 4 - TOTAL VERTICAL LOAD vs TIME
Vertical Load (N)
800
700
600
500
400
300
200
100
0
-100
0
20
40
60
80
100
120
Time (s)

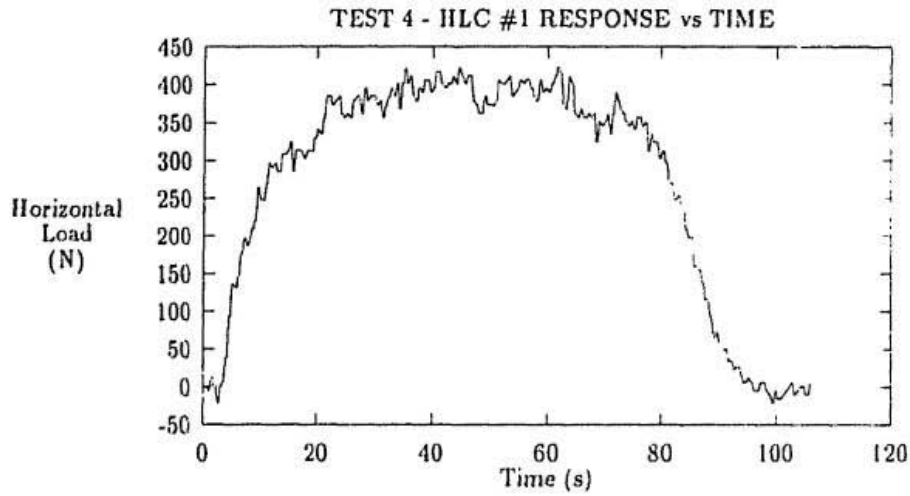
TEST 4 - HLC #1 RESPONSE vs TIME
Horizontal Load (N)
450
400
350
300
250
200
150
100
50
0
-50
0
20
40
60
80
100
120
Time (s)

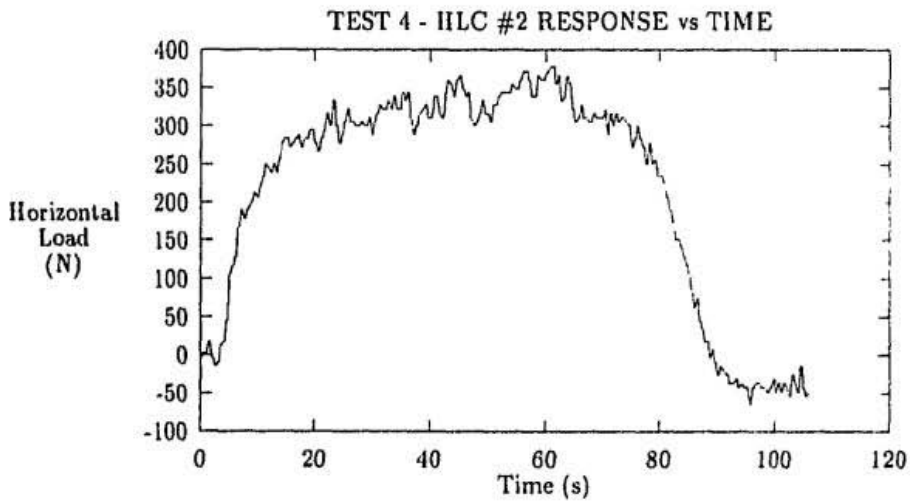
TEST 4 - HLC #2 RESPONSE vs TIME
Horizontal Load (N)
400
350
300
250
200
150
100
50
0
-50
-100
0
20
40
60
80
100
120
Time (s)

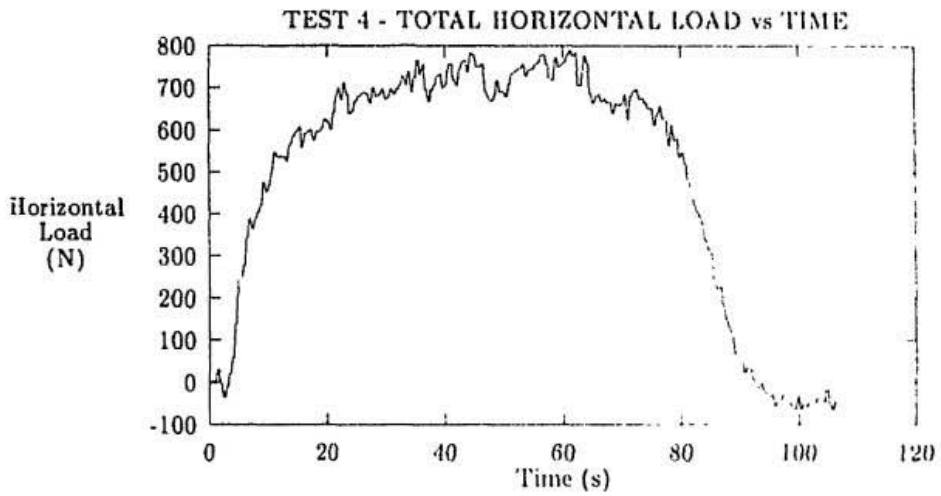
TEST 4 - TOTAL HORIZONTAL LOAD vs TIME
Horizontal Load (N)
800
700
600
500
400
300
200
100
0
-100
0
20
40
60
80
100
120
Time (s)

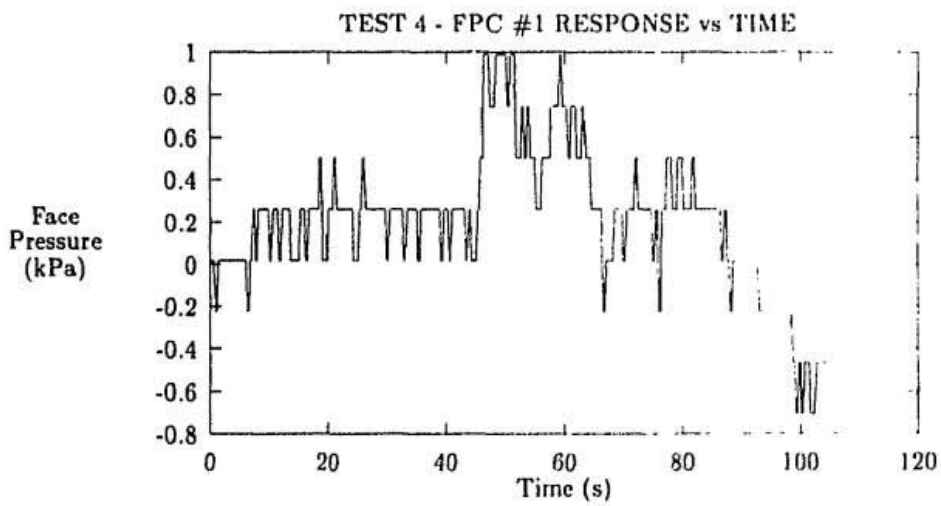
TEST 4 - FPC #1 RESPONSE vs TIME
Face Pressure (kPa)
1
0.8
0.6
0.4
0.2
0
-0.2
-0.4
-0.6
-0.8
0
20
40
60
80
100
120
Time (s)

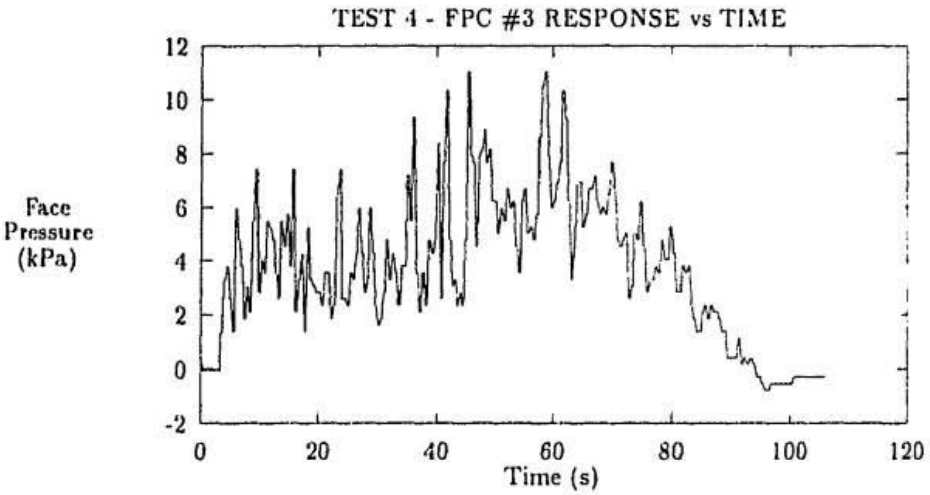
TEST 4 - FPC #3 RESPONSE vs TIME
Face Pressure (kPa)
12
10
8
6
4
2
0
-2
0
20
40
60
80
100
120
Time (s)

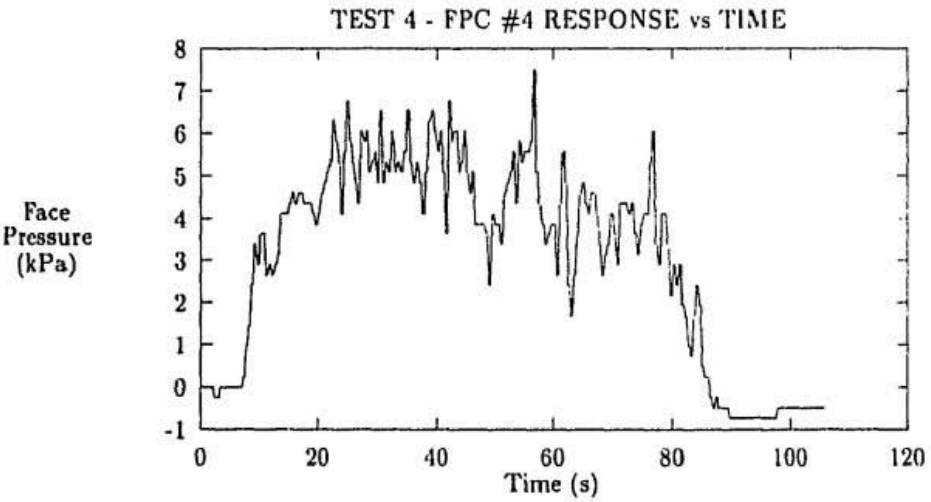
TEST 4 - FPC #4 RESPONSE vs TIME
Face Pressure (kPa)
8
7
6
5
4
3
2
1
0
-1
0
20
40
60
80
100
120
Time (s)

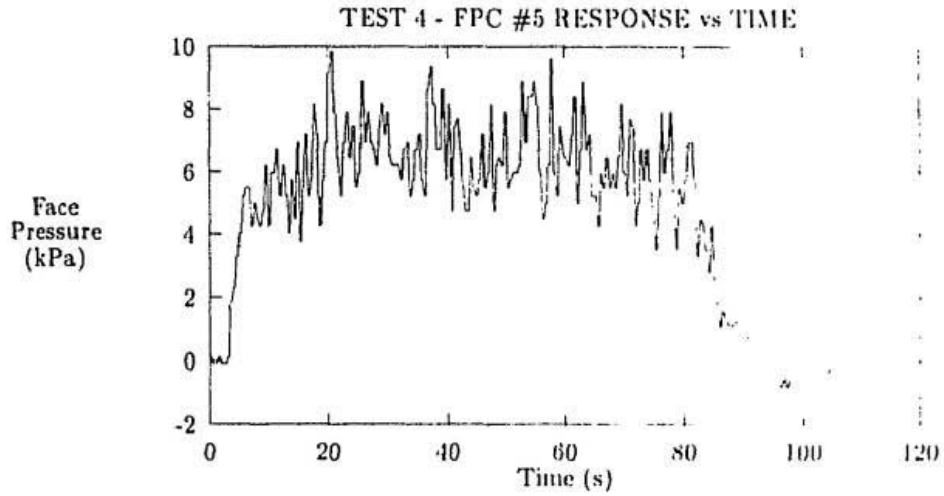
TEST 4 - FPC #5 RESPONSE vs TIME
Face Pressure (kPa)
10
8
6
4
2
0
-2
0
20
40
60
80
100
120
Time (s)

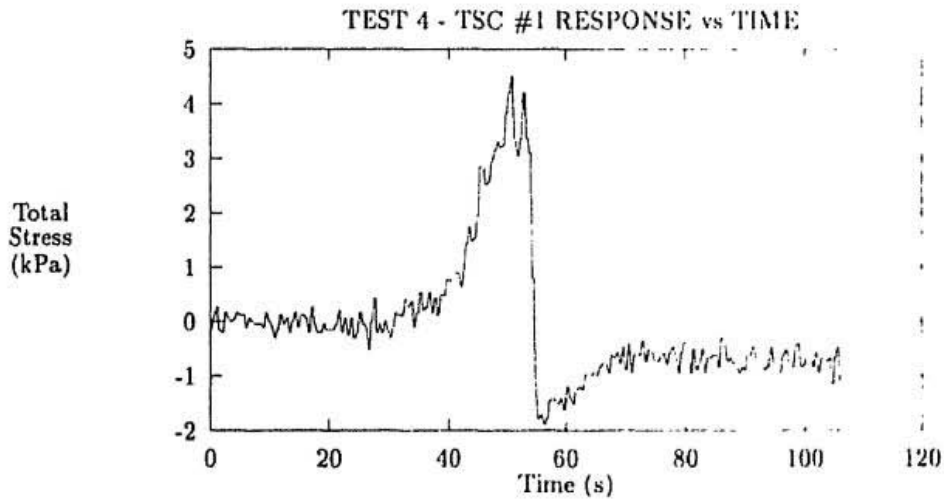
TEST 4 - TSC #1 RESPONSE vs TIME
Total Stress (kPa)
5
4
3
2
1
0
-1
-2
0
20
40
60
80
100
120
Time (s)

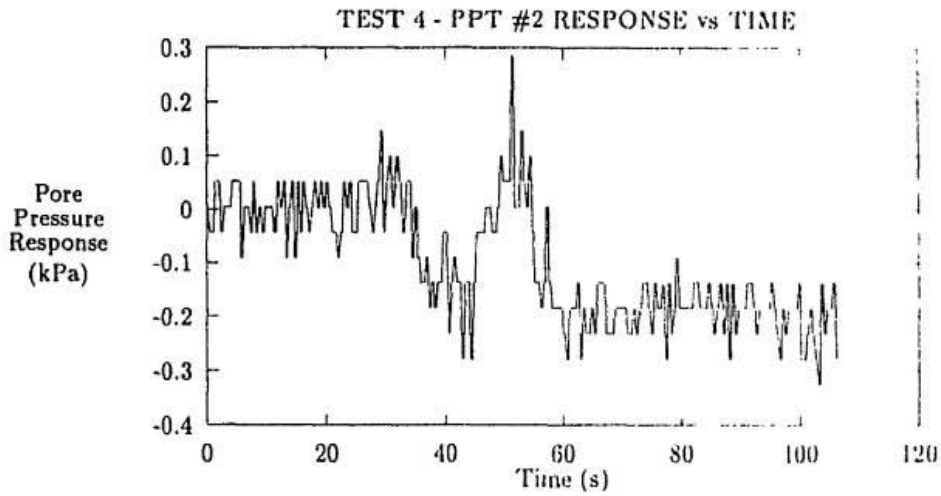
TEST 4 - PPT #2 RESPONSE vs TIME
Pore Pressure Response (kPa)
0.3
0.2
0.1
0
-0.1
-0.2
-0.3
-0.4
0
20
40
60
80
100
120
Time (s)

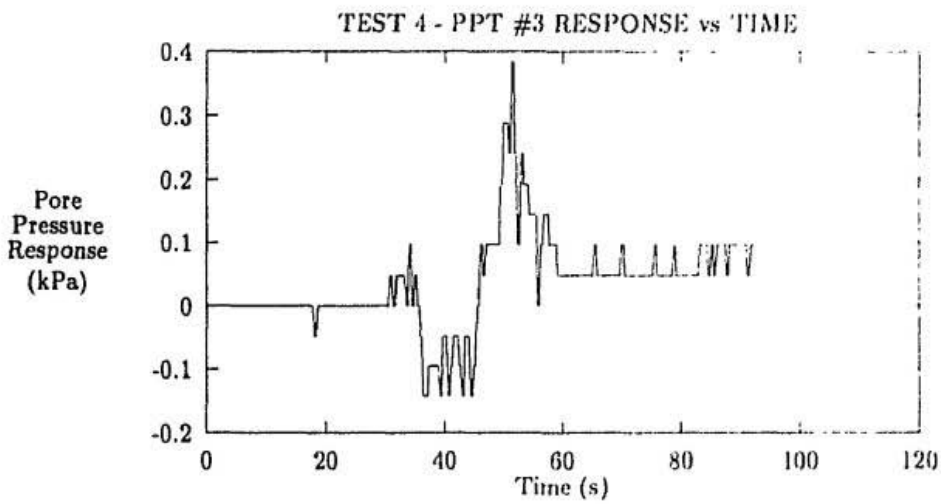
TEST 4 - PPT #3 RESPONSE vs TIME
Pore Pressure Response (kPa)
0.4
0.3
0.2
0.1
0
-0.1
-0.2
0
20
40
60
80
100
120
Time (s)

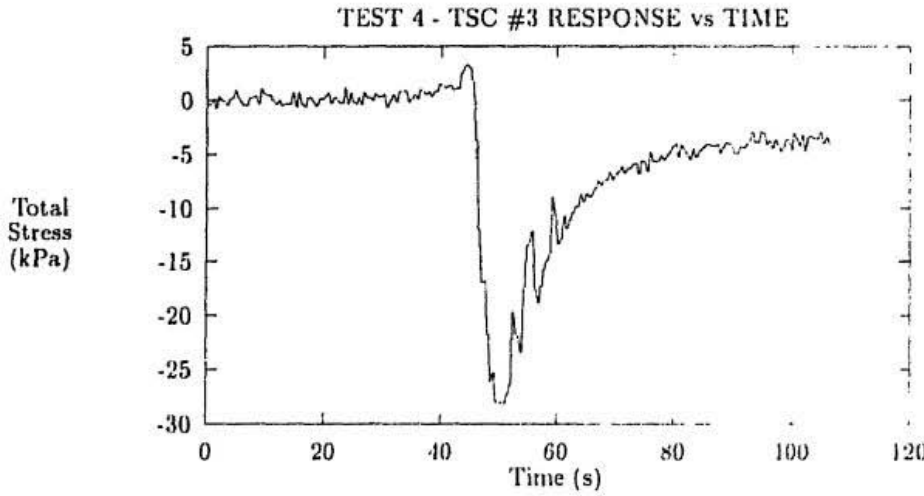
TEST 4 - TSC #3 RESPONSE vs TIME
Total Stress (kPa)
5
0
-5
-10
-15
-20
-25
-30
0
20
40
60
80
100
120
Time (s)

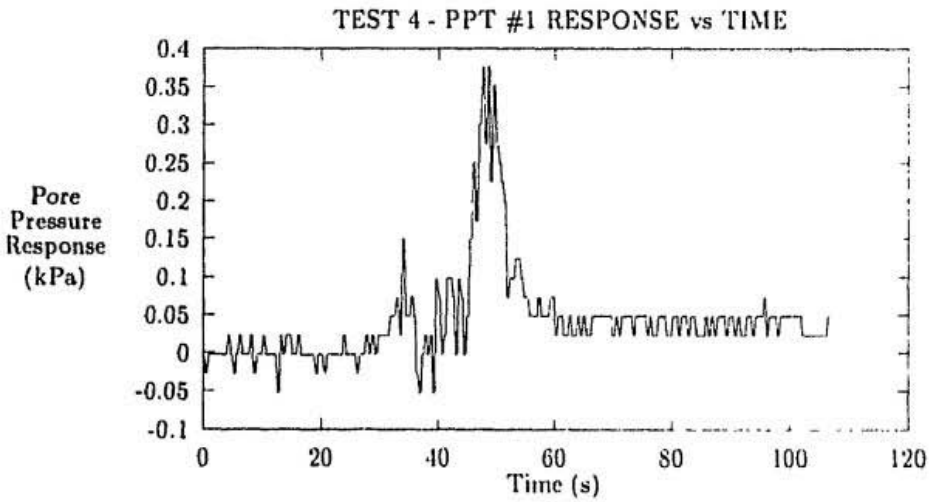
TEST 4 - PPT #1 RESPONSE vs TIME
Pore Pressure Response (kPa)
0.4
0.35
0.3
0.25
0.2
0.15
0.1
0.05
0
-0.05
-0.1
0
20
40
60
80
100
120
Time (s)

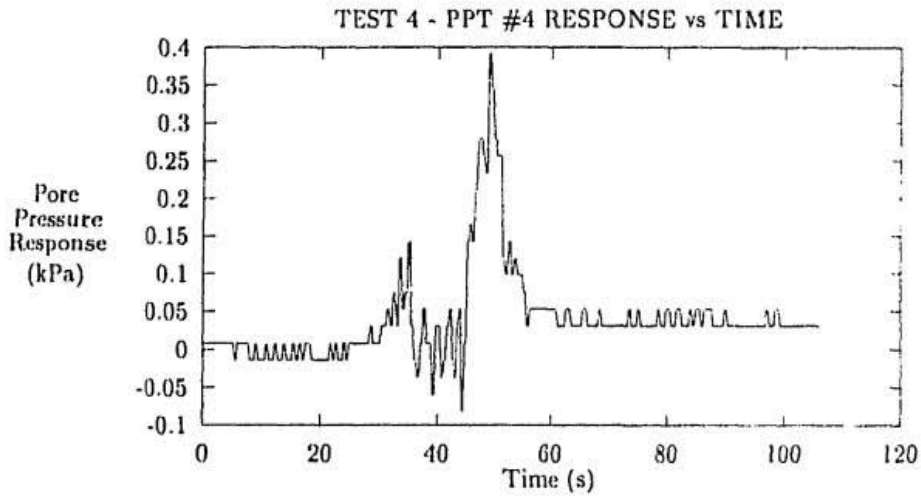
TEST 4 - PPT #4 RESPONSE vs TIME
Pore Pressure Response (kPa)
0.4
0.35
0.3
0.25
0.2
0.15
0.1
0.05
0
-0.05
-0.1
0
20
40
60
80
100
120
Time (s)

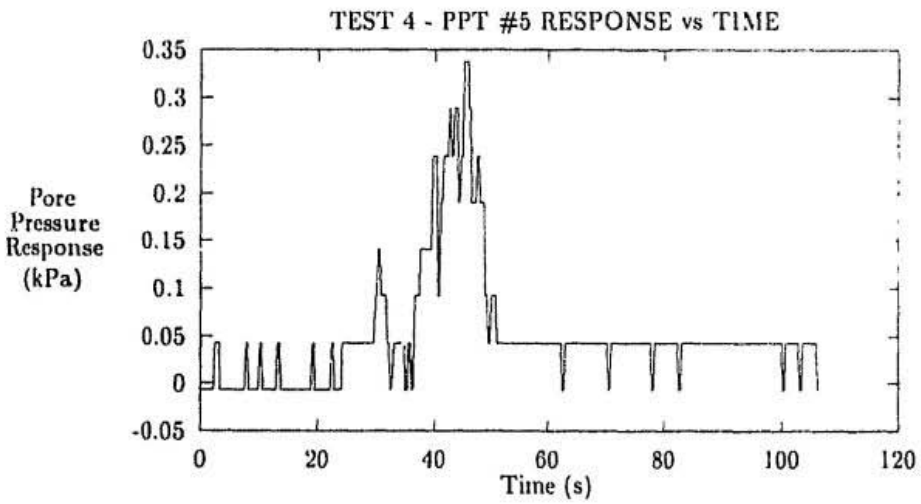
TEST 4 - PPT #5 RESPONSE vs TIME
Pore Pressure Response (kPa)
0.35
0.3
0.25
0.2
0.15
0.1
0.05
0
-0.05
0
20
40
60
80
100
120
Time (s)

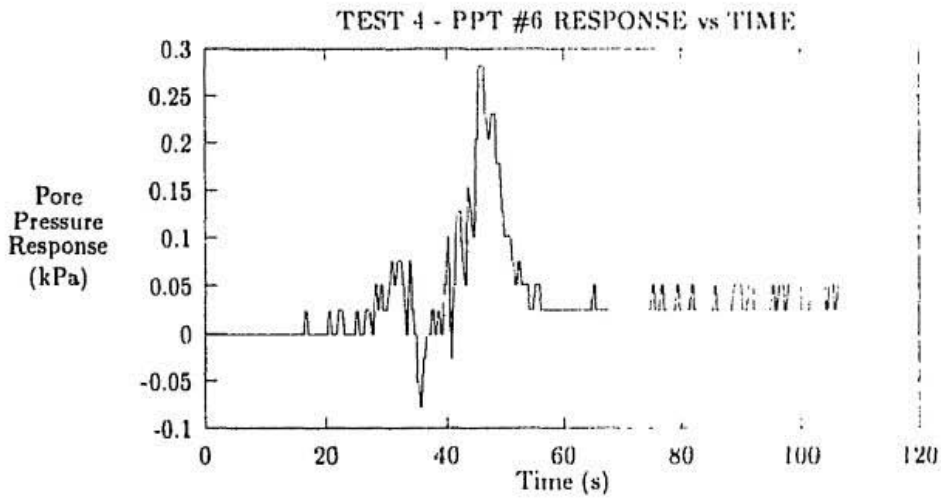
TEST 4 - PPT #6 RESPONSE vs TIME
Pore Pressure Response (kPa)
0.3
0.25
0.2
0.15
0.1
0.05
0
-0.05
-0.1
0
20
40
60
80
100
120
Time (s)

Scour Profiles

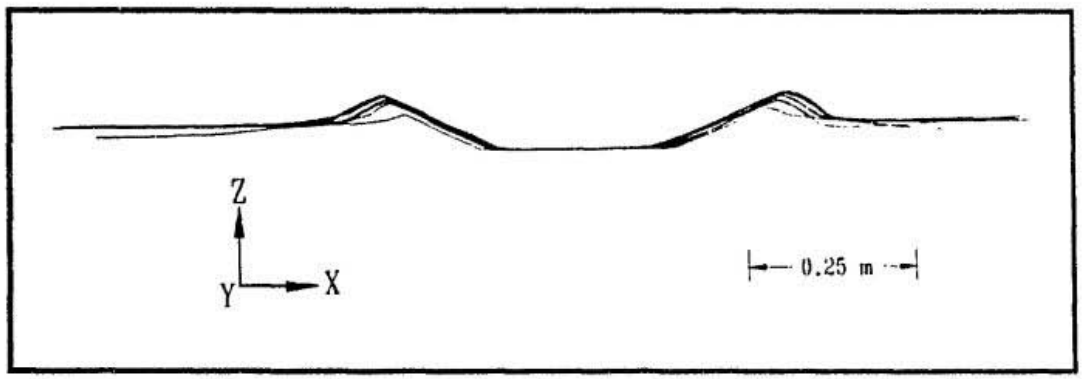
Z
Y
X
0.25 m

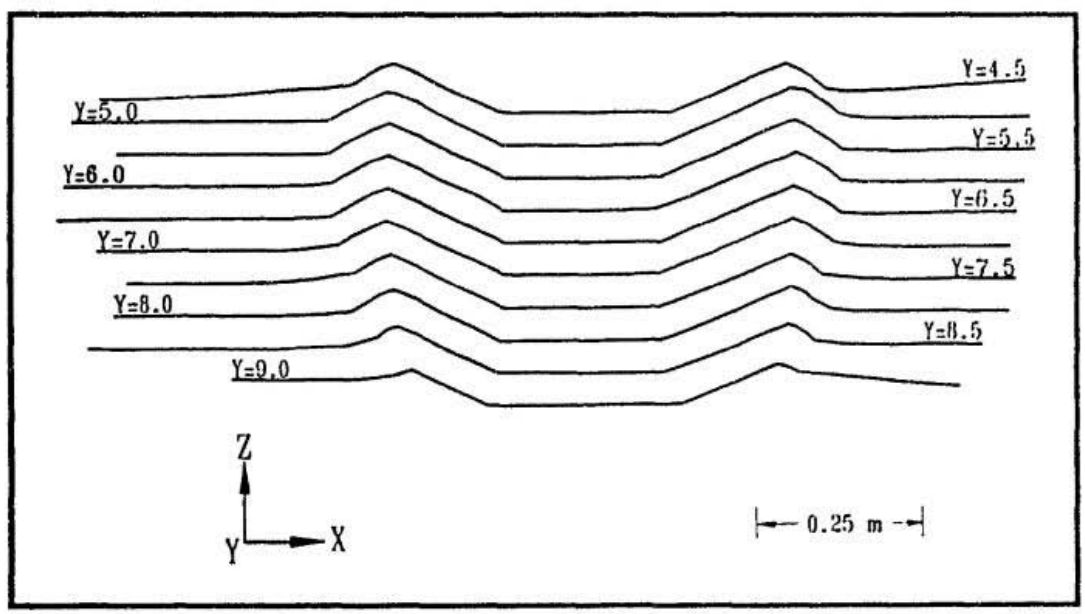
Y=4.5
Y=5.0
Y=5.5
Y=6.0
Y=6.5
Y=7.0
Y=7.5
Y=8.0
Y=8.5
Y=9.0
Z
Y
X
0.25 m

Ball Bearing Displacements

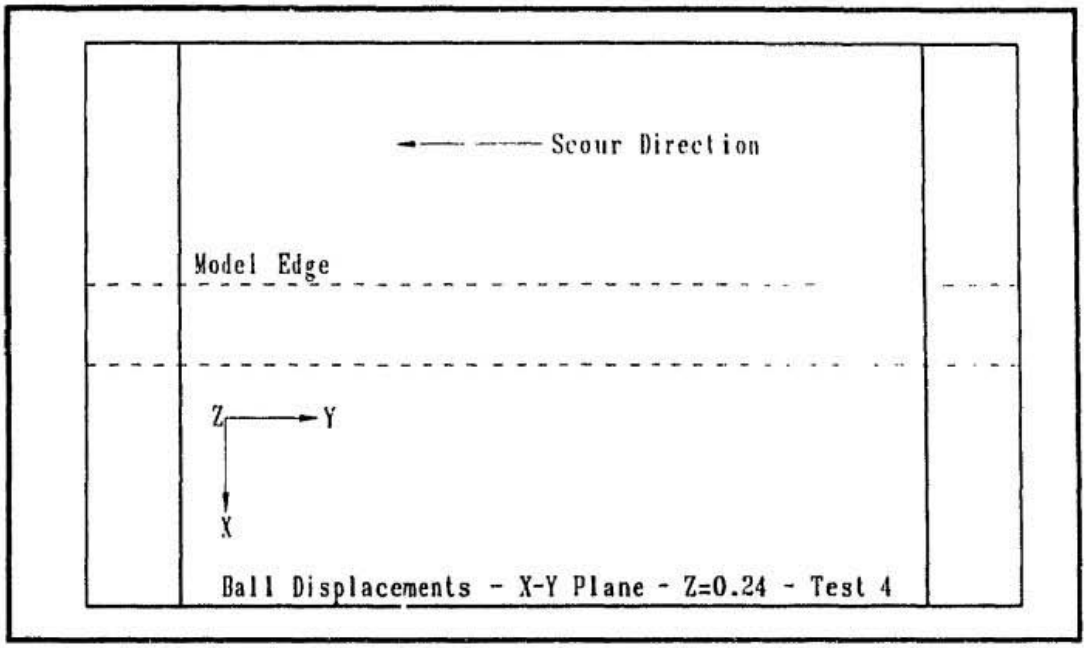
Scour Direction
Model Edge
Z
Y
X
Ball Displacements - X-Y Plane - Z=0.24 - Test 4

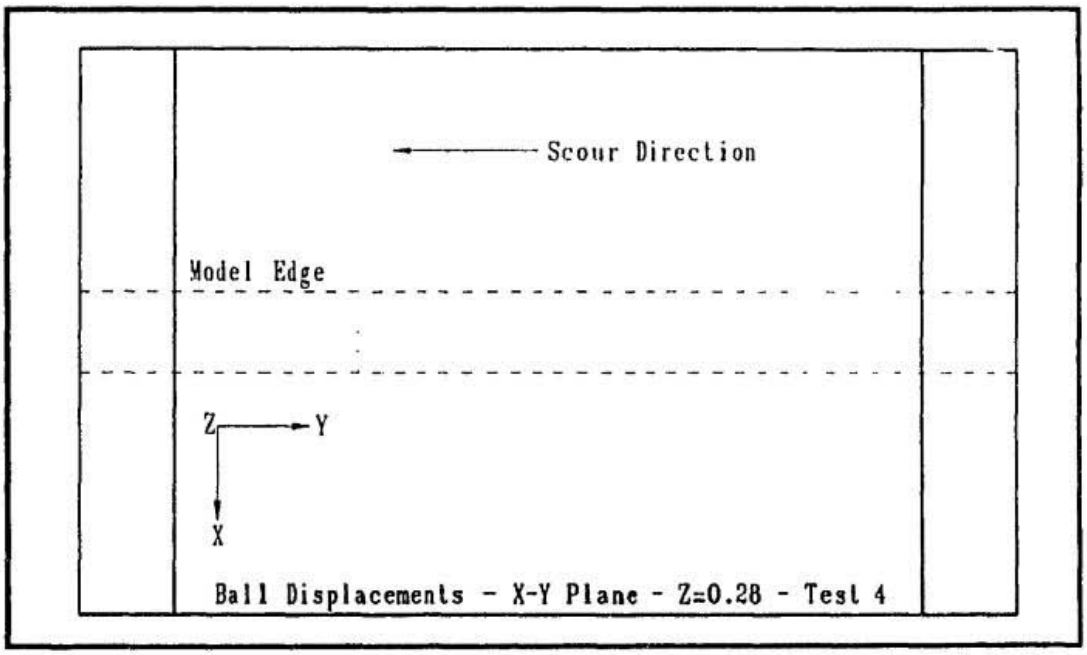
Scour Direction
Model Edge
Z
Y
X
Ball Displacements - X-Y Plane - Z=0.28 - Test 4

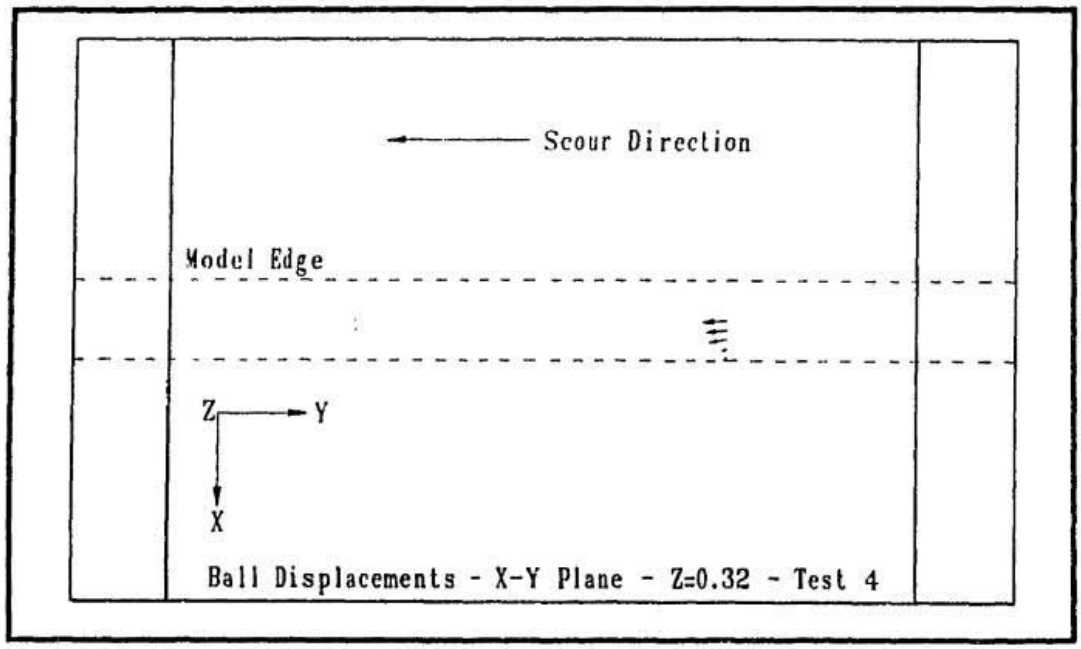
Scour Direction
Model Edge
Z
Y
X
Ball Displacements - X-Y Plane - Z=0.32 - Test 4

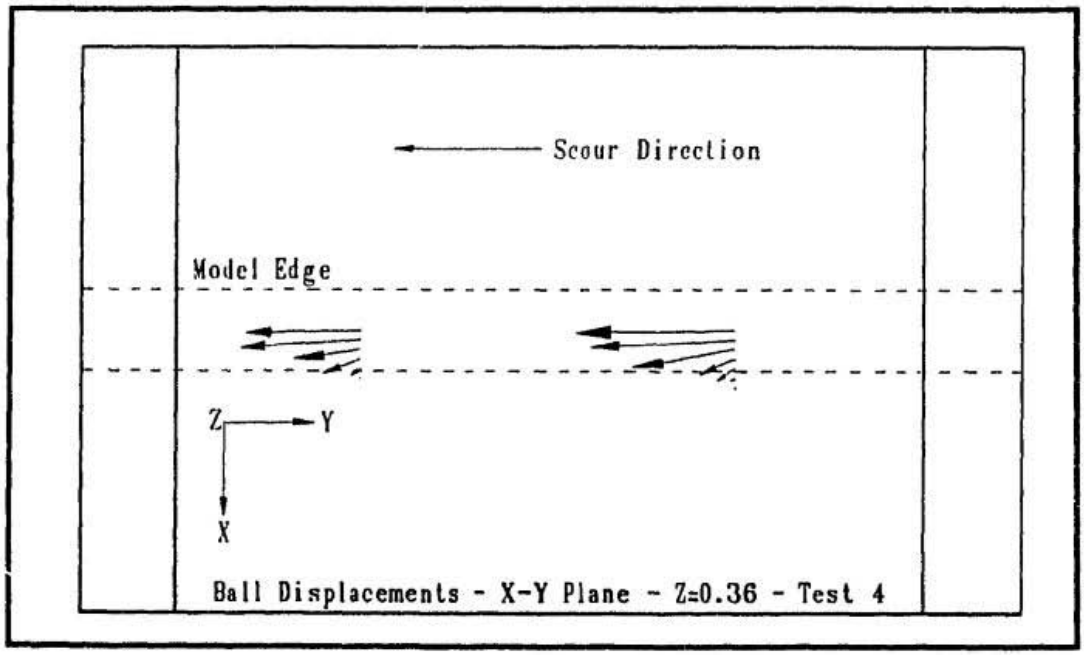
Scour Direction
Model Edge
Z
Y
X
Ball Displacements - X-Y Plane - Z=0.36 - Test 4

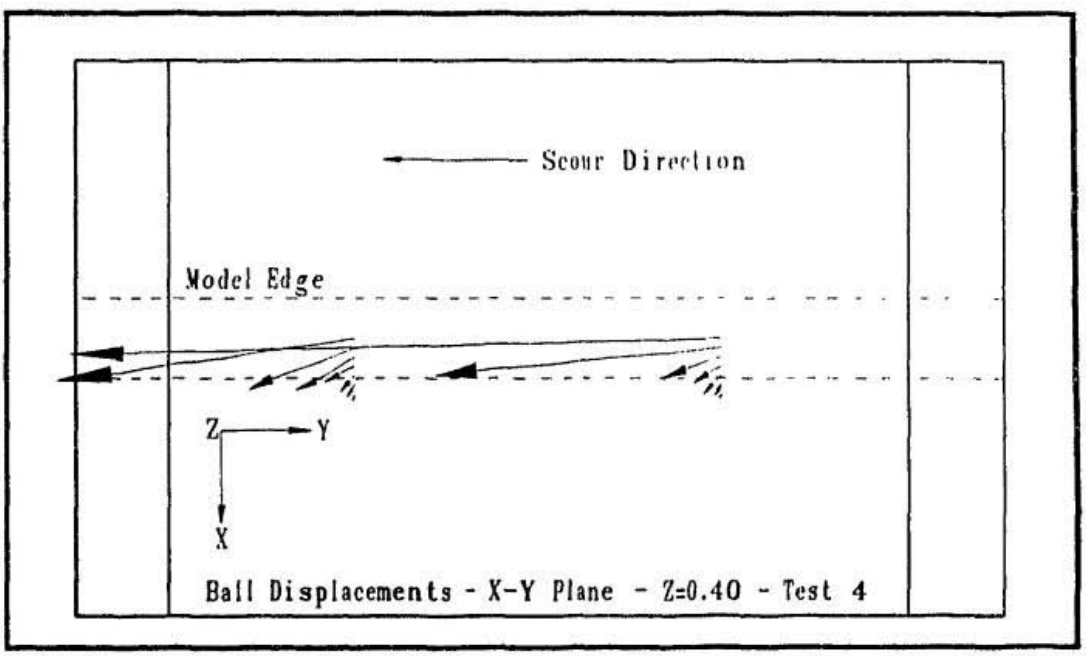
Scour Direction
Model Edge
Z
Y
X
Ball Displacements - X-Y Plane - Z=0.40 - Test 4

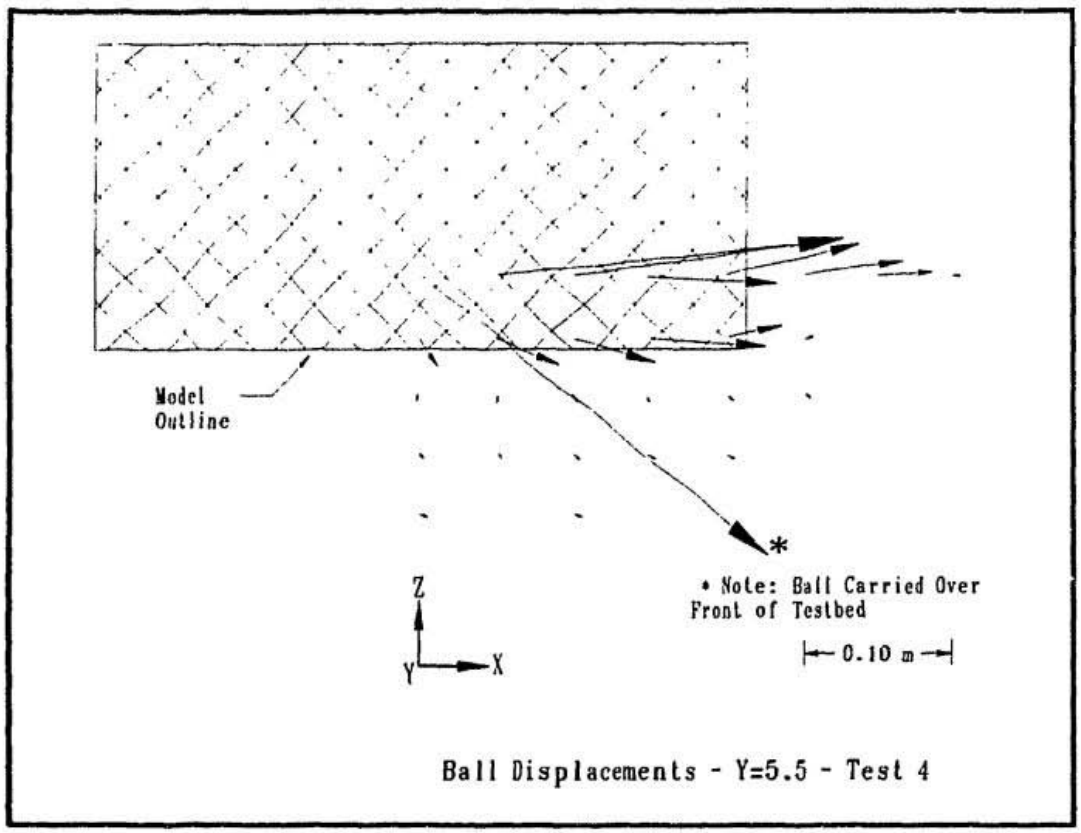

Ball Displacements - Y=5.5 - Test 4

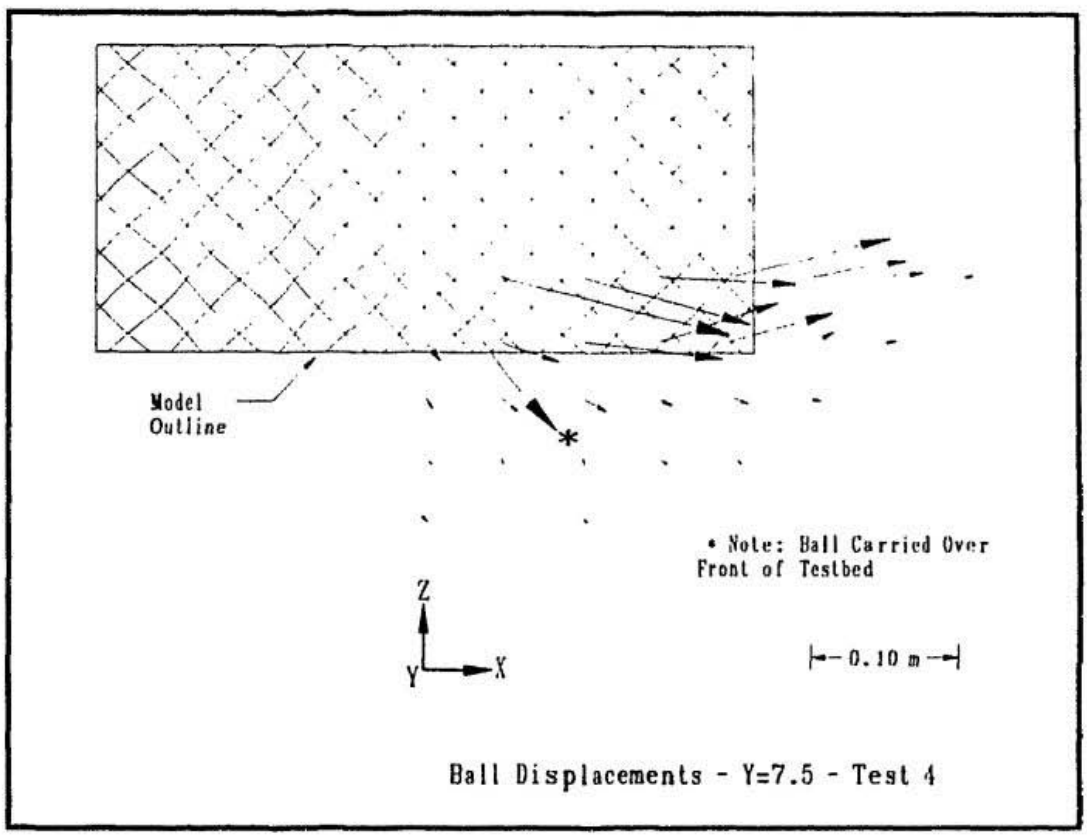

Ball Displacements - Y=7.5 - Test 4

Solder Strand Displacements

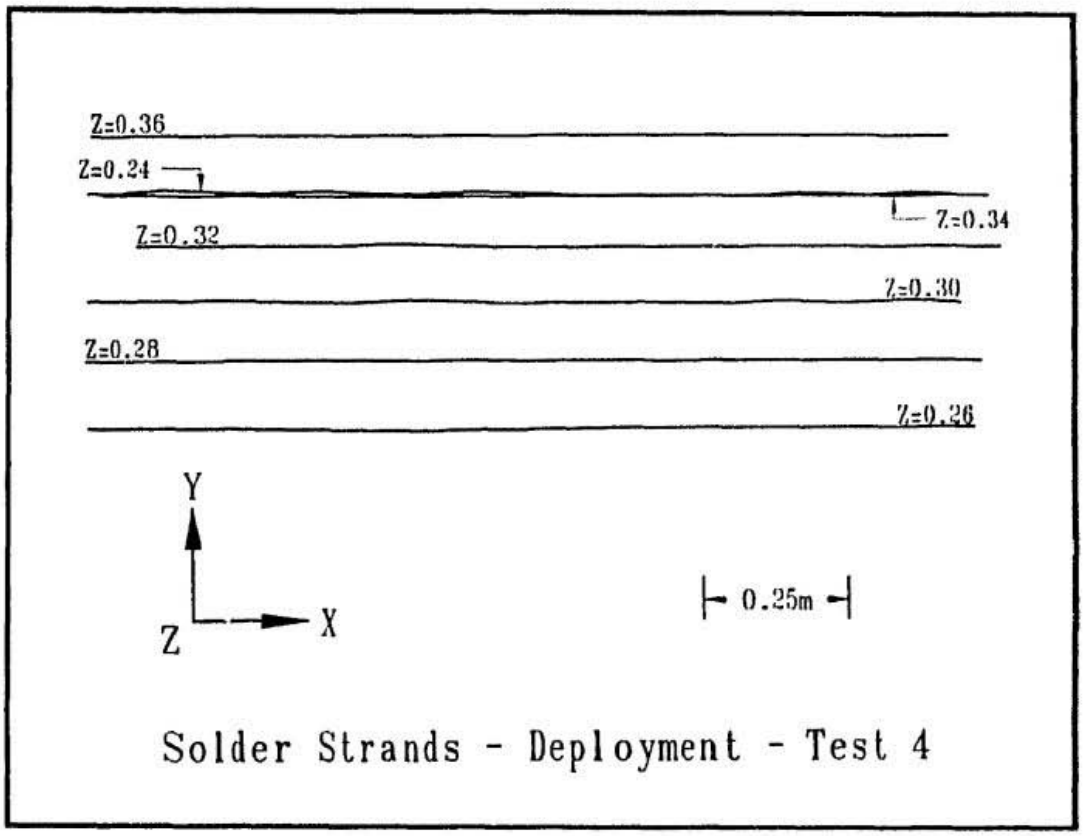

Solder Strands - Deployment - Test 4

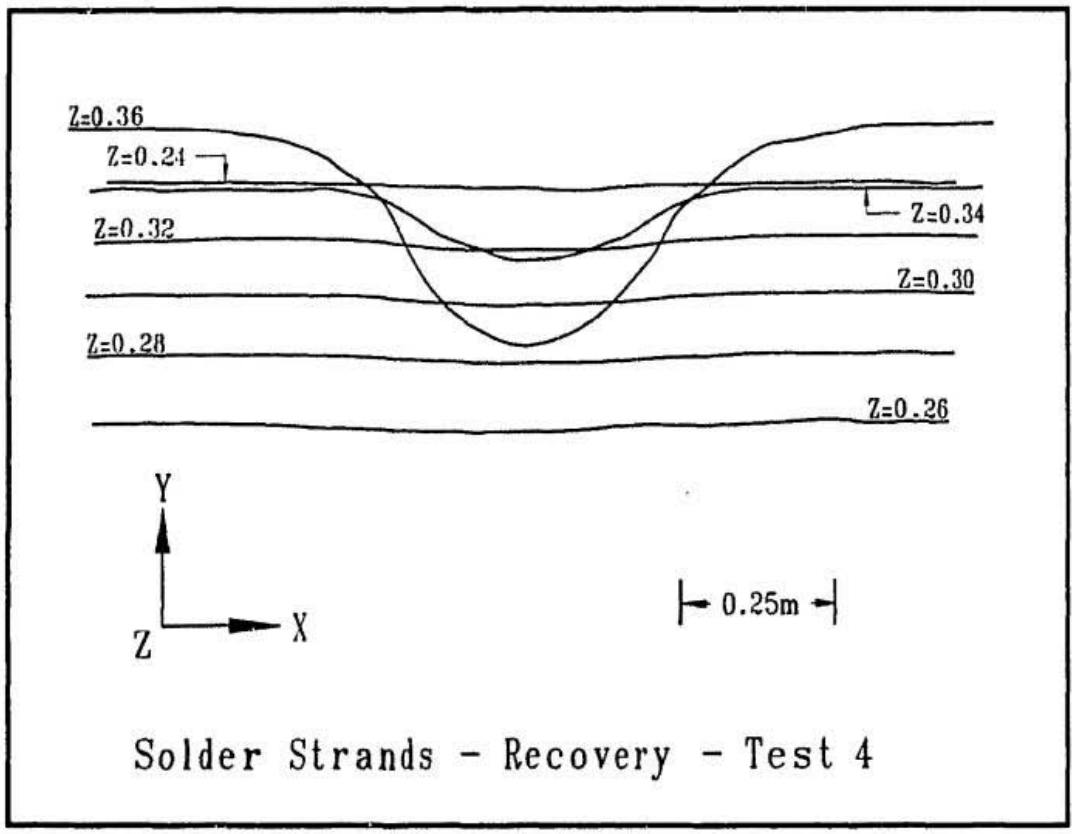

Solder Strands - Recovery - Test 4

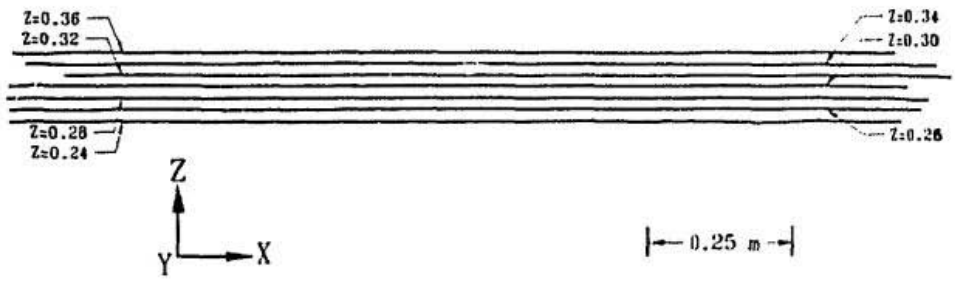

Solder Strands - Deployment - Test 4

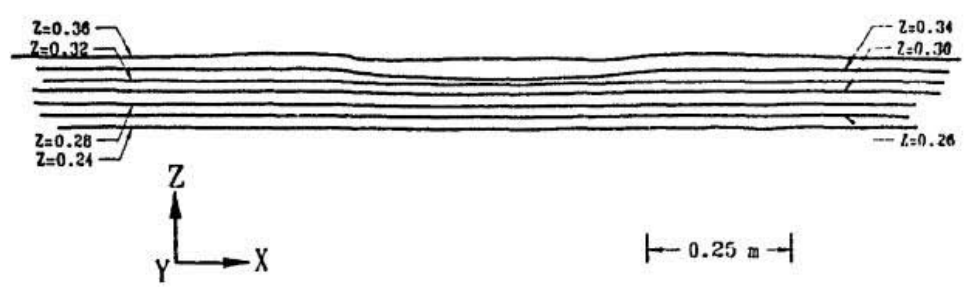

Solder Strands - Recovery - Test 4